The seismic activity associated with the large 2010 eruption of Merapi volcano, Java : source location, velocity variation, and forecasting

Agus Budi Santoso

UNIVERSITÉ DE GRENOBLE

THÈSE

Pour obtenir le grade de

DOCTEUR DE L'UNIVERSITÉ DE GRENOBLE

Spécialité : **Science de la Terre, de l'Univers et de l'Environnement**

Arrêté ministériel : 7 août 2006

Présentée par

Agus BUDI SANTOSO

Thèse dirigée par **Philippe LESAGE**

préparée au sein du **l'Institut des Sciences de la Terre (ISTerre), Université de Savoie,** et de **l'École Doctorale Terre, Univers, Environnement**

The Seismic Activity Associated with The Large 2010 Eruption of Merapi Volcano, Java: Source location, velocity variation, and forecasting

Thèse soutenue publiquement le **31 Mars 2014**,
devant le jury composé de :

Sylvie VERGNIOLLE
Directrice de Recherche à l'IPG Paris, Rapporteur
François BEAUDUCEL
Physicien de l'INSU à l'IPG Paris, Rapporteur
Philippe JOUSSET
Chercheur au GFZ Potsdam Germany, Examinateur
SURONO
The Head of Geological Agency Bandung Indonesia, Examinateur
Olivier COUTANT
Physicien de l'INSU ISTerre Grenoble, Examinateur
Jean-Luc GOT
Professeur Université de Savoie, Examinateur
Eric LAROSE
Chargé de recherche au CNRS ISTerre Grenoble, Invité
Philippe LESAGE
Maître de Conférences HDR Université de Savoie , Directeur de thèse

Université Joseph Fourier / Université Pierre Mendès France / Université Stendhal / Université de Savoie / Grenoble INP

Abstract

The 2010 eruption of Merapi is the first large explosive eruption of the volcano that has been instrumentally observed. In this work, we study the eruption precursors and the pre-eruptive volcano behaviour by linking seismic features with other available observations. The main characteristics of the seismic activity during the 2010 crisis, including the chronology of seismicity, the spatio-temporal evolution of earthquake source positions and the seismic velocity changes, are presented.

By performing absolute and relative locations, we obtain evidences of aseismic zones which are consistent with earlier studies and are interpreted as more ductile zones. Magma migration from the deep to the shallow part of the conduit through the upper aseismic zone is revealed by an upward shift of the hypocenters.

We analyse the seismic energy quantified by RSAM calculated for several frequency bands. These functions display clear accelerations in the last few weeks before the eruption. This behaviour is used to perform hindsight eruption forecasting with the Material Failure Forecast method (FFM). The onset of the first eruption is estimated with a good precision.

We propose an original method of event detection based on energy ratio. Using this method and waveform correlation, we identify 10 families of similar earthquakes. The seismic multiplets are located either below or above the upper aseismic zone and are composed of either volcano-tectonic or low-frequency events. Some of the clusters were active during several months before the eruptive crisis while a family that includes 119 repeating events appeared 20 hours before the eruption onset.

Seismic velocity variations associated mainly with magmatic activity are estimated using the coda of both multiplets and noise cross correlation functions. These variations display strong temporal and spatial variability of their amplitude and sign. Although they cannot be described by a unique simple trend, these velocity variations can be considered as an eruption precursor.

Using the preceding results together with other observations, we determine the specific features associated with the large explosive eruption of 2010. Furthermore, we propose a chronological scenario of the pre-eruptive activity of Merapi 2010 unrest.

Résumé

L'éruption de 2010 du Merapi est la première grande éruption explosive du volcan qui a été observée instrumentalement. Dans ce travail, nous étudions les précurseurs de l'éruption et le comportement du volcan avant l'éruption en reliant les caractéristiques sismiques avec d'autres observations disponibles. Nous présentons les principaux aspects de l'activité sismique au cours de la crise de 2010, tels que la chronologie de la sismicité, l'évolution spatio-temporelle des positions de source de séisme et les changements de vitesse sismique.

En effectuant des localisations absolues et relatives, nous obtenons des preuves de l'existence de zones asismiques, concordant avec des études antérieures, que nous interprétons comme des zones plus ductiles. La migration du magma de la partie profonde à la partie superficielle du conduit à travers la zone asismique supérieure est mise en évidence par un déplacement vers le haut des hypocentres.

Nous analysons l'énergie sismique quantifiée par le RSAM calculé pour plusieurs bandes de fréquences. Ces fonctions affichent des accélérations claires dans les dernières semaines avant l'éruption. Ce comportement est utilisé pour effectuer des prévisions d'éruption volcanique rétrospective avec la méthode « Material Failure Forecast » ou FFM. Le début de la première éruption est estimé avec une bonne précision.

Nous proposons une méthode originale de détection d'événement basée sur un rapport d'énergie. En utilisant cette méthode et la corrélation de la forme d'onde, nous identifions 10 familles de séismes similaires. Ces multiplets sismiques sont situés en dessous ou au -dessus de la zone asismique supérieure et sont composés soit d'événements volcano-tectoniques soit d'événements basse fréquence. Certains de ces groupes ont été actifs pendant plusieurs mois avant la crise

éruptive alors qu'une famille qui comprend 119 événements répétitifs est apparue 20 heures avant le début de l'éruption.

Nous estimons des variations de vitesse sismique, liées principalement à l'activité magmatique, en utilisant la coda des multiplets et les fonctions d'intercorrélation du bruit sismique. Ces variations montrent une forte variabilité spatiale et temporelle de leur amplitude et de leur signe. Bien qu'elles ne puissent pas être décrites par une simple tendance unique, ces variations de vitesse peuvent être considérées comme un précurseur de l'éruption.

En utilisant les résultats précédents ainsi que d'autres observations, nous déterminons les particularités associées à la grande éruption explosive de 2010. En outre, nous proposons un scénario chronologique de l'activité pré- éruptive du Merapi.

ACKNOWLEDGEMENTS

First and foremost I would like to thank Mr. Philippe Lesage as my thesis advisor for all I have learned from him and for his continuous help and support in all stages of this thesis. Both of his professional and personal quality inspired me very much. It has been an honor to be his Ph. D student.

Pak Surono, the former head office of the Pusat Vulkanology dan Mitigasi Bencana Geologi (PVMBG), he is the person who directed me to study with Mr Philippe Lesage. I appreciate all his support before and during my study. Thanks to Pak Subandriyo the Head office of Badan Penyelidikan dan Pengembangan Teknologi Kegunungapian (BPPTK) for his guidance and for allowing me to use the Merapi data in my thesis.

I would like to thank the Ministry of Energy and Mineral Resources of Indonesia for the doctoral scholarship. I acknowledge the European project of MIAVITA and VDAP USGS for the equipments of the broadband seismic stations and the short period stations respectively.

I acknowledge the kindness and hospitality upon the scientists and the students at Isterre Chambery that made me always enjoy working there. I appreciate the fruitful discussions with the experts like Jean Luc Got, Alain Burgisser, Virgine Pinel, and others.

I would like to thank my family, my parents for all their sacrifices, their love, and for their best wishes and supports. Thanks to my wife, to whom I talk my problems and my dreams with. She always cheers me up and stands by me through the good and bad times.

Finally, I am especially indebted to my thesis committee members: Syvie Vergniolle, Francois Beauducel, Philippe Jousset, Surono, Olivier Coutant, and Jean-Luc Got.

Table of Contents

ABSTRACT iii
ACKNOWLEDGMENTS vii
TABLE OF CONTENTS ix
LIST OF TABLES xiii
LIST OF FIGURES xv
Chapter 1 GENERAL INTRODUCTION 1
1.1 Background 1
1.2 Previous studies 5
1.2.1 Structural geology 5
1.2.2 Seismic studies 7
1.2.3 Other geophyisical methods 12
1.2.3.1 Deformation 12
1.2.3.2 Geoelectric Measurements 13
1.2.3.3 Gravimetry 14
1.3 Merapi seismic network 15
1.3.1 Historical review 15
1.3.2 Recent seismic network 16
1.3.3 Instrumental problems 18
1.4 Main features of Merapi seismic events 20
1.5 Thesis Structure 24
Chapter 2 SEISMIC CHRONOLOGY ASSOCIATED WITH THE 2010 ERUPTION 27
2.1 Introduction 27
2.1 Data and method 28
2.3 Seismic chronology during 2010 crisis 29

2.4 Discussion 37
2.5 Conclusion 41
Chapter 3 SOURCE LOCATIONS 43
3.1 Introduction 43
3.2 Data and method 44
3.2.1 Absolute and uncertainty estimation 44
3.2.2 Relative location using double difference method 46
3.3 Results 51
3.3.1 Absolute locations 51
3.3.2 Relative locations 53
3.3.3 Depths versus arrival time difference models 54
3.3.4 Temporal evolution of the hypocenter distribution 58
3.4 Discussion 59
3.4.1 Aseismic zone in Merapi eddifice 60
3.4.2 Magma migration 62
3.5 Conclusions and perspective 64
Chapter 4 RSAM AND ERUPTION FORECASTING 67
4.1 Introduction 67
4.2 Data and method 68
4.2.1 RSAM and modified RSAM (MRSAM) 68
4.2.2 Hindsight eruption forecasting 71
4.3 Results 73
4.3.1 RSAM and MRSAM 73
4.3.2 Eruption forecasting 76
4.4 Discussion 80
4.5 Conclusions 83
Chapter 5 FAMILIES ANALYSIS 85
5.1 Introduction 85
5.2 Data and method 87
5.2.1 Recursive event detections 88

5.2.2 Extraction of families 91
5.3 Results and discussions 94
5.3.1 Event detections 94
5.3.2 Families of events 100
5.4 Conclusions and perspectives 108
Chapter 6 VELOCITY VARIATIONS BASED ON CODA WAVE INTERFEROMETRY 111
6.1 Introduction 111
6.2 Data and method 114
6.2.1 Velocity variations in the coda of multiplets 114
6.2.1.1 Multiplets data 114
6.2.1.2 Doublet method 114
6.2.1.3 Stretching method 119
6.2.2 Velovity variations using noise correlation 120
6.2.2.1 Noise data 120
6.2.2.2 Data selection and time synchronization 123
6.2.2.3 Corrections of rain effects 126
6.2.2.1 2D location of velocity perturbations 128
6.3 Results 130
6.3.1 Velocity variations obtained from multiplets 130
6.3.2 Velovity variations obtained from noise correlation 136
6.4 Discussions 144
6.4.1 Comparison of the methods used 144
6.4.2 Velocity changes prior to the eruption 146
6.4.3 Comparison with earlier studies at Merapi 154
6.4.4 AVV and tectonic events 145
6.5 Conclusions and perspectives 156
Chapter 7 GENERAL CONCLUSSIONS 159
APPENDIX A 169
APPENDIX B 171

APPENDIX C 179

APPENDIX D 183

REFERENCES 189

LIST OF TABLES

3.1. Weighting and re-weighting parameters used in VTB and VTA cluster

6.1. Decrease rate and the cumulative decrease of each cluster recorded at PAS and PUS station calculated in some defined time periods. These time periods are chosen from which the linear decreasing trends are found.

B.1. Time delays of the maximum of NCF calculated on each station pair. The distance between station pairs are presented. It appears that there is no correlation between the time delay and the distance between stations. Low apparent velocities are displayed by the station pairs whose line path is in the north-south direction.

LIST OF FIGURES

1.1. Morphology of Merapi edifice seen from South flank before and after the 2010 eruption (Surono et al., 2012).

1.2. Structural evolution of Merapi before and after sector collapse during the period of Middle Merapi. Gunung Bibi is suggested to be a part of Pre-Merapi structure. The history of Merapi began 40.000 BP with a structure called as Ancient Merapi. It followed by Middle Merapi (began in 14.000 BP) where, a Saint Hellen type collapse occurred removing almost all new structure and the summit part of the Ancient Merapi. Middle Merapi period continued developing a new edifice. This structure is covered by the deposits of the eruption during Recent (2.200 BP) and Modern Merapi (1786). (Camus et al., 2000).

1.3. Cross-section of seismic hypocenters recorded on Merapi during 1991 (After Ratdomopurbo and Poupinet, 1995). The quasi-aseismic zone between the two clusters of VTA and VTB is interpreted as a shallow magma chamber. The absence of seismicity at depth >5 km might corresponds to the deeper magma chamber (Ratdomopurbo, 1995).

1.4. Location of seismic lines, source points, and mapped fracture zones. Profiles shown as dotted lines are not interpreted. Two circles mark the extend of possible weakness zone (Maercklin et al., 2000).

1.5. N-S cross section of the model resulted from regional events tomography zoomed for the area beneath Merapi. The background color is the result for P velocity anomalies.

1.5. N-S cross section of the model resulted from regional events tomography zoomed for the area beneath Merapi. The background color is the result for P velocity anomalies. Elongated ellipses show schematically distribution of channels, dykes, and lenses filled with magmatic material. Green lines indicate schematically sediment layers (after Koulakov et al., 2009).

1.6. Final 3-D model of the electric resistivity distribution under Merapi volcano (Muller and Haak, 2004). (A) Upper layer, 100 V m; (B) Intermediate conducting layer, 10 V m; (C) Conducting layer, 1 V m; (D) Central Conductor, 10 V m; (E) South–West anomaly, 1 V m; (F) Two 2-D extended conductors, 0.1 V m.

1.7. Monitoring network of Merapi and location of short-period and broadband stations, EDM reflectors and observation posts. Distance

from Kaliurang observation post to reflectors RK (dotted line) was measured by EDM. Another seismic station (CRM) located at 40 km south from Merapi is out of range of the map.

1.8. Operation intervals of seismic stations in 2009 and 2010. Black vertical line indicates end of year 2009. Dotted vertical lines show first eruption onset (26 October 10:02) and the largest eruption (4 November 17:01 UTC = 5 November 00:01 local time). Most of the stations were destroyed by the later eruption.

1.9. Clock synchronization by seismic noise cross-correlation. Two VT events recorded by stations LBH (top) and PUS (middle) when they were synchronized (a) and while GPS clock of LBH was out of order (b). Cross-correlation functions of noise (CCF, bottom panels) between the two stations when clocks were either synchronized (a) or not synchronized (b). Time lag between the two CCF is used to correct the clock drift.

1.10. Different types of seismic events observed at Merapi. For each sample, waveforms recorded at two stations and a spectrogram are displayed. a) Volcanotectonic type A (VTA). b) Volcanotectonic type B (VTB). c) Multiphase (MP). d) Low-frequency (LF).

2.1. Seismogram of the first precursory swarm of 31 October 2009. It lasted about 3 hours. Another larger VT event occurred about 3 hours afterward (right edge of plot).

2.2. Daily numbers of events for the period of September-December 2010. The panels (a) to (e) present the number of VT, MP, LF, rockfall, and pyroclastic flow events respectively. (f) The daily RSAM calculated during the crisis. The RSAM value on 5 November reaches 5 times that of 26 October. Dashed-dotted vertical lines indicate the change of the state of the alert level.

2.3. An episode of tremor that began on 1 October 2010 at 05:42. Top panel shows the seismogram recorded at station PUS; middle panel shows the spectrogram for this signal and illustrates the dominant frequency, overtones and gliding frequencies; lower panel is its spectrum.

2.4. A synthesis of the precursory data before the eruption 2010. The figure displays the number of VT and MP events (red line), the number of LF events (black), the distance measurements (blue), the tilt (magenta) and the ratio of CO_2/H_2O content in gas (green).

2.5. Seismogram of station PUS on 4 November until station destruction (at ~21:30 UTC). Dotted vertical red line indicates onset of largest eruption at 17:01 UTC. Although record was saturated, the climatic eruption

could be detected using a low-pass filtered (f < 0.1 Hz) seismogram (bottom panel).

2.6. Comparison of cumulative energy release of VT and MP earthquakes during one year prior to several eruptions from 1992 to 2010.

3.1. An illustration of the events pairs assumed in hypoDD (Dunn, 2004). Several parameters to be defined related with the sensitivity in clustering and relocation process are demonstrated. MAXSEP is the maximum distance for which two event-pairs are defined to be a neighbor; MAXDIST is the maximum distance between an event pair and a station; and WDCT is the maximum distance between event-pair.

3.2. Hypocenters of VT earthquakes. a) Map of epicenters, b) N-S cross section, c) E-W cross section. Hypocenters are indicated by crosses, and shown with their 67 % confidence intervals (pink ellipses). d) Histogram of the hypocenter depths (black solid bar) and probability density function of source depths (black hollow bar), calculated using Monte Carlo method. e) Histogram of uncertainties on depth. f) Depths as a function of differences of P-wave arrival times between stations DEL and PUS.

3.3. Hypocenter of VT resulted from hypoDD using homogeny velocity model with VP=3km/s and VP/VS=1.86. (a) Lateral, (b) N-S cross-section, (c) E-W cross-section hypocentral distribution. (d) Histogram of depths. The errors <0.5km are plotted in (c). The events colors indicate the cluster number based on their waveform similarity.

3.4. Difference of arrival times between stations DEL- PUS (a), and PLA-PUS (b). Each clusters show separated values against the others.

3.5. (a) Geometrical model of source depth as a function of difference of arrival times between DEL and PUS stations, assuming straight ray paths. Arrival time differences are proportional to the differences of distance between the source and the two stations (r1 and r2). (b) Depth versus Δt (or tDEL-tPUS). (c) Comparison of the depths estimated by the geometrical model (circles), and by absolute (plus sign) and relative (stars) locations.

3.6. Elevations of events plotted as a function of time for periods of June-October 2010. Different cluster numbers are indicated by different colors as showed in the legend. Daily numbers of VTA and VTB events are shown by brown and black bars, respectively.

4.1. Illustration of SSAM and MRSAM calculation with 4 different earthquake types. (a) Seismogram containing LF, VTB, MP, and VTA events. (b) RSAM values (cyan diamond) and SSAM values in frequency band 1 – 3Hz (black circle), 3 – 5Hz (red star), and 5 – 10Hz (blue diamond). (c) MRSAM values.

4.2. Plot of the RSAM data for the period 13 September – 26 October 2010 following equation 4 for estimating the value of α. The straight red line is the linear fitting which correspond to $\alpha = 2.1$.

4.3. RSAM calculated from station PUS (dark blue area) and its cumulative value (black line) during 3 months prior eruption. Cumulative MRSAM in the frequency ranges 0.01-0.1 Hz (yellow line), 1-3 Hz (brown line), 3-5 Hz (green line), 5-10 Hz (magenta line), and 1-15 Hz (red line). Grey dashed vertical lines and arrows indicate main explosions. RSAM units are in arbitrary units (A.U.). The MRSAM of 1-3Hz is very small, thus, it huddles with the time axes.

4.4. a) SSAM and its cumulative value for the range 1-3 Hz. b) MRSAM in frequency band 1 – 3Hz and its cumulative value c) Same as b, after removing tectonic events A marked increase of LF activity appears more clearly in the last few days before the eruption. SSAM and MRSAM values are in arbitrary units (A.U.). Grey dashed lines indicate the eruption times.

4.5. Cumulative RSAM (black line) before eruptions. Theoretical curves calculated with FFM with fitting windows from 13 September to 5 October (red line) and from 7 October to 26 October (blue line). RSAM units are in arbitrary units (A.U.). Grey dash lines indicate the eruptions.

4.6. Difference between predicted time t_f and time of eruption onset t_{erupt} as a function of ending time of the fitting window t_{end}, and calculated with t_{start} = 7 October. Observations are a) unfiltered RSAM, b) MRSAM in the frequency range 0.01-1 Hz, c) same for 3-5 Hz, d) 5-10 Hz , e) 1-15 Hz, and f) variation of the slope distance measured by EDM.

4.7. Variation of the slope distance between Kaliurang observatory and the southern part of the summit (circle) and theoretical FFM curves (black lines) obtained with different end times of the fitting windows. Starting time is 7 October.

5.1. An illustration of the LTE/STE method. The time of LTE values corresponds to the middle of the windows, while for STE, the time corresponds to the end of the windows. An arrival time is defined when the ratio LTE/STE decreases dramatically at which the STE get the first perturbation of P-onset (middle). The time at which this decrease occurs

is identified by the absolute differentiated values of LTE/STE. To show more clearly how it works, we change the y-axis scale to logarithmic scale (bottom).

5.2. Cross-correlation matrix of a cluster before (a) and after alignment (b). Pixels around the diagonal get darker indicated a better correlation.

5.3. Arrival time detections using the methods of STA/LTA, LTE/STE, kurtosis, and MER for a saturated-event in low noise level (0.2) and high noise level (8) (a and b). Time deviations between calculated and defined arrival time at different noise levels (c).

5.4. The same as Fig. 5.3 for an unsaturated event.

5.5. The same as Fig. 5.3 for a small-onset saturated-event.

5.6. Difference between calculated arrival times and manual picks (a, c, e) and their histogram (b, d, f). Blue colors correspond to STA/LTA results and red colors indicate the improved times using different methods as indicated in the legend.

5.7. Families of similar events recorded on PAS station. On the right part are the clusters waveforms, where the bold line is the stack of all the corresponding traces. The histograms of their daily occurrence are presented on the left part.

5.8. The same as Fig. 5.7 for events recorded at PUS station.

5.9. Spectra for the clusters obtained for PAS (blue) and PUS (red) stations. Cluster numbers are indicated.

5.10. Daily number of events in each group of clusters during September - October 2010. Deformation rate from Electronic Distance Measurement (EDM) of reflector RK4 is overlaid as the black line. Sharp increase of deformation rate at about 18 October 2010 corresponds to the strong increasing of VTB and the vanishing of VTA.

6.1. Illustrations of velocity change calculation using MWCS (doublet method) in noise cross-correlation function (NCF). Note that, the method works the same way on event coda data. (a) Reference and current NCF. (b) Zoom of the late part of time lapse of (a). (c) Time delay estimation from the phase of the cross-spectral of corresponding window. (d) Time perturbation estimation through linear regression of time delays versus time, which is equal to the velocity perturbation (Hadziioannou, 2011).

6.2. Illustration of velocity change estimation using stretching method. (a) The reference and the current signal at date x. (b) – (d) Same as (a) but after stretching of the current signal with different stretching degree(ε)

as indicated on (e). (e) Correlation coefficient obtained from cross-correlation between the reference and current signal at different stretching degree corresponding to the figure (a) – (d). It appears that they are better correlated at stretching degree $\varepsilon = -0.025$. This stretching degree is equal to the velocity change estimation (Hadziioannou, 2011) .

6.3. RCF obtained from all the station pairs. All their maximum values are located on the causal part except for pair PUS-KLA.

6.4. The daily NCF of DEL-PLA pair during June – October 2009 before (a) and after data rejection (b). It appears that after the data rejection the NCF are cleaner and better aligned. The values of NCF in the interval +/-5s were set to zero in order to display more clearly the coda part (c). Here we can see very late arrivals at time lag of up to 40s.

6.5. The maximum correlation time lag of NCF of station pair DEL-PLA before and after correction.

6.6. Velocity variations obtained from station pair DEL-PLA during the period before reinstallation using the causal part (top) and the anti-causal part (bottom) before (red) and after time lag correction (blue).

6.7. (a) The velocity change obtained from KLA-PLA (blue) is overlaid with the fitted GWL (red). (b) The corrected AVV obtained subtracting the fitted GWL from AVV. (c) The precipitation data (blue) is taken from Selo Post Observatory from which the GWL curve is generated.

6.8. Velocity changes obtained by the methods of stretching (a) and MWCS (b) for the shallow clusters recorded at PAS (left) and PUS (right).

6.9. Velocity changes obtained by the methods of stretching (a) and MWCS (b) for the deep clusters recorded at PAS (left) and PUS (right).

6.10. Cross-plot between velocity variations of cluster 10 using stretching method (red line) and absolute value of amplitude of DEL seismogram filtered on 0.1 – 1Hz (black line). The peaks of the seismogram correspond to VT events except those marked with other types of event e.g. T for tectonic event and auto-zero signal. The eruption onset is indicated by dot line. Auto-zero signal is generated periodically by the modulator to reset the seismogram offset.

6.11. Apparent velocity variations (AVV) obtained from NCF for different station pairs as indicated by the legends. (a) AVV of station pairs without PUS. (b) AVV of station pairs composed by PUS. The vertical lines indicate specific events related with volcanic (diamond marker) and tectonic (circle marker) activity. Regarding the volcanic activity, those are VT swarms (black dot line), felt VT (pink dot line); large LF's (green dot line), and first eruption (black dot line). As for tectonic

activity, they are classified into 3 groups based on their distance from the volcano and magnitude i.e. 0-50 km with magnitude > 4 (blue line); 50-150km with magnitude >5 (red line); >150km with magnitude >6 (green line).

6.12. Same as Fig. 6.12 but after rain effects corrections. Only the pairs PUS-KLA, KLA-PLA, and DEL-PLA experience significant corrections, since the other pairs have low correlation with the GWL.

6.13. The same as Fig. 6.13. but zoomed in period of August to October 2010.

6.14. L curve for different λ (indicated in the legend). Each point of the curve corresponds to different values of σ_m. The best parameters for which both the residual (miss fit) and the maximum velocity change are minimal are $\lambda = 1$ and $\sigma_m = 0.1$.

6.15. Modelled AVV (blue crosses) corresponding to each AVV measurement (red circles with error bars) of each station pairs at different time lags. The observed AVVs are well fitted with the modelled ones.

6.16. Velocity variations in an area of 15x15 km^2 around the volcano for the period around 21 October (a), 23 October (b), 26 October (c), and 3 November (d). The 4 stations and 6 station pairs used in calculation are indicated by black diamonds and white lines respectively. Two other stations used in earlier studies are marked by stars. The position of the summit is shown by a red circle. We can observe an increase in velocity around the lower flank and a decrease on the highest south part of the volcano.

6.17. Differences of velocity variation between the successive stages of 23 and 21 October (a); 26 and 23 October (b); and 3 November and 26 October (c). The scale is different for each figure depending on the corresponding range of VV values.

6.18. Examples of AVV calculation using MWCS method on the 6 last events of cluster 2. (a) Time delays calculated by cross-spectral method for each event. The blue and red straight lines are the linear regression using the windows in time interval of 1 – 4s and 2 – 6s respectively. (b) The resulted AVVs from the 2 linear regressions of (a) for each event.

6.19. AVV for all station pairs and for clusters 2, 3, and 4 are plotted with the normalized daily histogram of VTA (brown bars) and VTB (black bars). The eruption times, as well as the tectonic events are indicated like in Fig. 6.11.

6.20. Same as Fig. 6.19 but zoomed in the period of September-November 2010. The stages of velocity changes are indicated by dashed line and

are marked by P1 to P5 which correspond to the days of 13 September, 21 October, 23 October, 26 October, and 3 November 2010. We performed localization of all the stages but P1 using the reference day of 12 October (solid line;R)

A.1. Effects of the simulation of saturation on the apparent velocity variation for the first event of cluster 3 at PAS estimated using the MWCS (a) and the stretching methods (b). The amplitude of the first event was cut at levels of 70% (saturation of 30%), 50% (saturation of 50%), and 30% (saturation of 70%) of the maximum amplitude.

B.1. Schematic illustration of the effect of inhomogeneous noise sources distribution on the degree of symmetry of cross correlation function. (a) Symmetric cross correlation between 1 and 2 obtained when the sources of noise are evenly distributed. (b) Asymmetric cross correlation (but symmetric travel times) associated with a nonisotropic distribution of sources (from Stehly et al., 2006).

B.2. Map of the short period station (triangles) network on Merapi and the line paths of the station pairs (black lines). Summit is indicated by a star.

B.3. NCF obtained from all the station pairs. All their maximum values are located on the causal part except for pair PUS-KLA.

B.4. Satellite Image of the area showing Merapi volcano and the noise back azimuth angle of 20° which points to the city of Yogyakarta and the Indian Ocean.

B.5. Numerical simulation of the asymmetry of the reconstructed GF. (a) 40 sources S are aligned along x-axis (crosses). The reference point is at the center of the plot, indicated by a "+". (b) Snapshot of the cross-correlation between the field in A with the one at location (x,y) after averaging over the sources S for correlation time -30s. The converging wavefront is only partially reconstructed in the direction of the sources. (c) Snapshot for the correlation time t = 0s; the wavefront is focused on A. Note the high level of remaining fluctuations; (d) Snapshot for t = 30s; the diverging wavefront is defined only in the direction opposite to the source region (from Larose, 2006).

C.1. (a) The velocity change obtained from DEL-PLA (blue) is overlaid with the fitted Ground Water Level (GWL; red). (b) The corrected AVV obtained subtracting the fitted GWL from AVV. (c) The precipitation data (blue) is taken from Selo Post Observatory from which the GWL curve is generated.

C.2. The same as Fig. C.1. for the station pair of PUS-KLA.

C.3. The same as Fig. C.1. for the station pair of PUS-PLA.

C.4. The same as Fig. C.1. for the station pair PUS-DEL.

C.5. The same as Fig. C.1. for the station pair KLA-DEL.

D.1. Location of velocity change for the date of 21 October 2010 with a reference date of 12 October 2010 using parameters values of $l^* = 0.1$ km; $v = 1.3$km s^{-1}, $\lambda = 1$ km ; and varying σ_m of 0.05 (a), 0.1 (b), and 0.5 (c).

D.2. Same as Fig. D.1 using parameters values of $l^* = 0.1$ km; $v = 1.3$ km s^{-1}; $\sigma_m = 0.1$ km ; and varying λ of 0.6 (a) and 1.5 km (b).

D.3. Same as Fig. D.1 using parameters values of $\lambda = 1$ km; $v = 1.3$ km s^{-1}; $\sigma_m = 0.1$ km ; and varying l^* of 0.05 (a) and 1 km (b).

D.4. The same as Fig. D.1 using parameters values of $l^* = 0.1$ km; $\lambda = 1$ km; $\sigma_m = 0.1$ km ; and varying v of 1 (a) and 2 km s^{-1} (b)

D.5. Modelled AVV (blue crosses) and measured AVV (red circles with error bars) of each station pairs at different time lags for the stage of 23 October

D.6. The same as Fig. D.5 for the stage of 25 October

D.7. The same as Fig. D.5 for the stage of 3 November

Chapter 1

General introduction

1.1 Background

Merapi volcano is located in the middle of Java Island, where the Indo-Australian Plate is subducting under the southeastern margin of Eurasian continental Plate with the speed of 6 – 7cm/yr (Hamilton, 1979). Administratively Merapi is on the intersection between the two provinces of Jawa Tengah and Yogyakarta. Merapi volcano was born in the period of late Pleistocene - Early Holocene. It is situated at the intersection between two main volcanic alignments Ungaran-Telomoyo - Merbabu - Merapi (N164E) and Lawu - Merapi -Sumbing-Sindoro-Slamet and between two main quaternary faults, Semarang transversal fault (north south) and Solo longitudinal fault (east west) (Neumann van Padang, 1951; Kusumadinata et al., 1979).

Historical Merapi eruptions in the last two centuries before 2000 were reconstructed by Voight et al. (2000). Until 2010, there were about 50 eruptive episodes recorded with magnitude of up to 4 VEI, where magnitude (Pyle, 2000; Surono et al., 2012) is given by $M_e = \log_{10} m_e - 7$ (m_e = mass of eruptive products in kg). Most of the eruptions are considered to be small to moderate eruptions with VEI < 3. Typical Merapi eruption activity is associated with dome-collapse pyroclastic flows. Those eruptions were interrupted by at least 5 larger eruptions characterized by total dome destruction and fountain-collapse pyroclastic flows. The large eruptions mostly occurred in the 19th century. There were 4 large eruptions (VEI ≥ 3) including the 1872 (VEI of 4), whereas, there was only one eruption considered as large eruption in the 20th century in 1930.

It appears that the past eruptions are characterized by larger magnitudes (Voight et al., 2000; Camus et al., 2000). However the recurrence of violent explosive phases in 1768, 1822, 1849, 1872, and 1930–1931, suggests a high possibility of unusual large eruption in the future as a continuation of the previous behaviour (Camus et al., 2000). Indeed, the eruption 2010, the sole eruption in the century with VEI of 4, confirms this irregular eruption cyclic behavior, though its characteristics are different from the other VEI=4 eruption of 1872 (Innocenti et al., 2013; Costa et al., 2013).

Merapi 2010 eruption initiated on 26 October 2010 at 17:02 local time with an explosive eruption excavating ~$6x10^6$ m^3 of material (mainly non juvenile), destroyed more than 600 ha area (Charbonnier et al., 2013; Jenkins et al., 2013) and caused fatalities of 35 persons (Surono et al., 2012). It was then followed by many other eruptions until it peaked on 5 November 2010 at 01:00. The largest eruption of 5 November was preceded by an increasing tremor starting one day before which could be felt in a radius of 10 – 20 km from the summit with intensity of 2 – 3 on the Mercalli scale. More than 22 km^2 of area (Charbonnier et al., 2013) was destroyed by the 2010 eruptions. Despite an evacuation of almost 500 thousand people (Mei et al., 2013), about 347 people were killed. The dense-rock equivalent volume of erupted juvenile material is about 0.02 – 0.05 km^3 corresponding to a mass of $6x10^{10}$ – $1.2x10^{11}$ kg which is the argument for VEI 4 determination (Surono et al., 2012). The morphological change indicates both explosive cratering and dome collapse during the eruption (Fig. 1.1).

Fig. 1.1 Morphology of Merapi edifice seen from South flank before and after the 2010 eruption (Surono et al., 2012).

The 2010 eruption is a special event of Merapi firstly due to its unusual large magnitude, and secondly because the activities were well monitored. During the 2010 crisis, monitoring system of Merapi consisted of multidiscipline approaches such as seismic, deformation, and geochemistry. There were 10 seismic stations of Broadband (6 stations) and Short Period seismometer (4). One of the stations, located at a distance of 40 km from the volcano, had been useful for monitoring the eruption activity while the other stations on the volcano were saturated or destroyed. During the eruption the stations located around the volcano were destroyed one by one; where, the most distant station is the latest station being destroyed.

The deformation monitoring system is composed of tiltmeter stations and EDM. There were 2 tiltmeter stations installed at the north-west and south-east summit sectors before the eruption. Unfortunately not many data could be well transmitted to the observatory. As for EDM, there were 12 reflectors installed around the crater rim and 6 measurement posts which somewhat covered all directions. Slope distance between summit reflectors and measurement posts were measured first daily and then more frequently during the increasing activity.

Regarding geochemistry, in-situ monitoring of volcanic gas emissions (H_20, SO_2, CO_2, H_2S, CO, HCl, H_2, O_2, and CH_4) was carried out by collecting samples

(normally, every month) from the summit solfatara. Sampling was done by bubbling the gas through NaOH solutions contained in evacuated flasks (Giggenbach and Goguel, 1989). Measurement of insoluble gas in the NaOH solution was carried out by gas chromatography. The dissolved gasses were analyzed using spectrometric and volumetric methods (Surono et al., 2012). In addition, during the eruption some observations were carried out i.e. satellite images, realtime GPS measurements, and SO_2 remote sensing using DOAS and satellite images.

Many scientific papers have been published on the Merapi 2010 eruption in seismological aspects (Budi-Santoso et al., 2013; Jousset et al., 2013; Luehr et al., 2013), deformation (Saepuloh et al., 2013), geochemistry and petrology (Innocenti et al., 2013; Innocenti et al., 2013; Troll et al., 2013; Nadeau et al., 2013; Costa et al., 2013; Borisova et al., 2013), eruption product distribution, impact and deposit time scale (Bignami et al., 2013; Cronin et al., 2013; Charbonnier et al., 2013; Komorowsky et al., 2013; Jenkins et al., 2013; de Belizal et al., 2013), and in social and health aspects (Mei et al., 2013; Picquout et al., 2013; Damby et al., 2013).

Merapi volcano is interesting for the researchers and dangerous at the same time. It is interesting mainly due to its typical eruptions and short eruption interval (2 – 7 years) providing abundant and periodic data to be analyzed and to evaluate the previous results. On the other side its frequent eruption endangers tens of thousands population living in the disaster-prone area. For that reason, mitigation improvement is always concerned either by the governments, the non-government organizations, and people in general. The upstream of mitigation system is the monitoring of volcanic activity since all the branches of mitigation actions are activated based on the state of volcanic activity and the predicted scenarios.

The prediction of volcanic activity is typically based on two aspects i.e. the historical data of volcanic activities and current activity data. Therein, the important role of a volcano monitoring system is laid. Each monitoring system of volcanic activity aims at:

1. Identifying the level of current activities

2. Recognizing the current process and estimating the subsequent process

3. Predicting the potential of an eruption; its time and magnitude

4. Understanding the volcanic activity/eruption behaviour and its cycle

The more complete and continuous data available, the better study and prediction of eruptive activity could be achieved.

1.2 Previous studies

1.2.1 Structural Geology

Merapi structural history is divided into four Periods: Ancient, Middle, Recent and Modern Merapi, as revealed by field studies and geochronological data (Camus et al., 2000; Berthommier et al., 1990). The Ancient Period may have begun around 40 000 yr BP and lasted until 14 000 yr BP when the Middle Period begun. It lies on the basalt and basaltic older structure (Pre-Merapi). Auto-brecciated lava flows, St. Vincent-type pyroclastic flows and lahar deposits compose this structure. Saint Helens-type Edifice collapse took place during the Middle Merapi period which eroded the upper part of the Ancient Merapi structure. A new structure was rebuilt through the next eruptive episodes. The Middle Merapi structure was covered by the deposits of the Recent Merapi eruptions which began around 2200 yr BP. The summit part of Merapi is dominantly composed by the lava of the Modern Merapi eruptions (after 1786)

(Camus et al., 2000; Berthommier et al., 1990). The structural model of Merapi evolution based on these periods is presented below (Fig 1.2).

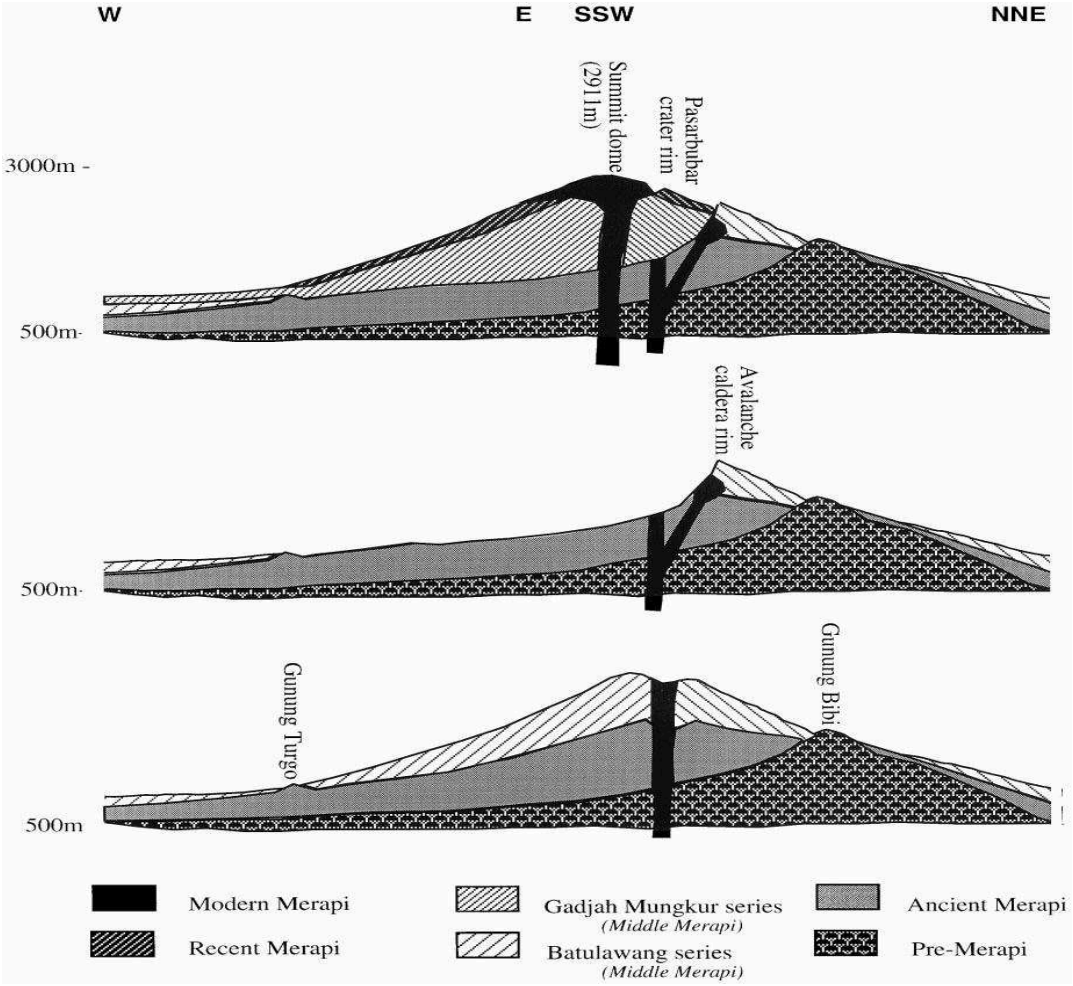

Fig. 1.2 Structural evolution of Merapi before and after sector collapse during the period of Middle Merapi. Gunung Bibi is suggested to be a part of Pre-Merapi structure. The history of Merapi began 40.000 BP with a structure called Ancient Merapi. It is followed by Middle Merapi (began in 14.000 BP) when a St Hellens type collapse occurred removing almost all the new structure and the summit part of the Ancient Merapi. Middle Merapi period continued developing a new edifice. This structure is covered by the deposits of the eruption during Recent (2.200 BP) and Modern Merapi (1786). (Camus et al., 2000).

1.2.2 Seismic studies

Some geophysical surveys were conducted to study the subsurface structure of Merapi. Based on the distribution of Volcano-tectonic (VT) events, Ratdomopurbo (1995) hypothesized a magma chamber located at depth >5 km and a secondary magma chamber located at 1.5 – 2.5 km depth. The absence of VT events at those two zones was interpreted as ductile zones with high temperature that might correspond to magma chambers (Fig. 1.3).

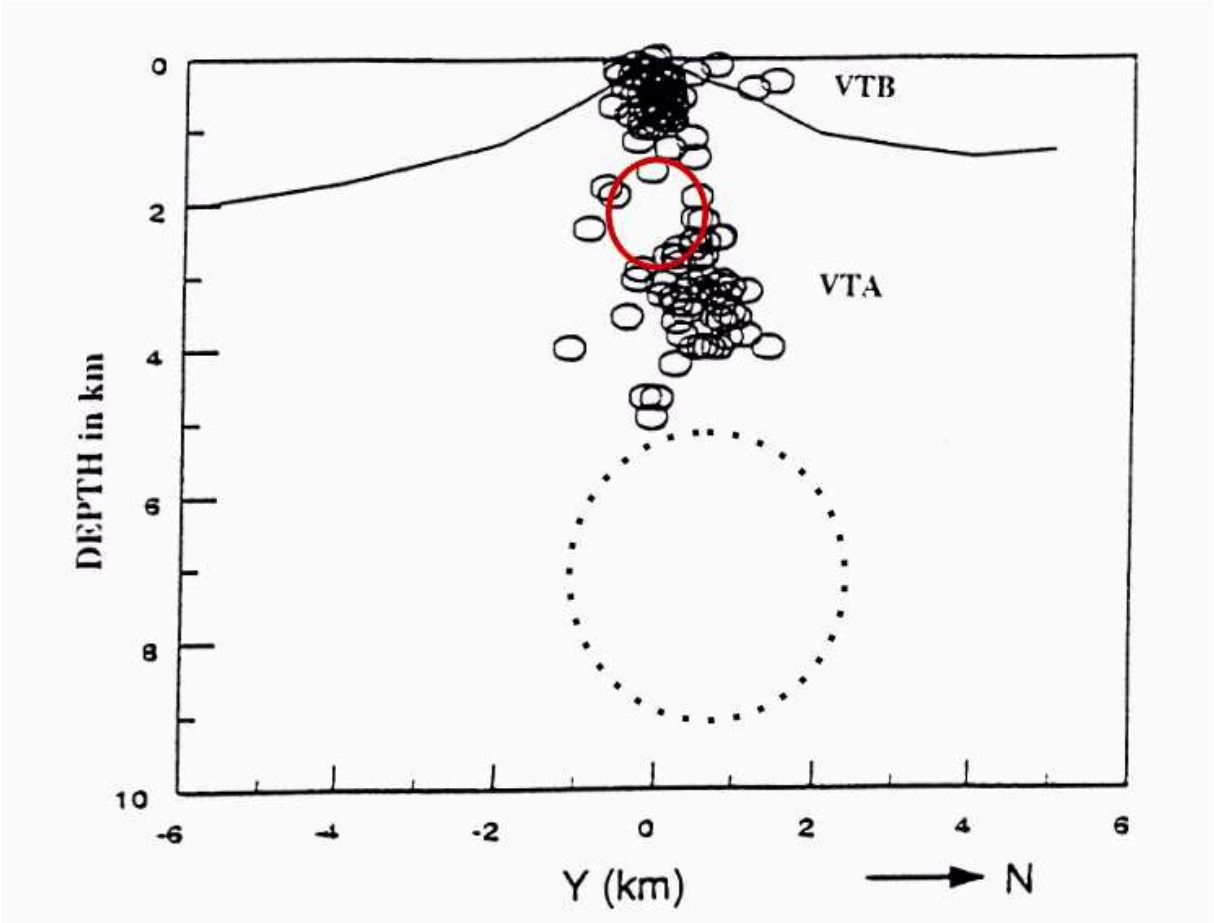

Fig. 1.3. Cross-section of seismic hypocenters recorded on Merapi during 1991 (After Ratdomopurbo and Poupinet, 1995). The quasi-aseismic zone between the two clusters of VTA and VTB is interpreted as a shallow magma chamber. The absence of seismicity at depth >5 km might corresponds to the deeper magma chamber (Ratdomopurbo, 1995).

Structural sounding were carried out using active artificial seismic sources in the framework of a cooperation between Volcanological Survey of Indonesia (VSI) and GeoForschungsZentrum Potsdam (GFZ) (Wegler et al., 1999; Wegler and Luhr, 2001; Maercklin, 1999; Wegler 2006). Three 3 km long seismic profiles, each consisting of up to 30 three-component seismometers with an interstation distance of 100 m, were built up in an altitude range between 1000 and 2000 m above sea level (Fig. 1.4).

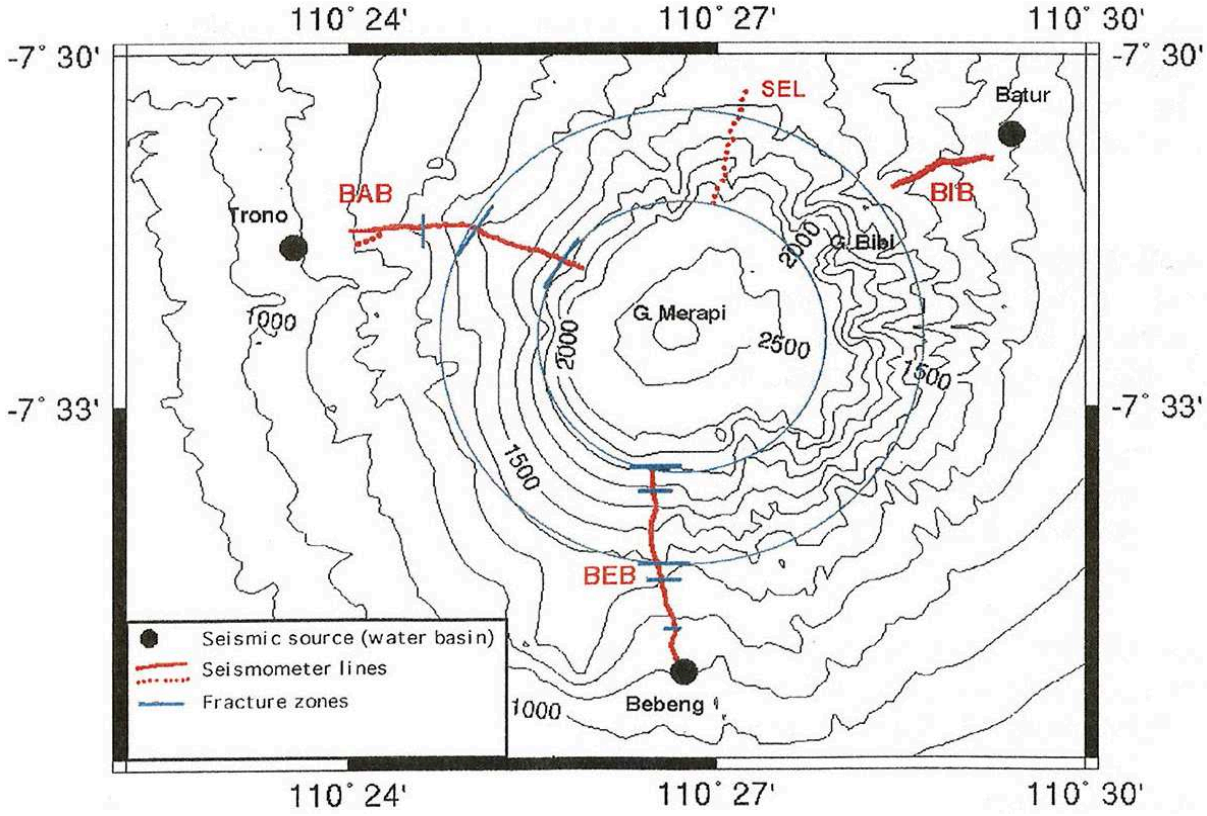

Fig. 1.4. Location of seismic lines, source points, and mapped fracture zones. Profiles shown as dotted lines are not interpreted. Two circles mark the extend of possible weakness zone (Maercklin et al., 2000).

The observed seismograms show a spindle-like amplitude increase after the direct P phase. This shape of envelope can be explained by the diffusion model. According to this model there are so many strong inhomogeneities that the direct wave can be neglected and all energy is concentrated in multiple scattered waves.

As a result of the inversion using the diffusion model, in the frequency range of 4–20 Hz used in this study, the scattering attenuation is at least one order of magnitude larger than the intrinsic absorption . The mean free path of S waves is as low as 100 m (Wegler and Luhr, 2001).

A low velocity layer above 300 m of depth was suggested where the velocities range from 0.7 to 3.4 km/s (Riedel et al., 1999). The south flank likely has lower velocity than the north-east flank which can be attributed to the different compactness of the different structural age (Riedel et al., 1999; Wegler and Luhr, 2001). In addition, according to Maercklin (1999), there are seismic reflectors which could be explained with a simple two dimensional model based on the ray theory, and it was shown that they are caused by open fissure zones.

A larger scale tomographic study including Merapi volcanic complex was done by Koulakov et al (2007; 2009) using body waves arrival times from tectonic earthquakes. In the crust beneath the middle part of central Java, north to Merapi and Lawu volcanoes, a large and very intense anomaly was observed with a velocity decrease of up to 30% and 35% for P and S models, respectively. Inside this anomaly, E-W orientation of fast velocity takes place that is probably caused by regional extension stress regime along the N-S direction. In vertical section beneath this anomaly, faster horizontal velocities were observed that might be explained by layering of sediments and/or penetration of quasi-horizontal lenses with molten magma (Fig. 1.5) (Koulakov et al 2009; Luehr et al., 2013).

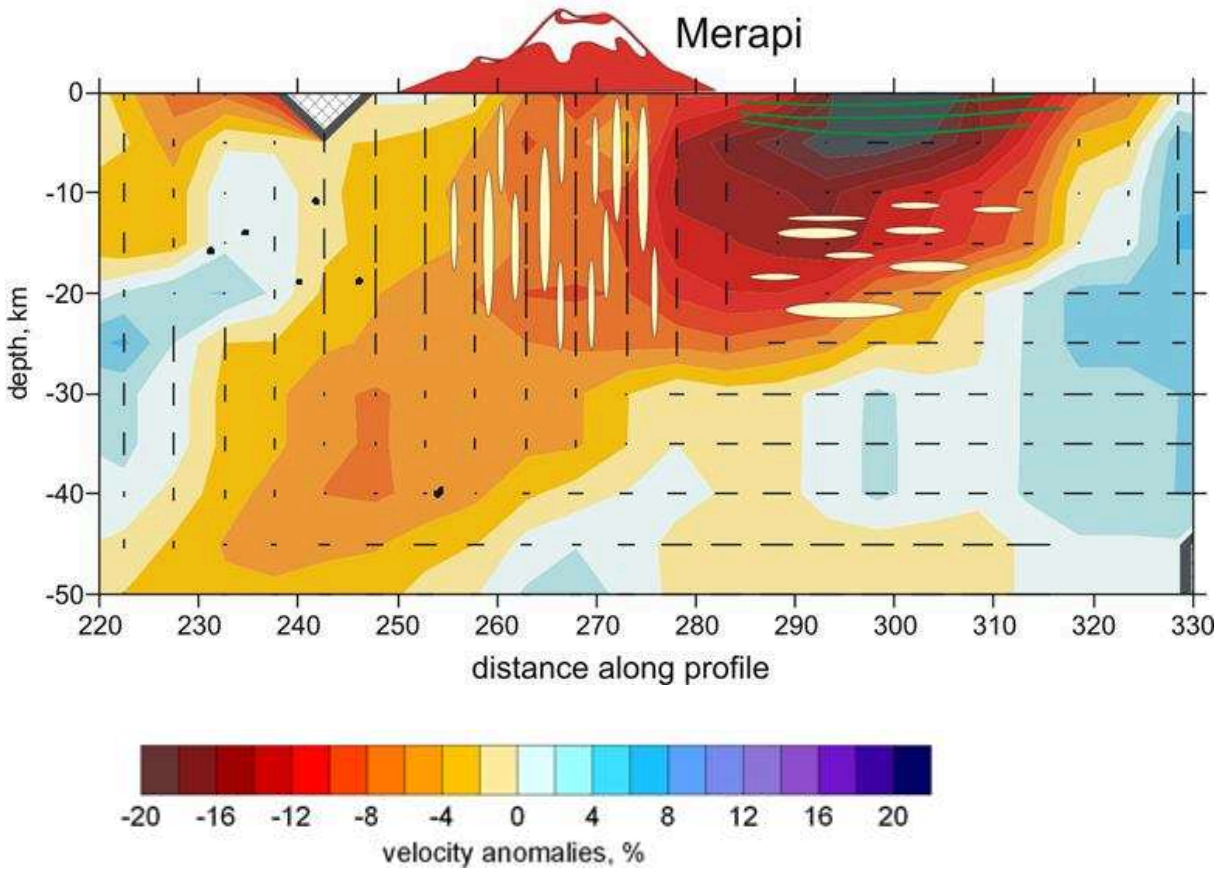

Fig. 1.5. N-S cross section of the model resulted from regional events tomography zoomed for the area beneath Merapi. The background color is the result for P velocity anomalies. Elongated ellipses show schematically distribution of channels, dykes, and lenses filled with magmatic material. Green lines indicate schematically sediment layers (after Koulakov et al., 2009).

Those tomographical studies could not confirm the existence of the aseismic zone suggested by Ratdomopurbo and Poupinet (1995; 2000) as a shallow magma chamber at depth between 1.5 and 2.5 km. Due to the very scattering behaviour of the shallow layer, the seismic waves recorded during the active source experiment (Wegler and Luhr, 2001) didn't contain much information of the deeper zone.

Eruptive precursors including seismic activity were reported by Ratdomopurbo and Poupinet (2000) regarding the activity from 1982 to 1995. There were two main eruptive cycles during this period, from 1984 to 1986 and from 1992 to

1994. Both cycles were preceded by VT earthquakes, whereas only the eruption of 1992 was preceded by tremor activity from more than 1 year before. A detailed chronology of pre-eruptive and eruptive activity of June 2006 was presented by Ratdomopurbo et al. (2013). The early precursors occurred in the middle of the year 2005 with seismic activity, increase in deformation, and possible increase of SO_2. The short term precursors were marked by an increase in number of VT, MP, and LF as well as deformation in the beginning of 2006.

Focal mechanisms of VT events recorded in 2000 - 2001 were estimated by Hidayati et al. (2008) using both polarity and amplitude of P-wave first motions. VTA and most deep VTB events are of normal-fault types, whereas VTB events located close to the surface yield both reverse and normal fault solutions. Hidayat et al. (2000; 2002) studied very long period (VLP) events that occurred in 1998 and determined that these have periods of 6 - 7 s, display similar waveforms from event to event, and are coeval with MP or LF earthquakes. They carried out moment tensor inversion of the waveforms and proposed a source model consistent with a dipping crack located at about 100 m depth under the 1998 dome. They suggested a source process involving the sudden release of pressurized gas through the crack over a time span of about 6 s. No VLP events were observed during the active periods of 2001 and 2006, whereas a significant number of VLP events were observed in 2010 prior to and during the eruption (Jousset et al., 2013).

Several works were dedicated to study the elastic property changes of the medium using seismic data. Based on the cross spectral method applied on the codas of similar events, Ratdomopurbo and Poupinet (1995) observed an increase of shear wave velocity of 1.2 % before the 1992 eruption.

Using the data of the active source experiment (Wegler et al., 1999; Wegler and Luhr, 2001; Maercklin et al, 1999; Wegler et al., 2006), Wegler et al. (2006) inferred temporal changes in the elastic properties of the edifice of Merapi before the 1998 eruption. They observed a total increase of seismic velocity of up to

0.23% in 2 weeks until 3 days after the eruption. Later, Sens-Schonfelder and Wegler (2006) reported a strong seasonal effect as a function of the Ground Water Level (GWL) of the velocity variation obtained from ambient noise with up to1 % of annual variation.

1.2.3 Other geophysical methods

1.2.3.1 Deformation

EDM measurements were conducted for the period of 1988 – 1994 on a summit trilateration network (Young et al., 2000). Cross-crater strain rates accelerated from less than 3 x 10^6/day between 1988 and 1990 to more than 11 x 10^6/day just prior to the January 1992 activity, representing a general, asymmetric extension of the summit during high-level conduit pressurization. During the effusive lava extrusion, strain decreased below the background level of less than 2 x 10^6/day. EDM measurements between lower flank and crater benchmarks during 4 years before the 1992 eruption revealed a long term displacements as high as 1m/year.

Later, in the period between November 1996 and March 1997, other deformation experiments were established using tiltmeters and GPS equipments (Beauducel and Cornet, 1999). An interpretation using a three-dimensional elastic model based on the mixed boundary element method and a near-neighbor Monte Carlo inversion lead to a suggestion of a magma chamber at the depth of 8 km below the summit and 2 km to the east of it. The estimated volume attributed to this magma chamber is about 11 x 10^6 m^3.

Within the Indonesia – German joint research project MERAPI, four tiltmeter stations were installed on the flank during 1995 – 1997 (Rebscher et al., 2000; Westerhaus et al., 2008). In spite of the absence of strong volcano-induced tilt anomalies, rapid, step-like drift changes were detected with amplitudes of 15 to 80 µrad which are generally related to the alternation of wet and dry seasons. Finite-Element-Modelling showed that sign and amplitude of these perturbations are compatible with a pressure source located 1.2 km below the summit with radius of 1.7 km which is consistent with aseismic zone revealed by hypocenter

distribution. These perturbations are interpreted as the effect of annual input of meteoric water to the pressure within deeper parts of the hydrothermal system on the central vent of Merapi (Westerhaus et al., 2008).

1.2.3.2 Geoelectric measurements

Based on DC resistivity survey, Friedel et al. (2000) developed resistivity models for the north, west, and south flanks with depth of investigation between 600 and 1000 m. For the high conductivity zones appearing in the West and South, a hypothesis was brought forward that the anomalies are caused by meteoric water penetrating highly permeable layers of volcanic deposits to great depth where it influences the extent of hydrothermal zones. In August 2000 a permanent SP and temperature monitoring station was established at the fumaroles field Woro. Correlations between SP, ground temperature anomalies, MP events and the appearance of lava dome during 2001 activity were observed (Friedel et al., 2004). Many SP anomalies and gas temperature coincided with the occurrence of Ultra Long Period (ULP) seismic events which are interpreted as the effects of gas emissions (Byrdina et al., 2003; Richter et al., 2004).

Muller and Haak (2004) derived a 3-D model of the electrical conductivity structure of Merapi volcano from magnetotelluric (MT) sounding and geomagnetic induction vectors (Fig. 1.6). The final model consists of two 3-D structures in the volcanic edifice, i.e. a central conductor (D) and a second conductor lying 5 km to the southwest of summit (E). The high conductivity material is probably hot saline water as suggested by position and lateral extent of the high conductivity material. Another conductive layer at the depth of 3.5 – 5.3 km (C) is attributed to a very porous regional layer containing seawater or fluid of comparable conductivity (Rittel et al., 1998; Muller and Haak, 2004).

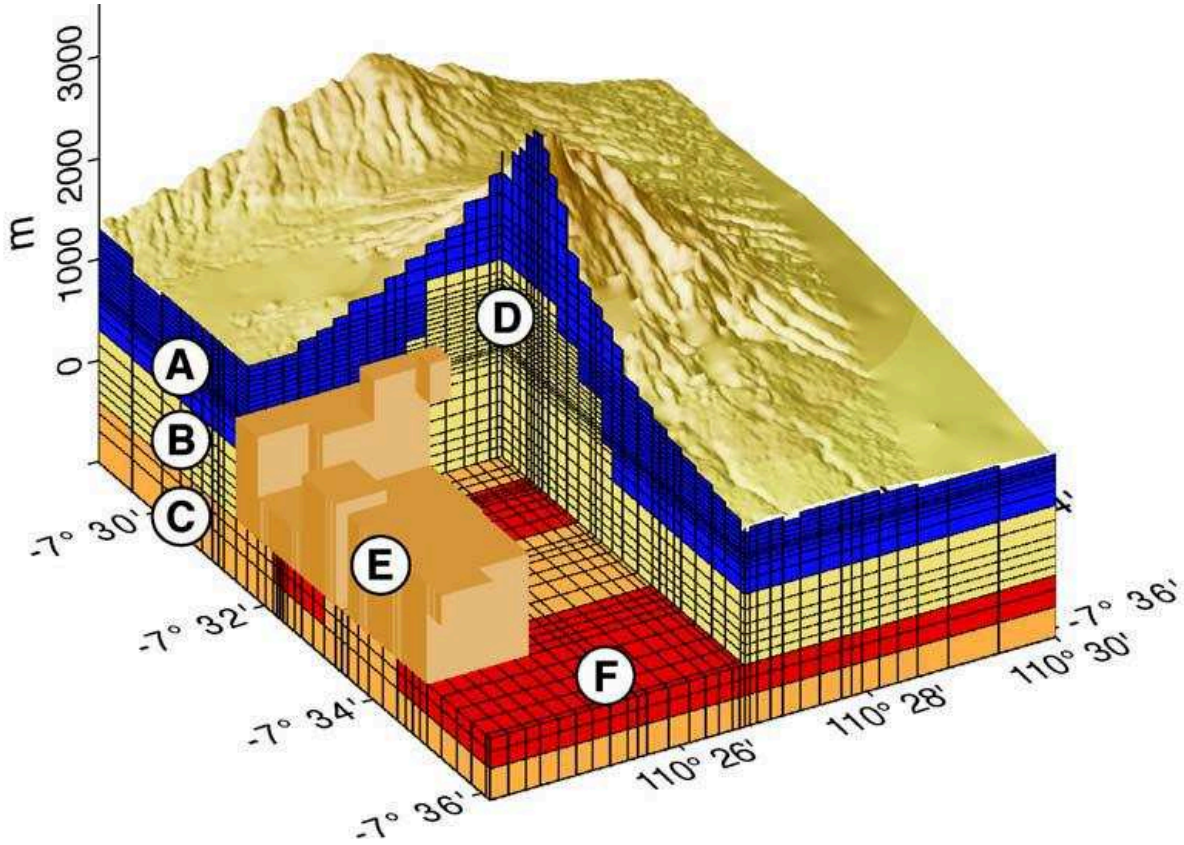

Fig. 1.6. Final 3-D model of the electric resistivity distribution under Merapi volcano (Muller and Haak, 2004). (A) Upper layer, 100 V m; (B) Intermediate conducting layer, 10 V m; (C) Conducting layer, 1 V m; (D) Central Conductor, 10 V m; (E) South–West anomaly, 1 V m; (F) Two 2-D extended conductors, 0.1 V m.

1.2.3.3 Gravimetry

Gravity measurements have been applied at Merapi both for mapping and monitoring purposes. The first gravity measurements around Merapi have been carried out by Yokoyama in 1970 (Yokoyama et al., 1970), Untung and Sato (1978). The Bouguer anomaly pattern shows that Merapi is characterized by a low anomaly centred on the summit area. A two-dimensional gravity model indicates that the material on the summit of Merapi area has a density contrast of –900 kg/m^3. Based on the model, there are three density values of Merapi: 2600 kg/m^3

around the foot, 1800 kg/m^3 in the mid-body, and 1600 kg/m^3 in the summit area. This model is calculated by assuming a mean regional density value of 2500 kg/m^3. The rocks in the summit areas are probably composed of sand, tuff, lava fragments and lava dome (Wahyudi, 1986; Sidik, 1987; Arsadi, et al., 1995b).

Continuous gravity monitoring and microgravity surveys including accurate levelling on Merapi volcano have been carried out by French-Indonesian teams during 1993 – 1995 (Jousset, 1996). Significant variations in gravity were observed for the period 1993-1994. The gravity increased by 100 to 400 µgal which was explained by the change of neighbouring topography due to the growth of the dome during the considered period. Residual drift of continuous data showed correlation with LF events and the occurrence of pyroclastic flows (Jousset, 1996).

1.3 Merapi seismic network

1.3.1 Historical Review

Monitoring volcanoes in Indonesia began in 1920 with the establishment of the Dinas Penjagaan Gunungapi by the Dutch East India Company (Dutch: Vereenigde Oost-Indische Compagnie, VOC). This establishment is a response to the eruption of G. Kelut in previous year which caused more than 5000 deaths. Shortly after, observation posts were established including at G. Merapi. In 1924 the first seismic station was installed at G. Merapi, with a Wichert type seismometer. It is an entirely mechanical seismometer, made in Gottingen (Germany). It is essentially an inverted pendulum, which records both components of horizontal motion on rolls of smoked paper. It weights 1000 kg, and has a natural period of 8 seconds. Damping is provided by two air-pistons on the top of the instrument. The pendulum is centered by placing a series of small weights on top of the main mass. This seismometer is no longer in operation, but is visible in BPPTK (Balai Penyelidikan dan Pengembangan Teknologi

Kegunungapian). This seismometer was installed at 14 km west of the summit (Neumann van Padang, 1933). He observed an increasing seismic activity before the eruption of 1930. In 1968, Shimozuru performed seismic observations by installing seismographs at about 10 km south of the summit. Seismic signals were recorded on magnetic tapes (Shimozuru et al., 1969). Using 6 months of observation, he proposed the first classification of events of Merapi and their associated physical process. He suggested that multiphase (MP) events are related with dome growth.

Along with the development of monitoring technology, monitoring system of G. Merapi was also improved. In 1982 telemetry system began to be implemented. In cooperation between USGS and VSI (Volcanological Survey of Indonesia, former of CVGHM, Centre of Volcanology and Geological Hazard Mitigation), 6 short period seismic stations were installed around G. Merapi whose data were transmitted directly to Yogyakarta using VHF telemetry system (Koyanagi and Kojima, 1984). In 2 January 1991 the seismic network was digitized by using a Data Translation board, a dedicated PC, a stabilized power supply and the PCEQ – IAVCEI software (J.-L. Got, pers. comm.), in the frame of the cooperation with the French foreign office. In August 1994, 6 more short period seismic stations were installed and digitized, among which the 3-component summit station, in the frame of the cooperation with the French CNRS (J.-L. Got, pers. comm.). Then in 1994 Broadband seismometers started to be used in Merapi with the cooperation between the VSI and the GeoForschungsZentrum Potsdam (Beisser et al., 1996).

1.3.2 Recent seismic network

The monitoring system of Merapi is operated by BPPTK, which belongs to CVGHM. Seismic network at Merapi is a combination of short period and broadband stations. At the beginning of 2010 (February to April) a major renovation was carried out. All instruments of short period stations have been replaced.

There were 4 short period stations equipped with L4C (1Hz) and L22 (0.5Hz) seismometers. Signals were transmitted to Yogyakarta by radio with VHF modulation and were digitized by a Güralp DM16S acquisition system at a rate of 100 samples per second with 16 bits accuracy. SP stations have been used as reference stations in routine analysis, such as event classification and counting, source location and seismic energy calculations. In addition, up to six broadband (BB) stations using Güralp CMG-40TD seismometers with period of 60 s and TCP/IP protocol for data transmission were operated between July 2009 and October 2010. Both types of stations use GPS clocks for synchronization and Güralp Compressed Format (GCF) for data file storage. Fig. 1.7 shows the configuration of the monitoring network; seismic stations are located on and around the volcano at distances to the crater ranging from 0 to 6 km.

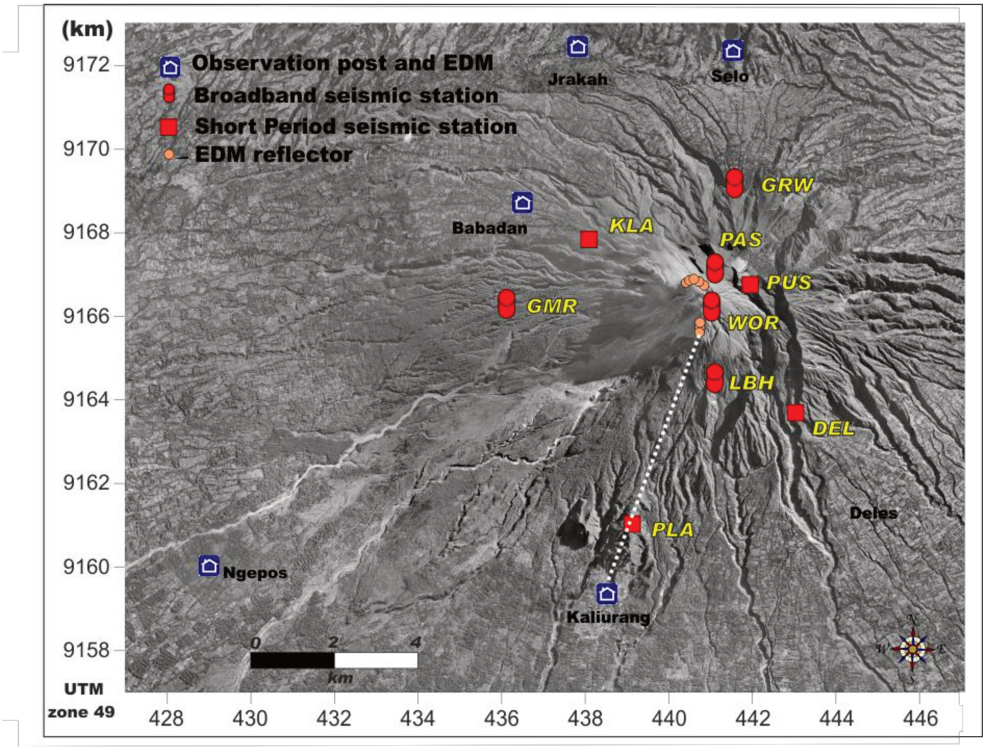

Fig. 1.7 Monitoring network of Merapi and location of short-period and broadband stations, EDM reflectors and observation posts. Distance from Kaliurang observation post to reflectors RK (dotted line) was measured by EDM. Another seismic station (CRM) located at 40 km south from Merapi is out of range of the map.

1.3.3 Instrumental problems

Replacements were carried out because of signal quality degradations. Noise came from electronic self noise of the modulator producing significant distortion of the signal. Their sensitivities had also declined. After re-installation, some problems appeared. There were periods when the signal polarities were inverted for some reasons. Noise coming from outside the system such as interference with some amateur radio communication distorted the signals quite frequently. Even though this kind of distortion wasn't continue, some treatment must be done before performing calculations especially those based on continuous data. The other problem is the limitation of a short period station i.e. amplitude saturation.

During the installation of broadband stations, new digital telemetry system was implemented. System based on TCP-IP protocol was chosen instead of conventional serial protocol. Despite the superiority in terms of transmission capacity, this system consumed much more power. In fact a typical power system consisting of a battery of 100 AH and 2 solar panels 40 W wasn't sufficient to allow the battery to be always in stable capacity. Some breakdowns in stations reduced the amount of available records during the 2010 pre-eruptive period (Fig. 1.8). Therefore, analysis based on continues data such as RSAM and noise cross correlation is difficult to perform on the broadband data.

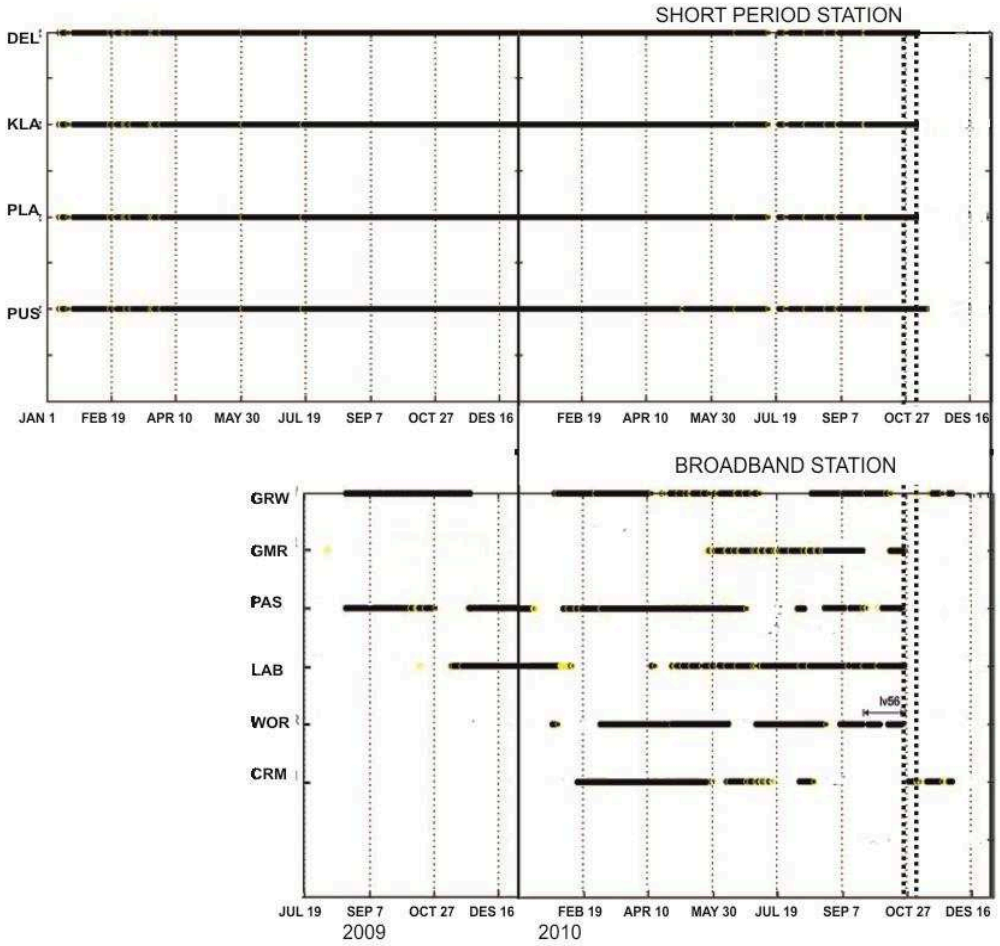

Fig. 1.8 Operation intervals of seismic stations in 2009 and 2010. Black vertical line indicates end of year 2009. Dotted vertical lines show first eruption onset (26 October 10:02) and the largest eruption (4 November 17:01 UTC = 5 November 00:01 local time). Most of the stations were destroyed by the later eruption.

Furthermore, the GPS clocks of some broadband stations failed during several time intervals. In order to use arrival times from these stations for source location, a procedure of clock re-synchronization, based on seismic noise correlation (Stehly et al., 2007; Sens-Schönfelder, 2008) was applied. The cross-correlation function (CCF) of the noise recorded in two stations is directly related to the Green function between the two sites (e.g. Campillo, 2006). When the clock of one of the stations has drifted, the CCF is delayed by the same lag with respect to that obtained when both clocks are synchronized. Thus, by looking for the

maximum of the correlation function between the shifted and the reference CCF, it is possible to estimate the delay and to synchronize the stations. An estimated precision of ~0.05 s was obtained with this approach, which uses low-pass (< 4 Hz) filtered signals (Fig. 1.9).

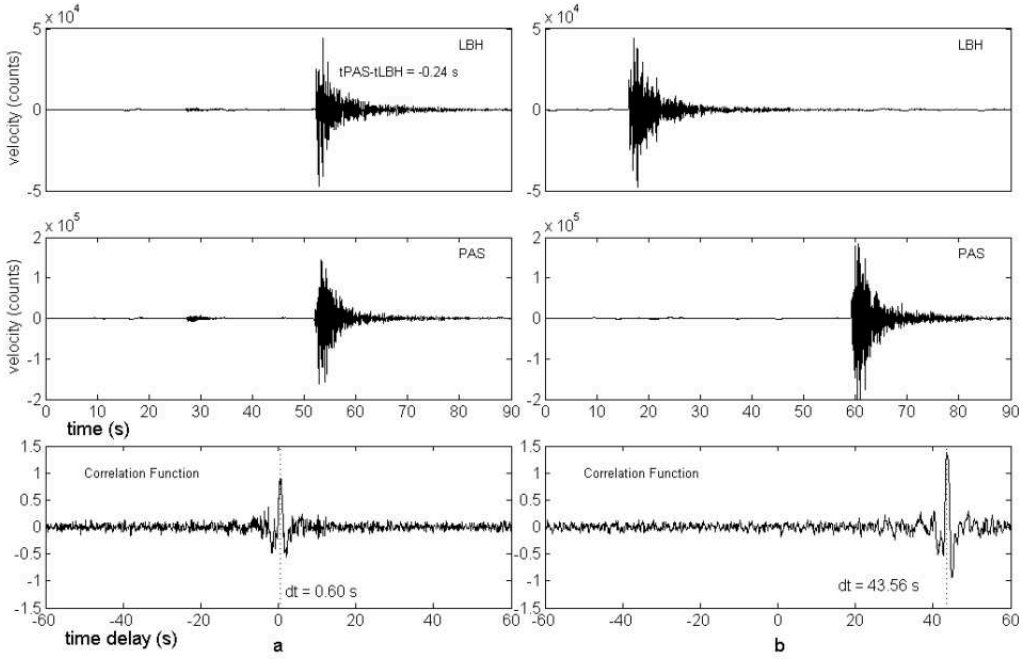

Fig. 1.9 Clock synchronization by means of seismic noise cross-correlation. Two VT events recorded by stations LBH (top) and PUS (middle) when they were synchronized (a) and while GPS clock of LBH was out of order (b). Cross-correlation functions of noise (CCF, bottom panels) between the two stations when clocks were either synchronized (a) or not synchronized (b). Time lag between the two CCF is used to correct the clock drift.

1.4 Main features of Merapi seismic events

For consistency, the same classification of seismic signals has been used at Merapi since the initial installation of a telemetered network in 1982 (Ratdomopurbo, 1995; Ratdomopurbo and Poupinet, 2000). The main types of signal are classified as volcanotectonic (VT), multiphase (MP), low-frequency (LF), rockfall (RF), and tremor. VT events are characterized by clear onsets and high frequency content (up to 25 Hz). These types of events are similar to

common tectonic earthquakes and are attributed to brittle failure of rock; they have mostly simple double-couple mechanisms (McNutt, 1996). The main difference with tectonic earthquakes are that VT events are related to volcanic activity, they frequently occur in swarms, and thus they do not follow main shock – aftershock progression (McNutt, 2000).

VTs at Merapi are sub-divided into deep (VTA) and shallow (VTB) events (Fig. 1.10). VTA events are characterized by hypocenters at depths greater than 2 km below the summit, and they have clear P- and S-wave arrivals. VTB events have depths less than 2 km and they have more emergent onsets at distant stations. For some VTB events, S-waves cannot be distinguished. VTA and VTB events are recognized principally by differences in amplitude ratios for the first arrivals between summit (PUS) and flank (DEL) stations. Differences in waveform and amplitude are probably related to greater degrees of scattering and attenuation for paths in the shallow parts of the structure (VTB) compared to deeper paths (VTA) (Wegler and Lühr, 2001).

Multiphase earthquakes are characterized by emergent onsets, maximum frequency of 4 to 8 Hz, and shallow depth (Fig. 1.10). These MP signals are similar to hybrid events in other classification schemes (McNutt, 1996). They are related to magma flow in the upper conduit and to dome growth (Ratdomopurbo and Poupinet, 2000). Their rate of occurrence is sometimes correlated with summit deformations (Beauducel et al., 2000).

Low-frequency earthquakes (LF), also sometimes called long-period (LP) events, have generally emergent onsets, lack S-wave arrivals, and have dominant peak frequencies in the range 1-3 Hz (Fig. 1.10). They are typically attributed to resonance of fluid-filled cavities resulting from pressure perturbations (Chouet, 1996). However, due to strong attenuation of the high-frequency waves, some events identified as LF at distant stations may be actually MP events (Hidayat et al., 2000). Very-Long-Period (VLP) events occurred at Merapi in 1998 (Hidayat et al, 2002) and 2010 (Jousset et al., 2013) but were not observed associated with

the 2001 and 2006 eruptions. VLP signals correspond generally to the low frequency component of MP or LF events and they are interpreted as mass transfer of fluid (Ohminato et al., 1998; Legrand et al. 2000; Chouet et al. 2005; Waite et al., 2008, Jolly et al., 2012).

Tremor consists of long-lasting vibrations and is associated with resonance effects in cavities (Chouet , 1988; Konstantinou and Schlindwein, 2002), fluid flow (Rust et al. 2008), or degassing (Lesage et al., 2006). At Merapi tremor episodes are relatively sparse, of low amplitude, and their spectra contain a few regularly spaced peaks, with fundamental frequencies of 2-5 Hz (Ch. 2, Fig. 2.3). Rockfalls (RF) are characterized by progressively increasing amplitude at the onset, long duration and high frequency content (5 to 20 Hz). Pyroclastic flows (PF; Ch. 2, Fig. 2.5), usually generated by dome collapse, produce RF-type signals with fairly long duration (up to tens of minutes) and large enough amplitudes to be recorded at the farthest stations in the network.

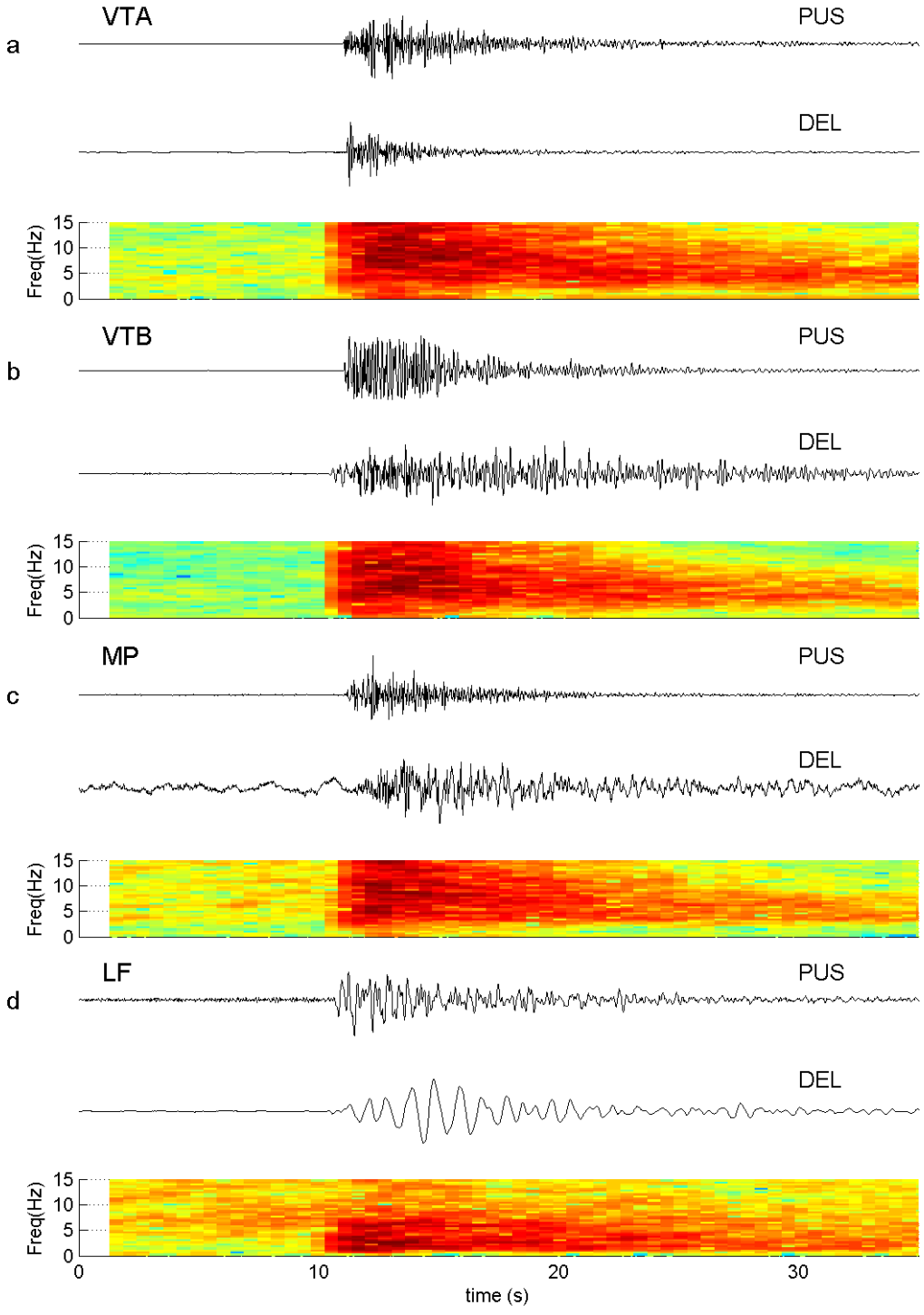

Fig. 1.10 Different types of seismic events observed at Merapi. For each sample, waveforms recorded at two stations and a spectrogram are displayed. a) Volcanotectonic type A (VTA). b) Volcanotectonic type B (VTB). c) Multiphase (MP). d) Low-frequency (LF).

1.5 Thesis structure

This thesis aims at better understanding the unusual behaviour of 2010 Merapi eruption. We'd like to determine the distinct features and processes related to this large explosive eruption from the other smaller effusive eruptions, using mainly seismic data. We divide the thesis in 7 chapters. The first four chapters are an extension of an article published by the Journal of Volcanology and Geothermal Research (Budi-Santoso et al., 2013). In addition we enriched the section of source location with relative locations.

Chapter 1 is a general introduction. We present the seismic chronology related with the 2010 crisis from the first symptom of unrest until the eruption in Chapter 2 which is based on monitoring data observations. We'd like to provide a general perspective and constraints about what possible physical scenarios that could have taken place related with the eruption.

Chapter 3 presents the aspect of events location. We aim at improving location precision. In this case we only used the events considered as VT events whose arrival times are clear. We propose a method to improve absolute location in spite of the low dataset quality we have. Relative locations based on double difference method were also performed.

In chapter 4, we analyse the continuous seismic energy using the algorithms of RSAM and modified RSAM (MRSAM). The objective is to recognize the seismic intensity behaviour prior to the eruption either through its total seismic energy or the energy that correspond to a specific frequency band. The dominant processes during different phases of activity could be estimated. The observed accelerating behaviour in both RSAM and MRSAM allows us to perform hindsight eruption forecasting with good precisions.

Chapter 5 aims to determine the clusters of similar VT events using waveform correlation and hierarchical clustering method. We'd like to recognize more in

detail the evolution of VT in time and to understand better the process related with VT events.

Chapter 6 presents estimations of seismic velocity changes of the edifice related with the eruption. We use both event data and noise data. We also compare the two methods in calculating the velocity variation. The response of the edifice to the increase of stress before the eruption is the process we want to quantify.

Chapter 7 concludes all the results obtained from previous chapters. We would like to propose a synthesis of chronological physical processes in an attempt for explaining all observation results. We try to make a list of data and behaviour that could be potential precursors of a large eruption including the conditions that must be present to be able to perform reliable eruption forecasts.

Chapter 2

Seismic chronology associated with the 2010 Merapi eruption

2.1 Introduction

Observations on many volcanoes in the world have suggested a general model of earthquake activity before volcanic eruptions (McNutt, 2000). In this model, the activity begins with high frequency earthquakes that reflect shear fractures of the country rock in response to increasing magmatic pressure. After a peak in the rate of high frequency earthquakes, the activity tends to calm down during some time. LF events and tremor may then occur sequentially, since the tremor itself can be a merging of LF events. Factors that may cause quiescence include strain hardening, increased water content lowering effective stress, or a reduction in strain rate. The seismic rate then re-increases toward the eruption which may indicate damaging process of the surrounding rocks.

In the case of Merapi, unrest is generally indicated by the presence of VT swarms from months to years before the eruption. Seismic intensity then increases during weeks or months before the eruption together with increasing of other parameters such as deformation and gas. When approaching the eruption onset, the number of rockfalls increases. Thus the values of daily number and magnitude of seismic events allow making assessment of the current state of activity. This scenario was typical for Merapi eruptions at least for the two decades before 2010 when detailed monitoring data have been obtained. However, some eruptions e.g. that of 1994 (Ratdomopurbo, 1995) that involved gravitational effects, presented different scenario.

The Merapi eruption of 2010 is the first large explosive eruption whose seismic activity was well monitored (Surono et al., 2012). Temporal evolution of the seismicity was clearly observed thus providing data for understanding what processes might be involved during the pre-eruptive and eruptive periods. Seismic monitoring data at Merapi commonly consists of daily number and energy of each type of observed earthquake and rough VT hypocenters if any. In this chapter, we aim at presenting the detailed chronology of seismic activity, particularly during the pre-eruptive period, and at suggesting the possible mechanisms that may be responsible for each phase of activity.

2.2 Data and method

The next section summarizes the history of the seismic activity during the year preceding the eruption, with a focus on the last few weeks as well as on the eruption itself. It mainly relies on routine manual counting and classification of events based on waveform shape. Daily statistics are reported in local time (GMT+7). Seismic energy reported below is calculated using the Gutenberg-Richter equation:

$$\log E = 11.8 + 1.5M \qquad 2.1$$

where M is the magnitude (Gutenberg and Richter, 1956) and E is in ergs. Magnitude of VT is calculated using the local magnitude definition of Richter (1935, 1958). To minimize the influence of distance on the determination of magnitude of VTA and VTB, amplitudes are measured at station DEL (2.6 km from summit) instead at the closest station PUS (0.5 km). DEL is at about the same distance to the clusters of VTA and VTB. On the other hand, since the MP events always occurs at shallow depth and have low amplitude at station DEL, PUS is used to calculate their magnitudes (Ratdomopurbo, 1995). Amplitude corrections are applied to each station in order to get consistent magnitude determinations.

2.3 Seismic Chronology during 2010 Crisis

2.3.1 Pre-eruptive activities

The level of seismic activity is usually very low during inter-eruptive periods at Merapi. For example, following the 2006 eruption, an average of 5 MP and less than one VT per day were registered. The total seismic energy (VT and MP) released per day was less than 0.4 x 10^8 J on average.

The first evidence of precursory unrest for the 2010 eruption consisted of four short duration (3 to 4 hours) VT swarms on 31 October 2009 (Fig. 2.1), 6 December 2009, 1 February 2010, and 10 June 2010. These swarms had a small number of detected events (14, 13, 6, and 30, respectively) with maximum local magnitude of 2.5 and shallow depths (< 1 km). This kind of activity is considered as an early precursor, as all the previous eruptions since at least 1992 were preceded by similar series of seismic swarms.

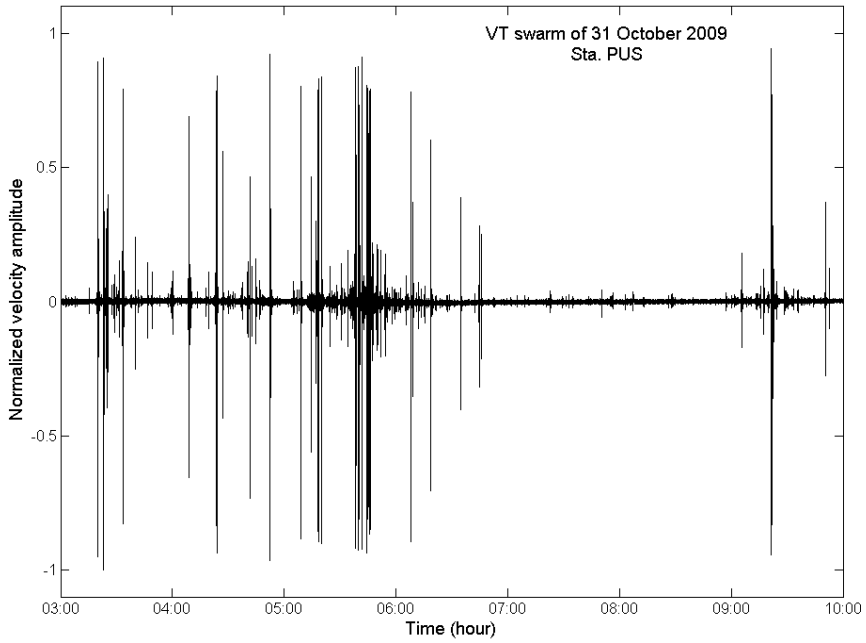

Fig. 2.1 Seismogram of the first precursory swarm of 31 October 2009. It lasted about 3 hours. Another larger VT event occurred about 3 hours afterward (right edge of plot).

In early September 2010, the level of seismicity began to increase, with about 10 MP and 3 VT events per day, corresponding to a seismic energy release of 0.6 x 10^8 J per day. On 12 September at 08:23 local time, a VT earthquake with local magnitude M = 2.5 and depth of 3 km was felt in the three northernmost observation posts (see the monitoring map on Fig. 1.7 in Ch. 1). The earthquake was followed by a large rockfall at 10:21. A similar VT event occurred on 13 September with magnitude of 2.2 and the same depth. On 19 September, the event rate reached 38 MP, 5 VTA, and 6 VTB per day, with energy of 6 x 10^8 J and maximum magnitude of 2.6 (Fig. 2.2). This increase in seismicity coincided with accelerating inflation of the summit, as revealed by repeated distance measurements (Surono et al., 2012). On the basis of these observations, the alert level was raised to II on 20 September 2010 (Surono et al., 2012).

Harmonic tremor episodes with weak amplitudes and durations of up to 70 minutes were detected from 30 September to 4 October at the closest stations to the crater. Spectrograms reveal three regularly spaced peaks and frequency gliding, corresponding to progressive decrease of the fundamental frequency from about 5 to 3 Hz with overtones (Fig. 2.3). This phenomenon occurred with cycles of about 17 minutes duration.

During the intrusive phase on 1-26 October more than 200 VLP events were recorded, mostly at the stations within ~3 km of the summit. These events had frequencies in the range 0.01 – 0.2 Hz. They were coeval with VT, MP, or LF events (Jousset et al. 2013).

The seismic activity continued to increase in October together with increasing rates of deformation and gas emission and with changes in gas composition (Aisyah et al., 2010). The daily number of seismic events reached 56 VT and 579 MP on 17 October and resulted in a total energy of 51 x 10^8 J by 20 October. An increasing number of rockfalls also occurred, with up to 85 such events on 20 October (Fig. 2.2). The alert level was raised to III on 21 October.

On 23– 24 October, several large LF events, which were saturated at short period stations, occurred. These events were recorded at all Merapi stations and were located a few hundreds of meters beneath the summit.

The level of seismicity dramatically increased on 24 to 26 October. On the 24, the number of VT, MP, RF events were 80, 588, 194, respectively and the seismic energy release was 59 x 10^8 J. On 25 October, the corresponding values were 222, 624, 454, and 132 x 10^8 J. The alert was raised to level IV (evacuation) on 25 October 25 at 18:00 local time, 23 hours before the onset of the eruption. By the time of the onset (26 October 2010, 17:02 local time) 232 VT, 397 MP, 269 RF and 4 LF had been counted, corresponding to an energy release of 197 x 10^8 J.

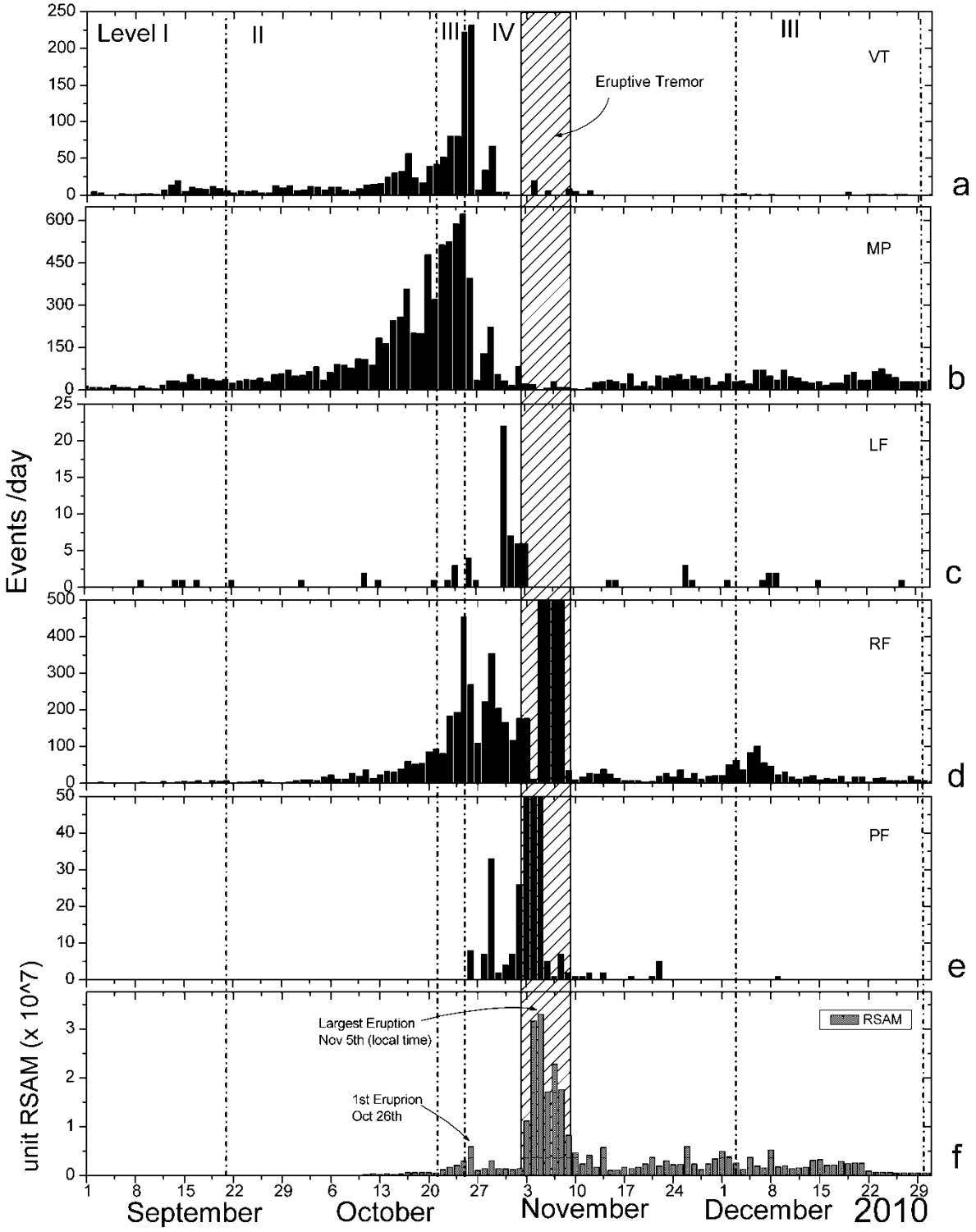

Fig. 2.2 Daily numbers of events for the period of September-December 2010. The panels (a) to (e) present the number of VT, MP, LF, rockfall, and pyroclastic

flow events respectively. (f) The daily RSAM calculated during the crisis. The RSAM value on 5 November reaches 5 times that of 26 October. Dashed-dotted vertical lines indicate the change of the state of the alert level.

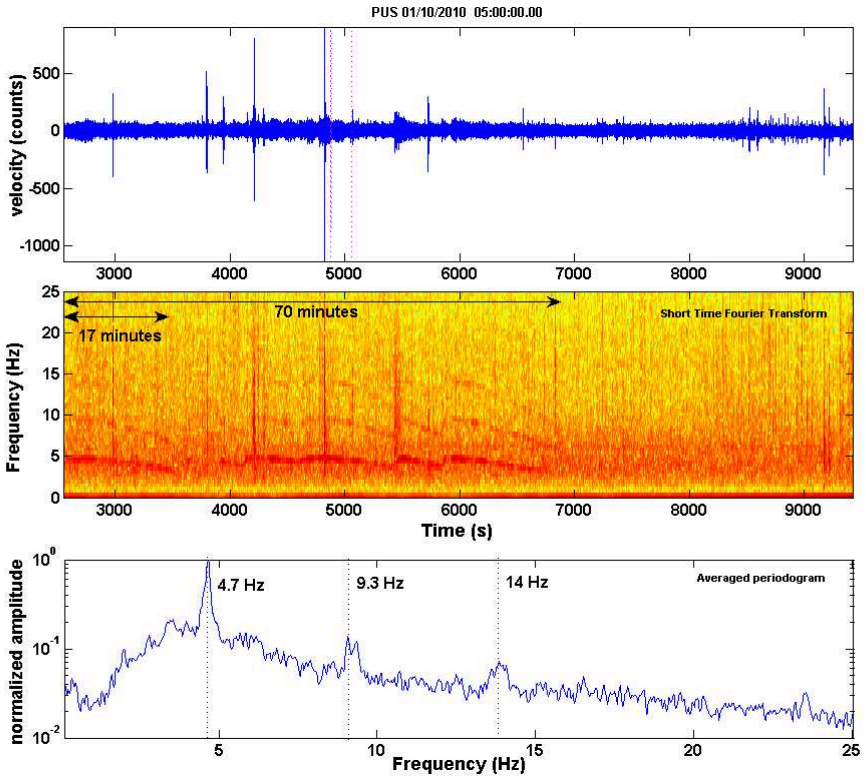

Fig. 2.3 An episode of tremor that began on 1 October 2010 at 05:42. Top panel shows the seismogram recorded at station PUS; middle panel shows the spectrogram for this signal and illustrates the dominant frequency, overtones and gliding frequencies; lower panel is its spectrum.

The main observations preceding the eruption are summarized in Fig. 2.4. The last swarm before the seismic crisis occurred on 10 June 2010. In July there was an anomaly on gas data compared with the normal condition. The ratio between CO_2 and H_20 contents increased 6 times from the background level. However, the seismicity and deformation did not show any significant increase until September 2010. An 'exponential' increase was observed on seismic and EDM data. Such behavior then could be modeled in order to perform hindsight eruption forecasting as it is demonstrated in Ch. 4.

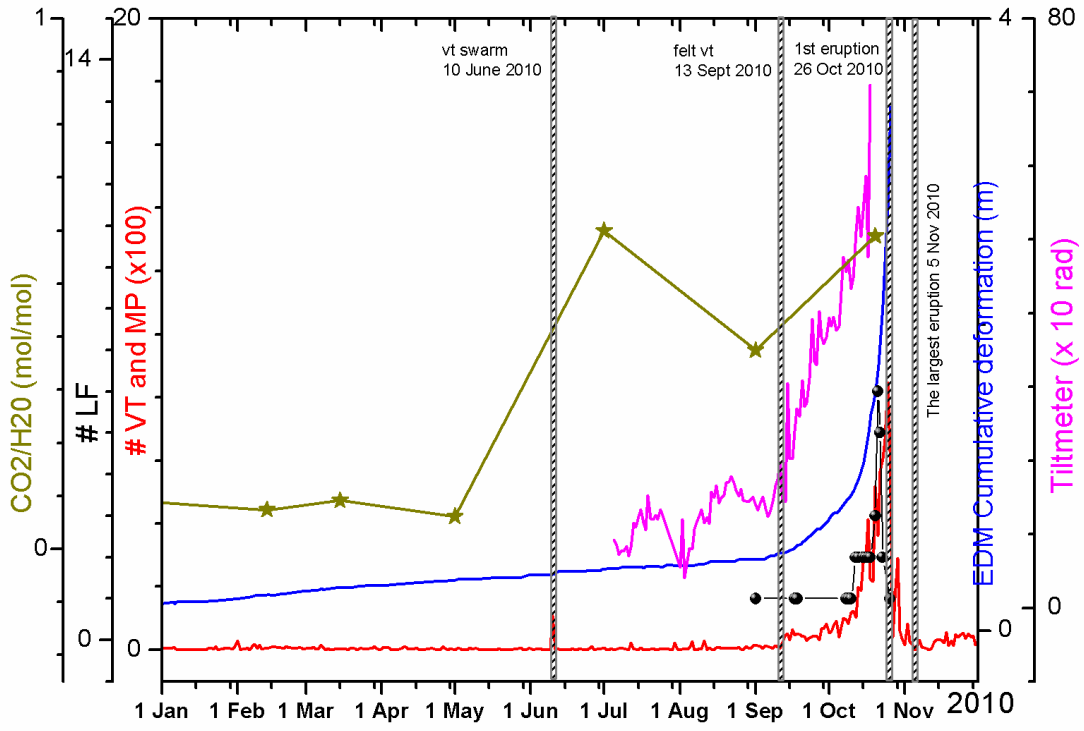

Fig. 2.4 A synthesis of the precursory data before the eruption 2010. The figure displays the number of VT and MP events (red line), the number of LF events (black), the distance measurements by EDM (blue), the tilt from summit station (magenta) and the ratio of CO_2/H_2O content in gas (green).

2.3.2 Activities during the eruptions

The first phase of the eruption was phreato-magmatic and explosive. It produced a pyroclastic flow that travelled 5 km to the south (Surono et al., 2012). The duration of the corresponding seismic signal was 330 s. On 27 October, seismicity decreased to 7 VT, 34 MP, 1 LF, and 109 RF. On 28 October, the daily number of events rose again to 34 VT, 129 MP, 222 RF, 7 PF, and then on 29 October to 67 VT, 223 MP, 354 RF, 32 small PF. The eruptive activity then decreased and only 4 PF were observed on 31 October. However, a burst of 22 LF events and a weak 13 minute-long episode of tremor occurred on 31 October.

High frequency tremor appeared on 3 November and was associated with more frequent pyroclastic flows. At 11:00 local time, this tremor became continuous. At 16:05 authorities decided to enlarge the restricted zone to a radius of 15 km from the summit. At 18:46 a pyroclastic flow reached a distance of 9 km and destroyed seismic station KLA. On 4 and 5 November, the short-period seismograms were saturated and individual events were indistinguishable. However, by using low-pass filter (for frequencies < 0.1 Hz), it was possible to detect that the largest eruption took place on 5 November at 00:01 local time (4 November, 17:01 UTC – Fig. 2.5). This largest event could also be recognized by the station located ~40 km south of the volcano (Surono et al., 2012). This eruption lasted about 27 minutes, produced pyroclastic flows that travelled up to 16 km, and destroyed stations DEL and PUS as well as the broadband stations at the summit of the volcano.

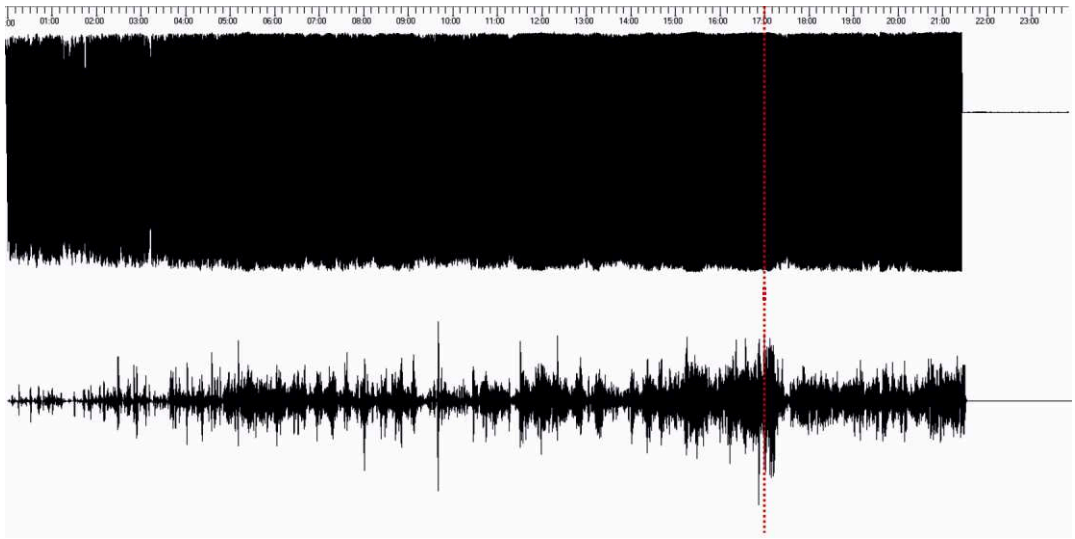

Fig. 2.5 Seismogram of station PUS on 4 November until station destruction (at ~21:30 UTC). Dotted vertical red line indicates onset of largest eruption at 17:01 UTC. Although record was saturated, the climatic eruption could be detected using a low-pass filtered (f < 0.1 Hz) seismogram (bottom panel).

2.3.3 Seismic energy level associated with large eruption of 2010

In addition to daily counting of earthquakes and source location, the cumulative energy of VT and MP events calculated over the preceding year was used at BPPTK for estimating the current state of activity at Merapi (Fig. 2.6). For eruptions before 2010, this energy ranged from 10^{10} J (10 GJ) in 1992 to 2.2 x 10^{10} J in 1997 and 2006. Thus in practice, special attention is paid to the monitoring observations when this energy reaches 10^{10} J. On 16 October, the cumulative energy was 2.2 x 10^{10} J and an eruption or a dome extrusion was expected. However, instead, the energy rate increased more rapidly, reaching a maximum rate of 0.62 x 10^{10} J per day on 25 October. Together with the accelerating rate and large local deformations (displacement of up to 3 meters), the very high value reached by the cumulative seismic energy was one of the key elements that pointed to a much larger eruption than usual and resulted in timely decisions to evacuate. It is also noteworthy that the early precursory cumulative energy level of the 2010 eruption was lower than that preceding all other recent eruptions (i.e., days 270-325, or 95 to 40 days before the eruption onset; Fig. 2.6). This suggests that although seismic energy is progressively released during a long period before effusive eruptions, in the case of an explosive crisis, most of the energy is produced in the last few days or weeks.

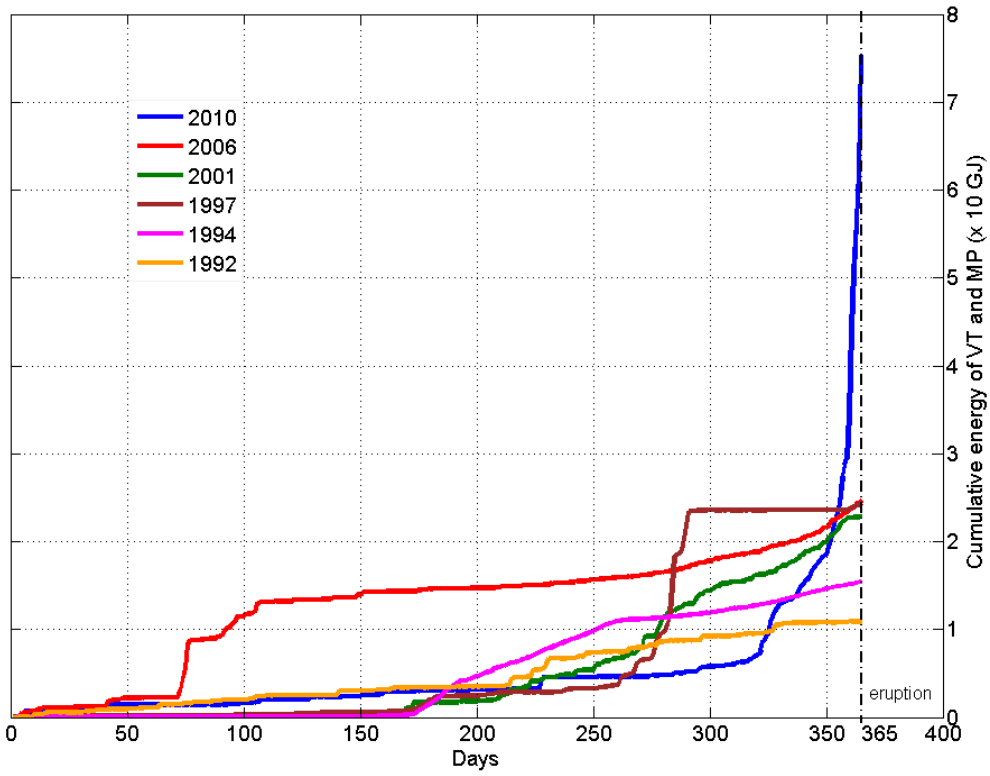

Fig. 2.6 Comparison of cumulative energy release of VT and MP earthquakes during one year prior to several eruptions from 1992 to 2010.

2.4 Discussion

The seismic activity of the 2010 eruption of Merapi during the pre-eruptive and eruptive periods presents both features commonly observed during previous monitored eruptions and some characteristics that had never been recorded before, such as an unusually high level of energy release. The types of events identified in 2010 are similar to those observed since seismic stations were installed on the volcano in 1982. Although empirically determined from waveform observations, the event classification also reflects a diversity of physical processes and locations of seismic sources. The two types of volcano-tectonic events, VTA and VTB, correspond to two hypocenter depth ranges. They are easily distinguished by different amplitude patterns in the seismic network and by distinct differences of P-wave arrival times between stations, although it is difficult to recognize them

with only one station. The most numerous events are multi-phase, as hundreds of MP signals were counted daily before and during the eruption (Fig. 2.2). They are interpreted as small ruptures that trigger resonance response of an adjacent magma-filled conduit or crack. They are mainly observed accompanying magma extrusions or in association with dome instabilities. However MP events can also occur during periods of quiescence. Consequently, their origins and source mechanisms are still not well-known.

Unlike many other volcanoes, low-frequency (LF) events and tremor are relatively unusual at Merapi. Most mechanisms proposed to explain these kinds of events involve fluids interacting with the surrounding medium (Chouet, 1996). In the case of Merapi 2010, LF events occurred mainly at shallow depths after the first phreatomagmatic explosions (Jousset et al., 2013). They probably result from the interaction of the intrusive magma body with the hydrothermal system that lies beneath the summit (Müller and Haak, 2004). The few harmonic tremors detected during the pre-eruptive period are probably associated with increasing gas emission. A possible mechanism for these vibrations is the periodic opening and closing of a "valve" within a crack and resulting in intermittent pulses of gas. In such a model, the resonant frequency could be stabilized by the resonance of the fluid-filled cavity, analogous to the musical resonance of a clarinet (Lesage et al., 2006). This process generates regularly spaced spectral peaks by the Dirac comb effect and is an efficient mechanism to radiate seismic waves (Rust et al., 2008).

Assuming there were gas emissions, those gas might be vapours resulted from the boiling groundwater within the upper conduit due to heat transfer from magma in depth. The downward frequency gliding could be attributed to the collapses of the resulting bubbles which change the wave velocity in the system.

Attributing directly these tremors to magma activity is unlikely considering two reasons. Firstly, it is suggested that the magma was still in the depth, whereas, the tremors were only recorded in the summit stations meaning that the tremor source was within the upper part of the volcano. Secondly, considering their weak

amplitude, we suggest a hydrothermal origin tremor rather than magmatic origin tremor. In fact, according to Benoit et al. (2001), tremor of hydrothermal origin will have smaller amplitude than tremor of magmatic origin. Weak amplitude of tremor associated with hydrothermal activity has been observed elsewhere. According to Kieffer (1984) tremors with small amplitude have been observed at Old Faithful which is associated with the boiling groundwater within conduit. Spurr noneruptive tremor on October 1992 is interpreted as a cyclic interaction between a heat source (magma) and water (Mckee et al., 1981; Kieffer, 1984; McNutt, 1992).

At least there are two main factors that cause the tremor of hydrothermal origin has weaker amplitude, i.e. smaller source dimensions (cracks and conduits within a hydrothermal system) and the intrinsically limited ability of hydrothermal boiling to generate strong tremor (Leet, 1988; Benoit et al. 2001).

The first seismic observation of unrest of the volcano were the series of shallow VT swarms in October 2009, December 2009, and in February and June of 2010. Seismic swarms are generally triggered by variations of the effective stress in fractures (Saccorotti et al., 2001). In the case of Merapi, they could be related to perturbations of the hydrothermal system due to the intrusion of a deep hot body, or to heating by increasing gas flow through the structure.

According to Norton (1999), extreme variation in fluid pressure in the near field region of magmas are caused by sparse but significant amount of H2O rich fluids that are ubiquitous in the host rocks and common in the magmas. Pore fluids typically in the host rocks have large positive values of the isochoric coefficient thermal pressure, whereas those in the magma have large negative values. Therefore, fluid pressure increases during dissipation of thermal energy from magma as a natural consequence of cooling process where temperature increases in the host rocks and concurrently decreases in the magma. Once the rock fails, fracture networks forms. Somewhere, the fluid accumulation results a large pressure leading to the rock failure producing observable earthquakes. This seems

plausible if we consider the existence of saline water saturated regional layer at the depth below sea level as a conductive layer (10 Ωm) suggested by electromagnetic data (Muller and Haak., 2004). Muller and Haak, (2004) also observed another conductive zone located at lower depth centered beneath the summit which might be also affected by the heat transfer from depth. As results, earthquakes could occur at near surface where the shear failure threshold is relatively weak due to fragmentations and the low lithostatic pressure.

This process likely has cyclic behaviour since the swarm occurred repeatedly. According to Voight et al. (1999) the cyclic activity at Soufriere Hills volcano in 1996 – 1998 was controlled by: (1) degassing and crystallization in the upper conduit, which created a viscoplastic magma plug that inhibited conduit flow, and (2) pressurization of magma under the plug. Similar process might take place related with repeated swarm of Merapi in 2010 crisis, where, degassing and crystallisation of magma in the main magma chamber could happen in a cyclic behaviour.

The heightened phase of precursory seismic activity started at the beginning of September 2010, about a month and a half before the eruption onset. As previously noted, most VTA events, with focal depths of 2.5 to 5 km, occurred before 17 October and after this date, VTA diminished while shallow (< 1.5 km) VTB activity increased. Although the focus of seismic activity is not necessarily close to the apex of a magmatic intrusion, the marked change in hypocentral positions is consistent with the rapid ascent of a magma body, as also indicated by petrologic data (Surono et al., 2012).

The cumulative seismic energy release through VT and MP earthquakes during the year preceding the eruption reached 7.5 x 10^{10} J. For the previous eruptions of 1992 to 2006, this energy never exceeded 2.5 x 10^{10} J. This much higher level of energy is the most important seismic characteristic of the 2010 eruption and is clearly consistent with its highly explosive nature. Most of this energy was emitted in the last 6 weeks before the initial eruption of October 26 during a

marked acceleration in rate. Together with deformation and gas emission measurements, this observation formed the basis for the initial identification of the impending large eruption and the timely decision of evacuation of a more extended region than usual (Surono et al., 2012).

Seismic activity originates mainly from mass movements inside the volcanic structure, such as magma intrusion and gas release. There is a consequent relationship between seismic energy release, deformation, and volume change (McGarr, 1976; Yokoyama, 1988). The bulk volume of juvenile deposits of the 2010 Merapi eruption was estimated at 0.03 – 0.06 km^3 (Surono et al., 2012), while the corresponding value was 0.01 km^3 in 2006 (Sri-Sayudi et al., 2007). The marked difference between seismic energy release in 2010 and that of previous eruptions can thus be related to the difference in magma volume.

2.5 Conclusion

After an exceptional eruption, it is of paramount importance to carry out a thorough analysis of the data from the monitoring network that could not be processed in detail during the crisis. Aside from early seismic swarms observed 12 to 4 months before the 2010 crisis, the seismic activity of Merapi increased almost monotonically during the 6 weeks preceding the eruption. The number of LF events, VLP events and tremors recorded in this period were larger than for smaller past eruptions. The most relevant characteristics of the 2010 activity were: 1) the high level of seismic energy release (about three times the maximum value obtained for the previous eruptions), and 2) acceleration in the occurrence rate of VT and MP events, in the release of energy, and in the RSAM values. This behaviour is consistent with an accelerated displacement rate of deformation at the summit measured by EDM. These features were taken as evidence that the impending eruption would be unusually large.

The chronology of seismic activity prior to 2010 Merapi eruption appears to be consistent with the generic model of swarm proposed by Mc Nutt (2000). However the LF activity which preceded the eruption was not accompanied by tremor. The tremor itself occurred about 1 month before the eruption with weak amplitude.

Chapter 3

Source locations

3.1 Introduction

Various earthquake types with different mechanisms exist in Merapi preceding the eruptions. Among them, only the events considered as VT have been located for at least the last 20 years. Despite the limitation of the data set due to the small number of stations and the lack of velocity model, the location of VT obtained during the past eruptions is somewhat consistent and convincing.

A first report related with the hypocenter calculation in Merapi was done by Ratdomopurbo (1995). Using simplex algorithm, he determined two zones where VT events are located and he distinguished two different types of VT. The first one, called VTB, is located at depths lower than 1.5 km and the other one, called VTA, is located in a zone deeper than 2.5 km. He further suggested that there are two aseismic zones located below 5 km and between 1.5 and 2.5 km. He interpreted these aseismic zones as the main and a secondary magma chambers respectively.

Hidayati (2008) determined the hypocenter and focal mechanisms of both types of VT occurring before the eruption of 2001. VTA events were found at depth below 2 km beneath the summit with normal fault mechanism. VTB events were located at depth <1 km, with reverse fault mechanism for the deeper VTBs and both reverse and normal fault for the shallower VTBs.

A method for automatic and non-linear hypocenter determination was implemented at Merapi by Wasserman and Ohrnberger (2001). The coherence of seismic waves observed at different arrays during 1997 – 1998 is used in this

method. The results show that the source region of the VTB type seismicity just before the 1998 eruption is closely related to the region of subsequent high eruptive activity.

In this work, we study the hypocenter distribution of the seismic activity preceding the 2010 eruption. This chapter is a part of studies for understanding the process involved in this large eruption. As in previous studies, we focus only on VT events, because of their clear onsets. However, due to amplitude saturation, some events considered as VT could rather be classified as LF events regarding their frequency content. We apply two approaches of hypocenter determination, based on arrival time data: absolute and relative location.

We have also attempted to implement a method of location based on the signal amplitude (Battaglia et al., 2003; Taisne et al., 2011). We faced many difficulties, such as problems of anisotropic and amplitude saturation, that prevented us from obtaining reliable results. Thus it remains work to do for implementing this method in Merapi.

3.2 Data and Methods

3.2.1 Absolute location and uncertainty estimation

From the database of Merapi seismic events, 679 events, recorded by 4 to 9 seismic stations, were located for the period October 2009 to October 2010. Thanks to the timing corrections based on noise cross-correlation (Ch.1), many data from broadband stations that experienced time synchronisation failure could be included. In this work, the Hypoellipse program (Lahr, 1999) was used. This program is based on Geiger's least squares method which collapse the data into a set of linear equations, with one equation representing each reading of P-phase time, S-phase time, or S-P interval time. Four unknown parameters, i.e. changes in latitude, longitude, depth, and origin time, are to be estimated. Thus, at least four observations are required to solve the problem. A homogeneous half space

velocity model assuming V_p = 3 km s^{-1} and V_p/V_S = 1.86 (Ratdomopurbo and Poupinet, 2000) is used throughout this work. Unlike other standard earthquake location algorithms e.g. Hypo71 (Lee and Lahr, 1975) and Hypoinverse (Klein, 1978), in Hypoellipse the elevation of the top of the flat-layered velocity model may be specified to match the elevation of the highest relief in the region under study. Stations at lower elevations are embedded within the model, and may be located within any layer. Travel times and take-off angles are computed for the true relative locations of source and station (Lahr et al., 1994).

Among the factors that may prevent the determination of true hypocenter locations are an incorrect velocity model, systematic and random reading errors, and timing of wrong phases. The absolute location accuracy is difficult to assess. There is considerable uncertainty in the parameters of the velocity model. To test the sensitivity of the locations to changes in the velocity model, Lahr et al. (1994) performed tests by modify the velocity model in several manners and evaluated the resulted RMS. Although an improved RMS could be obtained, a firm limit on the total bias that may be present in these locations is difficult to obtain, given that a horizontally layered model cannot represent the large lateral velocity variations of a volcanic structure (Lahr et al., 1994).

In order to estimate realistic uncertainties on hypocenter positions, a Monte-Carlo method of error simulation was applied. The observed arrival times were modified by random perturbations with Gaussian distribution and standard deviation of 0.1 s that corresponds to the picking error and hypocenter positions were obtained for each modified data set. This procedure was repeated 1000 times for each event. During the iterations we rejected the hypocenters whose internal calculation error are large (>1 km for the depths and 0.5 km for the horizontal positions). Therefore, it could be said that we are doing an optimization of hypocenter calculation in poorly constrained condition due to inexact provided velocity model in a complex structure of volcano.

For each event, the outliers among the obtained solutions (~1000 hypocenters) were removed by using the Thomson Tau method (Thomson, 1985). Each data value is scored by its absolute deviation value $\delta_i = |x_i - \bar{x}|$ versus the value of Modified Thomson (τ) defined as

$$\tau = \frac{t_{\alpha/2}.(n-1)}{\sqrt{n}\sqrt{n-2+t_{\alpha/2}{}^2}}, \qquad 3.1$$

where n is the number of data, $t_{\alpha/2}$ is the critical t value of student's distribution with degree of freedom df = n-2 and significance level α = 0.05 which is the most widely used (Norman et al., 2008). The outliers are determined if $\delta_i > \tau S$, where S is the sample standard deviation. These outliers represent a small proportion of the whole set of solutions. The remaining solutions were used to calculate confidence ellipses for each event by carrying out principal component analysis (Jackson, 1988) on the covariance matrix of positions (Got et al., 2011).

3.2.2 Relative location using double difference method

The resulted absolute location qualities vary depending on the precision of picking and the configuration of the available stations. During the period of interest, several stations were stopped due to various problems. Thus, the number and configuration of available stations are not always the same, yielding different spatial constraints in searching hypocenter solutions. In addition picking errors and lack of accurate velocity model might prevent the hypocenter to be consistent. In this case, the locations of some events that are expected to be similar may be significantly scattered.

Therefore, in order to improve the results, HYPODD (Waldhauser and Ellsworth, 2000) version 2.1b, a localization program based on the method of double-difference was applied. It is based on the fact that if the hypocenter separation between two earthquakes is small compared to event-station distance, then the ray paths can be considered almost identical along their entire length. With this

assumption, the differences in travel times for two earthquake recorded at the same station may be attributed to differences in spatial separation of the hypocenters.

For an event i observed at a station k, the difference between the observed (t_{ik}^{ob}) and theoretical (t_{ik}^{0}) traveltimes (traveltime residual) is:

$$\Delta t_{ik} = t_{ik}^{ob} - t_{ik}^{0} \approx \sum_{l=1}^{4} \left. \frac{\partial t_{ik}}{\partial m_l^i} \right|_{m_0^i} \Delta m_l^i \quad . \qquad 3.2$$

where $m^i=(x, y, z, \tau)$ defines the model parameters (i.e., hypocentre coordinates and origin time). The double difference is defined by the difference between traveltime residuals for stations i and j:

$$\Delta t_k^{ij} = (t_{ik}^{ob} - t_{ik}^{0}) - (t_{jk}^{ob} - t_{jk}^{0}) \approx \sum_{l=1}^{4} \left. \frac{\partial t_{ik}}{\partial m_l^i} \right|_{m_0^i} \Delta m_l^i - \sum_{l=1}^{4} \left. \frac{\partial t_{jk}}{\partial m_l^j} \right|_{m_0^j} \Delta m_l^j \quad . \qquad 3.3$$

The same equations are derived for all hypocenter pairs and for all stations to be combined in a system of linear equations of the form:

$$WGm = Wd \quad , \qquad 3.4$$

where G defines a matrix containing the partial derivatives, d is the data vector containing the double-differences, m is a vector containing the changes in hypocenter parameters to be determined, and W is a diagonal matrix of weights.

In the program hypoDD, two possible approaches are available to solve the equation. They uses either the singular value decomposition method (SVD), or the conjugate gradient LSQR algorithm (Paige and Saunders, 1982). The later one is used in this work. LSQR solves the damped least-squares problem:

$$\left\| W \begin{bmatrix} G \\ \lambda I \end{bmatrix} m - W \begin{bmatrix} d \\ 0 \end{bmatrix} \right\| = 0 \quad , \qquad 3.5$$

to find m, where λ is the damping factor and I is a identity matrix (Waldhauser and Ellsworth, 2000).

The use of hypoDD includes two steps. The first one consists of analyzing the catalog arrival time data and of deriving pairs of events with their travel times differences. In the second step, the differential travel time data are used to determine the relative hypocenter locations.

The first step is done by the ph2dt program in which P and S-phase data for event pairs are searched with travel time information at common stations and subsamples these data in order to optimize the quality of the phase pairs between the events. Ph2dt establishes a network of close events by building links from each event to other neighboring events within a search radius defined by MAXSEP as far the distance between the events and the stations is below MAXDIST. Fig. 3.1 illustrates the meaning of these crucial parameters.

By performing some tests, we found that the optimum parameters, which produce a clear separation between VTA and VTB clusters, are MAXSEP = 0.35 km and MAXDIST = 10 km. In order to control the quality of neighboring, several other parameters are used such as MINLNK and MINOBS which are the minimum number of pairs and observations. We used the value of 4 for both MINLNK and MINOBS considering the minimum number of available stations.

The second step, the double difference location, is done with hypoDD program. To prevent an ill-conditioned of double difference equations, connectedness between events is again evaluated with parameters such as OBSCT and WDCT which are similar to MINLNK and MAXSEP of ph2dt program respectively.

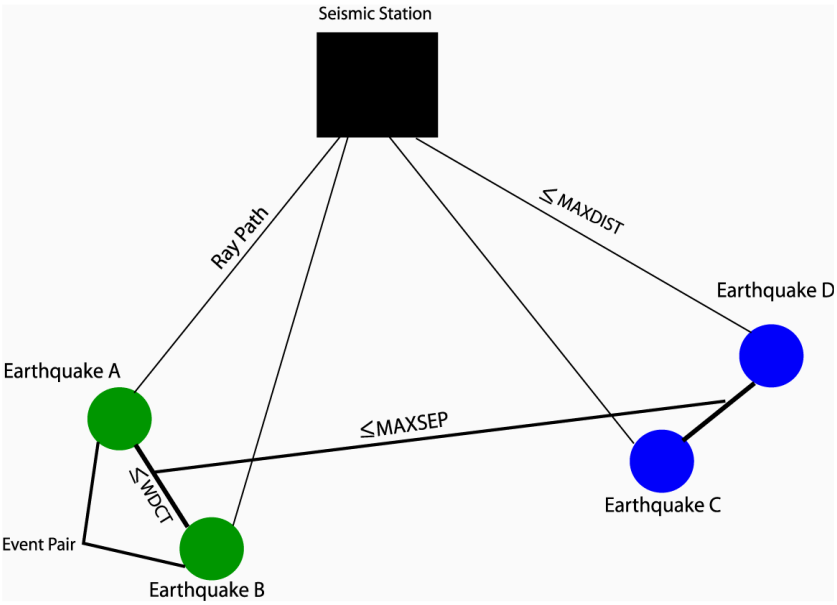

Fig. 3.1 An illustration of the events pairs assumed in hypoDD (Dunn, 2004). Several parameters to be defined related with the sensitivity in clustering and relocation process are shown. MAXSEP is the maximum distance for which two event-pairs are defined to be a neighbor; MAXDIST is the maximum distance between an event pair and a station; and WDCT is the maximum distance between event-pair.

HypoDD minimizes the residuals between observed and calculated travel times differences in an iterative procedure and, after each iteration, updates the locations and partial derivatives, and reweights the a priori weights of the data according to the misfit during inversion and the offset between the events. During the iterations, P and S-phase data are weighted (WTCTP and WTCTS) and re-weighted using re-weighting functions characterized by WRCT (residual threshold in second) and WDCT.

LSQR solves the damped least squares problem. The magnitude of the adjustment highly depends on the damping factor (DAMP). The choice for the damping factor is based on the conditioning of the system to be solved expressed by the condition number (CND), which is the ratio of the largest to smallest eigenvalues. In this case several tests are needed to find an optimal damping factor in order to obtain an appropriate CND i.e. between 40 and 80 (Waldhauser, 2012). Using too

low damping factor, the CND would be too high which means that the events are adjusted too much; on contrary, with too high damping factor, the CND would be too low and the events would not move from the initial location.

In the first step of the algorithm, we found several clusters that are separated at different locations. Since hypoDD solutions highly depend on the initial locations and their uncertainties (Waldhauser, 2001), we excluded the small clusters which are considered as poorly located. Thus, localizations were done only on two dominant clusters consisting in 375 and 92 events that represent the population of VTB and VTA, respectively. Different damping factors and number of iterations were used depending on the number of events of the corresponding cluster and the sparseness of the hypocenters. Two sets of iterations were performed in order to find the solutions with large and small thresholds respectively in order to minimize rejected events and optimal clustering in the same time. Table 3.1 displays the weighting and re-weighting parameters for localizing the VTB cluster. For the VTA cluster we used larger number in the second iteration set and lower damping factor of 6 to consolidate the sparse distributed events.

Table 3.1 Weighting and re-weighting parameters used in VTB and VTA cluster

# ITERATION	WTCTP	WTCTS	WRCT	WDCT	DAMP
VTB					
5	1	1	10	5	80
5	1	1	2.5	0.5	80
VTA					
5	1	1	10	5	6
10	1	1	2.5	0.5	6

The errors provided are the standard error for each model parameter computed by the conjugate gradient method LSQR.

3.3 Results

3.3.1 Absolute locations

A histogram of uncertainties in depth (Fig. 3.2e) shows that most uncertainties are smaller than 0.5 km, with a maximum number close to 0.3 km. Nineteen events with depth uncertainty larger than 1 km were removed before plotting the location map and cross-sections. Hypocenters are distributed at depths less than 5 km below the summit, in a cylinder with elliptical section of approximately 2 km x 1 km and longest axis in the NE-SW direction (Fig. 3.2a-c). The distribution in depth displays two separated clusters. The deepest (about 116 VTA events) lies between 2.5 and 5 km below the summit. The shallowest cluster has a maximum depth of 1.5 km and consists of VTB events. These results are consistent with observations from previous Merapi eruptions that indicate also an aseismic zone at depths of 1.5 to 2.5 km below the crater. This feature is evident both in the histogram of hypocenter depths and in the probability density function of source depths, which is histograms resulted from the whole data including the 1000 times of arrival time modifications, both of which display clear minima at 1.5 – 2.5 km depth (Fig. 3.2d). In order to verify whether this gap is due to an artefact of the hypocenter determination, source depths are plotted as a function of differences of P-waves arrival times ($t_{DEL} - t_{PUS}$) between stations DEL (located 1.5 km below the summit) and PUS which is close to and 200 m below the summit (Fig. 3.2f). Again, two clusters are observed in this representation, separated mainly along the ($t_{DEL} - t_{PUS}$) axis. Values of ($t_{DEL} - t_{PUS}$) in the range ~0 – 0.25 s are associated with deep VTA events, whereas time differences of 0.35 to 1 s correspond to shallow VTB earthquakes. The relative lack of values between 0.25 and 0.35 s is a robust observation and is consistent with the existence of an aseismic zone at 1.5 – 2.5 km depth.

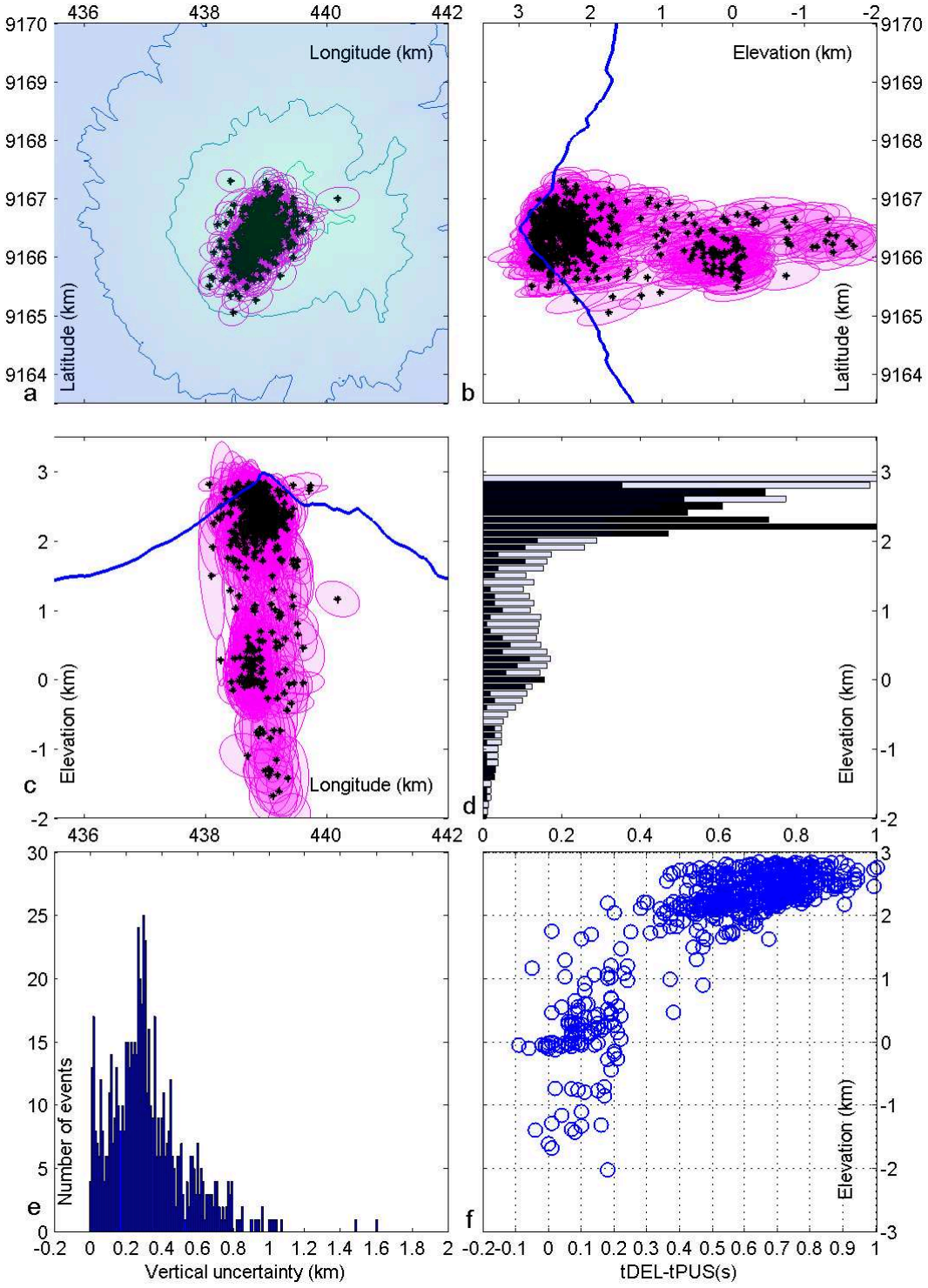

Fig. 3.2 Hypocenters of VT earthquakes. a) Map of epicenters, b) N-S cross section, c) E-W cross section. Hypocenters are indicated by crosses and shown with their 67% confidence intervals (pink ellipses). d) Histogram of the

hypocenter depths (black solid bar) and probability density function of source depths (black hollow bar), calculated using Monte Carlo method. e) Histogram of uncertainties on depth. f) Depths as a function of differences of P-wave arrival times between stations DEL and PUS.

3.3.2 Relative locations

Performing the hypoDD program using homogeneous velocity model with V_P of 3 km/s and V_P/V_S of 1.86, we find a distribution which is less scattered than that of previous absolute location. In fact, the aseismic zone found with the absolute location is even more obvious with the hypoDD results. The hypocenters are distributed vertically until the depth of about 3km. We obtain an average error of 120 m for the relative vertical position, and 50 m for the horizontal relative position. The results are plotted in Fig. 3.3. The colours of the events correspond to the cluster number obtained from the event family analysis (see the legend and Ch. 5). Black stars indicate the events that do not correspond to any clusters. This is partly due to a problem of time reference in the manual picking processing.

Here, VTA events are found at the depth of about 2.5 – 3 km, while VTB events are located from the depth of 1.5 km to the surface. As a consequence, the aseismic zone is placed at depth between 1.5 and 2.5 km. The waveform clusters provided from the analysis of families (Ch. 5) confirm the existence of aseismic zone since there are 3 clusters (number 4,5, and 9) that are located only at >2.5 km depth (deep VT zone/VTA zone) while the others are located only at <1.5 km depth (shallow VT zone/VTB zone). The histogram of depth distribution (Fig. 3.3.d) shows that the largest population is located at a depth range of 0.5 – 1 km. It is mainly composed by cluster 10 that occurred during the last day before the eruption.

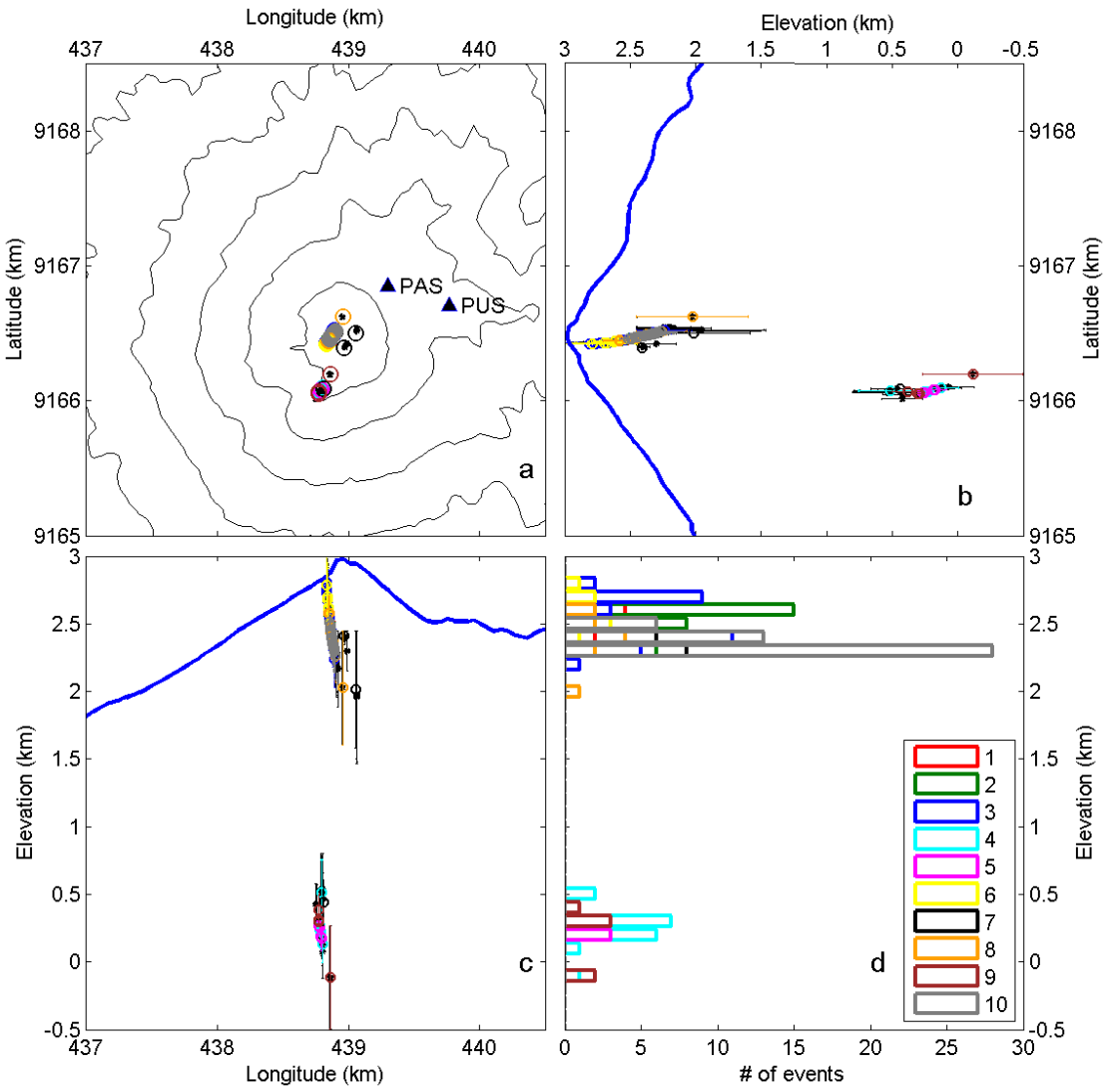

Fig. 3.3 Hypocenter of VT resulted from hypoDD using homogeneous velocity model with V_P=3 km/s and V_P/V_S=1.86. (a) Lateral, (b) N-S cross-section, (c) E-W cross-section hypocenter distributions. (d) Histogram of depths. The errors < 0.5 km are plotted in (c). The events colors indicate the cluster number based on their waveform similarity.

3.3.3 Relation between depths and arrival time differences between stations

As we found quasi-vertical alignments of the relative locations, we can verify whether the vertical separations between the clusters are valid or just an artifact. It is done by modeling the elevations with the arrival time difference between PUS

and DEL station assuming a distribution of sources located around a vertical conduit.

Fig. 3.4 shows that the differences of arrival time between DEL-PUS and PLA-PUS span limited ranges for each waveform cluster. Recall that DEL and PLA stations are located at low elevations of 1.5 km and 1.3 km respectively while PUS is close to the summit. These observations are consistent with the hypocenter separations of the clusters. Clusters 1 and 8 are located at about the same position in agreement with the similarity in arrival time differences. On the contrary, other clusters that are separated from each other have distinct ranges of arrival time differences.

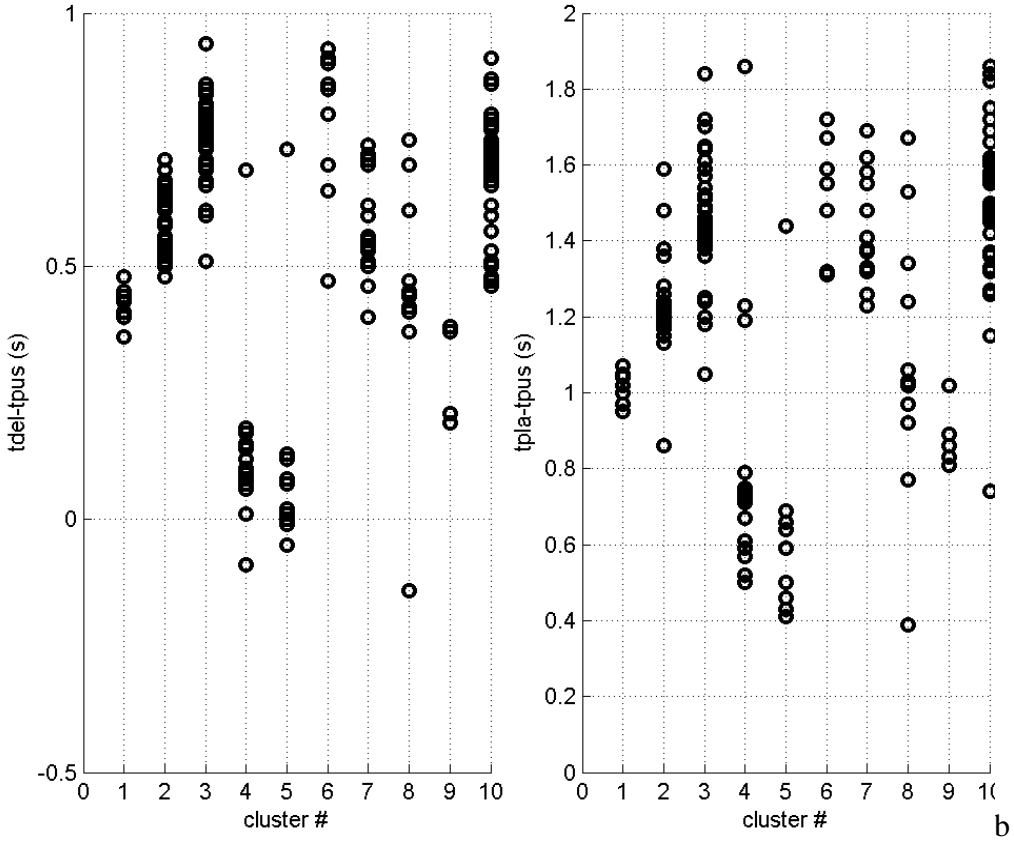

a b

Fig. 3.4 Differences of arrival times between stations DEL- PUS (a), and PLA-PUS (b). Each clusters show distinct ranges of values.

As illustrated in Fig 3.5a, assuming a vertical thin conduit and a straight ray path, arrival time difference Δt of an event located at coordinates (0, d) between DEL and PUS station can be estimated as:

$$\Delta t = (\sqrt{x_2^2 + (z_2 - d)^2} - \sqrt{x_1^2 + (z_1 - d)^2}) / v \qquad 3.6$$

where x_1, z_1, x_2, and z_2 are the horizontal and vertical distance between summit (0,0) and PUS and DEL station respectively; and v is the P wave velocity (3 km/s). Fig. 3.5b displays the relation between depth and Δt. The observed Δt of the clustered events can be projected to the model curve obtained (Fig. 3.5c) as indicated by circles. It appears that clusters 1 and 8 are the deepest VTB clusters with depth of 1 – 1.5 km. Clusters 2, 7, and 10 occur in larger ranges i.e. from 1.2 km to the surface. Cluster 3 is located between 0.7 km and the summit. Meanwhile, the VTA clusters (4, 5, 9) are located at depth larger than 2 km. Note that many events of cluster 6 could not be projected since their arrival time difference exceed the maximum value calculated by the model. However following the general relation between depth and arrival time differences, we suggest that cluster 6 should be the shallowest one.

Comparing these results with the absolute and relative locations, we found good consistency regarding the separation between shallow and deep clusters. However, among the shallow clusters and among the deep clusters, the separation is not always consistent. For example, cluster 1 and probably 8 are modelled to range on the deeper part of the VTB zone (1 – 1.5 km), whereas the elevations resulted from the absolute and relative locations are distributed at shallower depths. The depths resulted from the relative locations appear to be more concentrated at shallow depths.

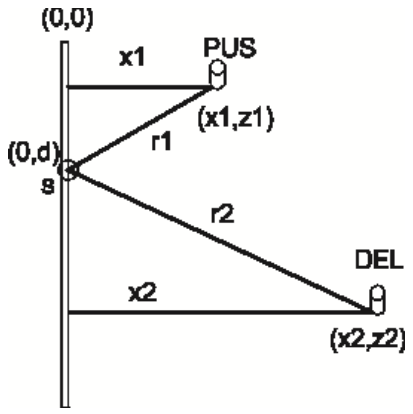

a

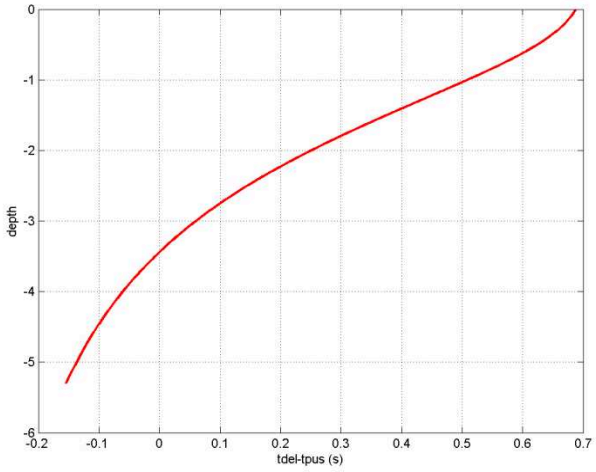

b

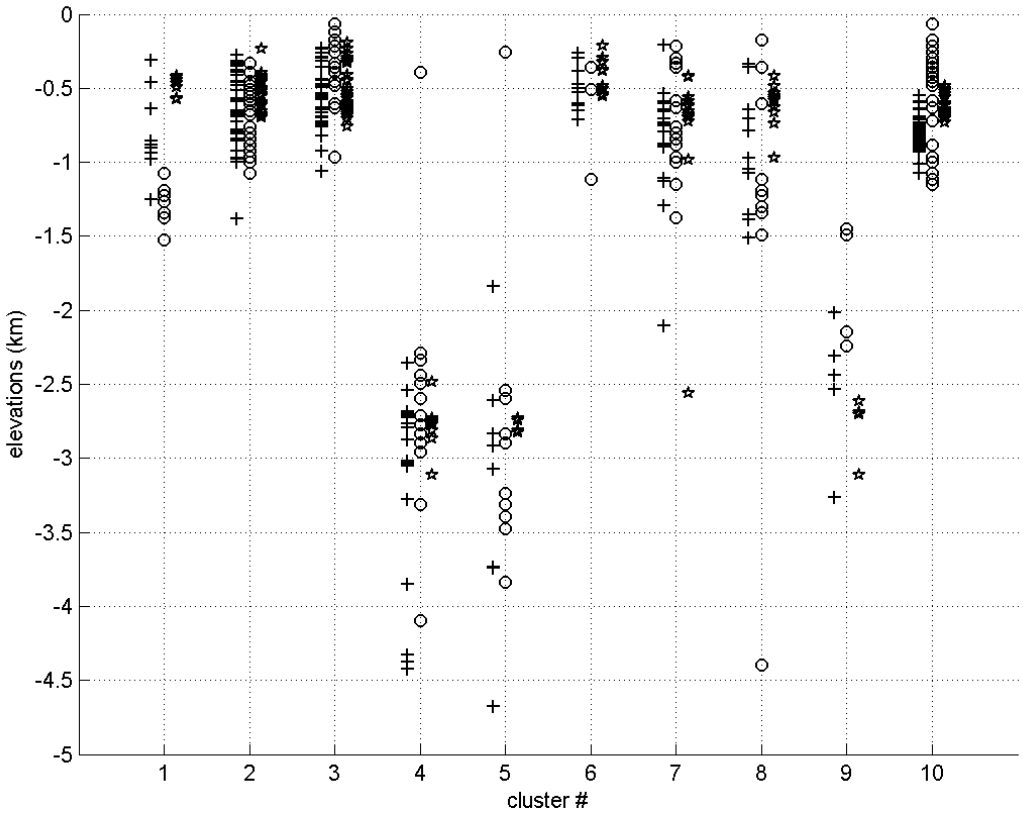

c

Fig. 3.5 (a) Geometrical model of source depth as a function of difference of arrival times between DEL and PUS stations, assuming straight ray paths. Arrival time differences are proportional to the differences of distance between the source and the two stations (r1 and r2). (b) Depth versus Δt (or tDEL-tPUS). (c) Comparison of the depths estimated by the geometrical model (circles), and by absolute (plus sign) and relative (stars) locations.

3.3.4 Temporal evolution of hypocenters distribution

In Fig 3.6, hypocenter depths are plotted as a function of time. The numbers of VTA and VTB per day are also presented. The four seismic swarms that occurred between October 2009 and June 2010 were located at less than 1 km below the summit and are therefore classified as VTB events. Only the last swarm is represented on the figure. The deep VTA events occurred during the first part of the pre-eruptive period in September and until mid -October. After that, while VTA activity was diminishing, a sharp increase of the number of VTB events occurred during the week before the eruption on 26 October.

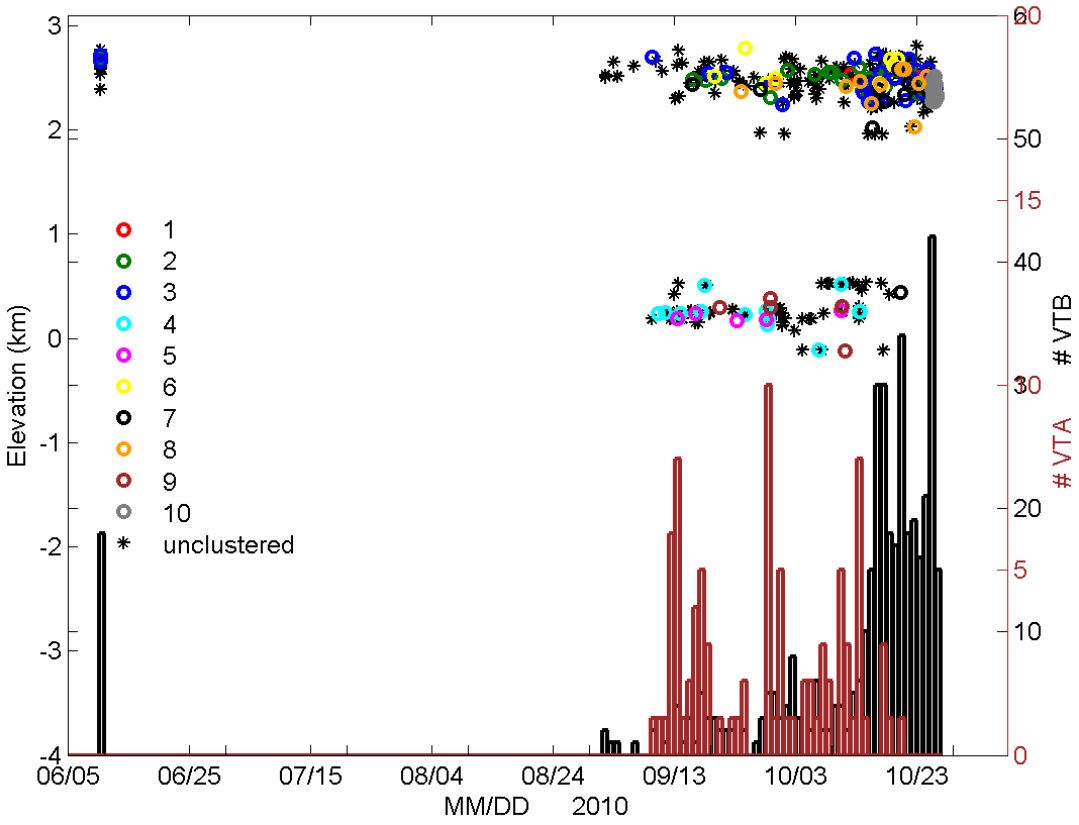

Fig. 3.6 Elevations of events plotted as a function of time for the period of June-October 2010. Different cluster numbers are indicated by different colors as shown in the legend. Daily numbers of VTA and VTB events are shown by brown and black bars, respectively.

3.4 Discussion

Hypocenter determination is a difficult task on volcanoes because of a lack of clear phase arrivals (especially for MP, LF, and tremor events), a highly variable topography, a limited knowledge of the velocity structure, and in many cases, a lack of sufficient stations or appropriate network configurations. These drawbacks typically result in large errors in hypocenter locations and "fuzzy" three-dimensional distributions that are difficult to interpret. It is thus necessary to obtain reliable estimations of uncertainties on source locations. Errors calculated by the programs of hypocenter determination depend mainly on the consistency between the observed arrival times. However, a Monte-Carlo approach gives more robust estimations as it takes the geometry of seismic rays and the uncertainty of the velocity model into account (Got et al., 2011). Following the Monte-Carlo approach, the clouds of points obtained during a simulation provide an approximation of the probability density function of the source position. The maximum of the probability density can be taken as the hypocenter and its spread and shape reflect the precision of the determination. Despite these uncertainties, the trends in hypocenter locations seen in 2010, such as the shallowing of events before the eruption, indicate that automatic data processing and estimation of source locations would be useful during subsequent crises.

Furthermore, relocation using the method of double difference improves the resulted hypocenters. The events distribution becomes much more concentrated, and the aseismic zone appears more obviously. Several bunches of events in the VTB zone are confirmed by their similarity in waveforms meaning that the method works quite well in linking the closely events.

Regarding the alignments observed on both shallow and deep events, even though it could result in part from the larger uncertainties in depth than in horizontal position, the vertical alignment could be plausible considering a dyke-type plumbing system. However, even the relative locations are too scattered to obtain precise vertical distribution of the events in each cluster. Verifying the arrival

time data, we found that this is partly due to the various combinations of available stations that lead to different spatial constraints between those events.

One of the main drawbacks of the seismic network on Merapi is the station sparseness. Thus, when one phase observation is missing, the result is significantly modified. Another consequence is the horizontal alignment of absolute locations along about the south-west direction. Indeed, there is no station in this direction to constraint the horizontal position.

Moreover the homogeneous velocity model used is not accurate. Modelling the depth versus arrival time difference between DEL and PUS station, we found that these time differences must not exceed 0.7 s when the events are close to the summit. However there are many events, particularly in clusters 6 and 10, whose time differences reach 0.9 s. The disparity between the maximum calculated and observed time difference could be caused by lower velocity in the shallowest part of the volcano, though the topography could also contribute to the longer ray path of the shallow events. Actually, a seismic experiment using active sources (Wegler and Luhr, 2001) suggests the existence of a thin low velocity layer. However, the features of such low velocity layer are not determined.

3.4.1 Aseismic zone in Merapi edifice

Our results suggest that the aseismic zones that appear between 1.5 and 2.5 km depth and below 5 km are a robust and permanent feature of Merapi. The present study confirms the findings of Ratdomopurbo and Poupinet (2000), Wassermann and Ohrnberger (2001), and Hidayati et al. (2008), obtained for seismic events recorded in 1991, 1998, and in 2000-2001, respectively, and shows that this zone has been present for at least 20 years.

Regarding the shallower aseismic zone (1.5 – 2.5 km), Ratdomopurbo and Poupinet (2000) postulated that it could correspond to the presence of a more ductile material related to a small shallow magma reservoir. The existence of such magma chamber is still controversy among the studies. It is not consistent with some studies such as a modelling of deformation observations of Beauducel et al.,

1999 and some geochemistry and petrology studies (Costa et al., 2013). However some other studies rather showed a consistency. Deformation study conducted by Westerhaus et al., 2008 confirmed a presence of pressure source that is located within the shallow aseismic zone.

We suggest that the aseismic zone could correspond to a more ductile part of the Ancient Merapi left by the Holocene sector collapses (Newhall et al., 2000). This layer is mainly composed of auto-brecciated lava flows, St. Vincent-type pyroclastic flows and lahar deposits (Berthommier et al., 1990). It is probably poorly consolidated, argillically altered and thus less seismogenic than the surrounding layers. Indeed, it lies between the older structure of the Pre-Merapi period and the series of andesitic lava flows and pyroclastic flows of the Middle and Recent Periods (Fig 1.2; Camus et al., 2000).

Those aseismic zones might also correspond to the conductive zones found by electromagnetic method (Ritter et al., 1998; Muller and Haak, 2004; Commer et al., 2006). The shallow aseismic zone likely corresponds to an upwelling conductive zone (10 Ωm) found in the central of Merapi edifice which is suggested to be a hydrothermal system (Commer et al., 2006). A very conductive layer (1 Ωm) is also found at depth between 3.5 km and 5.3 km. This layer is suggested to be a very porous regional layer rich in saline water and might corresponds to the deep aseismic zone. Considering that the conduit crosses over these conductive zones, a strong alteration must take place within these zones. Related with the alteration process within the conduit of Merapi, Troll et al. (2012) found hydrothermal alteration features among the rock samples of 2010 eruption. We suppose that during the unrest activity, the magma could expand within these zones due to their weaker rigidity.

Regarding the magma chamber location, other studies suggest deeper locations. Beauducel and Cornet (2000) inferred a depth of 8 km from GPS and tiltmeter data. Many studies of geochemistry and petrology propose even deeper location ranging from 12 to 45 km (Chadwick et al, 2012; Costa et al., 2013; Nadeau et al.,

2013; Innocentini et al., 2013). However there is pyroxene crystallized at depth of about 5 km from the summit (Chadwick et al. 2012) which somewhat supports an ephemeral magma storage at depth >5 km. Assuming a large uncertainty of the inverted depths, the regional conductive layer (Ritter et al., 1998; Muller and Haak, 2004) could correspond to the shallowest depth of pyroxene crystallization.

Considering the deep magma chamber proposed by many geochemistry and petrology studies, we suggest that the deepest aseismic zone might include this magma chamber.

3.4.2 Magma migration

As previously noted, most VTA events, with focal depths of 2.5 to 5 km, occurred before 17 October and after this date, VTA diminished while shallow (< 1.5 km) VTB activity increased. This might correspond to the migration process of magma toward surface. The magma from depth rose through the existing conduit. The volume of magma is suggested to be large enough to produce conduit enlargement and shear failures that are associated with VT earthquakes.

During the period of deep conduit enlargement, there were also VTB. We suggested that these VTB events are related with the hydrothermal activation due to heating from the rising magma, the same mechanism attributed to the swarms that occurred before. In fact the number of VTB events during this period are small compared to those occurred during the swarms.

On 15 October, the number of VTA starts to decrease sharply while the number of VTB increases until 18 October (Fig 2.4). This observation of magma migration from deep to shallow conduit is consistent with other observations e.g. deformation, seismicity, and apparent velocity variations as discussed later in chapter 7.

The long term lava flux at Merapi is about 0.1 x 10^6 m^3/month; and short term rates during eruption intervals can be 2–18 times greater (Siswowidjoyo et al.,

1995). Using a conduit radius of 15– 25 m, the average velocity of magma would be 0.02–0.05 mm/s, while, during pre-eruptive period, it could be 0.2 – 0.5 mm/s or 17 – 43 m/day (Hidayat et al., 2000). If we consider the first occurrence of VTA i.e. 9 September 2010 as the sign of the beginning of magma rise from a depth of 5 km, thus, we could estimate the movement rate corresponding to the pre-eruptive activity of 2010, simply by dividing the distance of 5 km with 35 days lapse time, to be 1.7 mm/s or 146 m/day which is 3 to 9 times larger than the common pre-eruptive value of Merapi. It supports the suggestion of Costa et al. (2013) regarding the rapid ascent of magma involved in the 2010 eruption. Furthermore, considering the magma passed through the different zones in depth i.e. the deep conduit (2.5 – 5 km), the middle aseismic zone (1.5 – 2.5 km), and the shallow conduit (<1.5 km), we could also estimate the different movement rates through these different zones. We obtained the movement rates of the magma to be 1 mm/s or 86 m/day during deep intrusion, 6 mm/s or 520 m/day during aseimic intrusion, and 3 mm/s or 260 m/day during shallow intrusion which are plausible regarding the different stress constraints corresponding to these different zones.

Generally, difference explosivity are attributed to two factors i.e. variations in magma types and/or volatile contents (Wilson et al., 1980; Neri et al., 1998; Papale et al., 1998; Mangan et al., 2004; Costa et al., 2013). The magma type of the 2010 eruption is found to be similar with that of 2006 eruption particularly with respect to the SiO_2 content which ranges from 52 to 56% (Costa et al., 2013; Innocenti et al., 2013; Surono et al., 2012), whereas the magmas from the most explosive eruptions (e.g. 1872, 1930) tend to have lower SiO_2 contents (Costa et al., 2013). Here the first factor, i.e. variation of magma type, is thus unlikely.

According to Costa et al. (2013), there is only little or no degassing-induced crystallization in the rock samples of 2010 eruptions, whereas it is significantly found in the rocks of 2006 eruption. Furthermore, based on the modeling of the Fe-Mg diffusion zoning in Clinopyroxene, the interval between the arrival of hot and gas-rich magmas in the intermediate or shallow reservoirs and the eruption of

2010 was estimated to be about 1.6 – 2.7 years which is half shorter than that of 2006 eruption. He concluded that the large volume of recharge magma was responsible to this rapid magma ascent that prevented an effective degassing and thus produced high explosivity of the 2010 eruption.

3.5 Conclusions and perspective

We located more than 600 VT events occurring in one year prior to the 2010 eruption using two approaches i.e. absolute and relative location. Our data set is not ideal to allow precise and accurate locations. The number of stations is too small; a velocity model consisting in only one layer is likely not representative to the complexity of a volcanic edifice; in addition the errors in manual picking are significant. Despite these limitations, some interesting results were obtained both from absolute and relative locations.

The hypocenters are distributed between the depth of about 5 km and the near-surface. The relative location improved the distribution yielding less scattered hypocenters and much smaller errors i.e. on the order of hundreds to tenths of meters. Two aseismic zones were identified during 2010 seismic crisis both by absolute and relative location. This is a robust feature of Merapi seismicity at least for the last 20 years. The aseismic zone located at 1.5 – 2.5 km is interpreted as a more ductile part of Ancient Merapi left by Holocene sector collapse. The other aseismic zone located below 5 km of depth might correspond to the conductive regional layer rich in saline water. It is suggested that strong hydrothermal alteration likely undergo within these zones, especially in the vicinity of the feeding system.

Although not all the clusters are clearly separated, some waveform clusters are gathered by relative localization. On the one side, this exhibits the ability of the method in linking nearby events. On the other side, this confirms the existence of different event families which may correspond to different mechanisms,

processes, and locations. An improvement of these hypocenter determinations would be very useful in distinguishing different processes that might evolve during pre-eruptive activity.

The upward shift of seismic activity from deep zone (VTA) to the shallow zone (VTB), which reveals magma migration prior to the eruption, is a specific feature of the volcanic activity preceding 2010 Merapi eruption. It might be attributed to the large volume of magma involved. Rapid magma ascent indicated by the temporal evolution of hypocenter is consistent with the results of a petrological study (Costa et al., 2013). The magma involved in 2010 eruption is rich in volatile because there was not enough time for significant degassing.

The number and combination of stations used for location are very crucial in small networks as that of Merapi. The nearby events predicted by their similarity in waveform, could be located far apart due to the absence of only one station. Therefore it is very important to improve the data continuity in order to obtain consistency of hypocenters. It is needed to increase the density of station to cover all directions and elevations. As for the lateral distribution, the south-west direction is a priority since the absolute locations are less constrained in this direction.

As it is shown in this chapter, the source locations are one of the most important information to be monitored for determining the current state of volcanic activity. However the limitations of the data available due to instrumental problem could prevent accurate locations. In this case, fast and simple procedure to estimate the depth of events from arrival time difference between stations, as it is demonstrated using DEL and PUS stations, would be meaningful. In fact, since it only uses 2 stations, almost all picked events could be located; therefore, time evolution of events depths could be monitored more continuously. However it must be noted that this approximation uses an assumption of a thin vertical dyke-type conduit.

Chapter 4

Rsam and eruption forecasting

4.1 Introduction

Almost all volcanic eruptions are preceded by an increase in seismic activity that tends to intensify prior to the eruption. Real Time Seismic Amplitude Measurement (RSAM) is a robust tool for monitoring volcanic activity because it provides a simple indicator of the level of seismic energy (Endo and Murray, 1991). This method is very useful particularly during the period of intense activity when the events can no longer be counted and classified. However, since it gathers all the occurring events, it cannot provide precise information about the ongoing processes. In this case an algorithm called Seismic Spectral Amplitude Measurement (SSAM) has been proposed to monitor the seismic energy in different frequency bands (Stephens et al., 1994).

Many observations have reported the reliability of RSAM in following volcanic activity (Power et al., 1994; McNutt, 2000; Sparks, 2003; Surono et al., 2012). Furthermore if acceleration behaviour is observed, it allows performing eruption forecasting (Voight, 1998; Cornelius and Voight, 1991; Kilburn and Voight, 1998; De la Cruz-Reyna and Reyes-Davila, 2001; Bell, 2011). Tokarev (1963, 1966, 1971, and 1983) used hyperbolic extrapolation methods for predicting eruptions at Bezmianny volcano in October 1959, April 1960, and March 1961. Based on experiments in landslide mechanics domain, Fukuzono and Terashima (1985) proposed a differential equation relating the rate and acceleration of displacement to describe a landslide process due to rain fall. Voight (1988)

initially proposed this empirical relation for predicting volcanic eruptions. His method has been widely used either in real time or hindsight eruption forecasting.

At Merapi, real-time monitoring by RSAM was carried out during the critical period of the eruptive crisis of 2010. A module made by BPTTK calculated the RSAM value every 5 minutes from the discriminator output of station KLA. This provided valuable information on the magnitude of the increase in seismic activity before the eruption as well as the relative energy of eruptive events during the crisis. This information was of great help in managing the crisis. However, the Material Failure Forecast Method (FFM) based on RSAM data was not performed at that moment.

In this chapter we present the RSAM analysis prior to the 2010 Merapi eruption and demonstrate the usefulness of the acceleration property of RSAM data in performing hindsight eruption forecasting.

4.2 Data and method

4.2.1 RSAM and modified RSAM (MRSAM)

Here we calculated the RSAM using digital raw data of PUS station from about 2 years before the eruption of 2010. RSAM values represent seismic energy evolution in time, commonly expressed as

$$\mathrm{RSAM} = \frac{\sum_{i=1}^{n} \left| A_i - \bar{A} \right|}{n} \qquad 4.1$$

where A_i is the signal amplitude, $\bar{A}$ the mean amplitude in the calculation window, and n the number of samples of the window. An initial window length of two minutes was used and for long-term analysis a mean value every two hours was calculated. Because the entire hardware at station PUS was replaced on April

2010 with new equipment having different sensitivity, an amplitude correction was applied for consistency between data recorded before and after the change. Furthermore, because tectonic earthquakes are not related to volcanic activity, they were removed from RSAM values using the daily catalogue of seismicity and low pass filtering to identify their coda.

In order to get more details and to separate contributions from different types of volcanic sources, the following procedure was applied: For each 1-mn long window, filtering was performed using the following frequency ranges: 0.01 – 1 Hz, 1-3 Hz, 3-5 Hz, 5-10 Hz and 1-15 Hz. Five series of filtered RSAM were thus obtained by calculating the RSAM for each filtered window. For each time window, we kept only the filtered RSAM values that are higher than 40% of the corresponding unfiltered RSAM value. Because a segment generally contains no more than one event, this classification of signals roughly corresponds to the different types of volcanic events defined in Ch. 1. It is particularly useful for extracting LF events whose amplitude is low. The 1-15 Hz range includes all but the VLP types of event, with reduced noise. A cumulative value of filtered RSAM was then calculated for each frequency range. Hereafter, for simplicity, we called this method and the corresponding values as the Modified RSAM (MRSAM). This procedure is distinct from the Seismic Spectral Amplitude Measurement (SSAM, Stephens et al., 1994), which gives the spectral amplitude in different frequency ranges.

In Fig. 4.1.the methods of SSAM and MRSAM were tested over four different types of event. Note that we use here a short record for sake of simplicity. We performed both algorithms on the frequency band 1 – 3Hz (black circle), 3 – 5Hz (blue diamond), and 5 – 10Hz (red star). SSAM yields about the same curves for the frequency bands 3 – 5Hz and 5 – 10Hz which are similar to RSAM curve as well. For the frequency band 1 – 3Hz, high values are attributed to LF. However, SSAM gives also maximum values for the VTB. Thus, the resulting SSAM curve for the low frequency band will not correspond solely to LF events. In the case of Merapi, the number of LF events is much smaller than that of the high frequency

events. Thus, the energy of low frequency signals would be buried completely and the low frequency SSAM would not represent the energy of low frequency events at all.

On the other side, the low frequency MRSAM shows good sensitivity to the LF event and ignores the other events. The whole curve represents the evolution of LF event solely. Because the VTB, VTA, and MP events do not have distinct frequency contents, their evolutions are difficult to be distinguished from each other even with MRSAM.

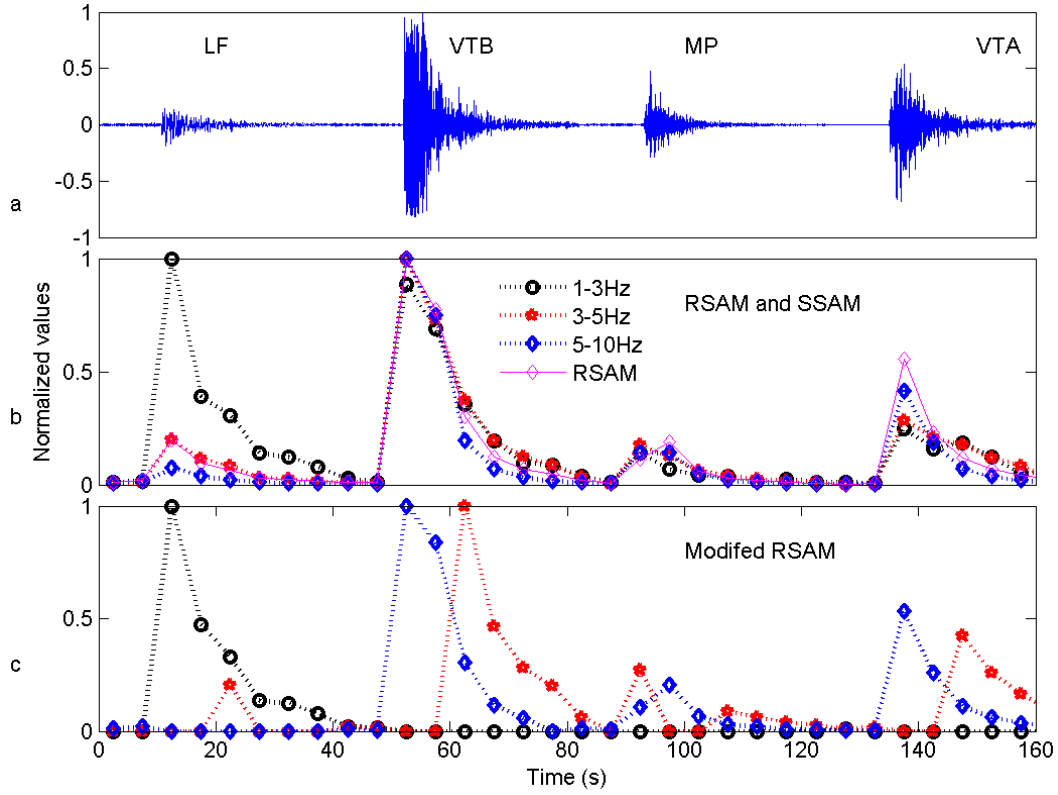

Fig. 4.1 Illustration of SSAM and MRSAM calculation with 4 different earthquake types. (a) Seismogram containing LF, VTB, MP, and VTA events. (b) RSAM values (cyan diamond) and SSAM values in frequency band 1 – 3Hz (black circle), 3 – 5Hz (red star), and 5 – 10Hz (blue diamond). (c) MRSAM values.

4.2.2 Hindsight eruption forecasting

The accelerating behaviour is the basis for the Material Failure Forecast Method (FFM) that has been used for estimating the time of eruptions (Voight, 1988; Cornelius and Voight, 1994, 1995; De la Cruz-Reyna and Reyes-Davila, 2001). First introduced for the study of landslides (e.g. Fukuzono and Terashima, 1985), the FFM assumes that a pre-eruptive stage is analogous to a damaging or creep process before the material failure. An observable data (Ω) related to this process (such as displacement, strain, or level of seismic activity) is governed by an empirical power law between its rate of change $\dot{\Omega}$ and acceleration $\ddot{\Omega}$:

$$\ddot{\Omega} = A\dot{\Omega}^{\alpha} \qquad 4.2$$

where A and α are constants that can be estimated from the observations (Cornelius and Voight, 1995). Note that RSAM is approximately proportional to the seismic moment-rate and energy-rate and thus can be used as $\dot{\Omega}$ (Cornelius and Voight, 1995).

In the case $\alpha \neq 1$, integration of equation 4.2 yields an equation containing the velocity. With the initial condition $\dot{\Omega}(t = t^{*}) = \dot{\Omega}^{*}$, the velocity is given by,

$$\dot{\Omega} = \left[A(1-\alpha)(t - t^{*}) + \left(\dot{\Omega}^{*}\right)^{(1-\alpha)}\right]^{1/(1-\alpha)} \qquad 4.3$$

Using the logarithm form of equation 4.3, we can evaluate the values of α and A under the assumption that $t^{*} = t_s$ = eruption time and $\dot{\Omega}^{*} = \dot{\Omega}_s = \infty$:

$$\log(\dot{\Omega}) = \frac{\log(t_s - t)}{1-\alpha} + \frac{\log(A(\alpha - 1))}{(1-\alpha)} \qquad 4.4$$

The constants α and A can be found with linear least squares fitting of the relationship $\log(\dot{\Omega})$ versus $\log(t_s - t)$. In the case of Merapi 2010 crisis, using as $\dot{\Omega}$ the daily RSAM data from the beginning of seismic crisis of 13 September 2010

until the eruption and t_s = 26 October 2010 at 10:00 UTM (first eruption), we found the values of α and A are 2.1 and 4 x 10^{-7} (Fig. 4.2).

Since α is very close to 2, we can take advantage of simplifying the equation using α=2. In this case, another integration of equation 3 yields the formula of *Ω*:

$$\Omega = \frac{-1}{A} \ln\left[\frac{A(t^* - t) + (\dot{\Omega}^*)^{-1}}{A(t^* - t_0) + (\dot{\Omega}^*)^{-1}} \right] + \Omega_0 = B \ln(1 + st) + C \qquad 4.5$$

(Cornelius and Voight, 1995), where $\Omega(t = t_0) = \Omega_0$ and $\dot{\Omega}(t = t^*) = \dot{\Omega}^*$. B and C are constants and C can be chosen as null. $s = -1/t_f$, in which t_f equals the predicted time of failure at which *Ω* is infinite. The time of failure t_f can be used as an estimate of the time of the eruption onset, although there may also be a time delay (Voight, 1988; Bell et al., 2011a).

Using the last equation, we benefit from a smoother data curve using cumulative values of *Ω*. Thus, exercises of hindsight prediction of the Merapi 2010 eruption time were carried out by fitting a function given by equation 5 to the observed cumulative values of RSAM. Note that RSAM is approximately proportional to the seismic moment-rate and energy-rate and thus can be used as $\dot{\Omega}$ (Cornelius and Voight, 1995). Accordingly, cumulative values of RSAM can be modelled using function *Ω* in equation 4.5. For each trial, constants B, s, and t_f are estimated by least squares fitting. In this exercise, a crucial issue is the choice of an appropriate time window used to fit the model to the data.

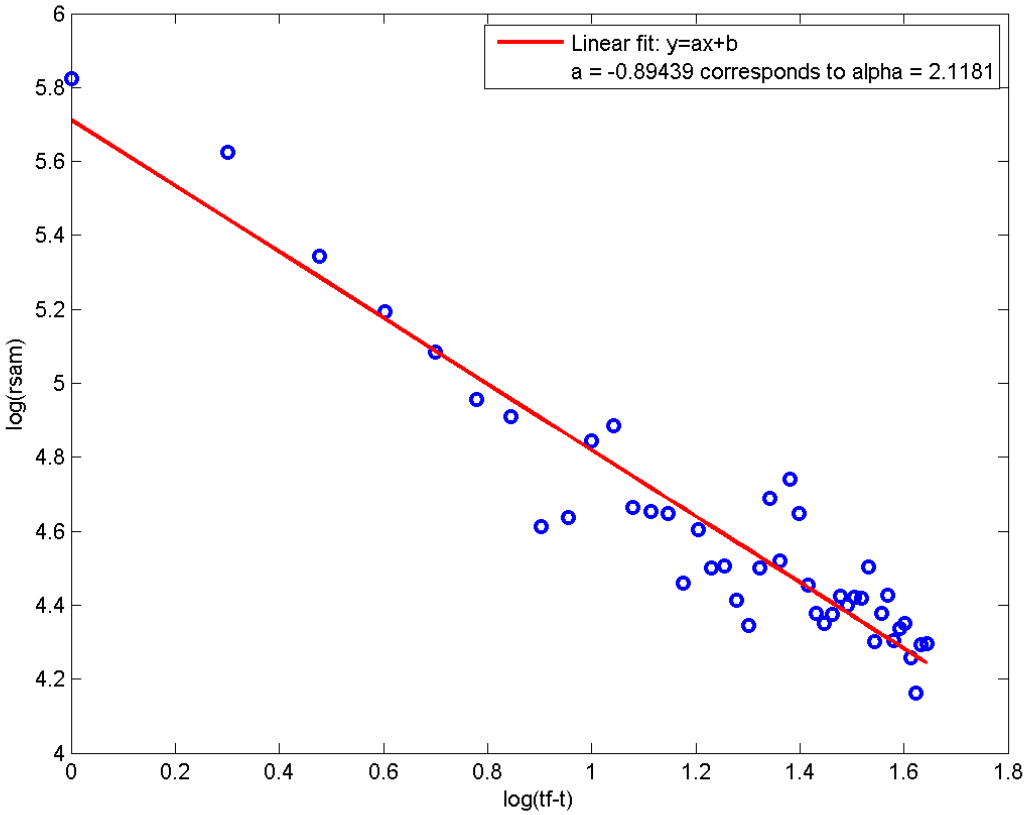

Fig. 4.2 Plot of the RSAM data for the period 13 September – 26 October 2010 following equation 4 for estimating the value of α. The straight red line is the linear fitting which correspond to $\alpha = 2.1$.

4.3 Results

4.3.1 RSAM and MRSAM

Starting in October 2009, the average value of RSAM was almost constant in spite of some small bursts of energy related to the seismic swarms. A slight increase of RSAM was first observed on 12 September 2010 and followed by an accelerating release of energy until 6 October 2010, when a marked decrease of RSAM took place. This behaviour appears clearly in the curve of cumulative values, which displays a discontinuity in slope on 6 October (Fig. 4.3). After this discontinuity,

RSAM values accelerated again until the first eruption on 26 October. Additional accelerating phases of the RSAM curve were observed before the eruptions of 29 October and 3 November. Note that the values of RSAM and MRSAM are in arbitrary units (A.U), since the absolute values are not considered in our analysis.

The maximum values of RSAM provide qualitative indications on the relative amplitude of the different stages of the eruptive sequence. The first eruption of 26 October is associated with a maximum RSAM value of 3.7 x 10^5 A.U. However, after the eruption onset many seismic signals became saturated and, as a consequence, RSAM associated with the various eruption phases is under estimated. Eruptions of 31 October, 1 and 2 November produced smaller maxima. RSAM peaked at 5.7 x 10^5 A.U on 3 November and then reached its highest value 6.7 x 10^5 A.U. on 4 November, when the station was destroyed.

The MRSAM in the frequency band of 1 – 3 Hz shows distinct behaviour compared with other frequency bands (Fig. 4.4). Prior to the eruption, the MRSAM in frequency bands other than 1 – 3Hz show similar behaviour with the RSAM (Fig. 4.3), while the 1 – 3Hz MRSAM demonstrates an abrupt increase from about 23 October until the eruption. After the eruption onset, MRSAM in the band of 3 – 5 Hz displays a relative decrease compared to the other frequency bands. As the 3-5 Hz range contained mostly VT events, this observation suggests that the fraction of energy released by brittle fracture was lower after the eruption onset, which is consistent with an open conduit condition.

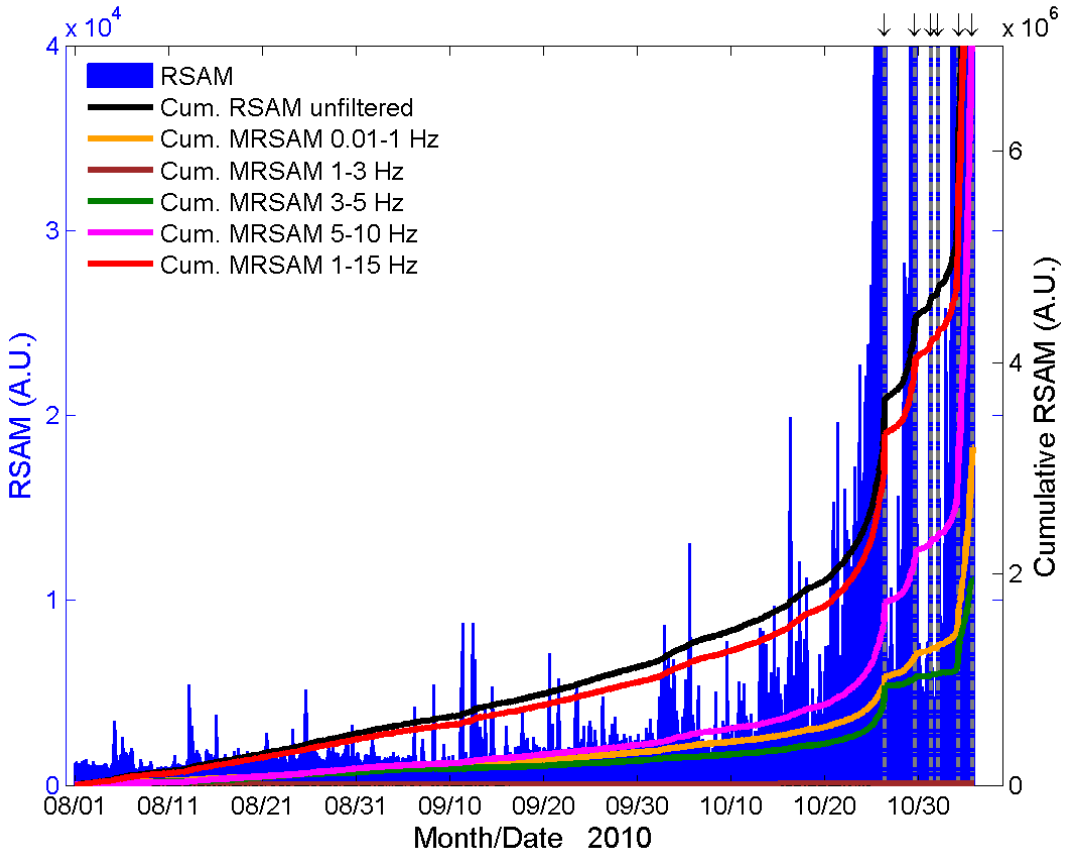

Fig. 4.3 RSAM calculated from station PUS (dark blue area) and its cumulative value (black line) during 3 months prior eruption. Cumulative MRSAM in the frequency ranges 0.01-0.1 Hz (yellow line), 1-3 Hz (brown line), 3-5 Hz (green line), 5-10 Hz (magenta line), and 1-15 Hz (red line). Grey dashed vertical lines and arrows indicate main explosions. RSAM units are in arbitrary units (A.U.). The MRSAM of 1-3 Hz is very small, thus, it huddles with the time axes.

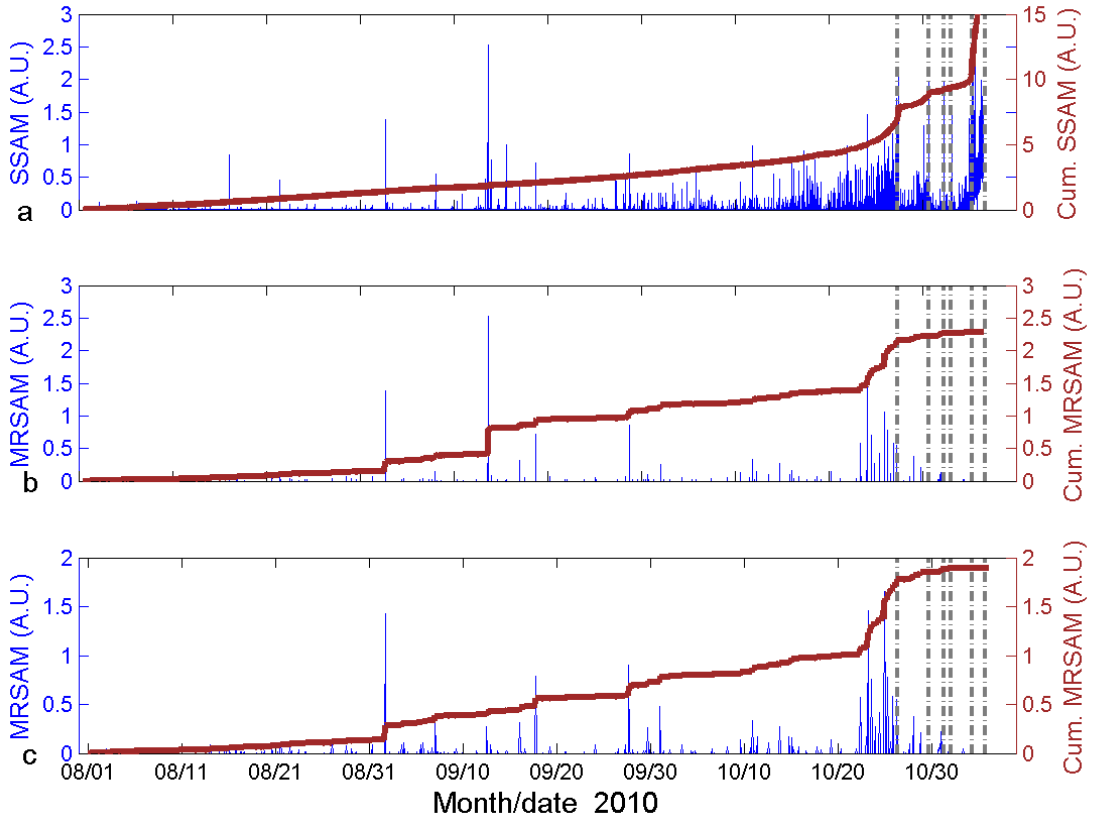

Fig. 4.4 a) SSAM and its cumulative value for the range 1-3 Hz. b) MRSAM in frequency band 1 – 3Hz and its cumulative value c) Same as b, after removing tectonic events A marked increase of LF activity appears more clearly in the last few days before the eruption. SSAM and MRSAM values are in arbitrary units (A.U.). Grey dashed lines indicate the eruption times.

4.3.2 Eruption forecasting

As described in Ch. 2, the first clear increase of seismicity was observed on 12 September. This was followed by a sudden decrease of the slope of the cumulative RSAM on 6 October, then by another acceleration stage until eruption onset on 26 October. Thus, a first trial of fitting a FFT law was made using a window from 13 September to 5 October (Fig. 4.5). For this interval, the adjustment is excellent (correlation coefficient of 99.9%) and the predicted failure time is on 26 October at 07:00, 3 hours before the eruption onset. However a clear

departure between the theoretical and observed curves appears after 6 October. Another trial was thus made with a fitting window starting on 7 October and ending on the 25th (Fig. 4.5). The predicted time is 26 October at 19:00 (yielding a time lag of 9 hours with respect to the eruption onset) and again, the correlation coefficient in this interval is very close to one. These first results confirm that the FFM model used is suitable to explain the observations in the two time periods. However large modifications probably occurred in the volcanic system around 6 October and make it more difficult to apply the method.

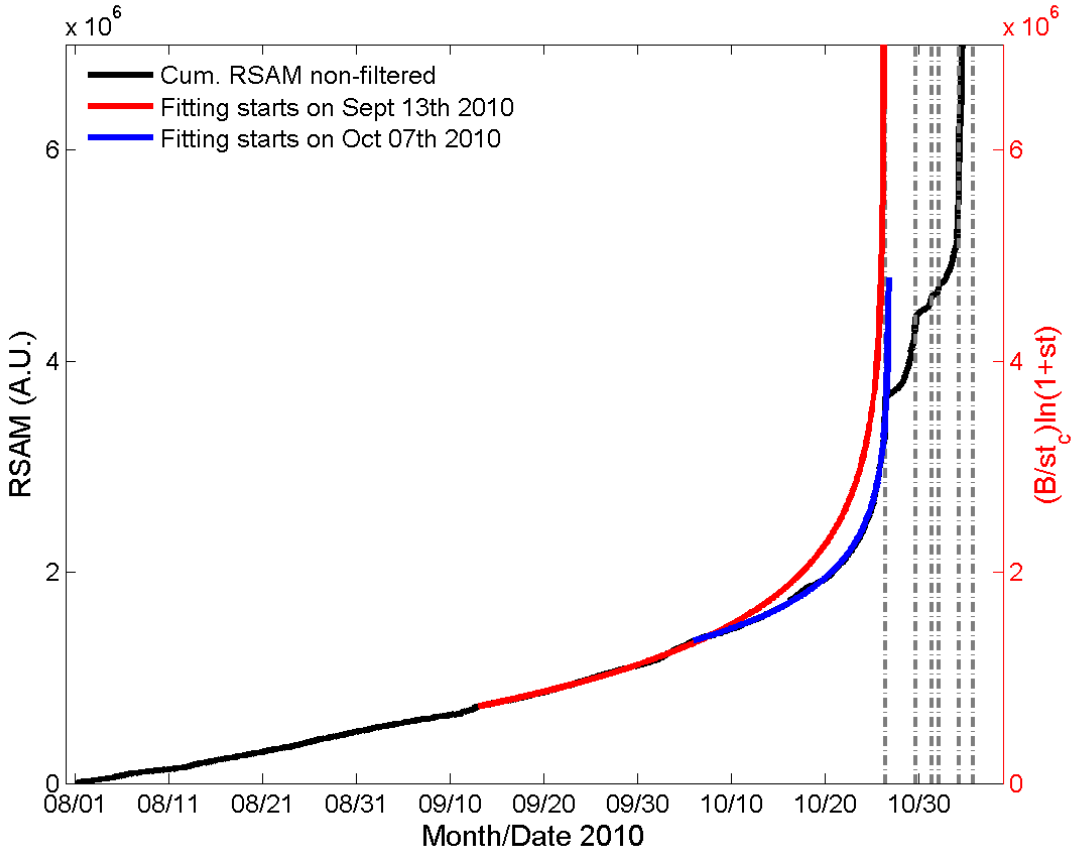

Fig. 4.5 Cumulative RSAM (black line) before eruptions. Theoretical curves calculated with FFM with fitting windows from 13 September to 5 October (red line) and from 7 October to 26 October (blue line). RSAM units are in arbitrary units (A.U.). Grey dash lines indicate the eruptions.

In order to test how robust the FFM model is as forecasting tool for the 2010 eruption, a series of trials was carried out using different fitting time windows. In the following discussion, all dates are in October. For example, t = 20 corresponds to 20 October 2010. The windows have starting time t_{start} = 7 and their ending times t_{end} varies up to 26. The data used are either cumulative RSAM or cumulative MRSAM. The differences between the predicted time of failure t_f and the time t_{erupt} of the first eruption (26 October 10:02 UTC) are plotted as a function of t_{end} in Fig 4.6.

For $t_{end} < 13$, the predicted time t_f is erratic and cannot be used. However, for $t_{end} > 13$, t_f varies smoothly as a function of t_{end}, displays variations between -5 and + 1.5 days around t_{erupt} and then converges toward t_{erupt} for $t_{end} > 20$ (Fig. 4.6a). Similar results are obtained with t_{start} = 6 or 8. The use of MRSAM appears to improve the precision of the prediction. For $t_{end} > 20$, $t_f - t_{erupt}$ is positive and smaller than 0.5 and 0.7 days, for ranges [0.01-1] and [1-15] Hz, respectively (Fig. 4.6b and 4.6e). For the band 5-10 Hz, $t_f - t_{erupt}$ is negative and approaches zero for increasing t_{end} (Fig. 4.6d). In the range 3-5 Hz, the estimated time of failure varies in the interval $t_f = t_{erupt} \pm 4$ hours during the last 6 days before the first eruption (Fig. 4.6c).

Because the deformation rate also accelerated before the eruption, the same FFM approach was applied. In this case, data used are the variations of the slope distance between Kaliurang observatory and a reflector located on the southern part of the summit (Ch. 1, Fig. 1.2). Measurements were carried out by EDM (Electronics Distance Measurement) almost every day. The adjustment between these observations and a function Ω given by equation 5 is not as good as that obtained for RSAM (Fig. 4.7). Moreover, the estimated values of t_f for the deformation data increase monotonically and approaches the time of eruption onset for t_{end} close to t_{erupt} (Fig. 4.6f).

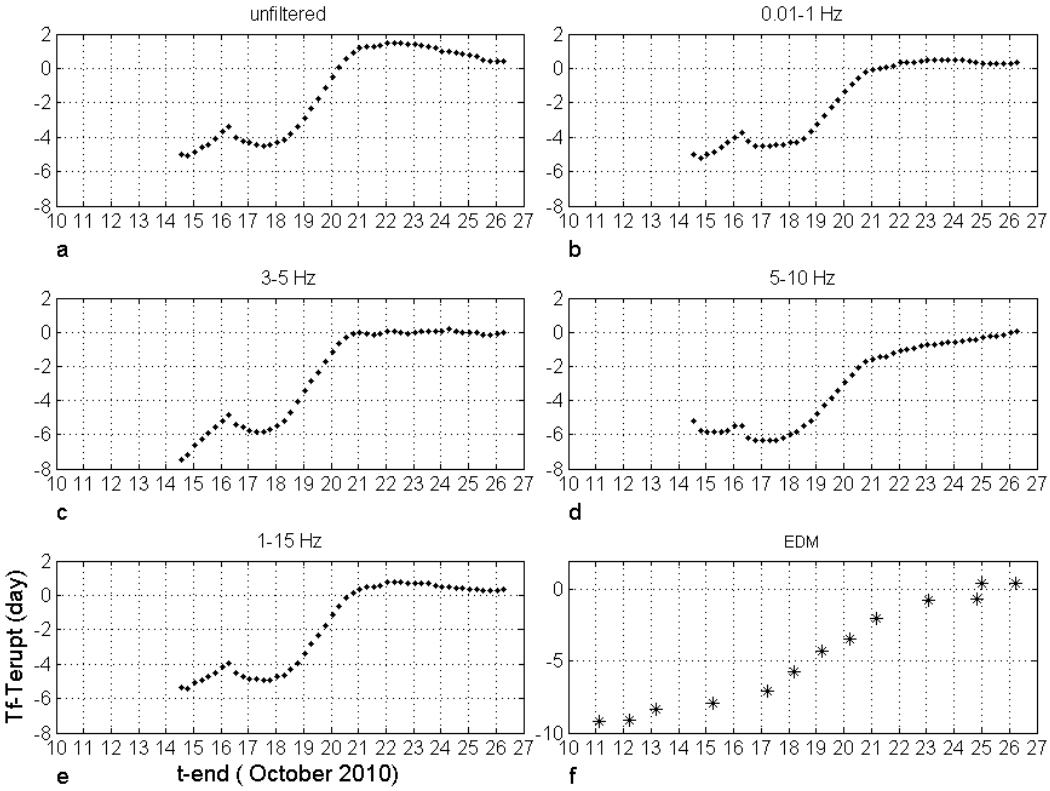

Fig. 4.6 Difference between predicted time t_f and time of eruption onset t_{erupt} as a function of ending time of the fitting window t_{end}, and calculated with t_{start} = 7 October. Observations are a) unfiltered RSAM, b) MRSAM in the frequency range 0.01-1 Hz, c) same for 3-5 Hz, d) 5-10 Hz , e) 1-15 Hz, and f) variation of the slope distance measured by EDM.

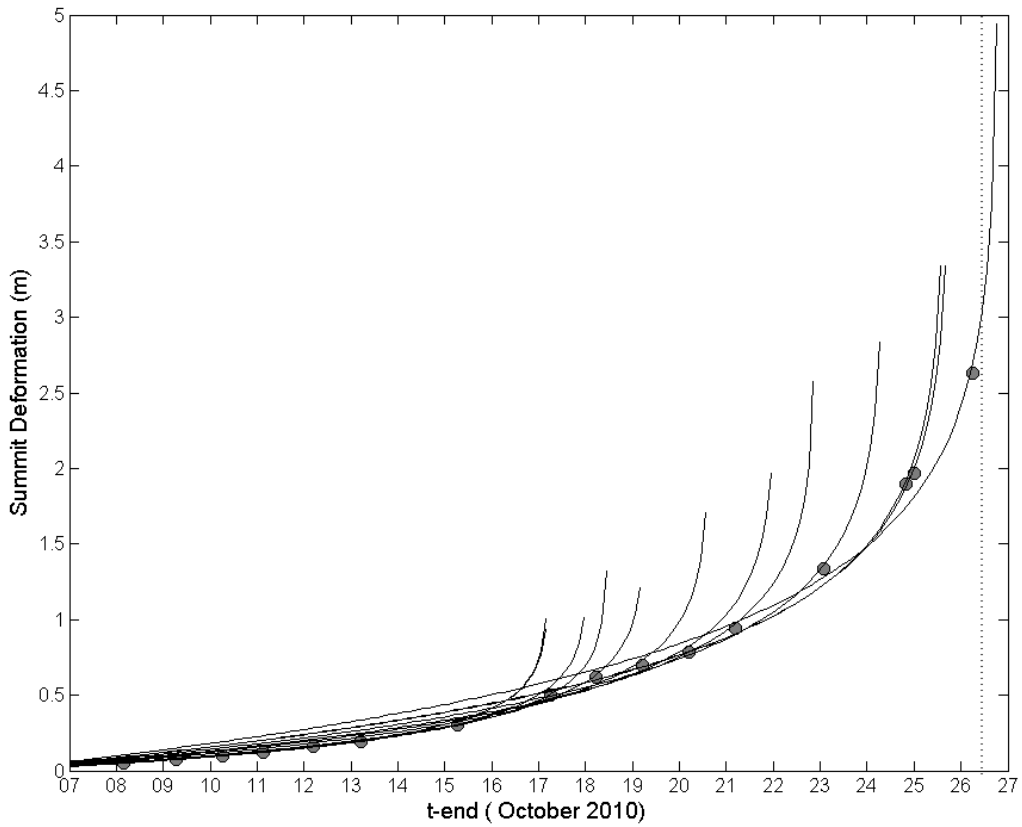

Fig. 4.7 Variation of the slope distance between Kaliurang observatory and the southern part of the summit (circle) and theoretical FFM curves (black lines) obtained with different end times of the fitting windows. Starting time is 7 October.

4.4 Discussions

The accelerated rate of seismic energy was clearly reflected in the RSAM values and MRSAM for the frequency bands other than 1 – 3Hz and offered an interesting opportunity to test the Material Failure Forecast method (Voight, 1988). The results obtained with this model show its ability to forecast the eruption time several days in advance with good precision. We can also use the analysis presented here to evaluate what would have happened had the FFM approach been applied during the pre-eruptive period. Using a start time of 12 September, a first estimation of the initial eruption time (26 October) would have

been obtained before 6 October with good precision (difference between predicted and eruption times of 3 hours). After this date, because of marked changes in the RSAM trends, the forecast time would have shown strong variation with larger and larger departure between observed and calculated curves. Then it would have been necessary to modify the start time of the fitting window to 7 October. However, in the subsequent daily trials, the estimated eruption time would have progressively converged toward the previous estimation. For ending times later than 20 October, the estimate of eruption time would have become relatively stable with a departure from the actual eruption time smaller than 1.5 days. The use of RSAM calculated with signals classified according their dominant frequency improves the results. For example, for dominant frequencies in the range 3-5 Hz, the forecast time is quite stable and its difference with the time of occurrence of the first explosion is smaller than 4 hours during the last 6 days of the pre-eruptive period.

The accelerated behaviour of some parameters used in volcano monitoring has been interpreted as resulting from damage to solid materials before their failure (Voight, 1988; 1989; Cornelius and Voight, 1994). Kilburn (2003) associated the accelerating rate of seismicity with the growth and the progressive connection of arrays of pre-existing fractures brought about by magma propagating to the surface. De la Cruz-Reyna and Reyes-Davila (2001) applied a Kelvin-Voigt viscoelastic model to describe the tertiary creep associated with degradation and weakening of a medium preceding rupture. They fitted a logarithmic curve, similar to equation 5, to the cumulative value of the root mean square of the seismic signal recorded before eruptions of Colima volcano, Mexico, and correctly predicted the eruptions. In these cases, the conduit system was considered closed before the unrest. Features of the seismic activity preceding the 2010 eruption of Merapi volcano indicate that the magmatic conduit was effectively closed; at least this was the case with respect to the large volume of magma that was intruding. Therefore the physical conditions of a closed system required by the models for good estimations of the time of eruption were probably

also fulfilled in 2010 at Merapi. On the contrary, before earlier eruptions of Merapi, such as that of 2006, marked accelerating behaviour was not observed, consistent with a much smaller volume of magma extruding through a more open conduit. Thus, it appears that better forecasts could be obtained with FFM for large explosive crisis than for small effusive events. Note that, although FFM can provide useful indications on the onset time, it cannot forecast the size on the impending eruption.

In retrospect, one of the main difficulties in using the FFM approach in real-time was the result of variation in the RSAM rate that occurred around 6 October. Similar variations were observed before two eruptions of Colima volcano (De la Cruz-Reyna and Reyes-Davila, 2001). Ascent of magma through layers of different mechanical strength likely produced variable load regimes on the material and yielded fluctuations in the rate of acceleration of RSAM values.

When using the FFM or similar methods for operational forecasting, it is of paramount importance to take into account the many possible sources of uncertainty on the estimation of eruption time (Bell et al., 2011b). Part of the uncertainty comes from the choice of the time window used to fit the theoretical curve (Boué et al., 2012; 2013). In this work, several starting times and many ending times of the window have been systematically tested in order to study the stability of the estimations and to obtain more confident results. The models are improved when frequency-binned signals are used to calculate RSAM. The best results are obtained for signals with dominant frequency in the range 3-5 Hz (mainly VT events). This is consistent with the mechanical interpretation of the FFM method as discussed above. The very short lag between the estimated times of failure and the eruption onset suggests that the first explosion occurred immediately after the rupture of the final plug in the shallow part of the conduit. Displacement of the summit also accelerated before the eruption; however, FFM analysis of the deformation data does not give stable and usable solutions. The pattern of deformation indicates that the deforming area (the south sector of the crater wall) was uncoupled from the rest of the volcano, and it subsequently

collapsed during the eruption. Consequently, its movement may not have been representative of the deformation of the whole structure. In fact, according to Saepuloh et al., 2013, the deformation during the crisis was only summital.

Based on the temporal evolution of hypocenters and the episode of relative quiescence of seismic and deformation activity, we suggest that a magma migration from deeper to shallower zone occurred through a more ductile aseismic zone. For t_{end} >20, the FFM results are stable pointing to the eruption time with small fluctuations. It likely means that this forecasting stability is obtained when the stresses are concentrated at the shallower zone where it produces an effective damaging process.

MRSAM in frequency band 1 – 3 Hz, which reflects mainly LF activity, shows distinct behaviour with an abrupt increase from about 3 days before the first eruption. We interpret this behaviour as gas escapes prior to the eruption which somewhat indicates the eruption would occur promptly.

4.5 Conclusions

Both seismic and deformation data show acceleration behaviour. These behaviours somewhat provided an indication that the impending eruption would be unusually large. Further, we took advantage of this behaviour by performing hindsight forecasting based on the FFM. The best FFM result is obtained using 3 – 5 Hz MRSAM data with fitting window starting 20 days before the eruption. As early as 6 days before the eruption, we could obtain prediction of the eruption times with accuracy of less than 4 hours. This successful hindsight forecast can be associated with the closed or almost closed state of the magmatic system before the eruption. Multiple trials of a posteriori prediction of the eruption time suggest that high precision can be achieved if magma and hypocenter migrations and/or changes of load regime are identified and the forecasting strategy adapted to these variables.

In the future, if an episode of unrest at Merapi produces an unusually large cumulative seismic energy release with a clearly accelerated rate and if other observables (e.g. deformation or gas emission) present similar behaviour, then a large explosion similar to (or possibly larger than) 2010 should be considered as highly probable. In this case and given that the limitations are well understood, the FFM would be of value in supporting decisions concerning evacuation. Another aspect in eruption precursor is also revealed by the MRSAM data. A sharp increase of 1 – 3Hz MRSAM a few days before the eruption is interpreted as gas escapes which implies short delay until the eruption.

Chapter 5

Analysis of families

5.1 Introduction

Until now seismicity is the most robust method for revealing the internal processes of active volcanoes. Therefore volcano activity monitoring relies strongly on seismicity data. One of the most conventional methods to understand and predict the volcanic activity is event classification and the simplest way to follow the evolving activity is to count the number of each type of events. In the case of Merapi eruptions, the increasing number of MP and VT earthquakes is a common eruption precursor since it reflects the stress accumulation due to magma rising to higher elevation. However the eruption caused by gravitational collapse of lava dome is a particular case which is more difficult to monitor.

In addition to the event classification, families of certain types of event observed in several volcanoes give more information about the evolving processes. Earthquake families, or seismic multiplets, are sets of events with the same waveform which implies the same source mechanism and locations (Poupinet et al., 1996). This phenomenon has been observed both in tectonic and volcanic region. As they are suggested to occur repeatedly at about the same locations, multiplets have many seismological applications such as: highly precise locations; detection of temporal variations of attenuation; shear wave splitting and medium velocity variations; dynamics of active faults and their slip rate; finally, in volcanic environments, evaluation of the volcano conditions (Cannata, 2012; Cannata et al., 2013). For example, in the case of volcanic region, Okada et al. (1981) reported earthquake families associated to the doming activity of Usu volcano in 1977-1978.

In Merapi family analysis had been reported as a procedure for calculating velocity variation based on the coda wave prior to 1992 eruption. There are 4 multiplets observed among shallow VT events (VTB) by visual comparison. Among these multiplets, two of them show an increase in seismic velocity up to 1.2 % at 4 months before the eruption of 2 February 1992 (Ratdomopurbo and Poupinet, 1995). These multiplets suggested that their hypocenters must be close each others. Thus, using cross-spectral technique for measuring differences in arrival times, the relative location of hypocenters could be improved from having errors of hundreds meters to the order of 10m (Poupinet et al., 1996).

Waveforms extracted from the continuous signals, either by manual extractions or automatic detections, are used as the input of the family analysis. The most popular method used in detecting arrival time of events is the STA/LTA method proposed by Allen (1982). The average of amplitude or amplitude square is calculated on short term windows (STA) and long term windows (LTA). An arrival time is defined when the ratio of STA/LTA reaches a given threshold. This method has been developing with many improvements and modifications. According to Tong (1995) a recursive STA/LTA is more efficient and less sensitive to background. Moreover, adaptive STA/LTA methods are claimed to be more accurate. Withers et al. (1998) proposed an adaptive STA/LTA to overcome the problem of short window length dependency which is considered as the disadvantage of STA/LTA. Meanwhile, an adaptive STA/LTA has also developed for automatic threshold selection (Akram end Eaton., 2012).

Besides STA/LTA, many other automatic picking methods have been used based on different approaches. Local Maxima Distribution (LMD; Panagiotakis et al., 2008), fractal (Sabbione and Velis, 2010), Modified Energy Ratio (MER; Wong et al,, 2009), kurtosis (Saragiotis et al., 2002; Gentili and Michelini, 2006; Kuperkoch et al., 2010), Standard Deviations (STD; Akram and Eaton, 2012), and Akaike Information Criterion (AIC; Akaike, 1974; Zang et al., 2003; Kurz et al., 2004; Jousset et al., 2011) are the examples of the method that use statistical criteria as the characterisation function (CF). Other approaches based on cross-

correlation (Rowe et al., 2000), wavelet (Tibuleac et al., 2003), and neural networks (Zhang et al, 2003; Gentili and Michelini, 2006) are also available.

The similarity of the events in family analysis is quantified by using the cross-correlation function between the short earliest windows of the events. Since a small time shift between the windows would largely decrease the correlation, thus, a high accuracy of arrival times is crucial. Because of this reason the selection of the automatic event detection method becomes important.

The aim of this work is to perform event detections and family analysis of the seismicity of Merapi during 2009-2010. For detecting the events, we propose a recursive method and we compare it with several other available methods. Afterward, we perform event clustering and family analysis related with pre-eruptive activity of Merapi in 2010.

5.2 Data and method

Data used are digital signals of PUS (short period) station and PAS (broadband) station between October 2009 and October 2010. These two stations are nearby stations (0.5 km) located close to the summit (0.5 – 0.7 km). Due to their close distance, we could expect to get the same information from both stations, although PAS station is better because it is located closer to the summit and even more it is a broadband station. The drawback of PAS station is that it has worked on a shorter time period. In fact it was no longer available after 23 October 2010 (3 days before eruption). We did not apply filtering in performing the events detection.

One of the information that must be provided in performing family analysis is the arrival times of the events. Actually in hypocenter calculation (Ch. 3) we have such information already. However, many arrival times provided are not absolute times (relative times instead). Therefore, a procedure of automatic event detection is needed in order to complete the existing set of arrival times.

5.2.1 Recursive events detections

The events were detected by means of a recursive method composed by the STA/LTA procedure and a method based on the ratio between long term and short term energy average (LTE/STE). The former is used to obtain coarse arrival times estimations, while the later is used for improving their precision. STA/LTA procedure is explained as follows. Let $\mathbf{x_i}$ be the times series representing a seismogram. Let the number of points in a short-term window be ns, and the number of points in a long-term window be nl, with nl > ns. Then the average absolute amplitudes in the short (STA) and long term windows (LTA) preceding the time index i are

$$STA = \frac{1}{ns} \sum_{j=i-ns}^{i} |x_j| \qquad 5.1$$

$$LTA = \frac{1}{nl} \sum_{j=i-nl}^{i} |x_j| \qquad 5.2$$

The arrival time estimation is defined when the ratio of STA/LTA reaches certain threshold. Likewise the end of the events could be estimated. Thus, in application several parameters are defined i.e. the threshold values of STA/LTA ratio by which the beginning and the end of the events are determined (tstart=2 and tend=1.2), the minimum time interval between two consecutive detections (dist=5s), and the threshold of time difference between tstart and tend by which the detection is considered as an event (mindur=5s). Those parameters values were chosen based on tests conducted with a trade off between reliability and accuracy.

The method using long term and short term energy ratio (LTE/STE)

Improvements of the estimated arrival times are needed since the precisions of the arrival times resulted from the method of STA/LTA vary, following the waveforms difference particularly on the onset part. In fact, we found that, for impulsive onsets, the detection is earlier than the correct arrival time. On the

contrary, for emergent onsets, the detection is later. In order to address this problem, we used a method which is the inverse of STA/LTA algorithm. While STA/LTA, as it is indicated by its name, uses long term window as denominator, our method use the inverse i.e. long term window divided by short term window. We use the square of amplitude (energy) instead of the absolute of amplitude. In the application of STA/LTA, many people use also square amplitude instead of amplitude. However we use another abbreviation to avoid confusion with STA/LTA which is applied before. Let short term energy be STE and long term energy be LTE. They can be written as:

$$STE_i = \frac{1}{ns} \sum_{j=i-ns}^{i} x_j^2 \qquad 5.3$$

$$LTE_i = \frac{1}{nl} \sum_{j=i-nl/2}^{i+nl/2} x_j^2 \qquad 5.4$$

According to equation 5.3 and 5.4, the time mark for STE is at the end of the window, whereas, for LTE is at the middle of the window. The LTE will find the onset first while STE is still within the background noise, thus, the value of LTE/STE starts to increase. When the short term window (STE) reach the onset, the ratio of LTE/STE will decrease dramatically (Fig. 5.1). Although it appears that the onset might correspond to the maximum value of LTE/STE, in fact for many cases it is not the case.

In order to detect the decrease in LTE/STE that corresponds to the arrival time, we search the maximum of the absolute values of the derivative of LTE/STE. The time interval on which we want to improve its arrival time must be not too large and thus contain only one maxima associated with the corresponding time arrival. In this study, we considered only a time interval of 5 s around the arrival time estimated from the previous method. We used short term window (sl) length of 100 points (1 s) and long term window length (nl) of 300 points (3 s).

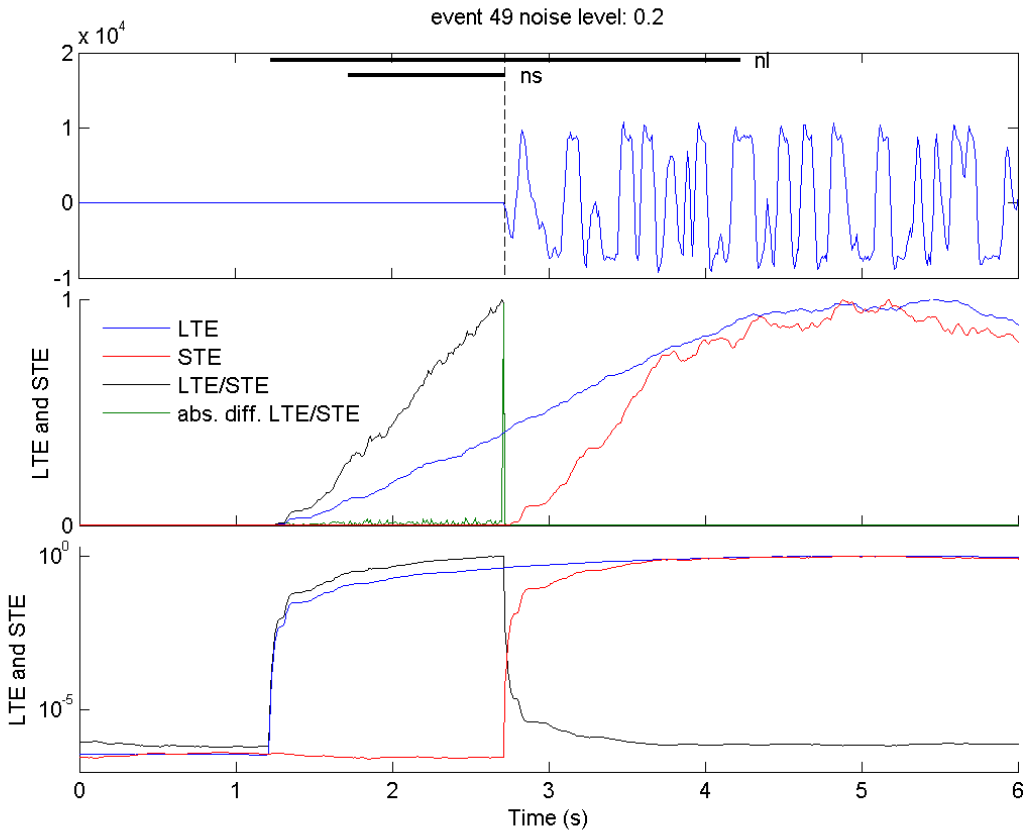

Fig. 5.1 An illustration of the LTE/STE method. The time of LTE values corresponds to the middle of the windows, while for STE, the time corresponds to the end of the windows. An arrival time is defined when the ratio LTE/STE decreases dramatically at which the STE get the first perturbation of P-onset (middle). The time at which this decrease occurs is identified by the absolute differentiated values of LTE/STE. To show more clearly how it works, we change the y-axis scale to logarithmic scale (bottom).

There are methods available which also use the maximum value of the characterisation function (CF) to define the arrival times such as kurtosis (see Saragiotis et al., 2002) and Modified Energy Ratio (MER) (see Han et al., 2008). We performed tests to show their reliability particularly against noise and compared with the proposed method. Initially, kurtosis method uses single moving window (Saragiotis et al. 2002). However, in this study we rather use ratio of kurtosis between two windows called current and previous window with

the same length. According to Dugda and Kadebe (2010), using such technique a better accuracy is obtained.

As it is explained by Han et al., (2008), in MER method we use two moving windows as that of kurtosis method. Furthermore, we use the same length as STE for the moving window of kurtosis and MER. The time attributes for MER window is at the beginning of the current window, while, for kurtosis, is at the end of the current window.

In performing the tests, first we created synthetic signals composed of an event and Gaussian random noise. Several standard deviations were used in the Gaussian random noise to provide different noise level. Here, level noise of 1 corresponds to the general background noise of the seismogram. There are 3 types of event selected i.e. a saturated event, an unsaturated event, and a saturated event with a small preceding onset. We compared also the implementation over the real signals. The test results are presented later on in section 5.3.

5.2.2 Extraction of families

Waveforms with duration of 20s are extracted with arrival times obtained from the previous events detection as the reference. Band-pass filtering from 0.5 to 8 Hz was performed. For the sake of computational efficiency, we down-sampled the waveforms from 100 to 50 Hz. Our family analysis is based on similarity of the events quantified by the maximum of the correlation functions between events pairs. Suppose there are two events recorded on the same station but with different arrival times i.e. a1 and a2. The maximum cross-correlation coefficient is calculated by using the formula:

$$r_{max} = \max\left(\frac{C_{12}(\tau)}{\sqrt{C_{11}(0)C_{22}(0)}} \right) \qquad 5.5$$

where $C_{12}(\tau)$ is the correlation function between a1 and a2:

$$C_{12}(\tau) = \int_{-\infty}^{\infty} a_1(t)a_2(t+\tau)dt \qquad 5.6$$

In volcanic domain, only a small part at the beginning of the signals is used to form the different families without many glitch-type events, i.e. that belong to several clusters, because a small perturbation of source location can change significantly the later part of the signal. Cross correlations were performed in 1.7 s windows length starting 0.5 s before the arrival time. Waveforms were clustered using hierarchical clustering algorithm based on similarity indicated by the correlation coefficients where hierarchy or tree-like structure is constructed to see the relationship among the entities. Average linkage which is one of the most popular agglomerative methods was chosen to build links between waveforms. It is based on the average distance from samples in one cluster to samples in other cluster (Lance and Williams, 1966).

Windows were shifted one with respect to the other using the time-lags resulting from the cross correlation in order to obtain a better alignment of the waveforms. To do this, preliminary clustering was performed with correlation threshold of 0.72. Alignment was then applied in each cluster obtained. Once the windows were aligned better correlation values were achieved (Fig. 5.2).

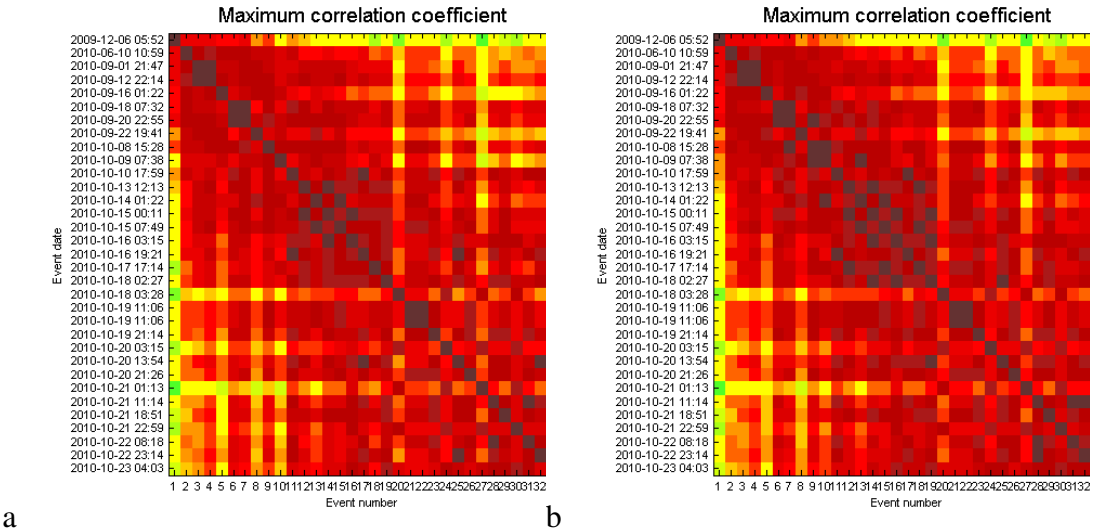

a b

Fig. 5.2. Cross-correlation matrix of a cluster before (a) and after alignment (b). Pixels around the diagonal get darker indicated a better correlation.

The most critical point of this process is to define the cross correlation threshold value over which it is considered that 2 events belong to the same family. Different thresholds were chosen for station PUS and PAS i.e. 0.78 and 0.75 respectively. Because PUS is a short period station who has a lower SNR (signal to noise ratio) then larger threshold is needed.

We found that this clustering method which is based on waveform correlation is limited by magnitude band. Such phenomenon was also reported by Deichmann and Garcia-Fernandez (1992) who demonstrated that event classification method based on cross correlation would consistently be biased when comparing waveforms differing from each other by more than one order of magnitude. In order to overcome this problem, two possible solutions are available which are to decrease the correlation threshold or to apply bridging technique. The former has low strictness and has high possibility of non appropriate events inclusions. The later was chosen for which if two couples of events (A, B) and (B, C) share a common event (B), then all three events are attributed to the same family. The algorithm is based on the equivalence class approach (Press et al., 1988) and has already been applied by Aster and Scott (1993), Cattaneo et al. (1997, 1999),

Ferritti et al. (2005), Cannata et al. (2013) and others. The bridging technique allows merging the clusters recorded on a number of stations without losing accuracy. However visual check is needed in order to avoid glitch-type cluster (Cannata et al., 2013). The ten largest clusters which are representative of the whole clusters were taken for the analysis. In fact, using lower correlation threshold most of the clusters could be included into the 10 first clusters. However, the numbers of events belonging to the other clusters are too small to be considered (1-3 events). Most of routines for performing event clustering were adopted from a correlation toolbox (West, 2008) with some modifications.

In order to perceive the frequency characteristic of the clusters, the spectrum of the first 5s was computed and normalized for each event. Spectra of all events in the same cluster are then stacked and normalized. In addition, the hypocenters of the clusters were also evaluated thanks to the previous VT localisation.

5.3 Results and discussions

5.3.1 Events detections

In order to detect the events we first used the procedure of STA/LTA. Although this method is very powerful for detecting the events, we obtained the arrival times with low accuracy. For improving the accuracy of the arrival times obtained, we used the LTE/STE method. We also compared this method with the kurtosis and MER methods. In this case we worked on a localized time interval (5s) according to the initial arrival times.

Application on synthetic data

First tests were performed on a saturated event. We consider this event as the easiest event to detect due to its very impulsive onset. We imposed noise on the signal with different amplifications. Fig. 5.3a,b shows how each method estimates the arrival time in low and high noise level. Their time differences with the

manually defined arrival time are presented on Fig. 5.3c. In this figure, the initial arrival time detected by STA/LTA method is plotted only at the noise level 1 which is considered to represent the real background noise. Later on, the figures corresponding to the tests using other events are displayed likewise.

On these tests LTE/STE method shows precise and stable result even with high noise level. Stable but deviated (-0.07 s from the defined arrival time) results are shown by MER method until the noise level of 6. Meanwhile, increase of deviations from 0.01s to 0.04 s as noise level increase is obtained for the kurtosis method.

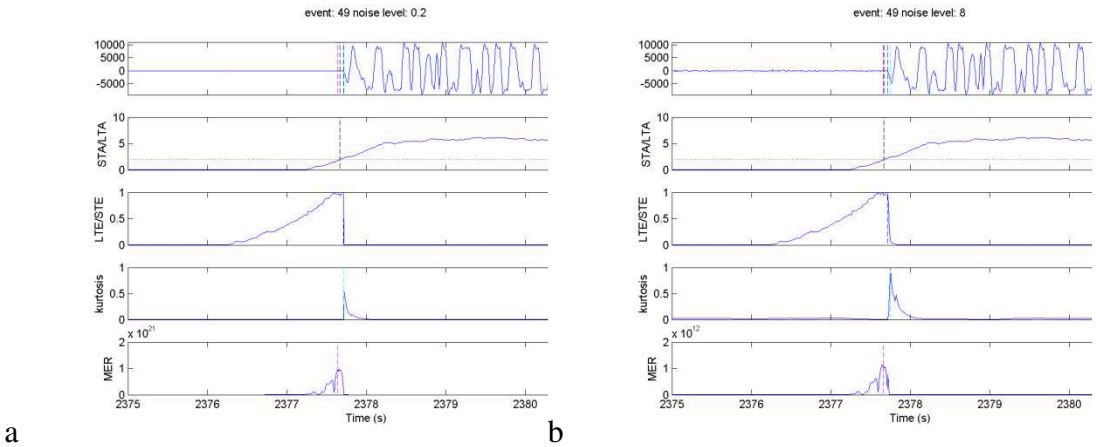

a b

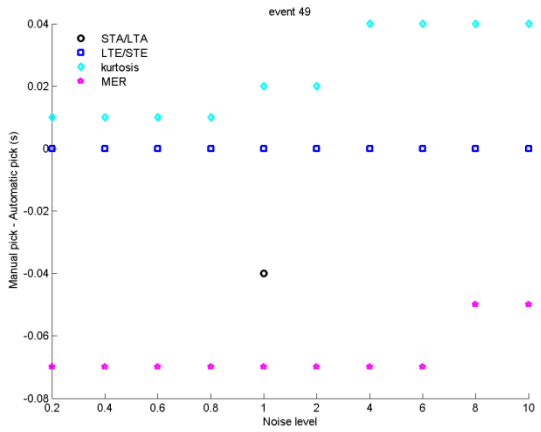

c

Fig. 5.3 Arrival time detections using the methods of STA/LTA, LTE/STE, kurtosis, and MER for a saturated-event in low noise level (0.2) and high noise level (8) (a and b). Time deviations between calculated and defined arrival time at different noise levels (c).

In the second tests, we used an unsaturated signal with emergent onset, to which the recent first break detection methods are addressed. Again, the method of LTE/STE yields precise and stable results until the highest noise level used (Fig. 5.4). The method of MER shows stable results, with deviations of -0.03 s which are smaller than that of previous tests with a saturated signal. Kurtosis method persists showing somewhat an increase in deviation from 0.02 s to 0.47 s with increasing noise level.

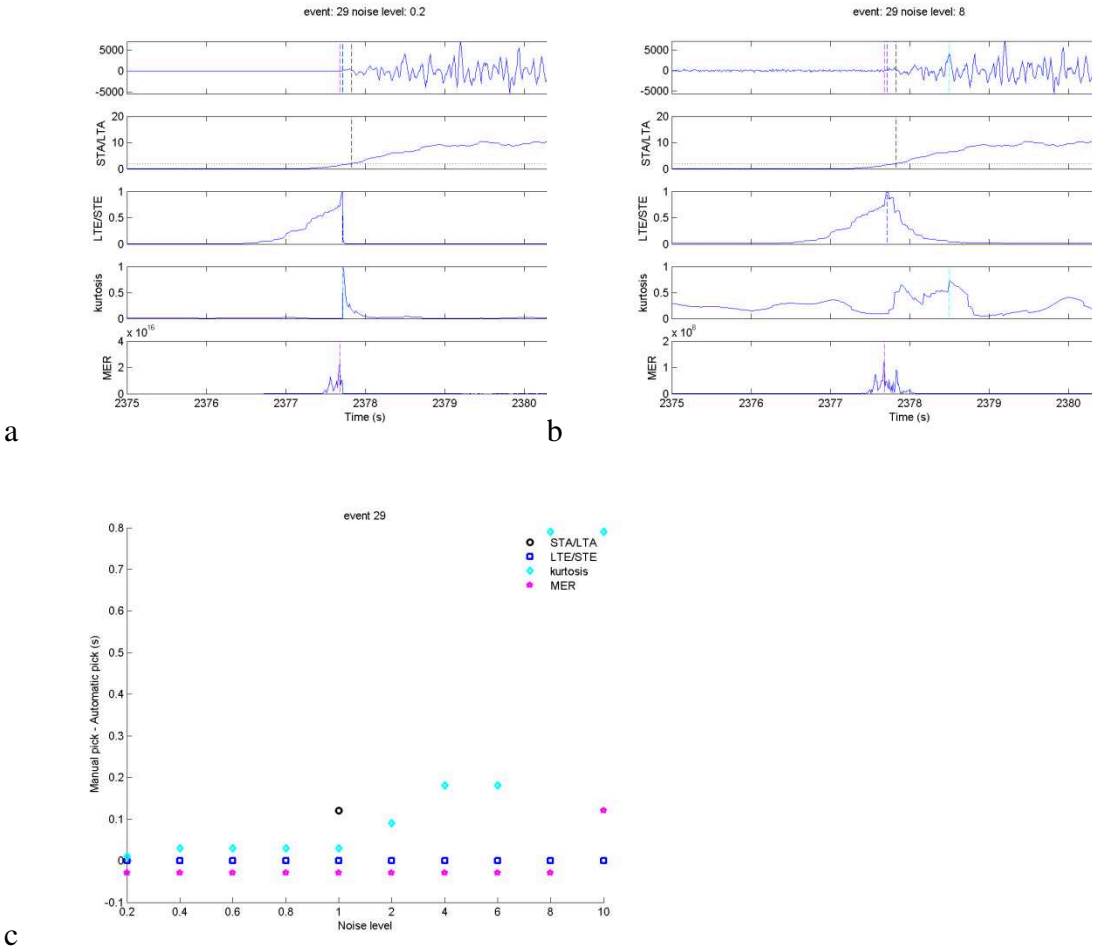

Fig. 5.4 The same as Fig. 5.3 for an unsaturated event.

For the third tests, using a small-onset saturated signal, the method LTE/STE shows precise and stable result until the noise level of 1. Meanwhile, precise times are pointed with MER method only for the noise levels of 0.2 and 0.4. The times then deviate significantly (0.32 s – 0.63 s) for the higher noise levels. With respect to the kurtosis method, stable but largely deviated (0.82 s) results are shown. This method seems to detect the beginning of saturated amplitudes rather than the event onset.

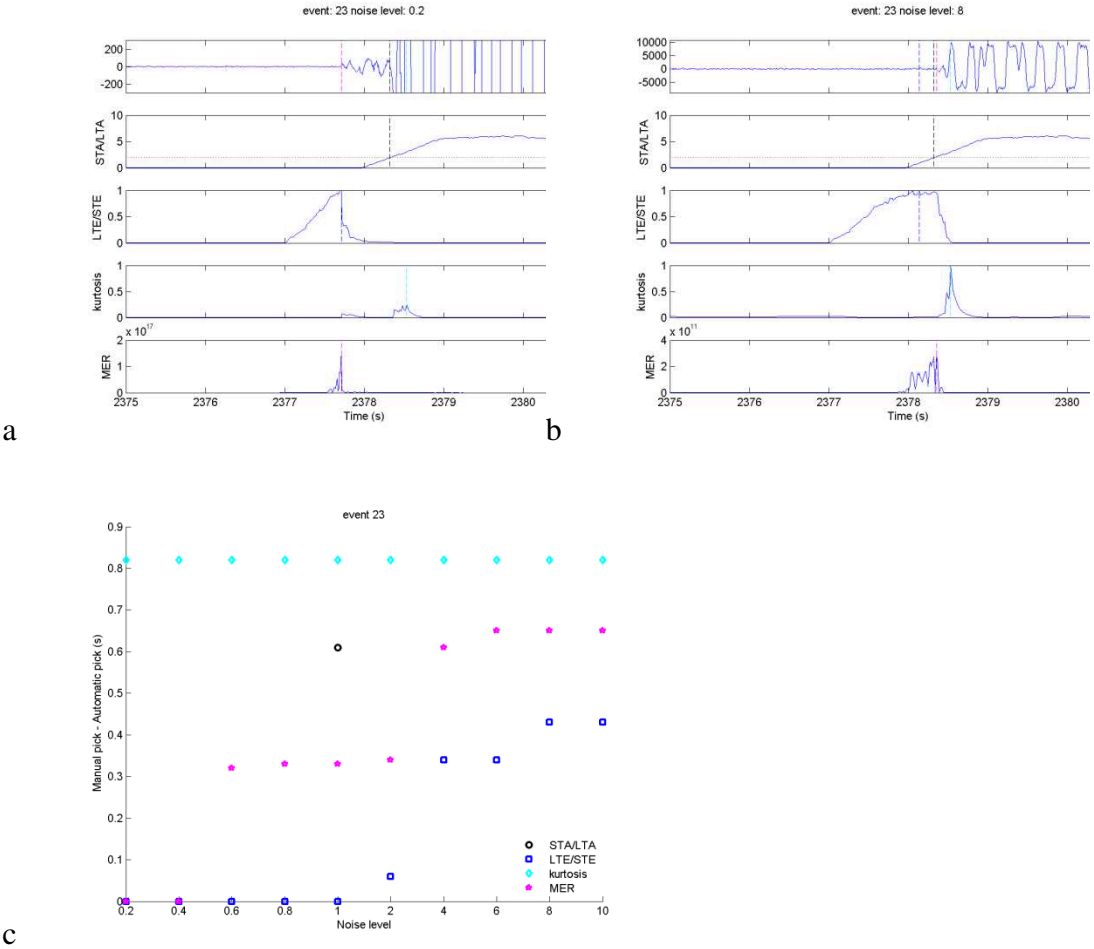

Fig. 5.5 The same as Fig. 5.3 for a small-onset saturated-event.

Summarizing those results, we found that the LTE/STE method shows stable results against noise levels for the different waveforms. Moreover, this method is

more sensitive in detecting the small onset of a saturated event until certain noise level compared to the other tested methods. The method MER yielded stable results only for the same event. It produces different deviation values for the other waveforms. It means that the deviations are not systematic and thus could not be recovered. Meanwhile, the results of the kurtosis method seem to have dependency on the noise level.

Implementation on real data

We performed detections on real signals using the same procedures. We used the data of PAS station for evaluating the results. Due to periods of station breakdown and lack of absolute arrival times, there are only a few picked arrival times that can be used for comparison i.e. around 100 events. Differences between resulted arrival times and manual picks and their histogram are presented on Fig 5.6. For the STA/LTA, the results are distributed around the zero with a standard deviation of 0.16s. By improving the resulted times using the methods of LTE/STE, kurtosis, and MER we obtained less distributed times with standard deviations of 0.015, 0.019, and 0.036 respectively. It appears that the methods of LTE/STE and kurtosis are quiet stable as they have small standard deviation. However, for kurtosis method, its maximum distribution is slightly deviated at -0.05s. Since this deviation appears stable over the evaluated events, we suggest that the background noise during the evaluated events is stable and fairly strong. Indeed, according to the tests using synthetic signals, kurtosis method seems to have dependency mainly on the noise level. Thus, in the case of events whose background noise is different, there is a risk to have different deviations with respect to the manual picks.

Based on these test results on synthetic and real data, we prefer to use the arrival times resulting from the method of LTE/STE since it gives more precisions and sensitivities over small onsets. Further we selected only the events which are also detected on the furthest station i.e. PLA station. The final results are arrival times of 795 events on PUS station, and 393 events on PAS station.

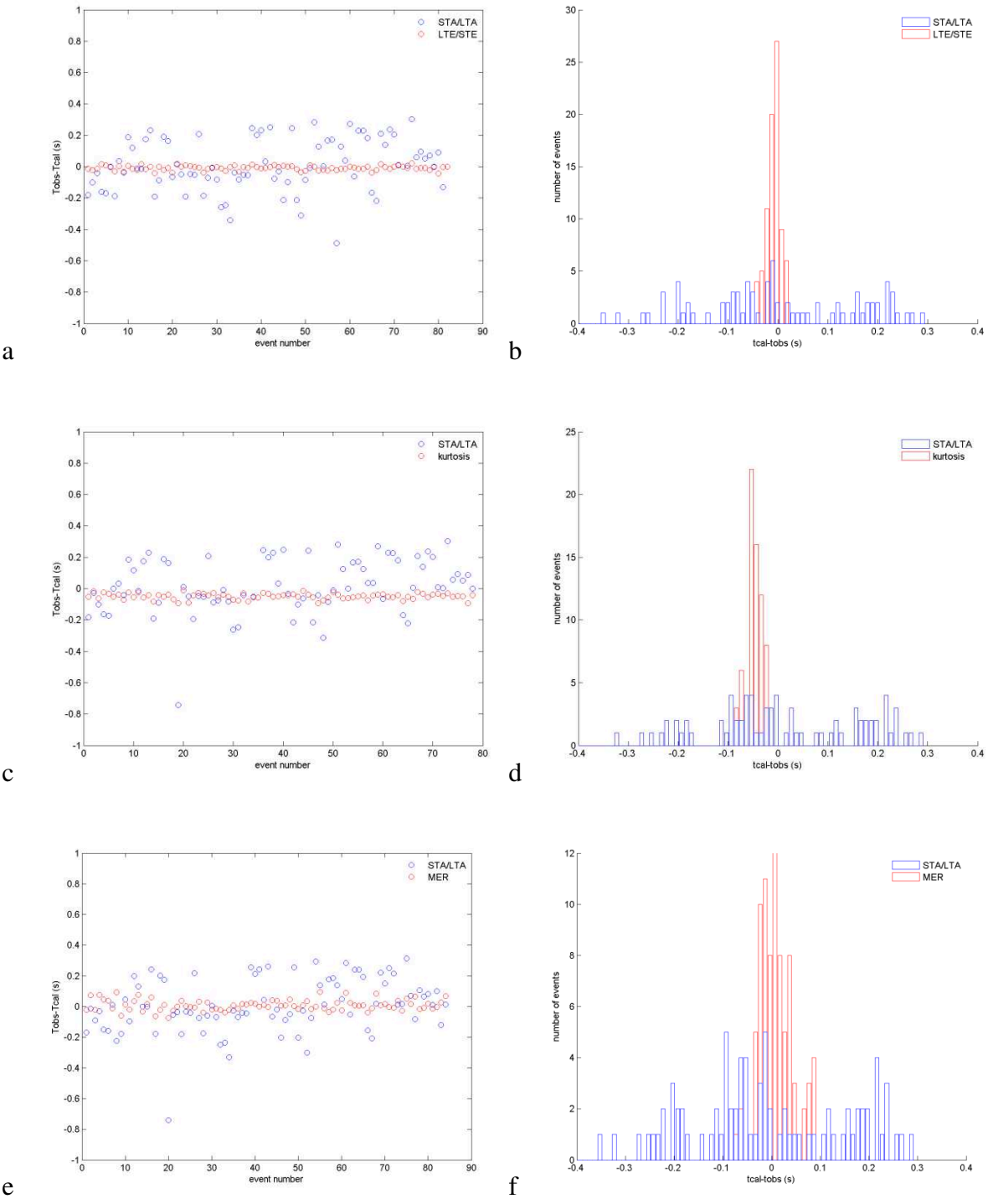

a b c d e f

Fig. 5.6 Difference between calculated arrival times and manual picks (a, c, e) and their histogram (b, d, f). Blue colors correspond to STA/LTA results and red

colors indicate the improved times using different methods as indicated in the legend.

5.3.2 Families of events

209 events among 393 events (53 %) of PAS and 322 events among 795 events (41 %) of PUS are clustered. Figures below are the clusters resulting from station PAS (Fig. 5.7) and PUS (Fig. 5.8). The cluster numbering of PUS corresponds to that of PAS. The last cluster of PUS (cluster 10) has no relation with the clusters of PAS because when this cluster occurred, station PAS was no longer available.

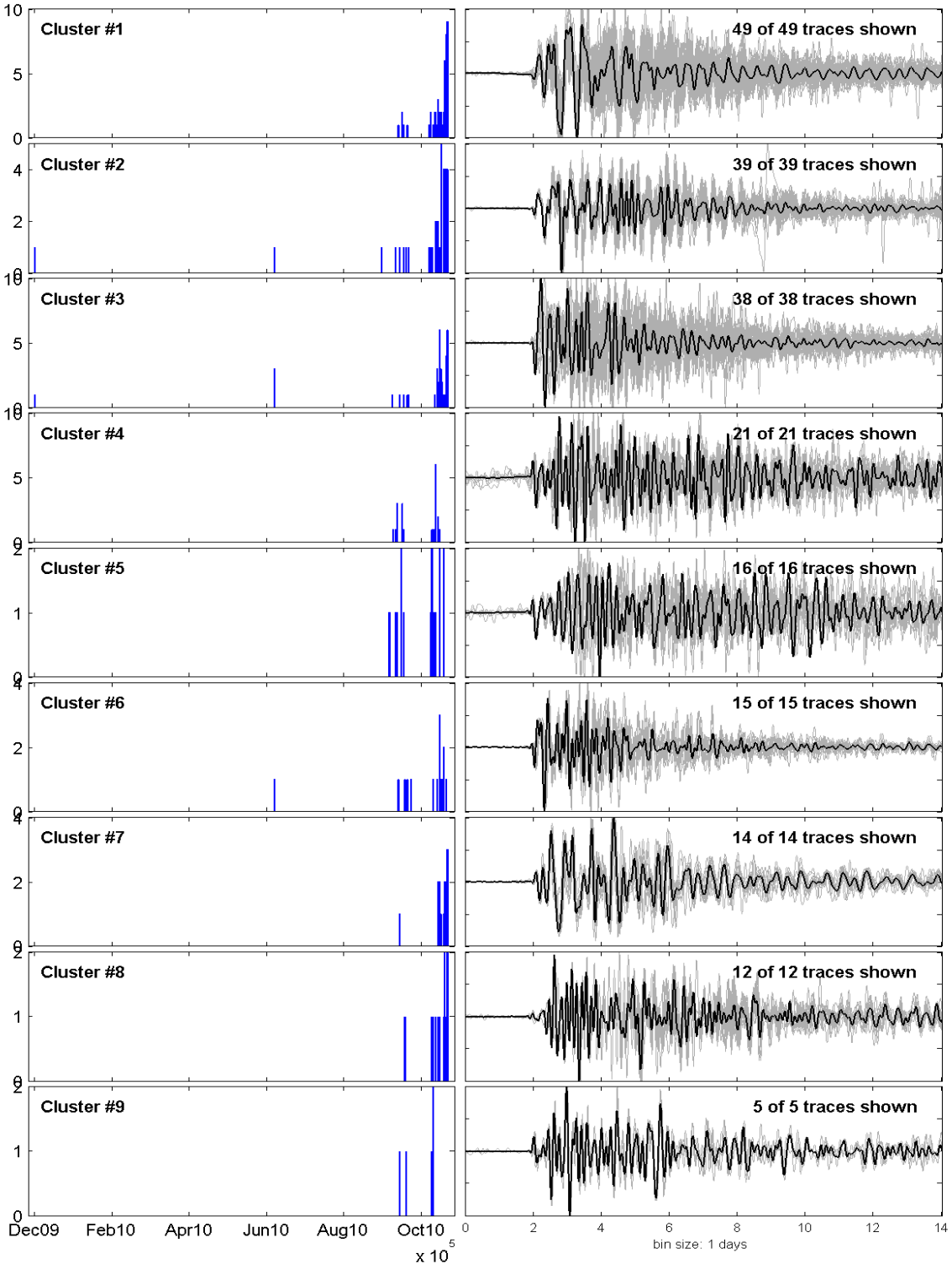

Fig. 5.7 Families of similar events recorded on PAS station. On the right part are the clusters waveforms, where the bold line is the stack of all the corresponding traces. The histograms of their daily occurrence are presented on the left part.

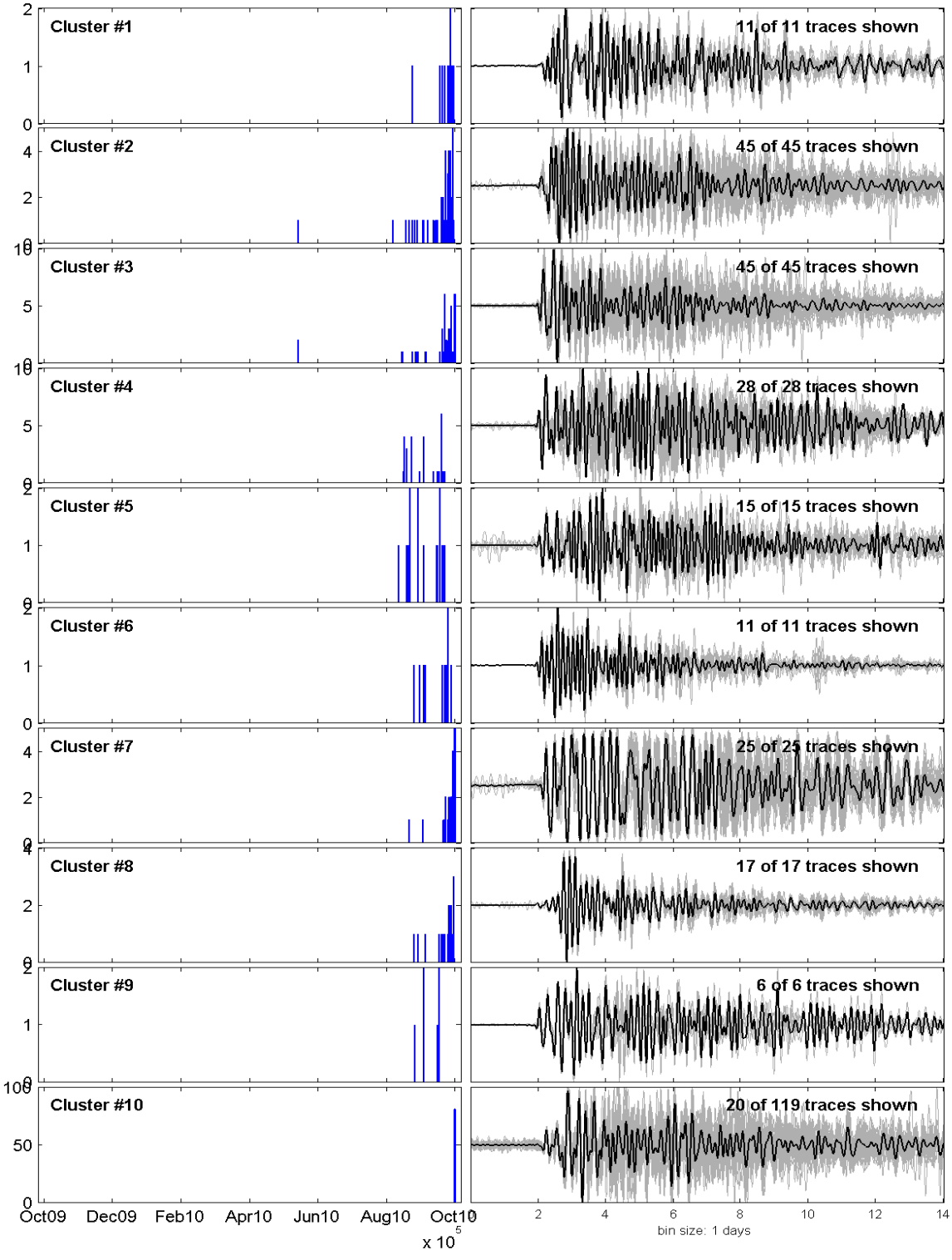

Fig. 5.8 The same as Fig. 5.7 for events recorded at PUS station.

Stacked spectra of the clusters are presented on Fig. 5.9. The dominant frequencies resulted from PAS and PUS clusters are not always similar. If this is the case, we favour those of PAS clusters rather than those of PUS station. One of the reasons is that we found saturated events on PUS station which are not found on PAS station. In certain saturation level, the spectrum calculated on the corresponding signal is no longer accurate. Furthermore, PAS station is more sensitive to low frequency signals. Although different frequencies between two stations can be related with site effects, in our case we suggest that such effects are not significant.

Based on their dominant frequency, 3 groups of clusters could be distinguished. The first group consists of cluster 1 and 2 categorized as low frequency events whose dominant frequencies are below 3 Hz. The second group consists of clusters 3, 4, 5, 7, 9, and 10 whose dominant frequencies are between 3 and 5 Hz. The last group covers the remaining clusters i.e. cluster 6 and 8 who have dominant frequency higher than 5 Hz. The second and third groups are then considered as VT (volcano tectonic) clusters, while the first group is formed by LF (low frequency) clusters.

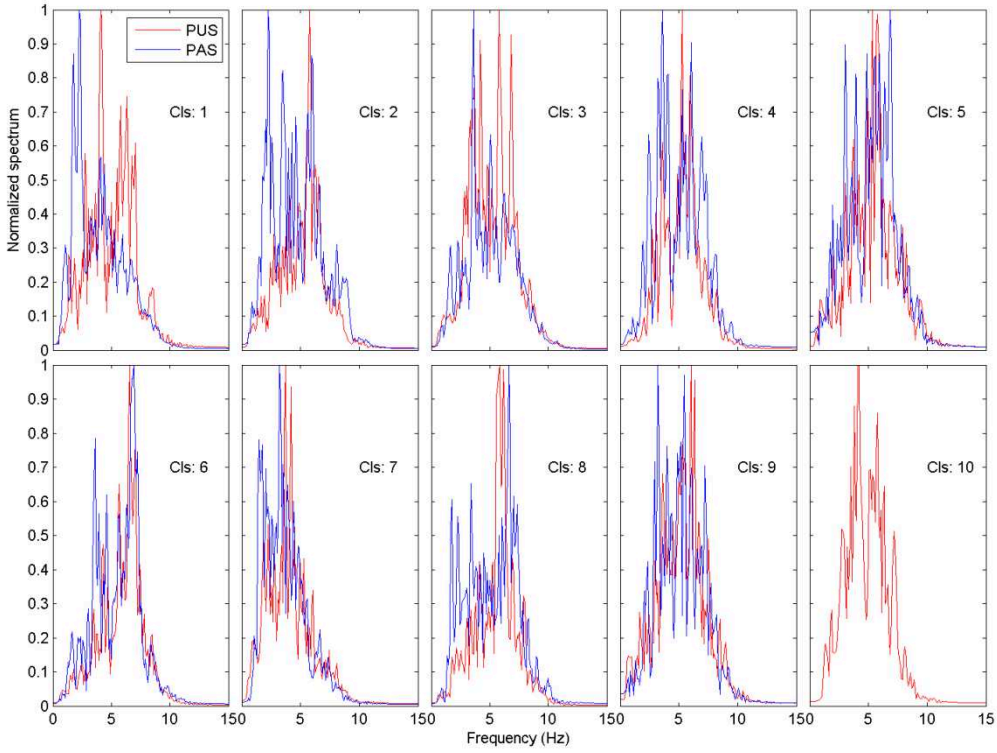

Fig. 5.9 Spectra for the clusters obtained for PAS (blue) and PUS (red) stations. Cluster numbers are indicated.

The hypocenters of the clustered events of PUS are plotted in Fig. 3.3 (Ch. 3). They confirm the existence of an aseismic zone since there are 3 clusters (number 4, 5, and 9) that are located only at >2.5km depth (deep VT zone/VTA zone) while the others are located only at <1.5km depth (shallow VT zone/VTB zone). Moreover, combining the hypoDD results and the depths estimated by arrival time differences between stations, we found at least 4 depth ranges of overlapping layers at which the shallow clusters are located. The deepest layer is in the range 1 - 1.5 km depth where clusters 1 and 8 are located. Shallower layer that starts at depth of 1.2 km is likely the location of cluster 2, 7, and 10. The third layer ranges between 0.7 km and the near surface and contains cluster 3. Based on its arrival time differences cluster 6 is suggested to be located at the shallowest layer above

the third layer since it has the largest arrival time differences between DEL and PUS station. However, because these values exceed the largest arrival times obtained in the model, the depth of most of the cluster 6 could not be estimated. The disparity between the maximum observed and modelled arrival time differences implies inaccuracy of the velocity model used particularly for the shallow depths. It also means that the depth ranges of shallow clusters are suggested to be deeper than those obtained. Nevertheless, the existence of different layers that correspond to the different clusters is well supported.

Cluster lifetimes and chronological activity preceding the 2010 eruption

Cluster lifetimes vary from hours to months. Following Chen et al. (2009), we could recognize "burst-type" and "non burst-type" families. The former are composed by earthquakes taking place in a "short" time, while the latter spread over a longer interval. Here, 3 clusters (number 2, 3, and 6) could be classified as non burst clusters as they occurred up to one year before the eruption during the VT swarms. These swarms are considered as early symptom of restless. Hydrothermal activity triggered by heat transfer from magma in depth is suggested to be an interpretation of these shallow VT swarms which occurred months before the seismic crisis of 2010 (See Ch. 2).

The remaining clusters can be considered as 'burst' clusters since they occurred several weeks to one day before the eruption. In order to look at the different processes related with the clusters, we gathered the clusters according to their source location and we separated the low frequency clusters. Their histograms during September – October 2010 are plotted together with the deformation rate (Fig. 5.10).

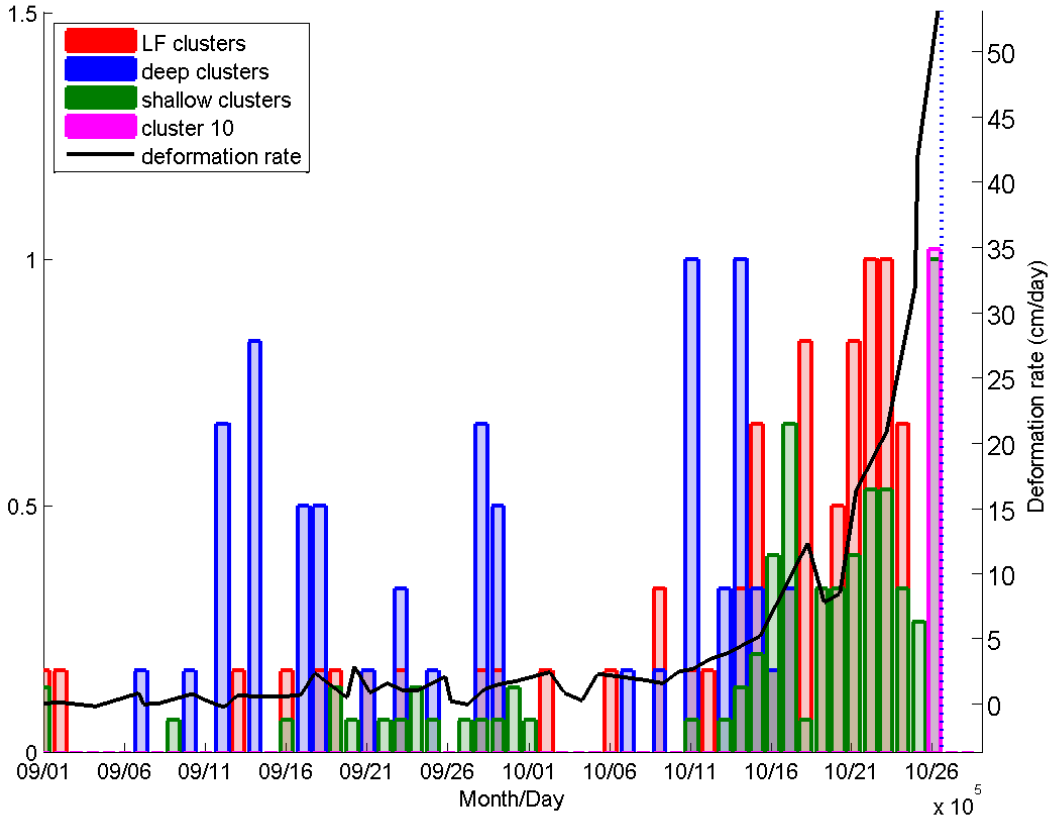

Fig. 5.10 Daily number of events in each group of clusters during September - October 2010. The values are normalized by their maximum. Deformation rate from Electronic Distance Measurement (EDM) of reflector RK4 is overlaid as the black line. Sharp increase of deformation rate at about 18 October 2010 corresponds to the strong increasing of VTB and the vanishing of VTA.

As described in the chronology section (Chap. 2), the seismic crisis preceding the eruption began on September 2010. It is attributed to an increasing magma volume in depth. The seismic crisis was initiated by an increasing number of VT dominated by the deep VTA events. Thereafter, VTA clusters were no longer observed since about mid October. When the VTA disappeared, the number of VTB events increased sharply. At the surface, the magma migration was reflected as a brief increase of deformation rate at 18 October 2010 that indicates a pressurisation of the edifice due to the ascending magma.

Approaching the eruption onset, another pressurisation took place on about 21 – 23 October which is revealed by a sharp increase of deformation rate from 8 cm/day to 16 cm/day. In the same time, the low frequency clusters culminated and then they vanished on 25 October. Considering a strong deformation and rockfalls activity during this period, we suggest that those LF originated from an abrupt mass sift of magma and or gas that inflated the conduit and produced such LF signal. The occurrence of LF events is often related with gas release of the magma at shallow depth (McNutt, 1996, Molina et al., 2003, Chouet et al., 2005, Neuberg et al., 2006, Gambino et al., 2009, Jousset, et al., 2013) and usually takes place in a relatively short time lapse respect to the eruption.

A relation between low frequency events and pressurisation process has been reported by Voight et al. (1998) at Mt. Montserrat. He observed an increase in number of low frequency events that preceded a cyclic behaviour of inflation-deflation of lava dome prior to dome collapse. Later, based on high-resolution image-analysis Johnson et al. (2008) reported a dome dynamics of the Santiaguito lava dome. A dome movement of 20 – 50 cm at the central of the dome propagating at 50 m/s towards the 200 m diameter periphery quantified by particle image velocimetry were observed to be consistent with displacement trace amplitudes of LF events.

Cluster 3, 7, and 10 culminated on the day of the eruption (26 October 2010). These clusters demonstrated that the pressurisation regime persisted toward the eruption. Among them, cluster 10 occurred only the day prior to the eruption. These events are located from the depth of 1.2 km to the near surface (Fig. 3.3 d). It could be attributed to the stick-slip process of magma approaching the surface. Multiplets associated with stick-slip motion were also observed at the base of alpine glaciers (Thelen et al., 2013). Deformation rate several hours before the eruption reached 53 cm/day which is 5 times higher than the maximum rate in previous eruptions. This also indicates that the damaging activity in this period was very strong.

5.4 Conclusions and perspectives

We performed tests over four automatic time picking methods i.e. STA/LTA, LTE/STE, kurtosis, and MER. We found that, in our case, the method of LTE/STE is the most reliable since it gives consistent results with different waveforms with a standard deviation less than 0.02 s, and it has good sensitivity to detect a small onset.

Using average-linkage hierarchical clustering, the seismic events during 2009-2010 activity could be classified into 10 clusters. Chronology of volcanic activity toward the eruption is revealed on these clusters. There are four clusters (2, 3, and 6) which occurred in swarms since several months to one year before the eruption. Theses swarms are considered as early symptoms of a new cycle of activity. The presence of magma in depth heated ground water and produced hydrothermal activity that triggered sporadic seismic activity.

Seismic activity that intensively increased during one month before the eruption is a sign of an ascending magma from deep magma chamber which allowed the conduit to enlarge and produce shear failures as VTA earthquakes. On the same time, the hydrothermal system was activated causing seismic activities in the shallower zone. The remaining clusters are associated with this phase and categorized as burst clusters. The clusters are separated into a deep zone (>2km) and a shallow one (<1.5km). Furthermore, in each zone, the clusters are also grouped at different depths. Although the proportion of clustered events is about 50%, the shift of hypocenter at about the middle of October revealed by the temporal evolution of the multiplets appears to be significant.

The two clusters categorized as low frequency events disappeared about two days before the eruption. We suggest these events are related with degassing activity of the rising magma approaching the surface. The cluster 10 which occurred only about 1 day before the eruption is interpreted to be related with stick-slip due to the rising magma in shallow conduit.

The mere chronology of clusters could be a useful information for detecting an impending eruption. In the case of 2010 Merapi eruption, migration of magma from VTA zone to VTB zone took place about 6 – 10 days in advance to the eruption. An increase in VTB number followed by large LF and the appearance of stick-slip related multiplets indicates a pressurisation of magma at the upper conduit which could be a sign of an eruption onset within days to hours. Moreover, knowing the time at which the pressurisation within the upper conduit takes place can improve the successfulness of the failure forecast method (FFM).

Although the general chronological activity could be revealed by family analysis, studies about the detailed physical mechanisms of each cluster are needed in order to obtain a better understanding of the pre-eruptive magma rising behaviour.

Chapter 6

Velocity variations based on coda wave interferometry

6.1 Introduction

The coda is defined as the long lasting diffuse wavetrain tailing a seismic event. The waves included in the coda are (at least partially) caused by multiple diffractions (Snieder et al., 2002) and have travelled much longer distances than direct waves. As a result, changes in the material causing small velocity changes, which may have almost no effect on the arrival time of the direct waves, may result in much longer time shifts in the coda (Niederleithinger et al., 2010).

Because of this property, coda wave has been used widely to detect and monitor subtle changes in velocity of the medium by comparing the coda waves of similar events recorded on the same station at different times. This technique which is known as coda wave interferometry (CWI) (Snieder R., 2002) has confirmed the existence of detectable precursory crustal changes (Clarke et al., 2011). Further, there are several methods which can be applied to perform CWI e.g. MWCS (Moving Windows Cross Spectral) and stretching method which will be explained later on.

Many efforts have been devoted to studies related with CWI using field or experimental data. In volcano domain, as volcanic eruptions are usually preceded by increasing magma pressures, such technique may allow us to recognize stress evolution toward the eruption and it could potentially be a deterministic eruption precursor. Cannata et al. (2012) and Cannata et al., 2013) observed a velocity decreasing during 2002-2003 Mt. Etna eruption using events families. Brenguier

et al. (2008) showed that volcano eruption forecasting could be done by implementing CWI using ambient noise as in the case of the 2006 and 2007 eruptions of Mt. Piton de la Fournaise.

Recently, it has been shown that the velocity changes preceding an eruption can be quite more complex and vary in time and space. Different behaviours of velocity changes were observed over the different parts of Piton de la Fournaise (PdF) during the crisis of 2010. Just before the eruption, the station pair in the vicinity of the crater showed a decay of seismic velocity (up to 0.6%). In the same time, a station pair located on the other side of the crater showed a velocity increase instead. The station pair located further away was not sensitive to velocity change prior to the eruption (Obberman et. al, 2013).

Anggono et al. (2012) reported a similar result for the activity of Miyakejima volcano in 2000. Using noise correlation data, he observed both velocity increase and decrease in about the same period for the different pairs. For the pair whose line path across the flank, a velocity increase is observed, whereas, for the pairs located around the summit or the pairs whose line path cross the caldera, a velocity decrease is observed.

The capability of CWI is confirmed also experimentally. Larose and Hall (2009) used concrete to show the behaviour of velocity-stress relation in the case of first order acousto-elastic relation behaviour. Afterward, Stahler et al. (2011) completed this observation by presenting the behaviour on the second order relation. A nonlinear behaviour was observed during velocity increasing and decreasing due to rising stresses. Further the CWI is proven to be superior to the conventionally used methods such as Time of Flight (TOF) method for calculating the velocity change in a sample, particularly for small velocity change (Shokouhi et al., 2010; Stahler et al., 2011).

As a visco-elastic material, concrete exhibits nonlinear elasticity that can be observed from stress-dependent velocity (Wu et.al , 1998). The acoustic velocity of a concrete sample under stress increases with the increasing stress until a

condition that the pressure will exceed the material strength (Niederletihinger et. al., 2010). By then the velocity will rather decrease (Niederletihinger et. al., 2010, Stahler et. al., 2011). The velocity increase occurs because crack density decrease as cracks close under pressure. Van der Neut et al., 2007 suggested an exponential increasing of velocity as cracks close under pressure, assuming an exponential distribution of initial aspect ratios. This is with an assumption of a second order elastic behaviour. In case of a first order elastic behaviour the velocity increasing follows linear trend as it is reported by Larose et. al. (2009). The later stage of sharp decreasing takes place due to cracks connection building larger fissures that change the elastic parameters (Stahler et.al., 2011). Different pressure/stress levels at which the velocity starts to decrease were reported. Whereas Niederletihinger et. al. (2010) found the level at about 50% of the strength, Stahler et.al. (2011) reported a smaller value of about 30%.

In Merapi analysis of seismic velocity variation had been performed in different period of times. Ratdomopurbo and Poupinet (1995) observed an increase of shear wave velocity within 4 months before the 1992 eruption of 1.2 %. Based on artificial repeated sources, i.e. airgun shots in water basin, Wegler et al. (2006) observed a small velocity increase (0.08 %) preceding the 1998 eruption. It was shown by Sens-Schonfelder and Wegler (2006) that the long term velocity variations observed from NCF between August 1997 and June 1999 at Merapi were well fitted with a hydrological model of ground water level (GWL).

In this work we aim at calculating the apparent velocity variations (AVV) during the seismic crisis of 2010 using similar events (multiplets) and ambient noise. With regards to the similar events, we compare two approaches used in CWI analysis i.e. the MWCS and the stretching method.

6.2 Data and Method

6.2.1 Velocity variations in the coda of multiplets

6.2.1.1 Multiplets data

Ten families of similar events were found by cluster analysis from the data of PAS and PUS stations during October 2009 – October 2010. In this study, we used waveform data which correspond to those clusters. Initially, data have sampling rate of 50 sps (sampling per second). For the processing they are decimated to 25 sps and filtered on frequency band of 0.5 – 10Hz.

6.2.1.2 Doublet method

There are at least two methods to estimate the relative velocity change based on coda waves i.e. the doublet and the stretching methods. Both of them were performed and compared in this work.

The first one, called doublet method, analyses the coda in a number of windows. The seismograms of two similar events recorded at a given station, a reference event $h_0(t)$ and a current one $h_c(t)$ are first aligned on the direct waves. Then the time shift in each coda window is calculated. Under the hypothesis that the velocity variation is uniform, the time shifts per window versus time shows a linear relationship, where the slope is equivalent to the mean of velocity perturbation. The calculation of the time shifts can be done either by cross-correlation (Snieder et al., 2002) or by cross-spectral approach. In the latter case, the corresponding doublet method is called Moving Windows Cross Spectral (MWCS) (Ratdomopurbo and Poupinet, 1995). This study used MWCS method since it shows more stable results than cross-correlation (Wu, 2007; Clarke et al., 2011).

For implementing MWCS method, we follow the mathematical procedure described by Clarke et al. (2011). This analysis consists of two computational steps. The first step is to estimate for a pair of events (doublet) the delay times

δt_i between a reference event T_{ref} and the current event T_{cur} within a set of overlapping time windows centered at t_i. The second step is to calculate the velocity change by a linear regression of the delay times in function of the center time of the corresponding windows obtained from the first step.

Regarding the first step, each trace is divided into N_w windows, one for each delay-time measurement. The windowed segments are mean adjusted and cosine-tapered before being Fourier-transformed into spectral domain. The cross-spectrum, X(v), between the two windowed time-series is calculated as follows

$$X(v) = F_{ref}(v).F^{*}_{cur}(v), \qquad 6.1$$

where F_{ref} (v) and F_{cur}(v) are the Fourier-transformed representations of the windowed time-series, *v* is frequency and the asterisk denotes complex conjugation. In the form of complex cross-spectrum, it is represented by its amplitude |X *(v)*| and phase *φ(v)*

$$X(v) = |X(v)|e^{i\varphi(v)} \qquad 6.2$$

The time-delay between the two windows can be obtained from the (unwrapped) phase, *φ(v)*, of the cross-spectrum, which will be linearly proportional to frequency (v_j).

$$\varphi_j = m \,.\, v_j\,, \qquad m = 2\pi\delta t_i. \qquad 6.3$$

The time delay, δt_i (subscript i for the i-th window), between the two signals is estimated from the slope m of a linear regression of the samples, j = 1, . . . , h, within the frequency range of interest. During the regression, a weight w_j, which depends on the cross-coherence (C_j) at each sampled frequency, is assigned to each cross-phase value.

$$w_j = \sqrt{\frac{C_j^2}{1-C_j^2}\cdot\sqrt{|X_j|}} \qquad 6.4$$

These weights incorporate both the cross-spectral amplitude and the cross-

coherence. This generates more differentiated weights in cases where the cross-coherence is relatively constant but the cross-spectral energy is variable.

Using a weighted least-squares inversion, the slope m is estimated as

$$m = \frac{\sum_{j=1}^{h} w_j v_j \phi_j}{\sum_{j=1}^{h} w_j v_j^2}. \qquad 6.5$$

The associated error, $e_{m,}$ is calculated using the rule of propagation of errors

$$e_m = \sqrt{\sum_j \left(\frac{w_j v_j}{\sum_i w_i v_i^j} \right)^2 \sigma_\phi^2}, \qquad 6.6$$

where σ_ϕ^2 is the squared misfit of the data to the modelled slope and is calculated as

$$\sigma_\phi^2 = \frac{\sum_j (\phi_j - m v_j)^2}{N-1}. \qquad 6.7$$

Following equation 6.3 the time delay, δt, and its error, $e_{\delta t}$, between the two signals are taken by simply dividing m and e_m, respectively, by 2π.Repeating this process for all windows, we obtain N_w delay-time estimates between the two time series, each corresponding to the central time, t_i (i = 1, . . . , N_w) of the window in which it was measured.

As for the second step, assuming a uniform velocity perturbation, the measured delays δt_i are expected to be a linear function of time t_i with a slope corresponding to the relative time perturbation which is equal with the relative velocity perturbation ($\Delta v/v$)

$$\frac{\Delta t}{t} = -\frac{\Delta v}{v} \qquad 6.8$$

Thus, the relative velocity perturbation can be estimated from a pair of two events (doublet) via linear regression of the following equation:

$$\delta t_i = -\left(\frac{\Delta v}{v}\right) \cdot t_i \qquad 6.9$$

become,

$$\delta t_i = a + b t_i \ , \qquad i = 1 \ldots N_w, \qquad 6.10$$

where coefficient a represents a possible instrumental drift (Stehly et al. 2007), and b corresponds to the relative time variation $\delta t/t$. Through a weighted least-squares inversion, these two parameters are estimated. Here, the weights, p_i, are determined using the estimated error of each time-delay measurement: $p_i = 1/e^2_{\delta ti}$. The resulting estimate for $b = -\delta v/v$ is then

$$b = \frac{\sum p_i (t_i - \langle t \rangle) \delta t_i}{\sum p_i (t_i - \langle t \rangle)^2} \qquad 6.11$$

with variance

$$e_b^2 = \frac{1}{\sum p_i (t_i - \langle t \rangle)^2} \qquad 6.12$$

where $\langle t \rangle = \sum p_i t_i / \sum p_i$ is weighted means of t (Clarke et al., 2011). Fig. 6.1 below illustrates how the MWCS method works (Hadziioannou, 2011).

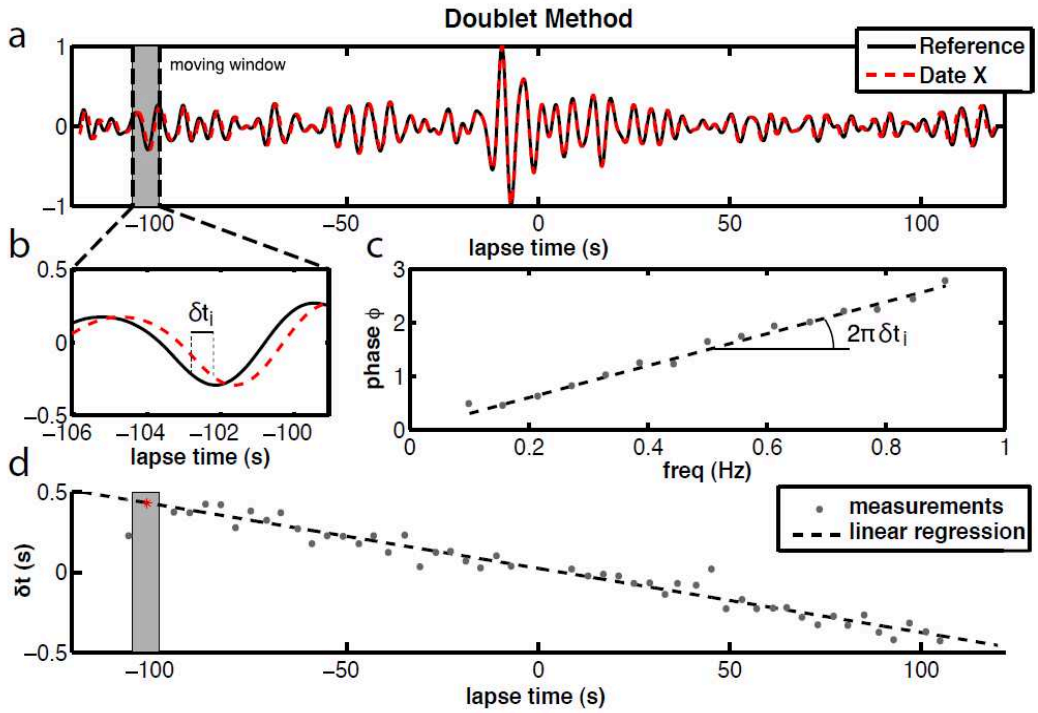

Fig. 6.1 Illustrations of velocity change calculation using MWCS (doublet method) in noise cross-correlation function (NCF). Note that, the method works the same way on event coda data. (a) Reference and current NCF. (b) Zoom of the late part of time lapse of (a). (c) Time delay estimation from the phase of the cross-spectral of corresponding window. (d) Time perturbation estimation through linear regression of time delays versus time, which is equal to the velocity perturbation (Hadziioannou, 2011).

We calculate the velocity variation using the events of each cluster. The best correlated and aligned waveforms are used. In each cluster, we cross correlated and re-clustered the waveforms using the first 2.5s data and a correlation threshold of 0.8. The largest cluster found in this re-clustering is selected. In order to obtain good coherency, waveforms are stacked per day. The number of events being stacked per day varies from one to five events. However, we did not observe a correlation between the number of events being stacked per day and the resulted velocities. We used the stack of the whole cluster as reference signal.

The time shifts were calculated on 1 s-long moving windows with 0.5 s overlap along 6 s-long interval starting 1s after the P-onset. The linear regression between

cross-spectrum phases and frequencies is calculated in the frequency interval from DC to 6 Hz. Low coherencies were found for the higher frequencies.

6.2.1.3 Stretching method

The second, and more recent, method used is the stretching method. Unlike the MWCS method, the velocity change is calculated directly in a given window of the corresponding time series. One of the two time series is stretched (or compressed) by a small relative change ε until an optimum correlation between the time series is reached:

$$CC(\varepsilon) = \frac{\int_0^T h_i(t) h_0(t \cdot (1-\varepsilon)) dt}{\sqrt{\int_0^T h_i^2(t) dt \int_0^T h_0^2(t) dt}} \qquad 6.13$$

where $h_0(t)$ represents the reference trace, $h_i(t)$ represents the current trace, and $CC(\varepsilon)$ is the correlation coefficient between both traces. In this case we use the reference time series as the stretched/compressed time series.

The error on the stretching value, i.e. on the velocity change, is calculated using the formula derived by Weaver et. al. (2009):

$$rms(\varepsilon) = \frac{\sqrt{1-X^2}}{2X} \sqrt{\frac{6\sqrt{\pi/2}T}{\omega_c^2 (t_2^3 - t_1^3)}}, \qquad 6.14$$

where X is the coherence of the waveforms after dilatation between starting time t_1 and end time t_2, T is the half bandwidth, and ω_c the center frequency of the signal.

In this method the same signal preparation as in MWCS method is applied. An interval window of 6s starting from 1 s after the arrival time is used. The reference signal is stretched or compressed with maximum stretching/compressing value of 0.05 and 0.0005 of steps. The current signal window is then correlated with each stretched reference window. The stretching value for which the optimum

correlation is obtained is equivalent to its relative velocity change between reference and current signal. An illustration of this method by Hadziioannou (2011) is shown in Fig. 6.2.

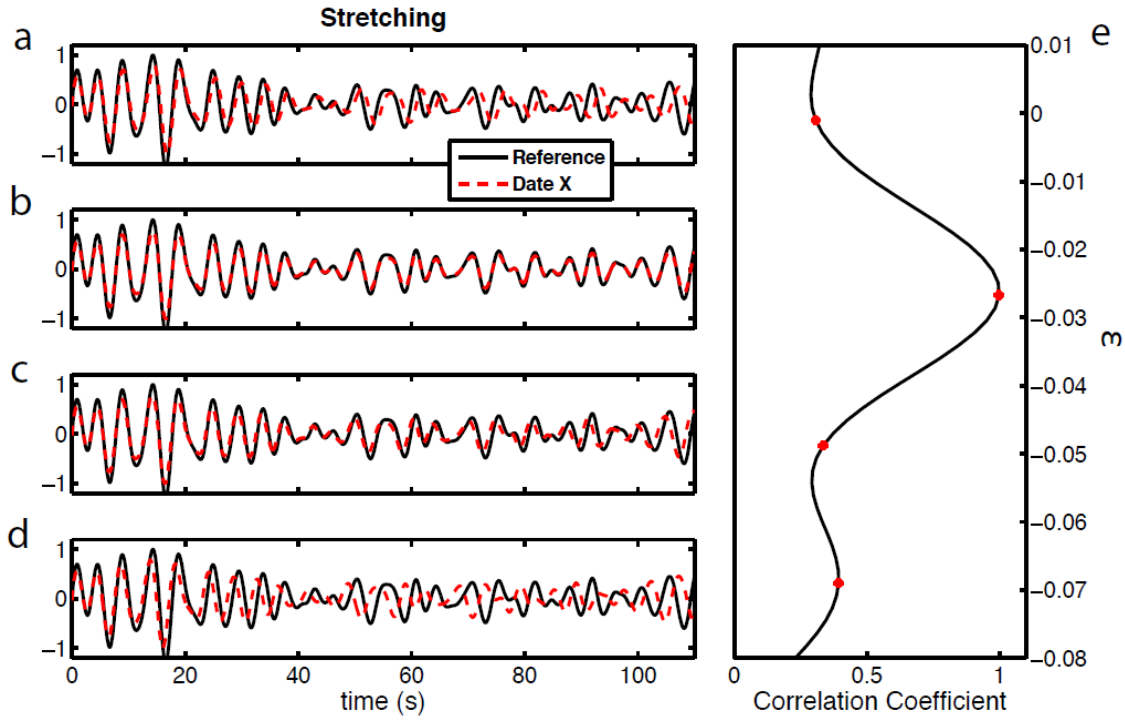

Fig. 6.2 Illustration of velocity change estimation using stretching method. (a) The reference and the current signal at date x. (b) – (d) Same as (a) but after stretching of the current signal with different stretching degree(ε) as indicated on (e). (e) Correlation coefficient obtained from cross-correlation between the reference and current signal at different stretching degree corresponding to the figure (a) – (d). It appears that they are better correlated at stretching degree ε = -0.025. This stretching degree is equal to the velocity change estimation (Hadziioannou, 2011).

6.2.2 Velocity variations using noise correlation

6.2.2.1 Noise data

We used the digital data of all the short period stations in the period from January 2009 to October 2010. All short period stations have been replaced at about 6 month before the eruption. For this reason, we separate the calculation into two

time periods i.e. before and after the station replacement. Hereafter we mention those periods as the first and the second periods. Since significant amount of gap occurred on broadband stations, we did not use these data.

As will be shown later with multiplet data, the stretching method yields more stable results than the MWCS one. Thus, for calculating velocity variations with ambient noise, we use the stretching method. In general the method used for calculating the velocity variation with noise is similar to that used on multiplets. The difference is that in noise data we use correlation functions instead of e.

First we extract 20 minutes-long time series. For each interval we apply spectral whitening, one bit normalisation, and band-pass filtering between 0.1 and 2 Hz. Using this procedure we reduce the influence of earthquakes since they have high energy in higher frequency. We cross-correlate the time series between stations of a given pair. The noise correlation functions (NCF) obtained are then stacked over one day and the stacks are used as current correlation functions (CCF). Since we calculate the AVV (Apparent Velocity Variation) on the first and second period separately, we use two reference correlation functions (RCF) obtained by stacking the CCF during calm activity for each period. Examples of stacked NCF for all station pairs are presented on the figure below.

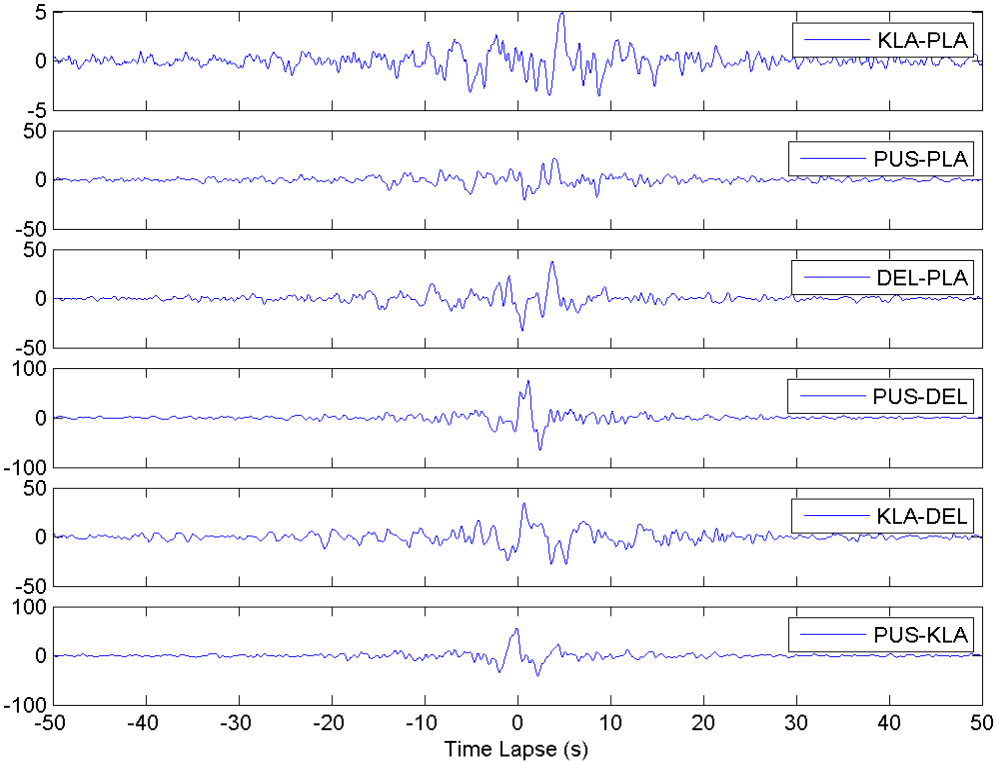

Fig. 6.3 RCF obtained from all the station pairs. All their maximum values are located on the causal part except for pair PUS-KLA.

For the the AVV estimations, we use the part of coda wave of the NCF in the time-lag interval of 10s to 30s. Because the sources of noise are dominantly in the ocean at the south of the volcano (Apendix B), the NCF are not symmetric. We thus use the most energetic part of the NCF which is the anti-causal one for all pairs but PUS-KLA.The RCF is stretched or compressed with a compression step of ± 0.05 % until it reaches ±10%. The CCF is then correlated with each stretched RCF. The stretching value for which the optimum correlation is obtained is equivalent to the relative velocity change. In order to reduce the daily perturbations, we smooth the CF by stacking the 5 CF's around each corresponding day.

6.2.2.2 Data selection and time synchronization

Since instrumental problems occurred sometimes, producing either timing problem or signal distortion, data selections are needed. For this purpose, we correlated the CCF with the RCF in interval of ±10 s around zero time lags. First we detected in the CCF possible polarity changes which are indicated by negative maximum correlation coefficient. After the polarity correction, we performed timing correction using the time delay of the maximum correlation. We then rejected the corrected NCF if its correlation coefficient against RCF is below 0.6. Fig. 6.4 displays NCF of pair DEL-PLA during 5 months before and after the correction and rejection procedures.

a.

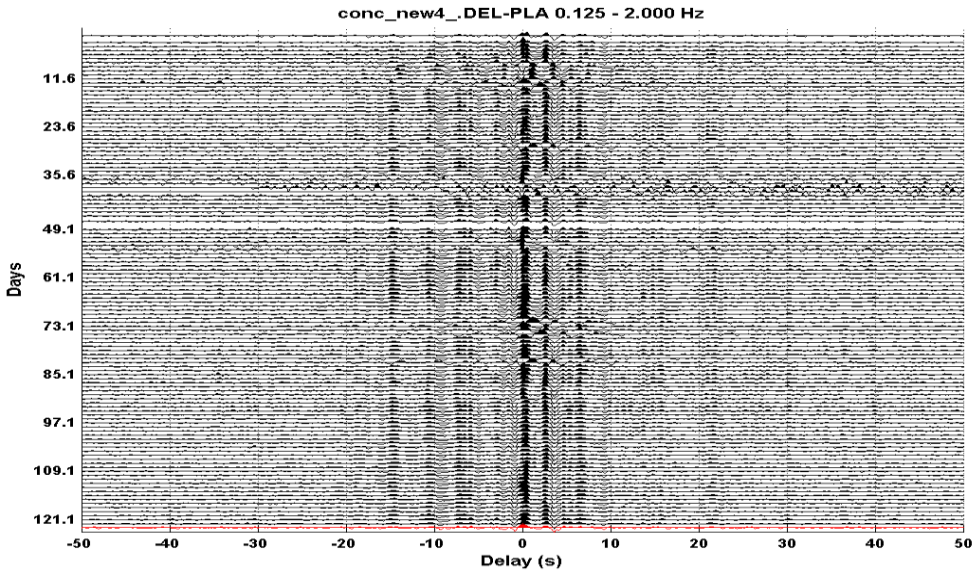

b

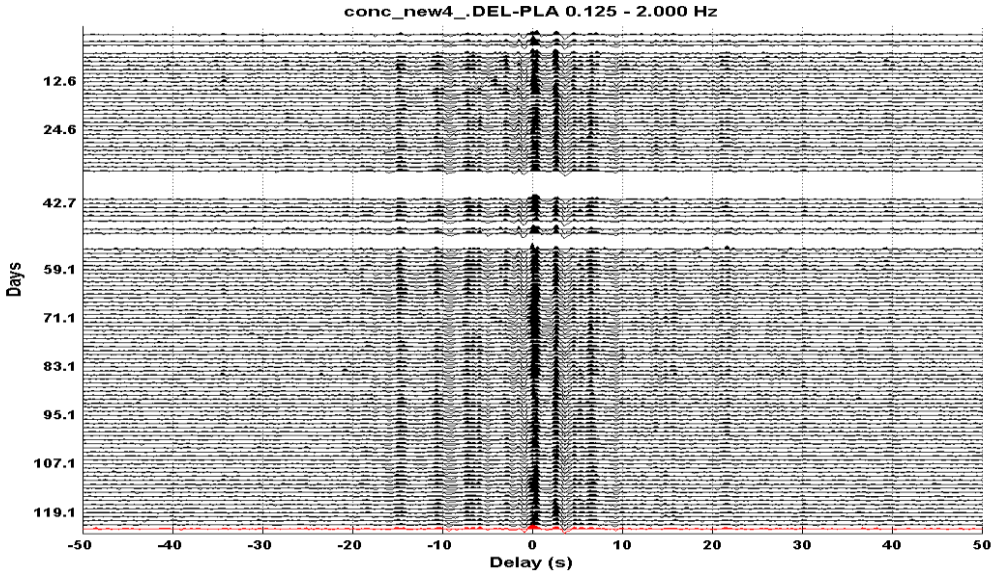

.

c.

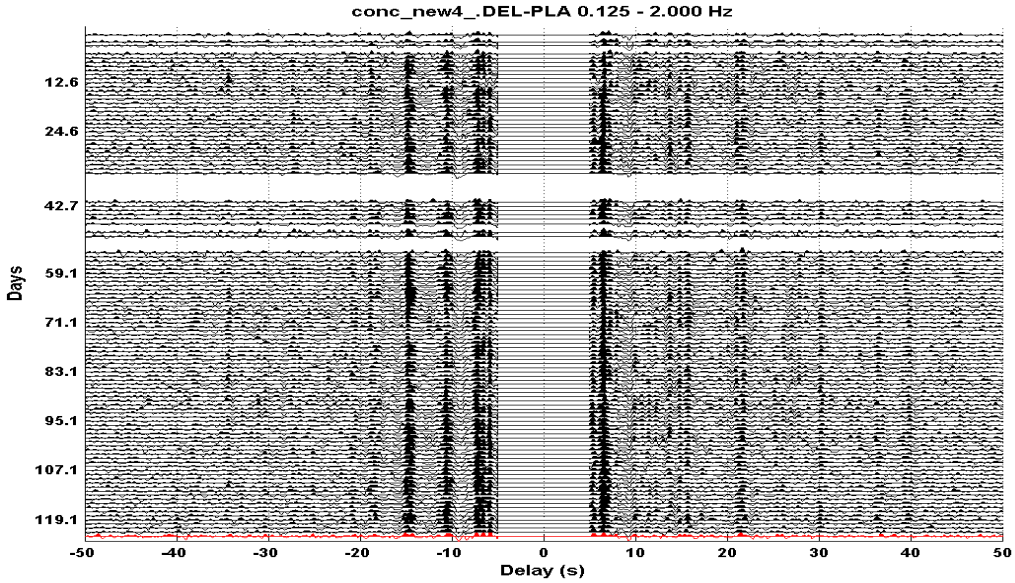

Fig. 6.4 The daily NCF of DEL-PLA pair during June – October 2009 before (a) and after data rejection (b). It appears that after the data rejection the NCF are cleaner and better aligned. The values of NCF in the interval +/-5s were set to zero in order to display more clearly the coda part (c). Here we can see very late arrivals at time lag of up to 40s.

We detected problems of synchronization especially before the station replacement. Using the time delay of maximum correlation obtained by cross-correlating the NCF with the RCF, we could recover and correct the time shifts

and then improve the results quality and continuity. However, the general trend of the AVV does not change too much. Fig. 6.5 and 6.6 displays the time lags of NCF and AVV obtained from DEL-PLA pair, respectively. Most of the NCFs whose time lag is larger than 0.5 s have correlation coefficients lower than the threshold (0.6), and thus they were rejected. Fig. 6.6 shows the effect of the time corrections on the AVV of DEL-PLA after rejecting the poorly correlated NCFs.

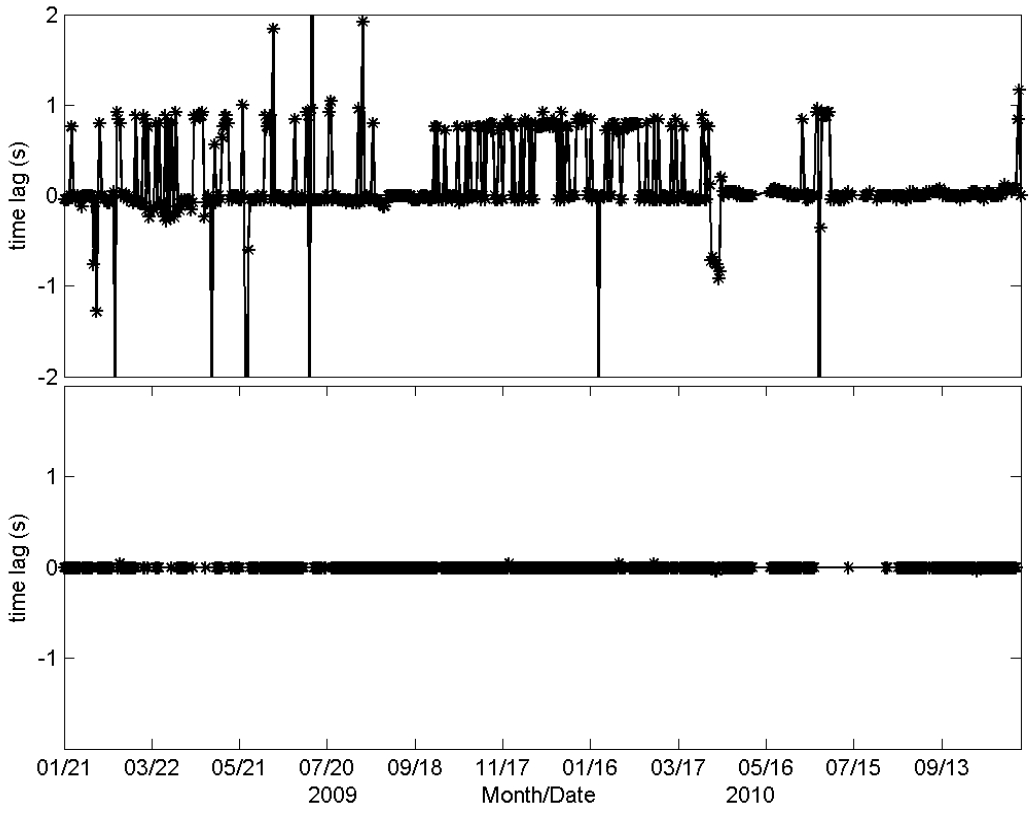

Fig. 6.5 The maximum correlation time lag of NCF of station pair DEL-PLA before and after correction.

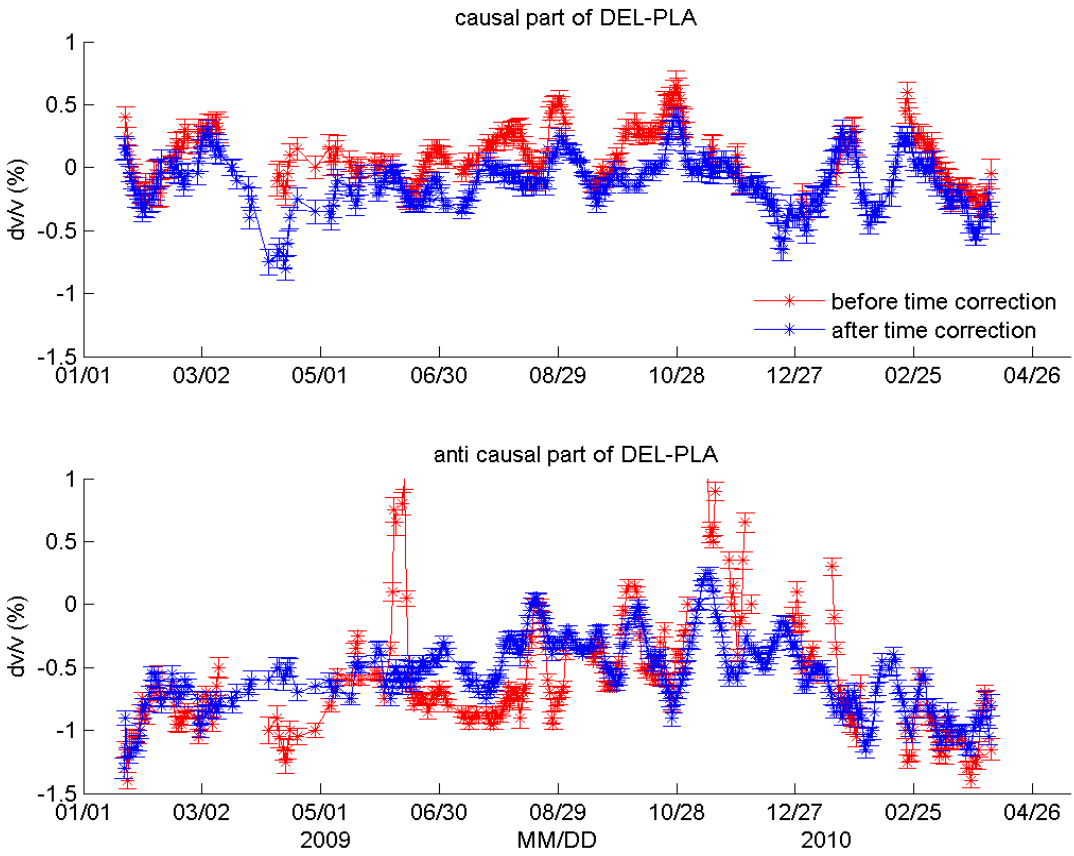

Fig. 6.6 Velocity variations obtained from station pair DEL-PLA during the period before reinstallation using the causal part (top) and the anti-causal part (bottom) before (red) and after time lag correction (blue).

6.2.2.3 Corrections of rain effects

We observed some correlation between AVV and the rainfall. In fact, the velocity decrease displayed by some station pairs can be correlated with intensifying rain (Fig. 6.7). Sens-Schonfelder and Wegler (2006) showed that the long term velocity variations between August 1997 and June 1999 at Merapi are well fitted with a hydrological model of ground water level (GWL). Assuming that drainage of ground water occurs through a stationary aquifer that can approximately be described by Darcy's law, the drainage is proportional to the height of the ground water table which results in exponential decrease of the water level after rain

events. The GWL at time t_i could be estimated by the convolution of the precipitation rates with an exponential function:

$$GWL(t_i) = GWL_0 - \sum_{n=0}^{i} \frac{p(t_n)}{\phi} e^{(-a(t_i - t_n))} \qquad 6.15$$

where ϕ is the porosity, a is the parameter describing the decay, GWL_0 is the asymptotic water level, and $p(t_n)$ is the daily precipitation. We then fitted the values of GWL over the AVV. Assuming that the long term AVV fluctuations are mainly attributed to the rain effects, we subtracted the fitted GWL from the AVV in order to get corrected AVV which are more closely related with volcanic activity. We show an example of such correction using station pair KLA-PLA which has the strongest rain effects (Fig. 6.7). However not all the station pairs show a good correlation between AVV and GWL. The corresponding correlation coefficients for pairs PUS-DEL, PUS-PLA, and KLA-DEL are smaller than 0.2. The remaining figures are presented in the Appendix C.

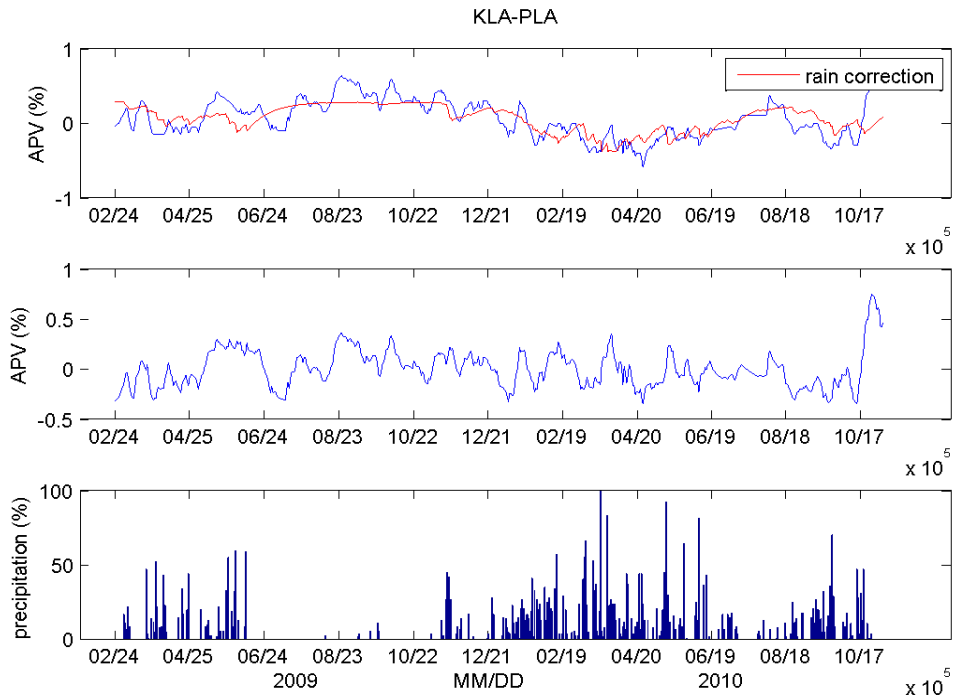

Fig. 6.7 (a) The velocity change obtained from KLA-PLA (blue) is overlaid with the fitted GWL (red). (b) The corrected AVV obtained subtracting the fitted GWL

from AVV. (c) The precipitation data (blue) is taken from Selo Post Observatory from which the GWL curve is generated.

6.2.2.4 2D location of velocity perturbations

Assuming that the coda of CCFs is composed of multiple scattered surface waves, Pacheco and Snieder (2005) proposed that the wave propagation follows a random walk process in a 2-dimensional medium. Velocity perturbations dv/v at x_0 produces travel time variations in surrounding medium as:

$$\delta t(t) = -\int_s K(s_1, s_2, x_0, t)\frac{\delta v}{v}(x_0)dS(x_0) \qquad 6.16$$

where s_1 and s_2 are the positions of the stations used for the CCF calculation, x_0 is the location of the velocity perturbation, and K is a sensitivity kernel given by:

$$K(s_1, s_2, x_0, t) = \frac{\int_0^t P(s_1, x_0, t').P(x_0, s_2, t-t')dt'}{P(s_1, s_2, t)} \qquad 6.17$$

P represents the intensity of the wavefield between two points as a function of time (Pacheco and Snieder, 2005). Here we used a solution of the radiative transfer equation in 2D (Shang and Gao; 1988; Sato, 1993; Paasschens, 1997; Planes, 2013; Obermann et al., 2013b), written as:

$$P(r,t) = \frac{e^{-ct/l}}{2\pi r}\delta(vt-r) + \frac{\Theta(vt-r)}{2\pi l ct}\left(1-\frac{r^2}{v^2t^2}\right)^{-\frac{1}{2}} \exp\left[l^{-1}(\sqrt{v^2t^2-r^2}-vt\right] \qquad 6.18$$

where v is wave velocity, r is the distance between source and receiver, l is the transport mean free path and Θ is the Heavyside function.

Travel time variations are related to the estimated apparent velocity variations (AVV):

$$\frac{\delta t(t)}{t} = -\frac{\delta v(t)}{v}\bigg|_{app} \qquad 6.19$$

The distribution of $\delta v / v(x_0)$ can be estimated by solving equation (6.16) as a linear inverse problem (Tarantola and Valette, 1982; Froment, 2011; Obermann et al., 2013b; Lesage et al., 2013). With the system of linear equation in matrix form of:

$$d = Gm, \qquad 6.20$$

d is a vector of data observation which in our case is the AVV between 6 station pairs at different time lags; G is a matrix which corresponds to the sensitivity kernel K for different station pair and different grid position; and m is a vector of modelled AVV.

A covariance matrix of the model is introduced in order to produce smooth models using a Sech type function:

$$C_m(s_1, s_2) = \left(\sigma_m \frac{\lambda_0}{\lambda}\right)^2 . \frac{1}{\mathrm{ch}\left(\frac{|s_1 - s_2|}{\lambda}\right)} \qquad 6.21$$

where λ is the correlation length, λ_0 is the grid interval, and σ_m is the a priori standard deviation. λ and σ_m were selected through L-curve criterion (Hansen, 1992). This criterion corresponds to the best agreement between the stability of the model for the velocity variations; and the minimized difference between the model predictions.

We focused the localisation on a 15x15 km^2 area centred on the volcano with grid length of 0.3km. In Appendix B, we demonstrate an inversion for estimating the noise source direction using triangulation technique. One of the inversion results is the surface wave velocity of 1.3 km/s that is used as the value of v in eq. 6.18. For the transport mean free path l, we used the value of 100 m estimated by Wegler and Luhr (2001) from an active source experiment. Performing tests for

some other values of l and v (Appendix D) showed that the defined values are acceptable.

6.3 Results

6.3.1 Velocity variations obtained from multiplets

We calculated the velocity variation using the similar waveforms resulted from the analysis of event families in Ch. 5. These analyses were performed on the data from PUS and PAS stations whose distances from the summit are 1 km and 0.7 km respectively. Due to their proximity, it is expected that they have similar behaviour in terms of velocity variation. Thus we could validate the velocity variations given by both stations.

There are 10 main clusters composed by 7 shallow clusters (above 1.5km) and 3 deep clusters (below 2.5km). Thus, an aseismic zone between 1.5km and 2.5km separates these two types of cluster. The clusters were recorded on both PUS and PAS stations consistently except for the cluster 10 due to the absence of PAS station on the lasts days before the eruption. The AVVs were calculated on all the clusters recorded on both stations using the methods of MWCS and stretching. The resulted AVV are presented in Fig. 6.8, 6.9, and 6.10.

The coda wave paths of shallow and deep clusters are significantly different because their locations are far apart. For this reason, their velocity change obtained may be different. To evaluate these differences, we plot the AVV of shallow and deep clusters separately (Fig. 6.8 for shallow clusters and Fig. 6.9 for deep clusters). Note that the errors resulted in stretching method are insignificant i.e. in the order of 10^{-2}%. Thus they cannot be observed visually in the figures.

Comparison of the results regarding the stations and the methods used

In general, the stretching method seems to give more stable results than the MWCS method. Indeed, it can be seen that the velocity variations obtained from the method of MWCS are more fluctuating than those from the stretching method either for PAS or PUS signals. In addition, stronger perturbations due to seismogram saturation in MWCS method than in stretching method are demonstrated later on. Therefore, for further analysis we consider only the results using the stretching method.

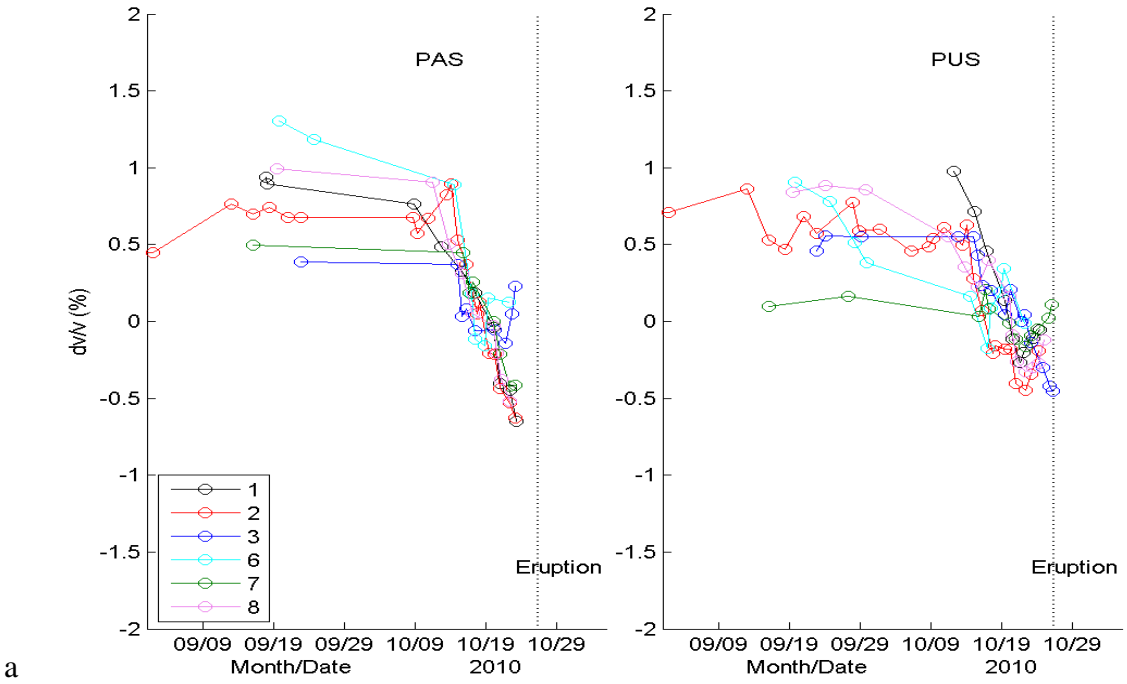

a

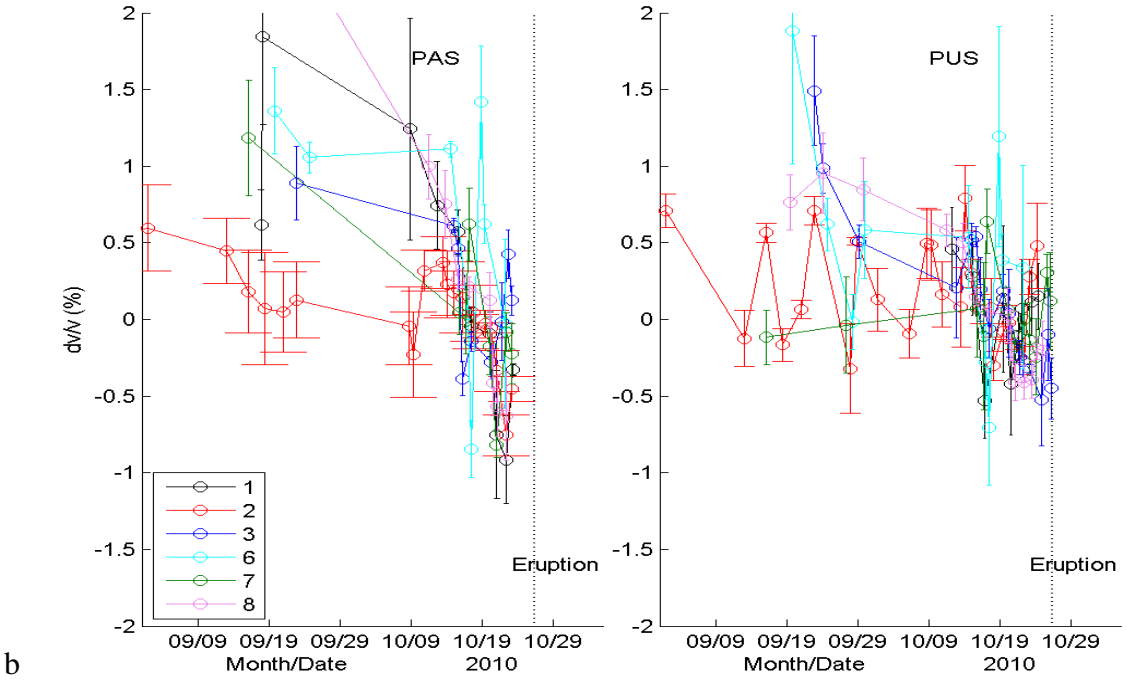

b

Fig. 6.8 Velocity changes obtained by the methods of stretching (a) and MWCS (b) for the shallow clusters recorded at PAS (left) and PUS (right).

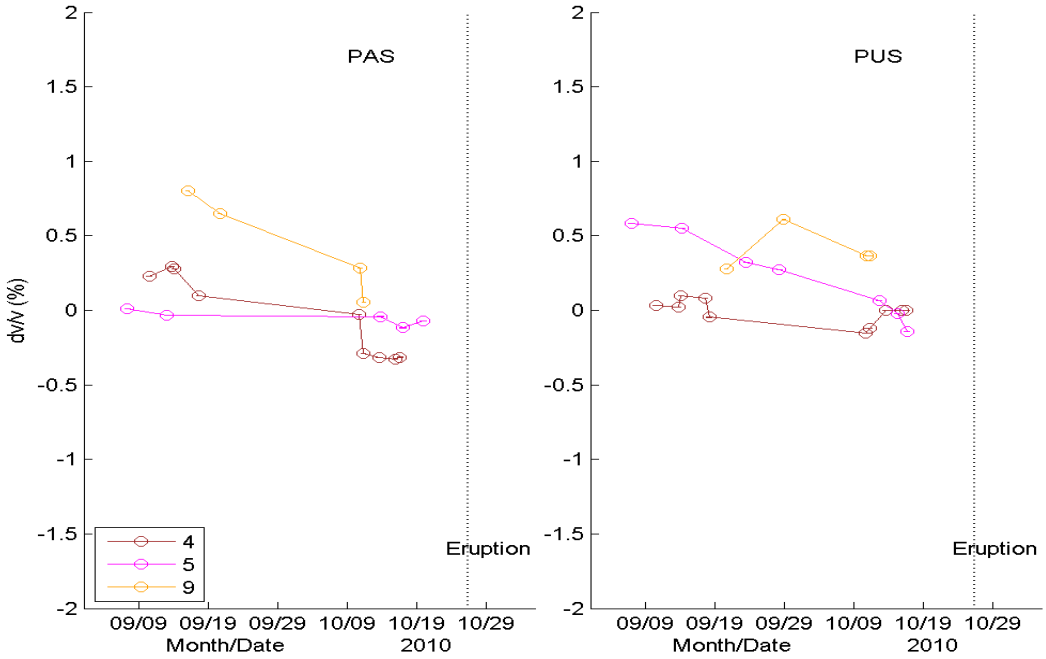

a

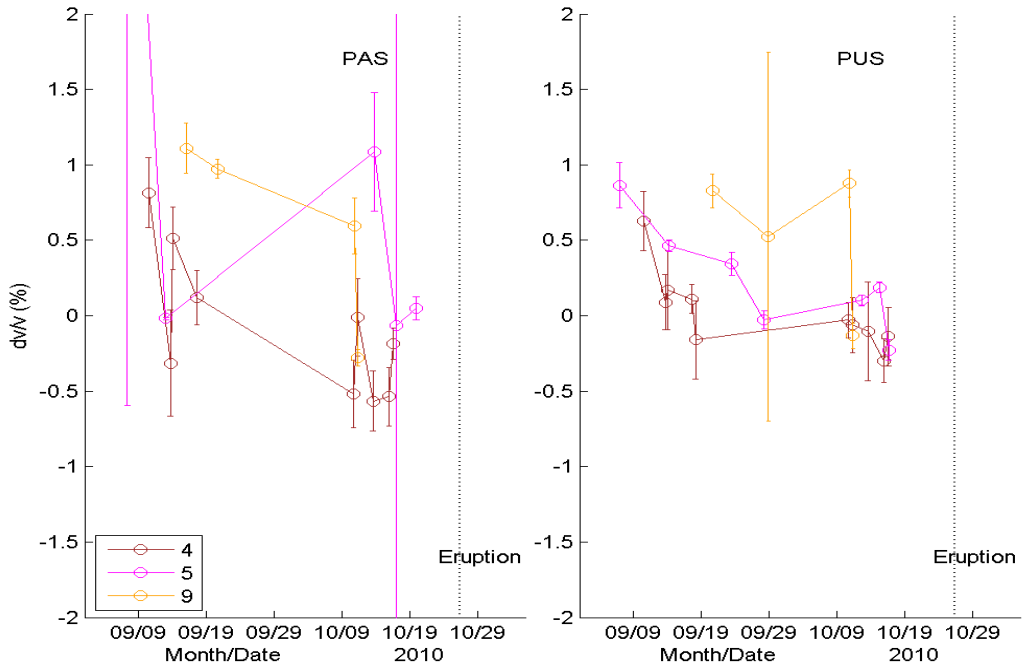

b

Fig. 6.9 Velocity changes obtained by the methods of stretching (a) and MWCS (b) for the deep clusters recorded at PAS (left) and PUS (right).

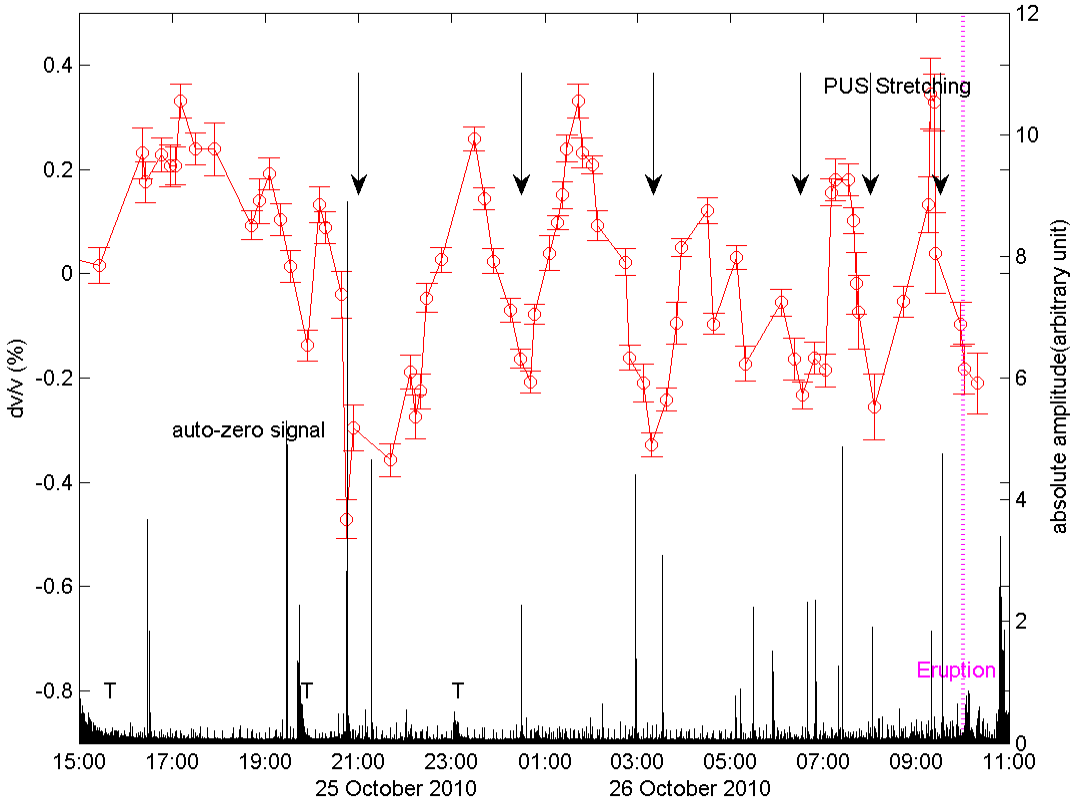

Fig. 6.10 Cross-plot between velocity variations of cluster 10 using stretching method (red line) and absolute value of amplitude of DEL seismogram filtered on 0.1 – 1Hz (black line). The peaks of the seismogram correspond to VT events except those marked with other types of event e.g. T for tectonic event and auto-zero signal. The eruption onset is indicated by dot line. Auto-zero signal is generated periodically by the modulator to reset the seismogram offset. Large VT events occurred during the velocity decreases indicated by arrows.

Table 6.1 Decrease rate and the cumulative decrease of each cluster recorded at PAS and PUS station calculated in some defined time periods. These time periods are chosen from which the linear decreasing trends are found.

Cluster	PAS			PUS		
	Decrease Rate (%/day)	Total (%)	Time period (DD/MM)	Decrease Rate (%/day)	Total (%)	Time period (DD/MM)
1	0.11	0.86	08/10 – 23/10	0.16	1.25	11/10 – 20/10
2	0.19	1.33	14/10 – 23/10	0.15	1.03	14/10 – 22/10
3	0.08	0.54	14/10 – 21/10	0.08	0.55	14/10 – 25/10
6	0.21	1.05	14/10 – 19/10	-	-	-
7	0.15	0.87	15/10 – 21/10	-	-	-
8	0.13	1.40	11/10 – 22/10	0.08	0.85	11/10 – 22/10
4	0.017	0.62	10/09 – 11/10	0.006	0.18	10/09 – 10/10
5	0.002	0.10	07/09 – 20/10	0.019	0.72	07/09 – 16/10
9	0.029	0.74	16/09 – 11/10	-	-	-

Among the clusters of similar events (multiplets), the cluster 2 has the longest availability i.e. from December 2009 to 23 October 2010 (PAS station). From the beginning of the data until 2 September 2010 the AVV appears to be stable on the range of 0.3 – 0.5%. Starting from 13 September 2010 it increased and remained in the range of 0.6 – 0.9% until 14 October 2010. However such increase is not shown on the data of PUS station.

A decreasing velocity at about 12 – 15 October is observed on almost all the shallow clusters. However such decrease is not clearly observed on cluster 6 and 7 at PUS station. The magnitude of decreasing varies among the clusters and the stations. To evaluate this magnitude we calculate the total decrease and its rate in certain periods in which both stations show decreasing values (Table 6.1). Stronger decreases are shown at PAS station except for clusters 1 and 3. The decrease shown at PAS station lasted until the last available data (23 October) except for cluster 3 which returns to increase on 21 October. On the contrary, cluster 3 at PUS station is the sole cluster whose decrease lasted until 25 October (last data). The remaining clusters at PUS station return to increase at about 21 – 22 October. The strongest decrease rate is shown by cluster 6 at PAS station (0.21%/day) and cluster 1 at PUS station (0.16%/day).

All the deep clusters recorded at PAS station show clear decrease from about the beginning of the data (7 – 14 September), though the decrease is weaker for cluster 5. Meanwhile, at PUS station, cluster 5 on contrary shows the strongest decrease, cluster 4 displays a decrease but then returns to increase at 10 October, while cluster 9 doesn't show a clear trend. We find that the magnitudes of decrease for the deep clusters are about one order lower than those for shallow clusters (Table 6.1) and the variations are not synchronous on the two types of clusters.

The cluster related with damaging prior to eruption

Besides separating the clusters based on their depth, we also analyse cluster 10 separately since it only appears during less than 2 days before the eruption and thus analysing the changes at short time is needed. In addition it was only recorded at PUS station. The corresponding AVVs are plotted on Fig. 6.10 together with the seismic amplitude at low frequency (0.1 – 1 Hz) of station DEL. Here, this latter station is used since many VT events are saturated in PUS station even with such filtering.

Fluctuations in the range of about ± 0.3% are obtained without continuous trend. There is a sharp decrease on 25 October at about 20:00 UTC coinciding with the occurrence of a large VTB which saturated all available stations. Although there were many VT which were saturated as well, thanks to the filtered amplitude we could identify this earthquake as the largest VT event during the crisis (September – October 2010). Along the fluctuations of AVV, several other saturated VT events also coincided with decreasing AVV in Fig 6.10.

6.3.2 Velocity variations obtained from noise correlation

We adjust the AVV of the second instrumental period to the end of the first period, assuming there is no significant AVV change on the transition between both periods. In Fig. 6.11 and 6.12 we overlay AVV resulted from each pair without and with rain correction respectively. In order to show the trend clearly we plot the results of the pairs containing PUS station separately. Events related

with volcanic and tectonic activities are indicated. Tectonic earthquakes are classified into 3 groups based on their distance from the volcano and their magnitude i.e. 0-50 km with magnitude of > 4 (blue line); 50-150km with magnitude >5 (red line); >150km with magnitude >6 (green line). Hereafter, we mention those groups as local, regional, and far tectonic events, respectively.

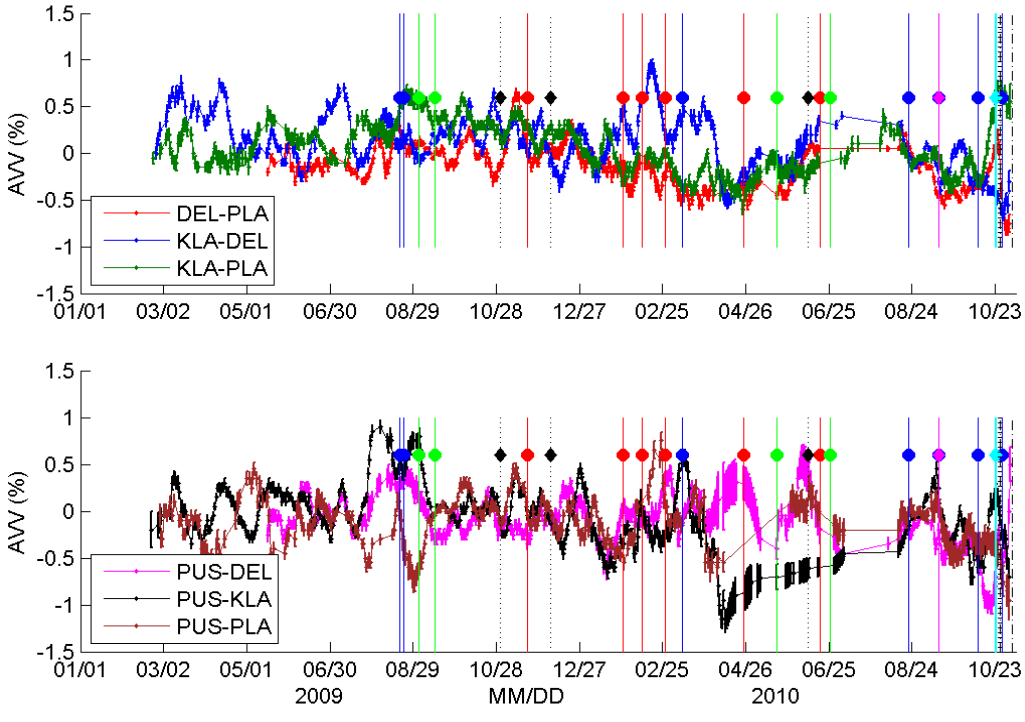

Fig.6.11 Apparent velocity variations (AVV) obtained from NCF for different station pairs as indicated by the legends. (a) AVV of station pairs without PUS. (b) AVV of station pairs composed by PUS. The vertical lines indicate specific events related with volcanic (diamond marker) and tectonic (circle marker) activity. Regarding the volcanic activity, those are VT swarms (black dot line), felt VT (pink dot line); large LF's (green dot line), and first eruption (black dot line). As for tectonic activity, they are classified into 3 groups based on their distance from the volcano and magnitude i.e. 0-50 km with magnitude > 4 (blue line); 50-150km with magnitude >5 (red line); >150km with magnitude >6 (green line).

Regarding the rain effects corrections, we found significant changes for pairs PUS-KLA, KLA-PLA, and DEL-PLA, whereas, due to their low correlation with GWL curve, the other pairs didn't experience a significant correction (Fig. 6.12).

The largest fluctuation due to rain effects is about ±0.3% shown byfor KLA-PLA pair.

We cannot observe clear velocity changes related with neither discrete volcanic nor tectonic events. Nevertheless, from about 12 – 14 October, there is likely a different behaviour shown by each of the station pairs (Fig. 6.12; Fig. 6.13). A velocity decrease up to 0.7% is observed from 12 to 17 October on the PUS-DEL pair followed by an increase from 22 October until the eruption. On the contrary, from 14 October, velocity increases are shown by KLA-PLA (1%), DEL-PLA (0.7%), and PUS-KLA (0.7%) until 25 October, while PUS-PLA likely remains stable until 24 October and slightly decreases afterward. As for KLA-DEL, though it is not clear, we observe a weak decreasing trend from 10 October.

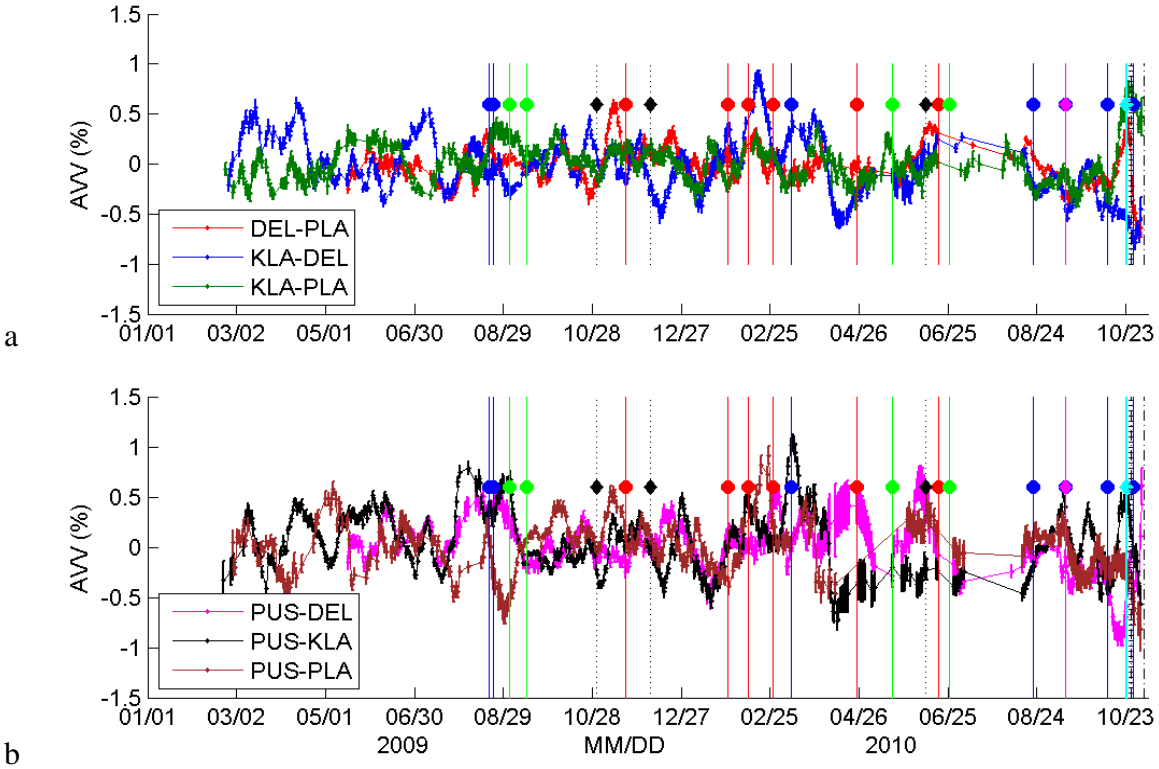

Fig. 6.12 Same as Fig. 6.11 but after rain effects corrections. Only the pairs PUS-KLA, KLA-PLA, and DEL-PLA experience significant corrections, since the other pairs have low correlation with the GWL.

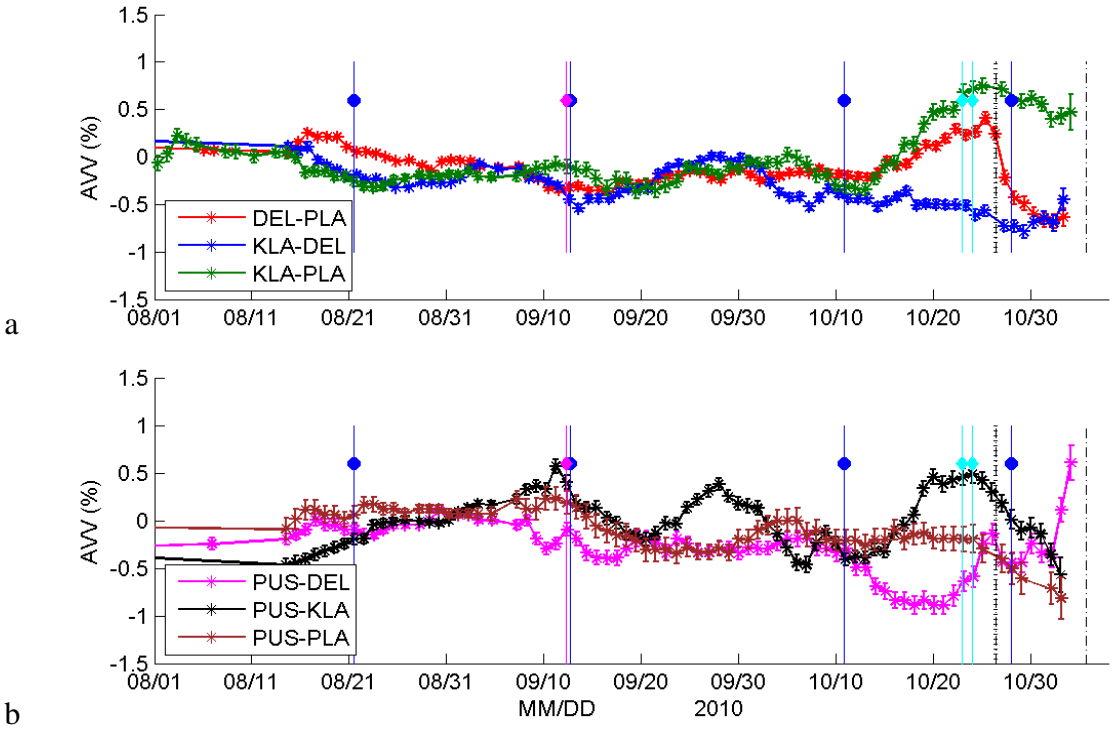

Fig. 6.13 The same as fig. 6.12. but zoomed in period of August to October 2010.

Location of the velocity perturbation

We took the reference state around 12 October 2010 when there is no significant change in velocity. We located the velocity perturbations that occurred between the reference state and the following dates: 1) 21 October, 2) 23 October since there is a marked change in velocity behaviour corresponding to these dates, 3) 25 October, the day before the first eruption, and 4) around 3 November, just before the largest eruption of 4 November 17:00 UTC.

As already mentioned, for choosing the smoothing parameters of λ and σ_m we used the L-curve criterion (Hansen, 1992). In Fig. 6.14 the misfits are plotted as a function of maximal velocity fluctuations in the model, for different values of λ and σ_m. The optimal smoothing is found for minimized values on both axes, which correspond to a maximal bending of the curve (Obberman et al, 2013). We found that the best parameters are λ=1km and σ_m=0.1.

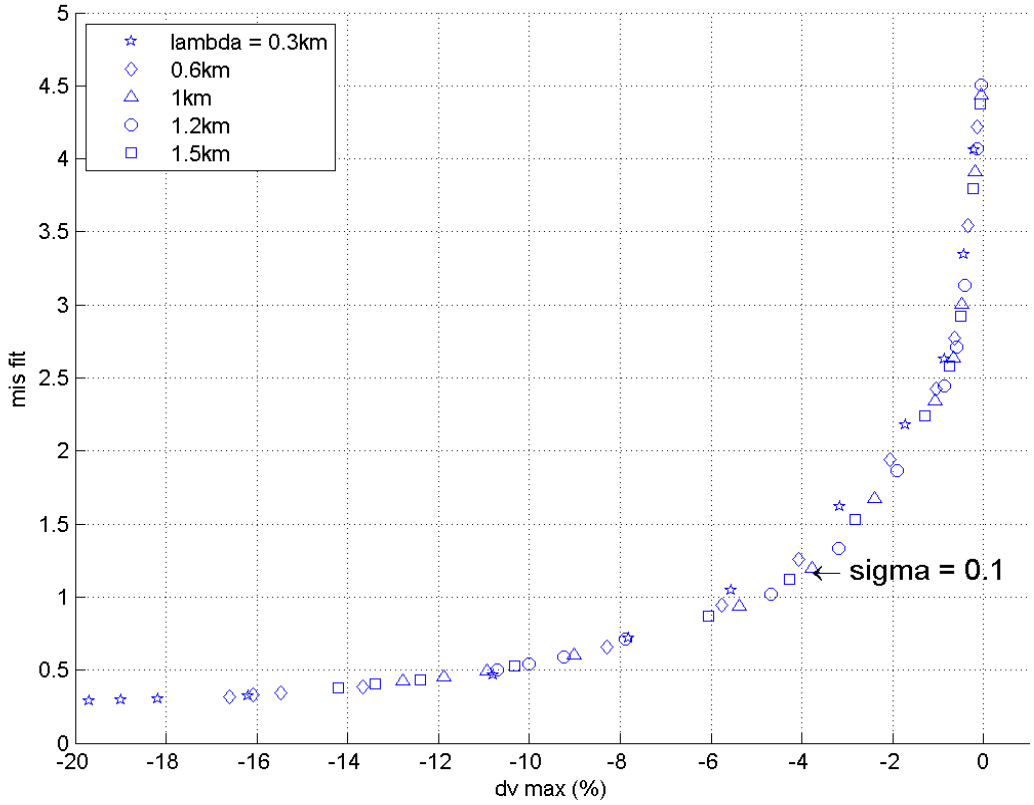

Fig. 6.14 L curve for different λ (indicated in the legend). Each point of the curve corresponds to different values of σ_m. The best parameters for which both the residual (miss fit) and the maximum velocity change are minimal are λ=1 and σ_m=0.1.

Using the chosen parameters, we obtained that the modelled values of AVV fit well the observed. Fig. 6.15 overlays the modelled velocity variations with the initial AVV for the day of 21 October. The same figures for the other dates are presented in the Appendix D. Fig. 6.16 displays the map of velocity variations corresponding to the days of interest.

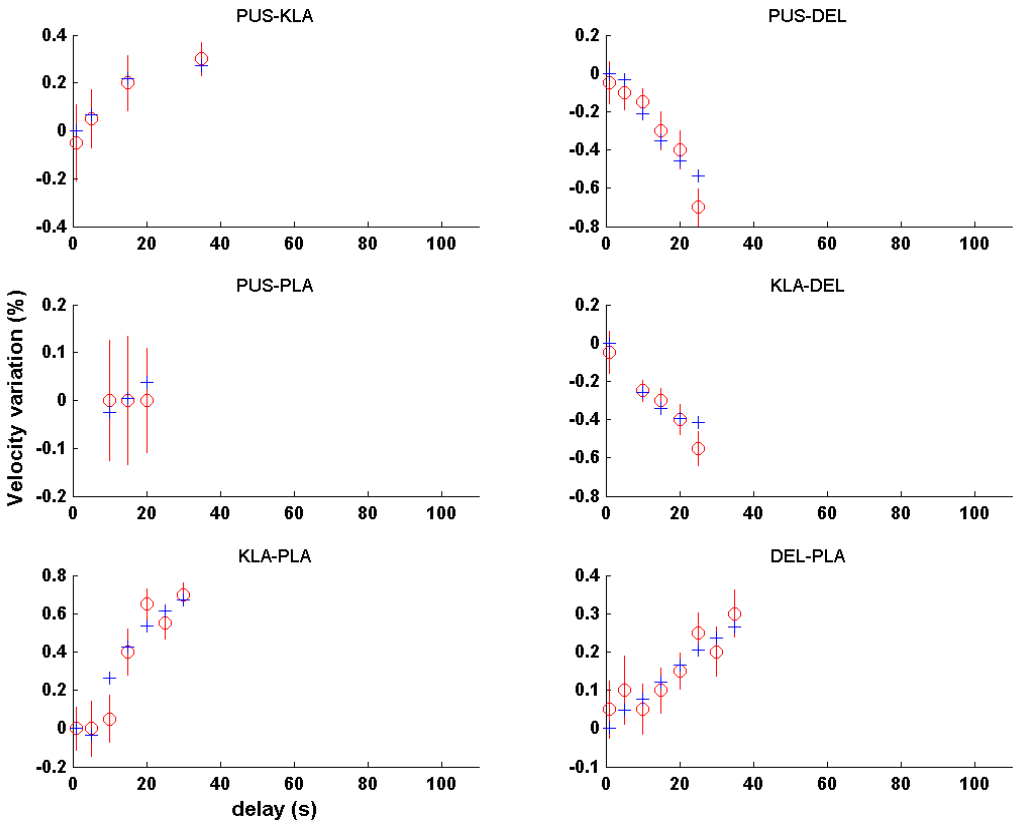

Fig. 6.15 Modelled AVV (blue crosses) corresponding to each AVV measurement (red circles with error bars) of each station pairs at different time lags. The observed AVVs are well fitted with the modelled ones.

For the day of 21 October, it appears that a velocity increase occurred on the lower part of volcano, particularly for the south part of the volcano. The upper part of the edifice including the summit seems to experience a decrease (Fig. 6.16a).

On 23 October, we observe an increase in velocity rounding almost all the lower parts of volcano. Meanwhile, a velocity decrease observed on the east side before is disappeared (Fig. 6.16a).

Regarding the day of 26 October 2010 (Fig. 6.16c), the lower part of the volcano still experienced a velocity increase. The circular pattern of the increase can be observed more clearly as the north part of the volcano shows a stronger increase

in velocity than before. A velocity decrease around the summit and the south part of the edifice persisted.

On the last day before the largest eruption i.e. 3 November, we no longer observe a circular pattern of velocity increase around the volcano. Instead, a strong velocity increase appears on the west and east sides of the volcano, whereas the other parts experienced a velocity decrease (Fig. 6.16d).

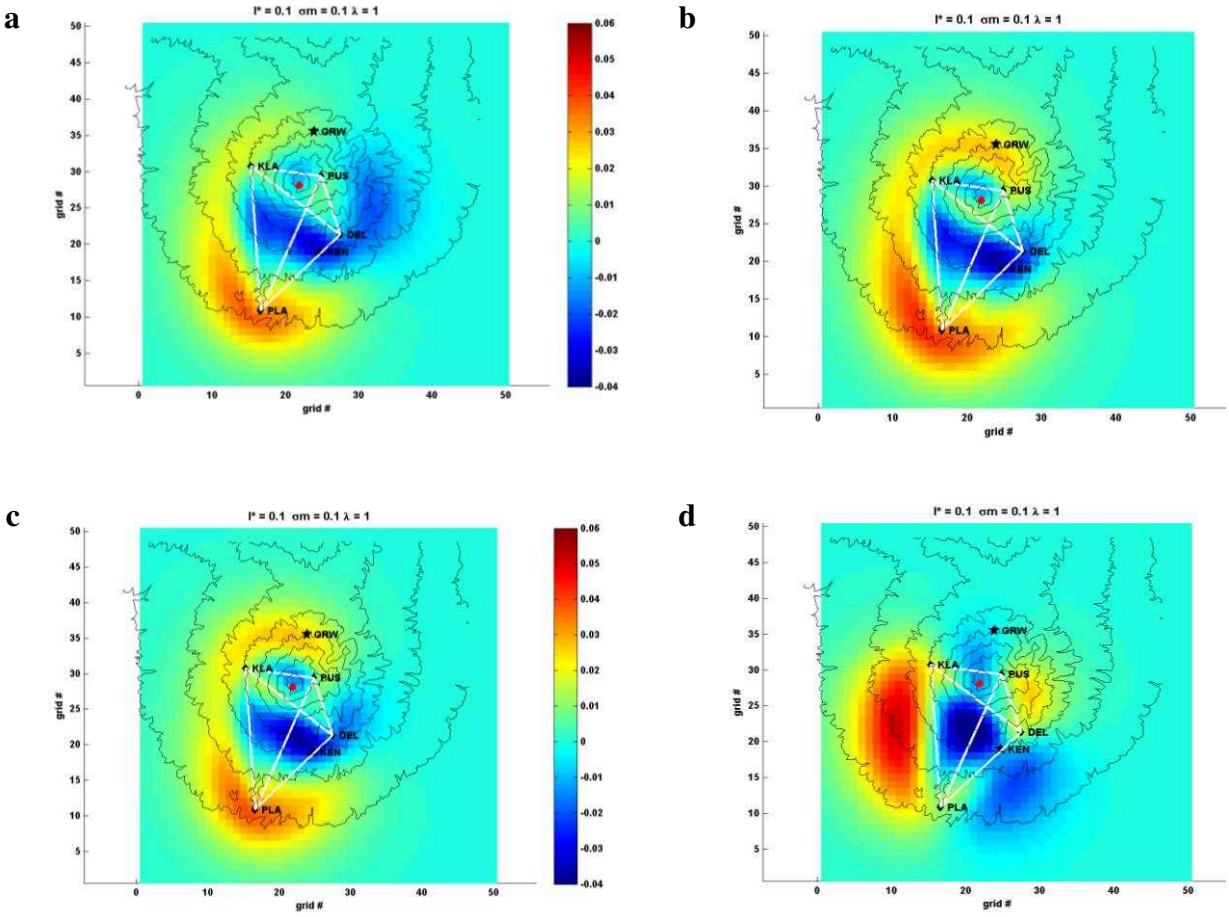

Fig. 6.16 Velocity variations in an area of 15x15 km^2 around the volcano for the period around 21 October (a), 23 October (b), 26 October (c), and 3 November (d). The 4 stations and 6 station pairs used in calculation are indicated by black diamonds and white lines respectively. Two other stations used in earlier studies are marked by stars. The position of the summit is shown by a red circle. We can observe an increase in velocity around the lower flank and a decrease on the highest south part of the volcano.

In order to evaluate the velocity change between consecutive periods of interest, we calculated the differences between the velocity variations obtained at the corresponding periods displayed in Fig. 6.16. Between 21 and 23 October (Fig. 6.17a), a circular slight increase in velocity is observed around the lower part of the edifice. The increase is stronger on the north-east upper part. Meanwhile, inside the seismic network velocity decrease is dominant except for the south part of summit where a small velocity increase is observed.

Compared to the date of 23 October, the VV on 26 October shows a decrease around almost the whole lower part of volcano (Fig. 6.17b). The upper part experienced an increase except for the south part of summit where a decrease is observed.

For the period 26 October to 3 November, (Fig. 6.17c), the previous circular pattern is no longer observed. Instead, a velocity decrease is shown on the north part, the south part, and across the volcano in north-south direction, whereas west and east sides experience an increase.

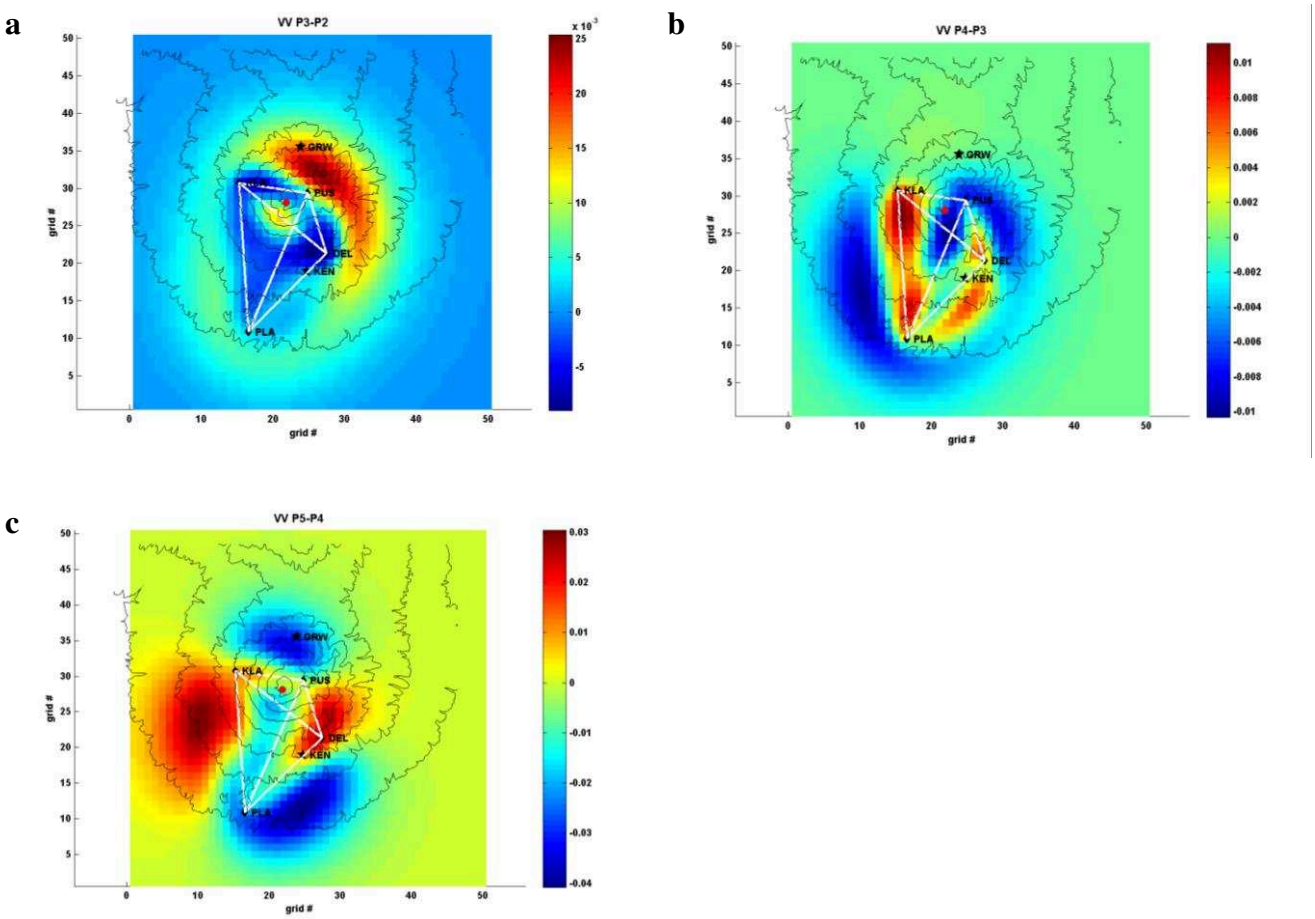

Fig. 6.17 Differences of velocity variation between the successive stages of 23 and 21 October (a); 26 and 23 October (b); and 3 November and 26 October (c). The scale is different for each figure depending on the corresponding range of VV values.

6.4 Discussion

6.4.1 Comparison of the methods used

We used the methods of MWCS and stretching for analyzing the earthquake coda and calculating velocity changes. We found that the velocity changes resulting from the stretching method are more stable than those from the MWCS method. With the latter method, in most cases, a linear variation of time delay along the coda is somewhat difficult to obtain. In addition the coherencies become poor for the windows time >4 s. Therefore, we used only the windows in interval of 1-4 s

which might be too small preventing accurate AVV results. In Fig. 6.18, the linear regression in this time interval is shown by blue lines. The calculations using coda windows of 2 – 6 s (red lines) produce different results. This likely implies that the assumption of an homogenous velocity change is not valid for our case.

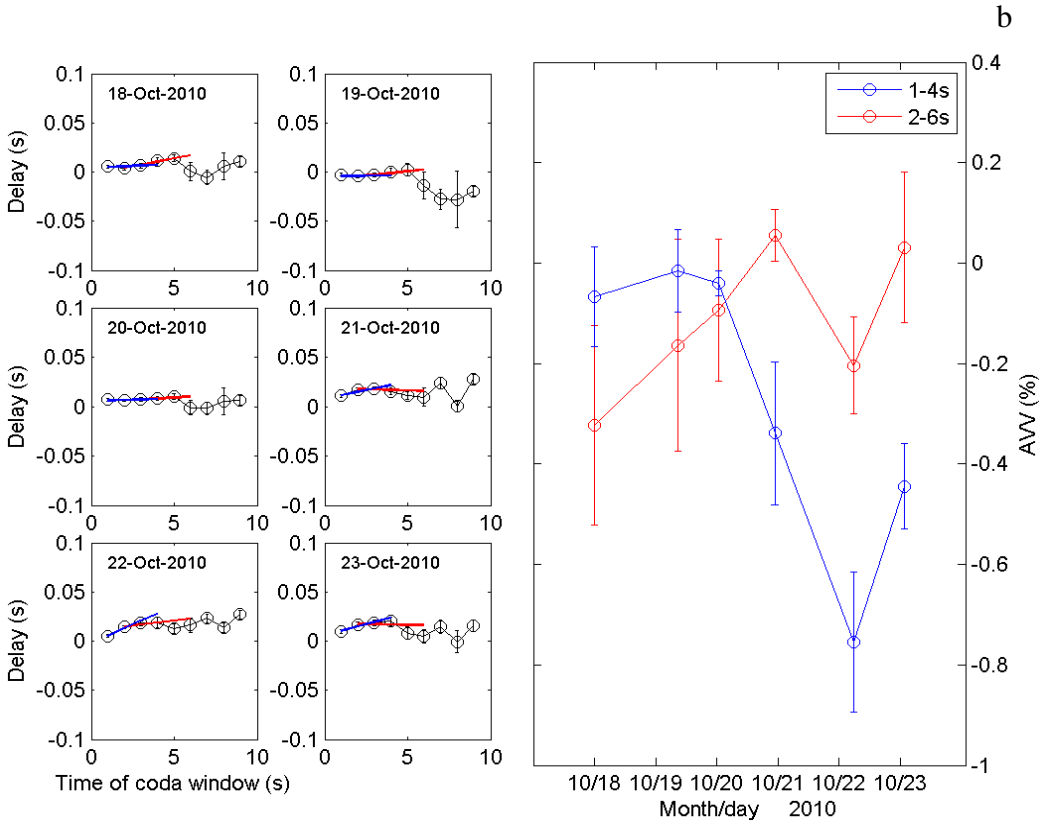

Fig. 6.18 Examples of AVV calculation using MWCS method on the 6 last events of cluster 2. (a) Time delays calculated by cross-spectral method for each event. The blue and red straight lines are the linear regression using the windows in time interval of 1 – 4 s and 2 – 6 s respectively. (b) The resulted AVVs from the 2 linear regressions of (a) for each event.

Further, simulations of the effects of seismogram saturation suggest that large spurious changes may result from the MWCS method (Appendix A). These results are consistent with the report of Hadziioannou et al. (2009) which explains that the stretching method gives more stability when fluctuations (noise) perturb the data and could provide an opportunity to increase the sensitivity of detection

of weak velocity changes. However, we suggest that it depends also on the cases since several works have reported encouraging results using the MWCS method such as in Brenguier et al. (2008), Clarke et al. (2011), Zaccarelli et al. (2011), and others.

6.4.2 Velocity changes prior to the eruption

We must acknowledge that our data are not ideal to obtain a clear feature of velocity changes prior to the 2010 eruption. We did not have many events associated with each cluster of multiplets yielding a sparse sampling of velocity change as a function of time, particularly for the period before October 2010, though some available data during this period seems to show stable values. Besides the instrumental problem in the period before and during reinstallation, the amplitude saturations which are the drawbacks of short period station also caused many events to be rejected due to their poor correlation. As demonstrated in Appendix A, the amplitude saturations generate bias in the resulted velocities, although the effect shown by the stretching method is smaller.

The quality of noise data is even worse before and during the reinstallation period. The declining data quality leads to the poorness of correlation. Among the problems is the time synchronisation which also results biases on the AVV. Although, we have tried to minimize these problems, large fluctuations remain particularly in the period before reinstallation. Even more, there are fluctuations induced by the rain effects. These fluctuations make the perturbations prior to the eruptions to appear feeble. However for the period after the reinstallation, the anomalies occurring several days before the eruption are much easier to observe since the background fluctuations are weaker than before. The corrections for the long term fluctuations due to rain effects also improved the results, although the anomalies themselves are generally larger than the rain induced fluctuations.

As for the location of velocity perturbations, it is important to note that we used an assumption of homogenous and isotropic medium, which is too simplified considering the complexity of volcanic medium. The inversion itself was very

poorly constrained since it used only 6 stations pairs. Considering these limitations, the resulted locations might not be precise. Nevertheless, the consistency between the data and resulted model demonstrated in Fig. 6.15 and in Appendix D suggests that the rough spatial behaviour of velocity change is somewhat correct.

In spite of all the limitations, we try to interpret the AVV calculated from both multiplets and ambient noise data. To help interpreting the results, we identified several stages characterised by different behaviour of AVV. Based on these stages we propose a speculative interpretation combining other observations.

We exclude the results from MWCS method in the interpretation regarding the multiplets. Furthermore, we mainly consider the results from PAS station though in some cases we have to use those of PUS station when PAS station is no longer available. For sake of simplicity, multiplets 2 and 4 are taken as representative of the shallow and deep events respectively. Meanwhile, we use all the AVV resulted from the NCF.

Synthesis of spatial and temporal velocity changes

Fig. 6.19 and 6.20 represent the synthesis of the AVV estimated from NCF and several multiplets together with the histograms of occurrence of the deep and shallow clusters. We divide the behaviours of velocity change associated with the 2010 crisis into five stages corresponding to the dates of 13 September to 14 October, 21 October, 23 October, 25 October, and 3 November respectively. The first velocity change of about +0.3% occurred in the interval of 1 to 13 September 2010 on the data of cluster 2 which remains stable afterward until 14 October 2010. Simultaneously, the deep cluster (cluster 4) which was active between 9 September and 15 October shows a decreasing trend. Thus, we consider the period between 13 September and 14 October as the first stage. Note that, in the course of this stage, we cannot observe velocity changes from NCF that exceeds the background fluctuations.

The apparent velocity variation estimated from cluster 2 display a large decrease from 14 October up to the end of the multiplet activity. Meanwhile, during the period from 12 October to the main eruption, the AVV estimated from NCF for six station pairs present distinct behaviours. In order to describe in detail these observations, we divide this interval into two sub-periods. The first sub-period corresponds to the velocity decrease of PUS-DEL which began at about 12 October, and the second one is associated with the velocity increase for the same pair at about 21 – 24 October. As for the second sub-period, it might also correspond to the changing in trend i.e. from decrease to increase shown by the cluster 3 (Fig. 6.8a). The station pairs of KLA-PLA, DEL-PLA and, to a smaller extent, PUS-KLA show an increase during the two sub-periods. Meanwhile, the station pairs of PUS-PLA and KLA-DEL show stability. It seems that, there is difference behaviour between the AVV of the lower part and the upper part of the volcano. We attribute these two sub-periods to the second and the third stage respectively.

During the period 24-26 October, almost all of the station pairs, except PUS-DEL, indicate a maximum of velocity before the eruption onset. However, it appears a slight decrease on the day before the eruption shown by a few pairs e.g. PUS-KLA. As for the AVV from multiplets, we observe in the cluster 10 several quasi-periodic fluctuations of velocity whose decreases correspond to the events of large VTB (Fig. 6.10). We consider this period as the fourth stage.

The fifth stage corresponds to the velocity change after the first eruption. Velocity decreases took place after the first eruption onset observed on all the station pairs. For the station pairs of KLA-PLA, DEL-PLA, PUS-PLA, and probably PUS-KLA the velocity decrease lasted until about 3 November, whereas for station pair PUS-DEL and probably KLA-DEL, it turned to increase on 29 November.

Interpretation

Among the physical processes that can induce seismic velocity change in volcano are temperature, pressure, stress, fluid, and strain effects. It was demonstrated by

Anderson et al., 1992 that an increase in temperature can induce a decrease of the rock elastic bulk and shear modulus. The pressure has an important role in the velocity change through the porosity and fractures within the rocks (Tutuncu et al., 1994, Van der Neut et al., 2007, Larose et al., 2009, Niederletihinger et. al., 2010, Shokouhi et al., 2010, Stahler et al., 2011). Elastic velocities are found to vary with variation of pore fluids in terms of saturation degree and types of fluid (Kitamura et al., 2006). Brenguier et al. (2008) proposed that the velocity increase before the eruption of Piton de la Fournaise is due to summit dilatation. All these processes might happen during the 2010 Merapi crisis. However, which process is dominant depends on the current magmatic activity as it will be discussed below.

The present interpretation regarding each stage of velocity changes is mainly based on seismic data. A more comprehensive interpretation involving all observations will be presented in Ch. 7. Locations of the velocity perturbations in the structure have been estimated for the stages 2 to 5. The day corresponding to each stage and the day of reference in localization are shown in Fig. 6.20. Further, we calculate the residual values between the modelled VV obtained from two consecutive stages. We use these locations for interpreting the AVV resulted either by multiplets and NCF.

The first stage, which includes an increase in velocity on the beginning of September shown by cluster 2, can be interpreted as the compression of the edifice due to an inflation of the deeper conduit as the response of a huge volume of rising magma. This interpretation is supported by the fact that the seismic crisis began around this period that is characterized by the occurrence of VTA and VTB.

Regarding the second stage (around 21 October), we interpret the velocity decrease shown by cluster 2 and NCF of PUS-DEL pair as the effect of the presence of magma in the aseismic zone (depth of 1.5 – 2.5 km) whose velocity is relatively low compared with the surrounding rocks. The high temperature might decrease the elastic property of the surrounding rocks that also provoke a velocity

decrease. The increase in velocity demonstrated by the pairs KLA-PLA and DEL-PLA might correspond to the magma pressure in depth that increased the stress around the lower part of the edifice. Despite the lack of precision, the location of velocity perturbation shows some consistency in the velocity increase on the lower part of the volcano and a decrease on the upper part (Fig. 6.16a).

During the third stage (23 October), the apparent velocity for pair PUS-DEL turned to increase while the velocity keeps increasing shown at KLA-PLA and DEL-PLA. A similar change of trend is also observed on cluster 3. During this stage, the VTB activity intensified, while VTA had already disappeared during the previous stage. These observations may result from a pressurization within the upper conduit. In the map of velocity perturbation localization (Fig. 6.16b), we observe a stronger increase in velocity on the north part of the edifice and an absence of velocity decrease on the east side. A circular pattern of velocity increase appears around the edifice. The velocity differences between this stage and the second one show such pattern even clearer with a stronger change at the north-east side (Fig. 6.17a). An increase around the south part of summit is also observed. This suggests a stronger and more localized source of pressure than that of 21 October. We interpret these observations as a pressurization of magma above the aseismic zone that might enlarged the upper conduit as a point or volumetric source of compression.

The fourth stage is associated to the velocity variations that occurred during the last two days before the eruption (26 October). As mentioned, there were fluctuations of AVV observed from multiplet 10, where almost all the episodes of velocity decrease are ended by a large saturated VTB.

Some experimental studies using concrete under stresses show similar phenomena (Larose et al., 2009; Niederletihinger et. al., 2010 ; Shokouhi et al., 2010; Stahler et al., 2011). The acoustic velocity of a concrete sample under stress increases with increasing stress until the pressure exceeds the material strength (Niederletihinger et. al., 2010). By then the velocity rather decreases

(Niederletihinger et. al., 2010, Stahler et. al., 2011). The velocity increase occurs because crack density decrease as cracks close under pressure (Van der Neut et al., 2007, Larose et al., 2009). The later stage of sharp velocity decrease takes place due to cracks connection building larger fissures that change the elastic parameters (Stahler et.al., 2011).

Similarly, we interpret the repeated velocity decreases that are followed by VT earthquakes several hours before the eruption as the gradual destruction of the summit plug due to magma intrusion. The heterogeneity of volcanic medium allows magma to break through the surrounding rock progressively before it could emerge to the surface. When the velocity decreases, it is interpreted as a cracking activity toward the failure of the corresponding rock under stress. The failure itself is indicated by the occurrence of one or several VTBs afterward.

Although the AVV of NCF does not provide hourly variations, the decrease or at least stabilisation of the apparent velocity during the last days before the eruption likely represents the mean of velocity fluctuations shown by the cluster 10. The location of velocity variations corresponding to this stage shows a relatively weaker variation compared to the previous stage of 23 October (Fig. 6.16c). In fact the differential values between 23 and 26 October in the lower part of the edifice as well as in the south part of the summit show a clear decrease (Fig. 6.17b). A process that might be involved at the beginning of the velocity decrease is a relatively small stress release due to gas escapes during the occurrence of LF on 22 – 24 October. Many of the VLP earthquakes observed during the pre-eruptive period, which are attributed to the gas releases through cracks and conduit permeability supports our interpretation. However, this gas release did not balance gas accumulation due to the large magma flux, which powered the highly explosive stages of the eruption (Jousset et al., 2013).

Stage 5 is related with the velocity variations after the first eruption (26 October) and before the largest eruption of 4 November. We suggest that during this period the volcanic system can be considered as an open system which means that the

magma and gases can discharge more easily than before the first eruption. The decreases in velocity shown by most of the station pairs likely indicate a stress relaxation around the edifice. However, due to the large magma volume that still remained, the upper part of the volcano underwent a strong compression indicated by the increase in velocity of station pair of PUS-DEL and probably KLA-DEL. The location of velocity variations regarding this period no longer show a circular pattern of velocity increase implying an absence of focused pressure in depth (Fig. 6.16d; Fig. 6.17c).

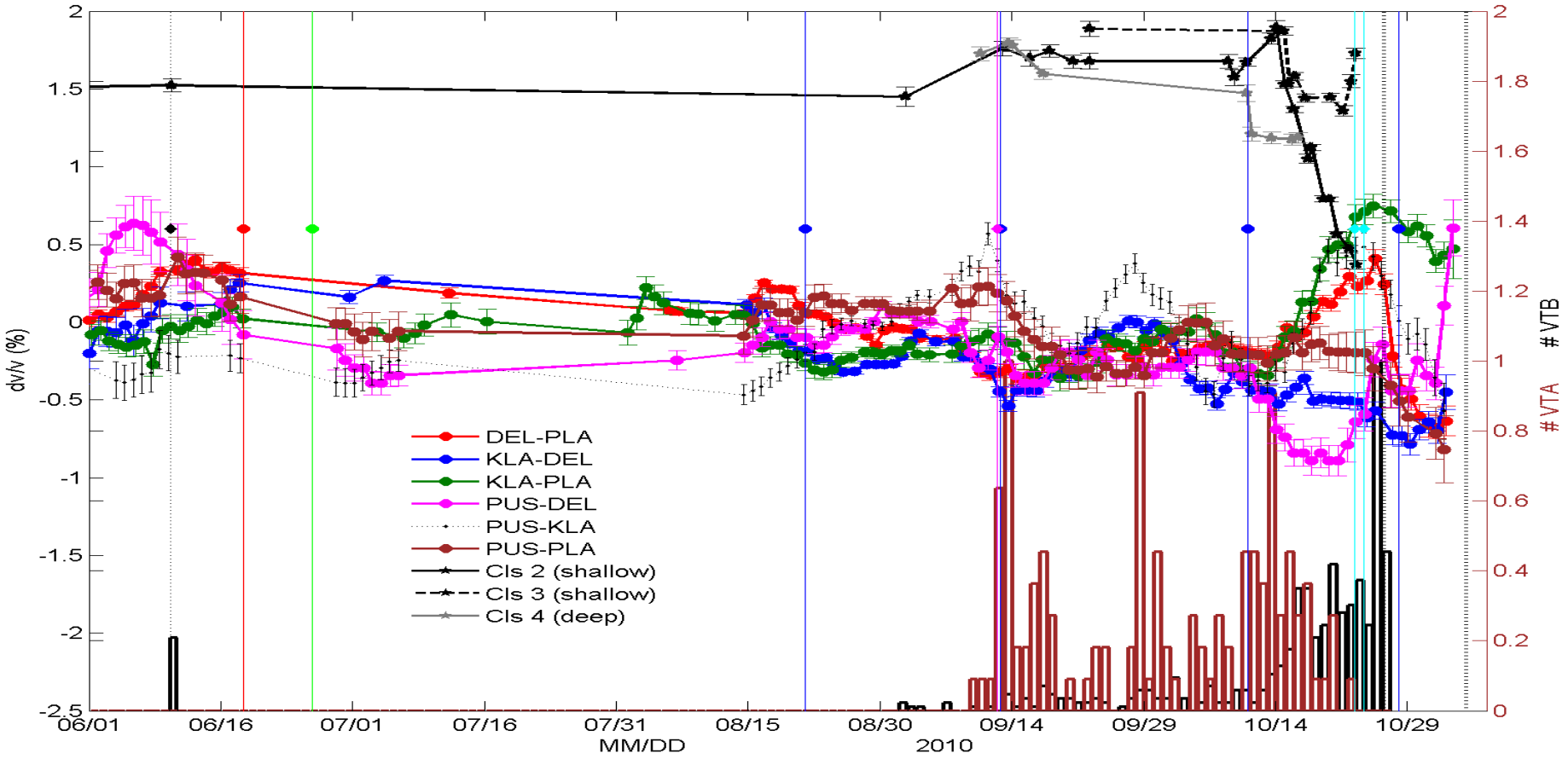

Fig. 6.19 AVV for all station pairs and for clusters 2, 3, and 4 are plotted with the normalized daily histogram of VTA (brown bars) and VTB (black bars). The eruption times, as well as the tectonic events are indicated like in Fig. 6.11.

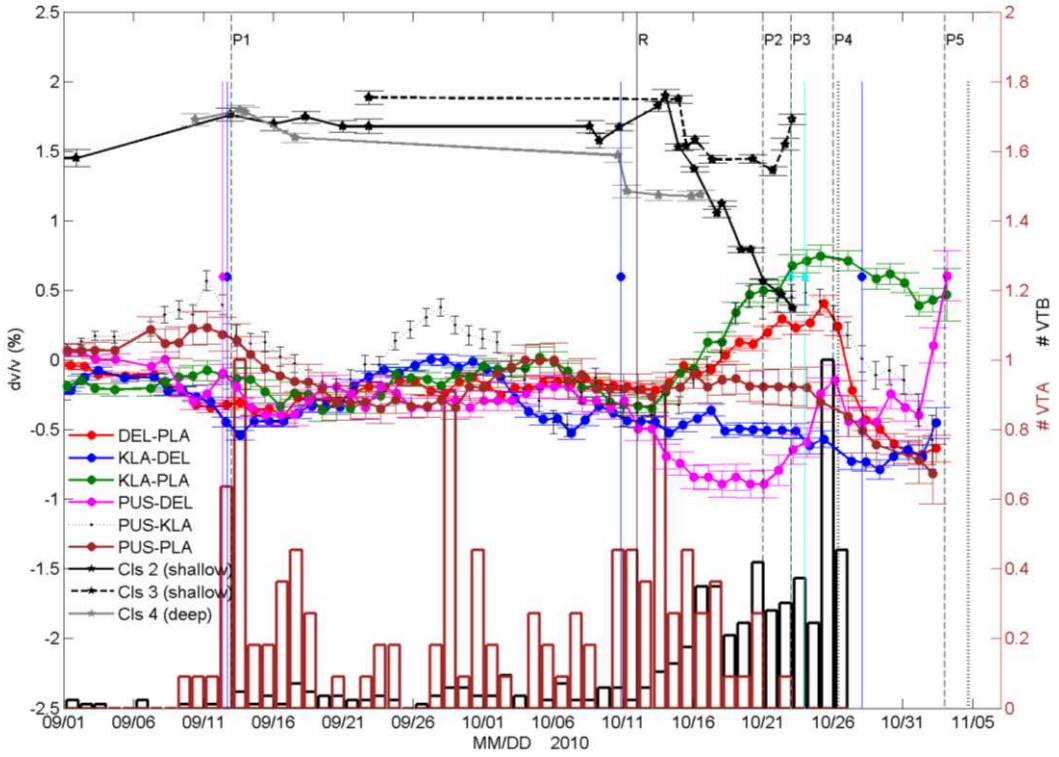

Fig. 6.20 Same as Fig. 6.19 but zoomed in the period of September-November 2010. The stages of velocity changes are indicated by dashed line and are marked by P1 to P5 which correspond to the days of 13 September, 21 October, 23 October, 26 October, and 3 November 2010. We performed localization of all the stages but P1 using the reference day of 12 October (solid line;R).

6.4.3 Comparison with the earlier studies at Merapi

As mentioned in the introduction, there are at least 3 studies on seismic velocity variation at Merapi. Here we discuss earlier results with that observed in the 2010 crisis. Ratdomopurbo and Poupinet (1995) observed an increase of shear wave velocity of 1.2 % during May – September 1991, about 4 months before the eruption of February 1992. Four months before the 2010 crisis, we do not observe yet any significant velocity change neither with multiplets nor with NCF. The first clear velocity change is observed using multiplets about 1.5 months before the eruption. However, considering the difference of eruption type between the 1992

and 2010 crisis, the results suggest a possible similar velocity increase on beginning of each volcanic crisis.

Wegler et al. (2006) observed a small velocity increase (0.08%) one week prior to the eruption of 1998 based on artificial multiplets on temporary stations KEN and GRW whose distance from the summit is about 2.3 km. It is difficult to compare this observation with our results from multiplets since they used stations much farther from the summit than ours. Considering that there is a slight increase shown by cluster 2 just before its strong decrease on 14 October (12 days before the eruption), the velocity change observed by Wegler et al. is likely. However, because they provided only 3 values of AVV prior to the eruption it is somewhat speculative to make an interpretation.

According to Sens-Schonfelder and Wegler (2006), who used data of GRW station, the long term fluctuations of AVV are of the order of 1% which are attributed to the seasonal variations i.e. precipitation. These authors conclude that the AVV reported by Ratdomopurbo and Poupinet (1995) and Wegler et al. (2006) are secondary. On the other hand, such fluctuations have amplitude of ±0.3% (in average) in 2010 and likely depend on the location of the station pairs. This difference in amplitude suggests that the effect of rain around GRW might be stronger than the other area surrounding the volcano especially the sites close to the summit.. On the other side, the period studied by Sens-Schonfelder and Wegler (2006) is a quiescent period. Thus, we do not expect that significant velocity changes related with magmatic activity could be detected in particular when using distal station such as GRW. In fact the response of the medium in terms of velocity variation would vary for different positions as it is demonstrated in numerical modelling (Poupinet et al., 1996) and real cases (Anggono et al., 2012; Obermann et al., 2013a).

6.4.4 AVV and tectonic events

In order to analysis the relation between AVV and tectonic activities, all tectonic earthquakes with magnitude ≥3 located in a radius of 200km from the volcano

during 2009 – 2010 are listed. We found 147 of events, where about 36 of them are located at ≤60 km from the volcano (mostly on land). In spite of the large number of tectonic earthquakes during the period of the AVV calculation, no clear relationship between AVV and tectonic events is observed.

6.5 Conclusions and perspectives

Earlier studies proposed that increases in apparent velocity are eruption precursors at Merapi (Ratdomopurbo and Poupinet, 1995, Wegler et al., 2006). Note that Ratdomopurbo and Poupinet (1995) used data from 2 multiplets which represent about 22% of detected events in a period of 4 months before the eruption, whereas Wegler et al. (2006) provided only 3 points during about 2 weeks prior to the eruption. In the present study we used 10 multiplets recorded on two stations during one year before the eruption, which include about 50% of the detected events. We used also the NCF, calculated for 2 years before and during the eruption, on 6 pairs of stations covering the volcano in a radius of about 6 km. Using such a large data set, we found very complex behaviour of the AVV associated with the eruption. We thus suggest that the precursory velocity changes cannot be represented merely by a unique trend; neither of increase nor decrease. In fact, the pre-eruptive velocity variations must be considered as a function of time, space, and probably depths.

We found different behaviours shown by multiplet and NCF as well. Yet among the 10 multiplets, different features are demonstrated particularly between shallow and deep clusters. The joint interpretation of the AVV from multiplets and NCF taking into account their large uncertainties is somewhat challenging. According to our references, such study involving a number of multiplets and NCF to understand the temporal and spatial velocity change behaviour prior to a volcanic eruption has never been done before.

Comparing the methods of MWCS and stretching in the coda of similar events, we find that the results with stretching method are more stable than those with MWCS method. It might be because the stretching method is less sensitive to noise and amplitude saturation. Besides that, the assumption of homogeny velocity change on the medium might not be the case of Merapi. PAS station which is a broadband station is more reliable for calculating the velocity variation thanks to its larger clip level and its larger frequency response.

We realise that that our data are not ideal for providing clear and convincing results regarding velocity change prior to the 2010 eruption. As mentioned, among the limitations are the small number of stations; instrumental problem; saturation of short period stations; and others. In spite of all these limitations, we propose interpretations of the results taking into account that large uncertainties might be involved.

We identified five stages related with pre-eruptive velocity changes associated with the 2010 eruption. The first stage is the increase of about 0.3% shown by cluster 2 in an interval of 1 to 13 September 2010 which remained stable until 14 October 2010. It is interpreted as an initial marked pressurization due to hydrothermal activity triggered by heat transfer from magma in depth. The second stage is mainly characterized by the decrease in AVV shown by cluster 2 and PUS-DEL pair around the date of 21 October 2010. It is interpreted as the presence of new magma in the aseismic zone. The third stage (23 October) took place when the pressurization resumed above the aseismic zone due to the rising magma into the upper conduit which produced an increase in velocity shown by NCF and also by cluster 3. We interpret these observations as a pressurization of magma above the aseismic zone that might enlarged the upper conduit as a volumetric source of compression.

Rapid velocity fluctuations are observed during several hours before the eruption which indicates a gradual destruction of the summit plug due to magma penetration. It implies the fourth stage. The heterogeneity of the medium allows

magma to break through the surrounding rock progressively before it could emerge to the surface. The stage 5 is related with the velocity variations after the first eruption (26 October) and before the largest eruption of 4 November. The decreases in velocity shown by most of the station pairs likely indicate a stress relaxation in the edifice.

The locations of the modelled velocity variations are found to be consistent with the calculated AVV as well as with our interpretations. However, it appears that the precision regarding the spatial distribution of velocity variation is poor due to small number and sparseness of the stations. We suppose that adding more stations to increase the station density covering both the region around the summit and the flank or further would improve the results. The broadband stations are preferred due to their large frequency response and larger dynamic range. Indeed, some studies demonstrated that the AVV as a function of frequencies can provide estimations of the depth of the velocity perturbation (Lesage et al., 2013, Obermann et al. 2013d).

The next interesting study might be to combine the multiplet and the NCF observations into the inversion of velocity perturbation. Since the location of the multiplet sources are known, we could expect to get more information of AVV closer to the source of velocity perturbation. It would be thus possible to obtain 3-D or 4-D images of velocity perturbations.

Chapter 7

General conclusions

The feature of Merapi plumbing system

Based on VT locations, we suggest that the Merapi plumbing system at depth <5 km during the 2010 pre-eruptive activity did not change with respect to the previous eruptions. Two aseismic zones have been observed at depth 1.5 - 2.5 km and below 4 km at least from 1984. The lack of observable earthquakes at these depth ranges may be related with rheological characteristic of porous and unconsolidated layers. Regardless the possible magma body that might persist within, the existence of aseismic zones are consistent with conductive zones observed by electromagnetic measurements (Ritter et al., 1998, Commer et al., 2000, and Müller and Haak, 2004). The upper aseismic zone is likely within the layer of Ancient Merapi left by Holocene sector collapse (Newhall et al., 2000; Camus et al., 2000). A numerical modelling of tiltmeter data supports a pressure source located at about this aseismic zone (Westerhaus et al., 2008), although it is not consistent with the other deformation study (Beauducel and Cornet, 1999). We interpret the deep aseismic zone as an ephemeral magma chamber.

This model of structure of Merapi is consistent with the following interpretation of the seismic pre-eruptive activity (Fig. 7.1).

Phases of activity

The features of the pre-eruptive seismic activity that have been obtained in this thesis, as well as some other observations, lead us to propose a chronology of the magmatic activity prior to the 2010 eruption as follows:

Phase 1: Feeding of the deep magma chamber (October 2009 – September 2010)

In Fig. 7.1 we illustrate our proposed chronology of magmatic activities prior the explosive eruption of 26 October 2010. The ephemeral magma chamber (>4 km) feeding began at least 1 year before the eruption as indicated by the presence of VT swarms (Fig. 7.1a). The heat of the rising magma might have triggered hydrothermal activity within the regional layer (Ritter et al., 1998; Muller and Haak, 2004; Commer et al., 2006) and the Ancient Merapi that are crossed by the conduit. Steam and magmatic gases arose and therefore increased local stress around the upper part of the conduit producing VTB earthquakes. These VT events make up clusters 2, 3, and 6 which persisted until October 2010. Since cluster 2 is classified as a low frequency cluster, it likely involves gas transfer. The rate of summit inflation increased from 0.3 mm/d to 1.2 mm/d.

Phase 2: Magma chamber and conduit enlargement (September – 17 October)

As the magma supply continued, the overpressure of magma increased. Once the overpressure exceeded the lithostatic load around the magma chamber roof, due to large volume of magma, it allowed the existing conduit to enlarge as the magma rose and thus produced the VTA earthquakes (starting from September 2010). Part of the VTA events are clustered in clusters 4, 5, and 9. Pressurization also took place in the upper part of the structure as indicated by the increase in shallow seismic activity and increase in deformation up to 8 cm/d (Fig. 7.1b). Since some clusters found in this period were also found during the first phase, the mechanism of this pressurization might be the same for both periods but the closer is the magma, the stronger is the pressurization. The decrease and increase in velocity showed by cluster 4 (deep) and by cluster 2 (shallow) during this phase are consistent with the interpretation. The velocity decrease of deep cluster might indicate magma filling of the plumbing system, dilatation of the conduit, and/or damaging of the surrounding medium.The increase observed by shallow cluster

might be resulted by an increase in local stress within the upper part of volcano due to hydrothermal activity.

Tremors were observed from 30 September to 4 October 2010. We interpret this as a transfer of magmatic gases and/or steams produced in the aseismic zone due to heating of the approaching magma. These observations along with the intensifying seismicity signify a continuous magma supply that leads to an eruption.

Phase 3: Magma migration from the deep to the shallow conduit through the aseismic zone (18 – 21 October)

The shifting of VT hypocenters from VTA zone to VTB zone starting from 17 October 2010, the relative quiescence of seismic and deformation activity on 19 – 20 October 2010, and the decrease in AVV showed by PUS-DEL station pair and cluster 2, indicate that magma migrated through the ductile layer about one week before the eruption (Fig. 7.1c). The decrease in velocity during this phase may be interpreted as an effect of the presence of magma in this layer.

Phase 4: Shallow conduit enlargement and partial gas escape (20 – 24 October)

When the magma reached another rigid zone, the overpressure then caused the shallow conduit to enlarge producing brittle failure on the surrounding rocks that produced the VTB earthquakes, an increased in rate of deformation (Fig. 7.1d), and triggered a marked increase in number and magnitude of Rockfalls (RF). Based on the reports from the post observatories, on 20 October there were at least 7 large RF that could be heard from the post observatories. These magmatic processes allowed the gases, particularly the steam resulted from water-magma interaction, to escape producing large LF earthquakes that culminated on 23 – 24 October (Fig. 7.1e). These LF events constitute clusters 1 and 2 and are observed on MRSAM (Modified Real-time Seismic Amplitude Measurement) on the frequency band of 1 – 3Hz. As mentioned, cluster 2 also occurred during VT swarm.

During this phase, two distinct velocity change behaviours are observed. First, AVV of station pair PUS-DEL turned to increase along with a persisting velocity increase showed by KLA-PLA and DEL-PLA since about 14 October. Such trend is also observed on cluster 3. Locating these velocity perturbations, a circular pattern of velocity increase appears around the edifice, with a stronger change at the north-east side. These observations are consistent with a pressurization of magma and gas above the aseismic zone that might enlarge the upper conduit as a point or volumetric source of compression.

The second behavior is the stop of the velocity increase observed from ambient noise of PUS-KLA, KLA-PLA, and DEL-PLA pairs on 24 - 26 October. Our inversion shows a decrease in velocity around the lower part of the volcano and the south part of summit. These observations support a relative relaxation of stress with respect to the state of 23 October due to gas escape.

Phase 5: Damaging prior to the failure (25 – 26 October)

During this period, the number of VTB events per day increased sharply up to 200. Meanwhile, the deformation rate increased reaching 50 cm/day, the highest level ever observed at Merapi. This supports a strong damaging activities that started to occur as the magma rose to the shallower part of the conduit (Fig. 7.1e). The rising magma might involve a stick slip mechanism considering a large magma volume breaking through a relatively small existing conduit. It is somewhat indicated by the presence of cluster 10. AVV related with the cluster 10 shows fluctuations whose decreases coincided with the large VTB events. It is interpreted as a gradual destruction of the summit plug due to magma penetration.

Phase 6: Explosive eruption (26 October)

Intrusion phase culminated as a phreato-magmatic explosion on 26 October 2010 10:02 UTC (Fig. 7.1f). This initial eruption was followed by many other eruptions until it peaked on 4 November 2010 at 18:00 UTC. During period after the first explosion, the decreases in velocity were observed by most station pairs. It likely indicates stress relaxation around the edifice. The distribution of velocity increase

in this period has no longer a circular pattern implying an absence of strong localized pressure in depth. Thus, we suggest that during this period the volcanic system was an (almost) open system which means that the magma and/or gases can discharge more easily than before the first eruption. The rapid rates of dome extrusion on 1 – 4 November (Pallister et al., 2013) and the continuous high frequency tremor occurring from 3 November associated with continuous pyroclastic flows and degassing are also consistent with an open volcanic system.

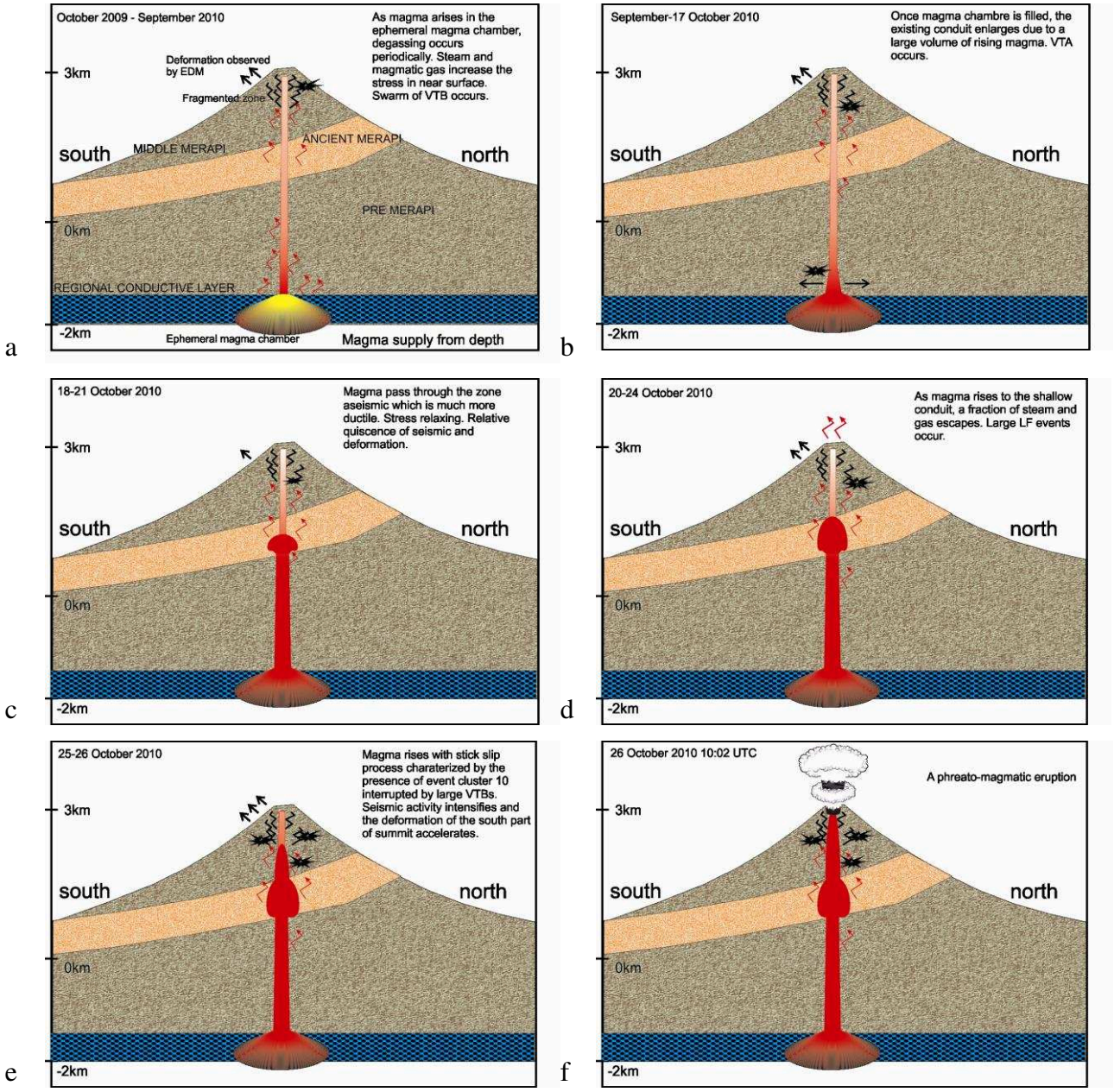

Fig. 7.1 A model of the seismic and volcanic activities prior to the eruption of 26 October 2010. The simplified geological structure is adopted from Camus et al. (2000) and Muller and Haak (2004). The conductive regional layer and the layer of Ancient Merapi are suggested to be more ductile than the surrounding layers which allows the magma to cross over without much resistance. Please note that, for sake of better visualisation, the location and size of the structures are not precise.

The specific characteristics of 2010 activity

After an exceptional eruption, it is of paramount importance to carry out a thorough analysis of the data from the monitoring network that could not be processed in detail during the crisis. We found, that the most relevant characteristics of the 2010 activity were: 1) the high level of seismic energy release (about three times the maximum value obtained for the previous eruptions), 2) acceleration in the occurrence rate of VT and MP events, in the release of energy, and in the RSAM values, and 3) complex velocity variations. This behaviour is consistent with an accelerated displacement rate of deformation at the summit measured by EDM. These features were taken as evidence that the impending eruption would be unusually large.

Furthermore the rapid magma migration of about 150 m/day (3 to 9 times higher than that of previous pre-eruptive conditions) observed from hypocenter shifting and deformation suggests that all the unusual precursors and the large magnitude of the eruption itself may be attributed to the large volume of magma involved.

Hindsight Eruption Forecasting

Several observations could be considered as eruption precursors are:

- the behavior change of velocity variations shown by NCF with a time delay toward the eruption (Δt) of ~14 days
- velocity drop shown by multiplets with Δt of ~12 days
- the shift of hypocenter distribution from the deep to shallow zone with Δt of ~10 days
- large energy of low frequency signal with Δt of ~3 days
- the presence of cluster 10 with Δt of ~2 days
- velocity fluctuations interrupted with large VT with Δt of ~1 day.

Those observations would be useful as considerations for evaluating the current state of activity during the future crisis.

Further, we used the Material Failure Forecast Method with seismic and deformation data in order to carry out hindsight eruption forecasting. The best FFM result is obtained using 3 – 5 Hz MRSAM data with fitting window beginning 20 days before the eruption. Starting from 6 days before the eruption, we get very good predicted eruption times with accuracy of less than 4 hours. The successful hindsight forecasts can be associated with the closed or almost closed state of the magmatic system before the eruption. Multiple trials of a posteriori prediction suggest that high precision can be achieved if magma and hypocenter migrations and/or changes of load regime are identified and the forecasting strategy is adapted to these variables.

In the future, if an episode of unrest at Merapi produces an unusually large cumulative seismic energy release with a clearly accelerated rate and if other observables (e.g., deformation or gas emission) present similar behaviour, then a large explosion similar to (or possibly larger than) 2010 should be considered as highly probable. In this case and given that its limitations are well understood, the FFM would be of great value in supporting decisions concerning evacuation.

Future potential studies

Although the general chronological activity has been highlighted by family analysis, studies about the detailed physical mechanism of each cluster are needed in order to obtain a better understanding of the pre-eruptive magma rising behavior.

With regard to the encouraging results related with velocity changes calculations, it would be interesting to study the physical mechanism attributed to these velocity change behaviors. This includes a numerical modeling to study the influence of the position of stations or the line path of the station pairs to the observed velocity change for different locations and or dimensions of the velocity

perturbation. For instance our localization of velocity perturbations is based on the AVV of NCF solely. We believe, combining both the AVV from NCF and multiplets data will improve the localization. Since the location of the multiplet sources are known, we could expect to get more information of AVV closer to the source of velocity perturbation. It would be thus possible to obtain 3-D or 4-D images of velocity perturbations.

Appendix A

Effects of seismogram clipping on velocity changes

It is worth noting that short period stations such as PUS have low dynamic range and thus low clip level. Therefore many records from station PUS were saturated particularly during the last days before the eruption. The velocity variations estimated from multiplets can then be biased due to this problem. This might explain why the results of PUS are less stable than those obtained from the broadband high-dynamic station PAS. On the other hand, we observed that the MWCS method is more sensitive to the saturation of the record than the stretching method. In order to show better this effect, we artificially produced the saturation of the first event of cluster 3 recorded at PAS station. We cut the amplitude at levels corresponding to 2/3, 1/2, and 1/3 of the maximum. We define the corresponding saturation levels of 30%, 50%, and 70% respectively. Velocity variations were then calculated with these modifications using both methods and compared to the results obtained without saturation. As it is shown in Fig. A.1, the stronger saturation the larger deviation of the velocity variation resulted. Although the deviations are observed on both methods, the MWCS method shows much larger deviations as well as errors. It is also interesting to note that the two methods display opposite effects. While the saturation yields a larger velocity with the MWCS method, a slight decrease of the velocity is obtained with the stretching method for the saturated event.

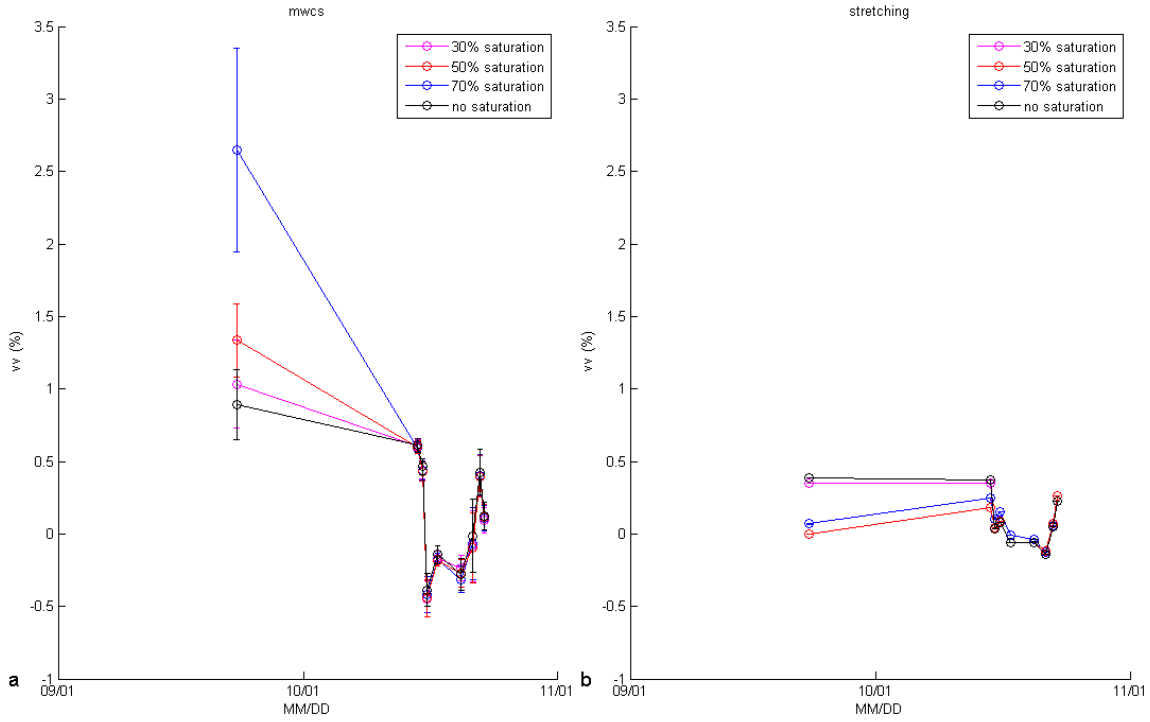

Fig. A.1 Effects of the simulation of saturation on the apparent velocity variation for the first event of cluster 3 at PAS estimated using the MWCS (a) and the stretching methods (b). The first event has saturation level of 0, 30%, 50%, and 70%.

Appendix B

Estimation of the direction of noise source

In case of uniformly distributed noise with respect to a station pair (receiver 1 and 2), it is expected that the noise correlation function (NCF) between both receivers will be a symmetric function. The causal part of the NCF represents the green function from station 1 to station 2 and vice versa because ambient noise sources are distributed on both sides of the station pairs (diffused). If noise energy of one side is dominant, the amplitude will not be symmetry, but the time delay remains symmetric (Fig. B.1). However for predominant noise source, the NCF will not be symmetric, even for the time delay (Sabra et al., 2005).

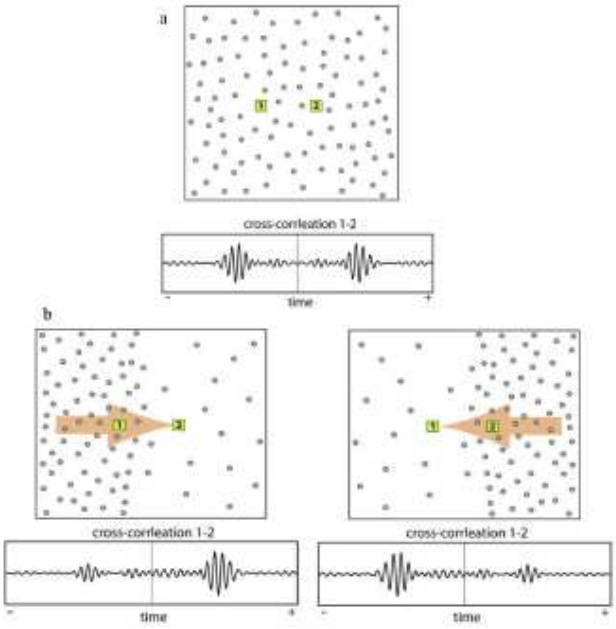

Fig. B.1 Schematic illustration of the effect of inhomogeneous noise sources distribution on the degree of symmetry of cross correlation function. (a) Symmetric cross correlation between 1 and 2 obtained when the sources of noise are evenly distributed. (b) Asymmetric cross correlation (but symmetric travel

times) associated with a nonisotropic distribution of sources (from Stehly et al., 2006).

Regarding the Merapi data, asymmetric NCF were observed for all station pairs (Fig. B.3). The stations used for the calculation and their line path of station pair are showed in Fig. B.2. The time lapses at which the maximum correlation function occur are considered to be the delay time between the noise arrival at the station pair. The resulted delay times (Table B.1) suggest that the NCF is likely dominated by directional noises. Then in this case, the Green function is not well reconstructed. Note that, in case of directional noise, the time delay will be positive if the signal arrives at the later station first and vice versa. It is the opposite in the case of a diffuse noise.

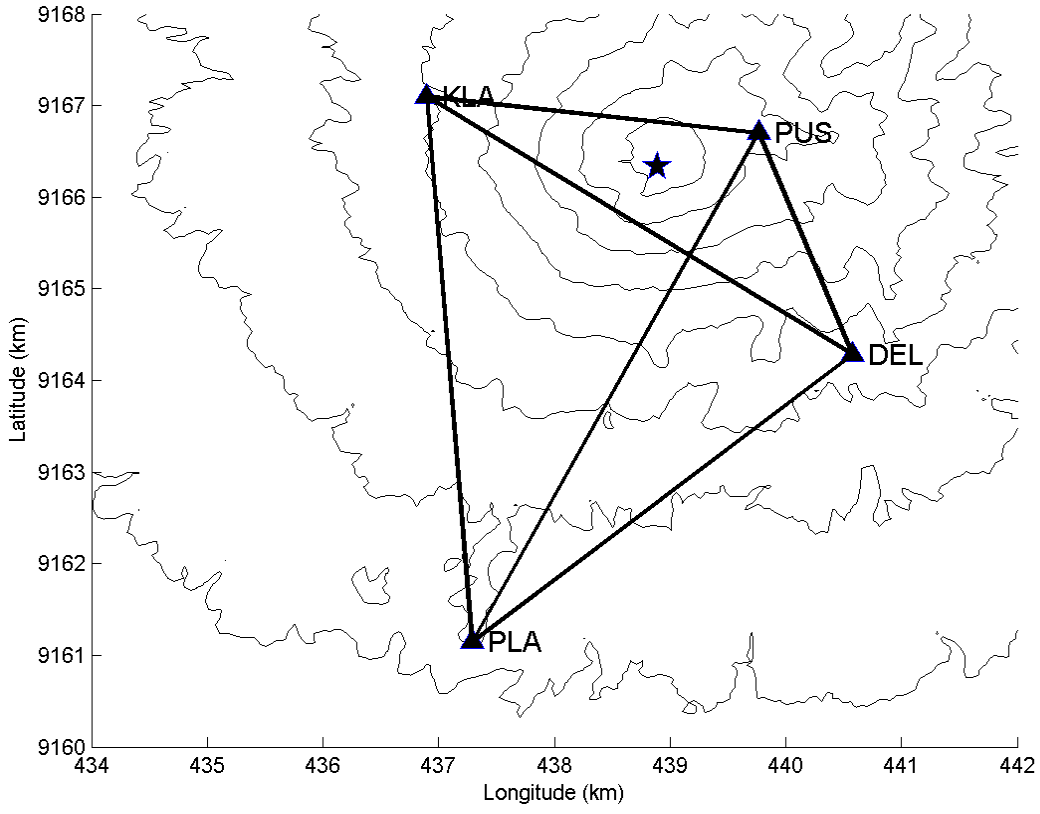

Fig. B.2 Map of the short period station (triangles) network on Merapi and the line paths of the station pairs (black lines). Summit is indicated by a star.

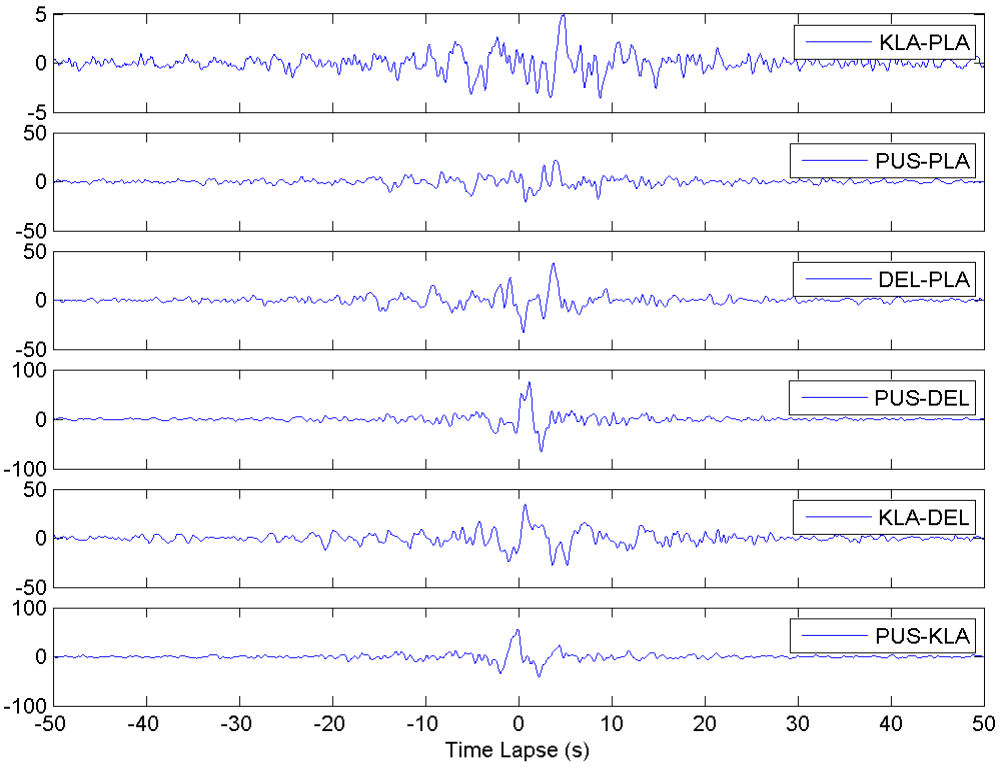

Fig. B.3 NCF obtained from all the station pairs. All their maximum values are located on the causal part except for pair PUS-KLA.

On Table B.1, we can observe that the dominant signals always travel from the southernmost station to the northernmost one. Furthermore although the distance KLA-DEL is larger than that of PUS-DEL, its time delay is smaller. However the projected distance of KLA-DEL on the south direction is much smaller than that of PUS-DEL. Therefore, we suggest that the noise we work with mainly comes from the Indian Ocean which is at the south of Merapi.

Table B.1 Time delays of the maximum correlation between the ballistic part of NCF calculated on each station pair. The distance between station pairs are presented. It appears that there is no correlation between the time delay and the distance between stations. The ratio of the station distance to delay is considered as an apparent velocity. Low apparent velocities are displayed by the station pairs whose line path is in the north-south direction.

Station Pair	Stations distance (km)	Maximum correlation time delay
PUS-KLA	3.0	-0.08
PUS-DEL	2.8	1.28
PUS-PLA	6.2	4.20
KLA-DEL	4.7	0.72
KLA-PLA	6.0	4.88
DEL-PLA	4.5	3.64

In order to determine the azimuth of the noise direction, we performed a simple inversion adopting the method used in array technique (Metaxian et al., 2002). Assuming the distance between noise source and Merapi seismic network is large, we can consider the network as one point meaning that each station records the same noise wavefront (approximation of plane wave). Further we can simplify the network geometry to be two dimensions in order to estimate the azimuth of the noise source. The time delay between stations i and j can be written

$$\tau_{ij} = \mathbf{s} \cdot \mathbf{r}_{ij}$$

Where the dot denotes the usual scalar product, $s = (-s\sin\theta, -s\cos\theta)$ is the slowness vector, θ is the back-azimuth measured clockwise from the north, $r_{ij} = (r_{ij}\sin\phi_{ij}, r_{ij}\cos\phi_{ij})$ is the relative position vector of the station pair line path, r_{ij} and ϕ_{ij} the corresponding distance and azimuth. Given a set of time delays τ_{ij} the slowness vector (s) can be recovered by inversion of a system of linear equations $d = Gm$. Here d is the observed time delays between the station pairs; G is the slowness vector (s); and m is the relative position vector (r_{ij}). Solving 6

sets of equation corresponding to 6 station pairs, we could obtain the slowness vector and the azimuth angle of the noise source as:

$$\phi = \tan^{-1}(r_{ij,y}/r_{ij,x}),$$

where $r_{ij,y} = r_{ij}\sin\phi$ and $r_{ij,x} = r_{ij}\cos\phi$.

A back azimuth of about 20° and a wave velocity of 1.3 km s^{-1} are obtained by the inversion of maximum correlation time lags between the station pairs. The back azimuth leads the direction to the city of Yogyakarta or the Indian Ocean (Fig. B.4). The quality of the inversion solutions is only fair, since it has large residuals of the calculated time delays ranging 0.3s to 0.5s for the different station pairs. Several factors might contribute to these large residuals. Firstly, the assumption of a homogeneous slowness vectors might be not valid. Secondly, the observed time delays do not accurately represent the true arrival time difference between stations, since the local noise could perturb the remote noise.

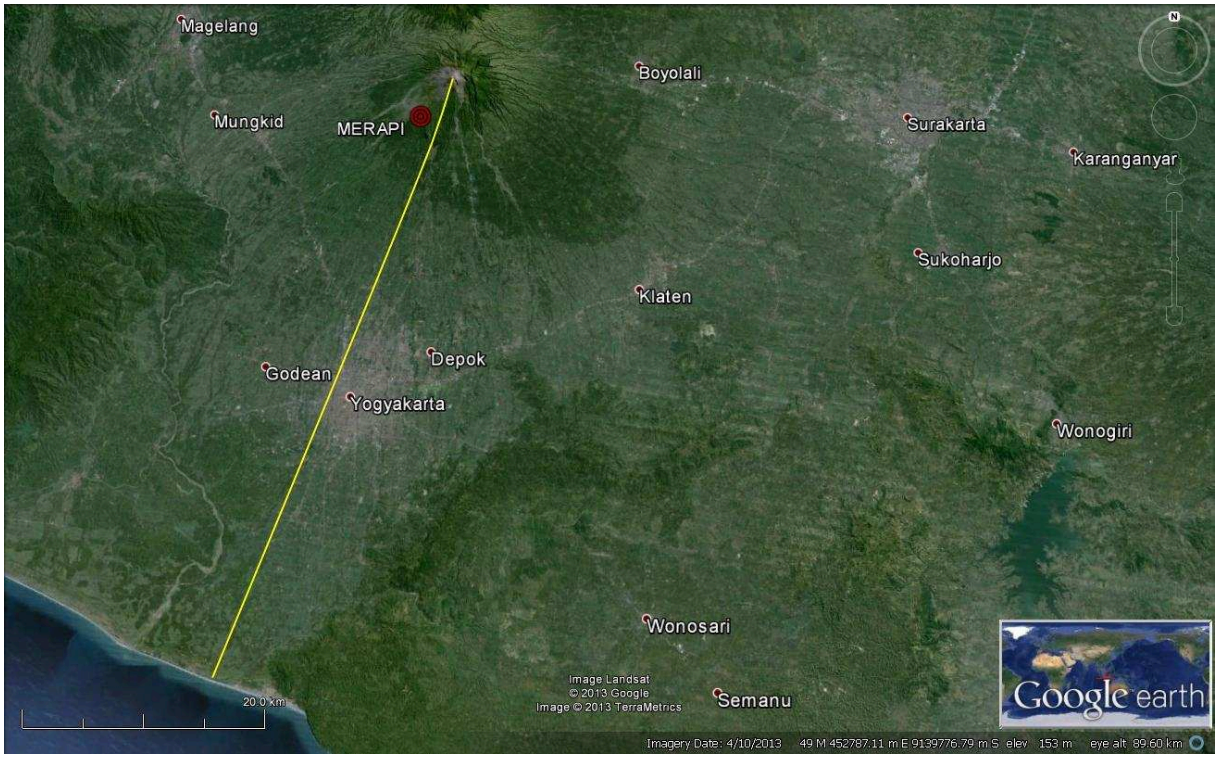

Fig. B.4 Satellite Image of the area showing Merapi volcano and the noise back azimuth angle of 20° which points to the city of Yogyakarta and the Indian Ocean.

In spite of the large residuals, it supports the directional noise. According to Larose (2006), in the case of directional noise source, the wavefront is only partially reconstructed on the anti-causal part of the station pair in the direction to the source or on the causal part of the station pair in opposite direction to the source (Fig. B.5.). Since our station pairs (except for PUS-KLA) is relatively in the direction of the source which is on south direction, for calculating the velocity variation we consider only the anti-causal part except for PUS-KLA for which we take the causal part. Note that, here we used the ballistic wave only to estimate the source position of the noise, whereas, in estimating the velocity variations we used the coda part in the range of 10 – 30 s.

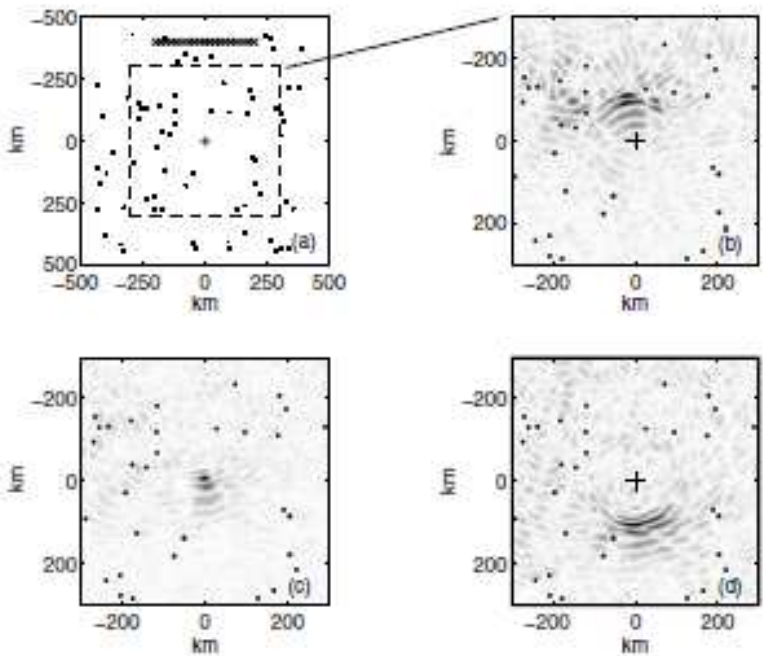

Fig. B.5 Numerical simulation of the asymmetry of the reconstructed GF. (a) 40 sources S are aligned along x-axis (crosses). The reference point is at the center of the plot, indicated by a "+". (b) Snapshot of the cross-correlation between the field in A with the one at location (x,y) after averaging over the sources S for correlation time -30s. The converging wavefront is only partially reconstructed in the direction of the sources. (c) Snapshot for the correlation time t = 0s; the wavefront is focused on A. Note the high level of remaining fluctuations; (d) Snapshot for t = 30s; the diverging wavefront is defined only in the direction opposite to the source region (from Larose, 2006).

Appendix C

Rain correction on AVV of NCF for each station pair

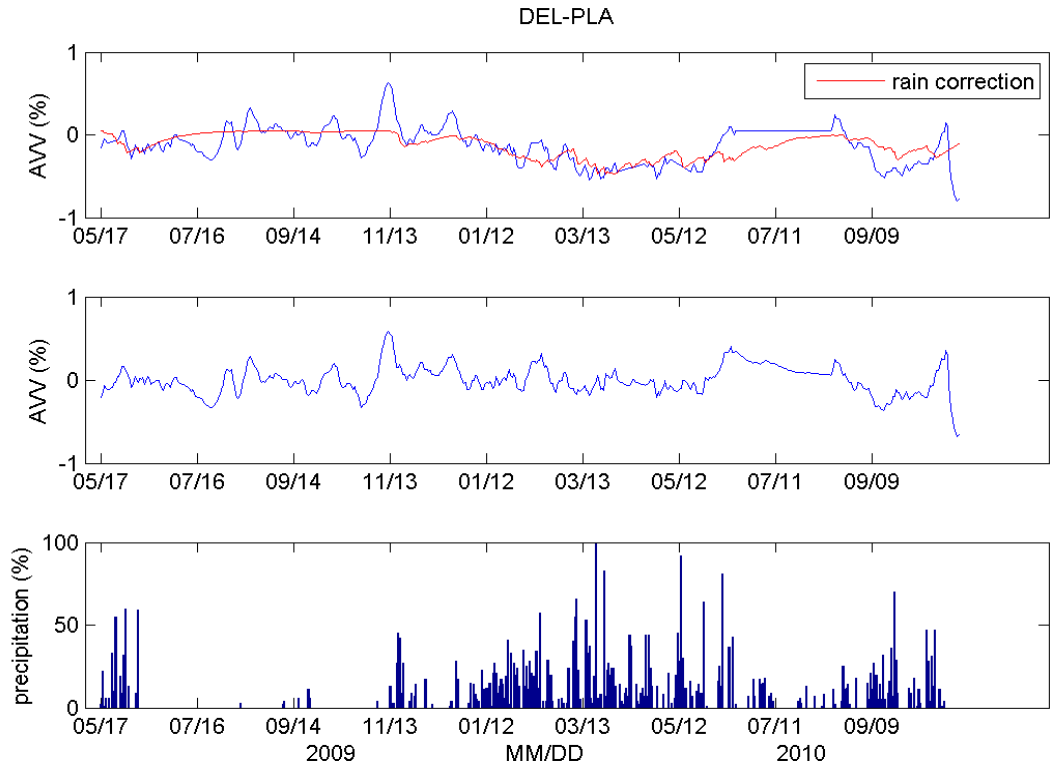

Fig. C.1 (a) The velocity change obtained from DEL-PLA (blue) is overlaid with the fitted Ground Water Level (GWL; red). (b) Corrected AVV obtained subtracting the fitted GWL from AVV. (c) The precipitation data (blue) is taken from Selo Post Observatory from which the GWL curve is generated.

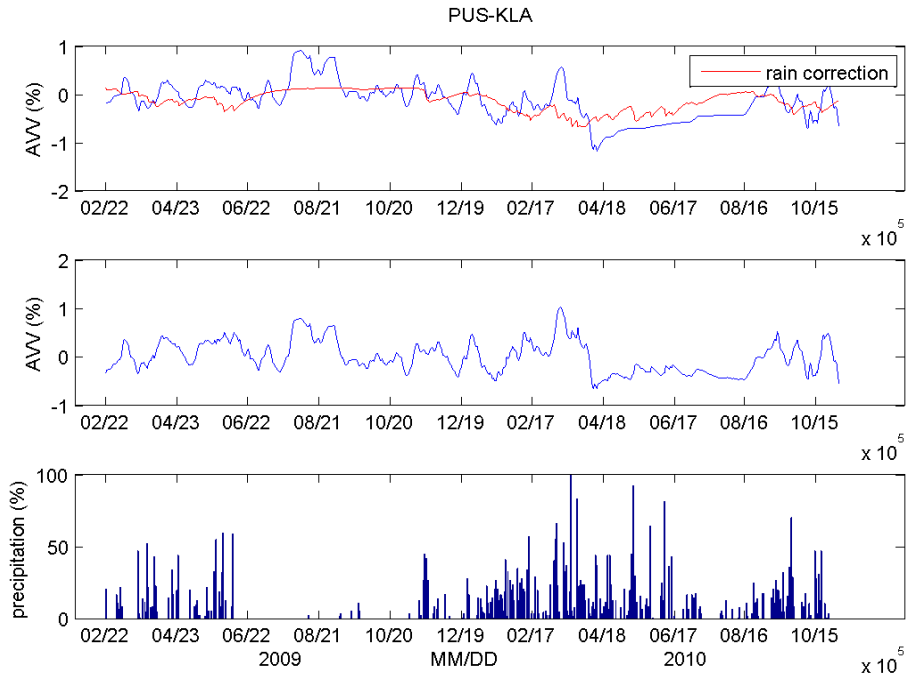

Fig. C.2 Same as Fig. C.1. for the station pair of PUS-KLA

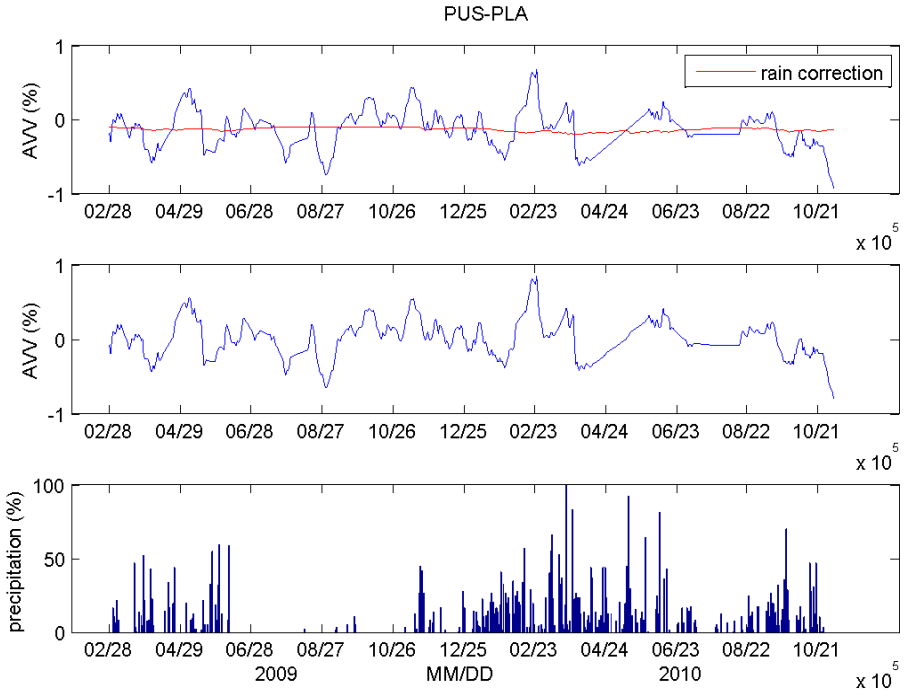

Fig. C.3 Same as Fig. C.1. for the station pair of PUS-PLA

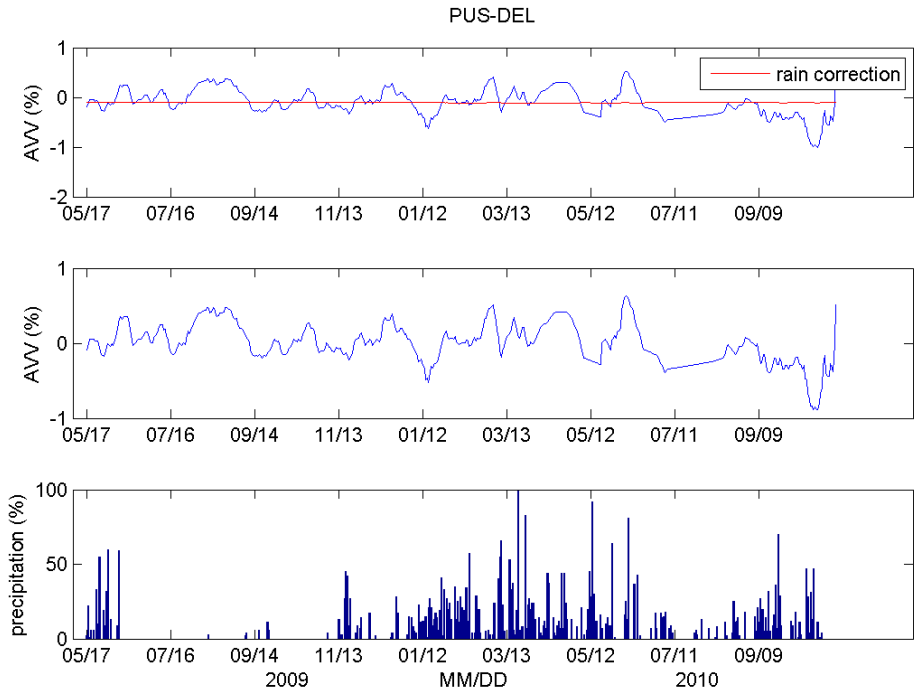

Fig. C.4 Same as Fig. C.1. for the station pair PUS-DEL

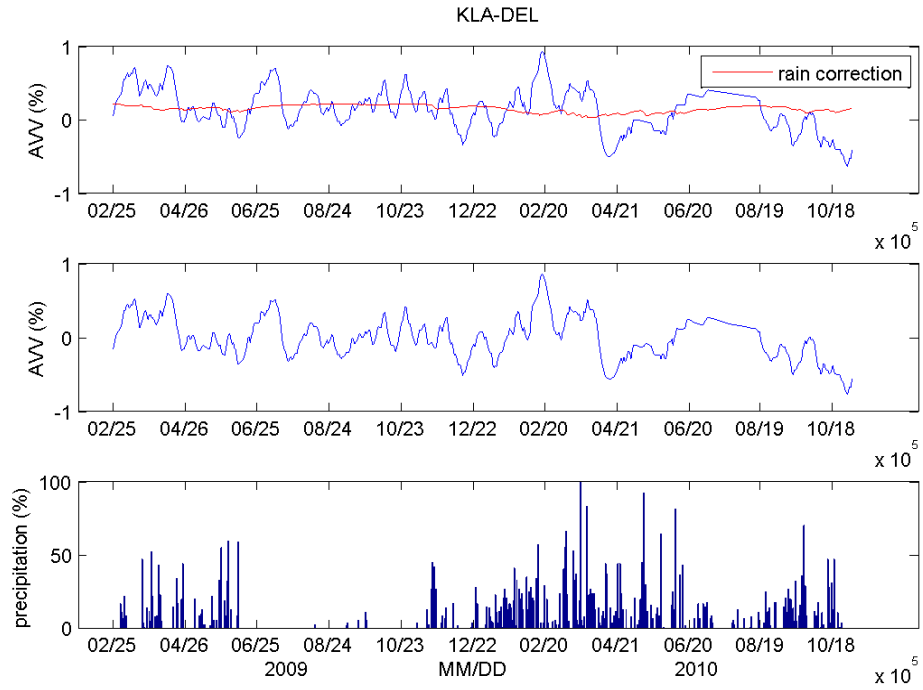

Fig. C.5 Same as Fig. C.1. for the station pair KLA-DEL

Appendix D

Parameter tests for the location of the velocity perturbations and comparison of the calculated and the observed AVV

D.1 Some tests of parameters

For locating the velocity perturbations in 2D, we used mean free path $l^* = 0.1$ km (Wegler and Luhr, 2001) and surface wave velocity $v = 1.3$ km s^{-1} which is resulted from our inversion of noise source direction (Appendix B). Regarding the parameters of correlation length (λ) and a priori standard deviation (σ_m), we determined these values through L-curve criterion (Hansen, 1992). The misfits are plotted as a function of maximal velocity fluctuations in the model, for different values of λ and σ_m. The optimal smoothing is found for minimized values on both axes, which correspond to a maximal bending of the curve (Obberman et al, 2013).

The values of the various parameters used in the inversion were chosen after carrying out a series of tests. In this appendix we represent some figures related with our tests. The first set of figures (Fig. D.1) show maps of VV using the same values of $\lambda = 1$ km with varying σ_m of 0.05, 0.1, and 0.5 km. The second set (Fig. D.2) corresponds to fixed value of $\sigma_m = 0.1$ and λ of 0.6 and 1.5 km. For both set of figures, the pre-defined values l^* and v are used. Fig. D.1b that corresponds to $\lambda = 1$ and $\sigma_m = 0.1$ shows the best trade-off between the strength of the velocity change and the smoothness.

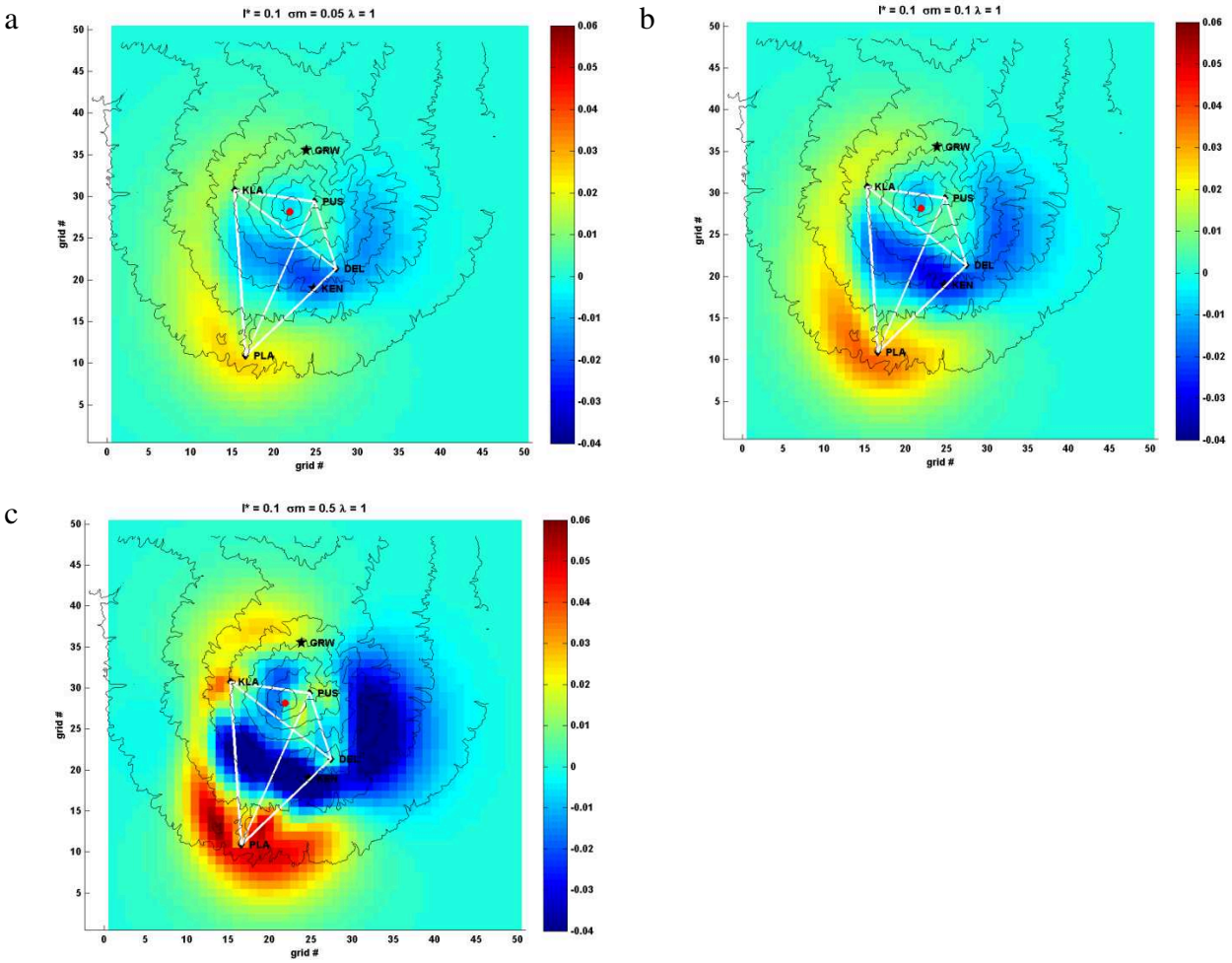

Fig. D.1 Location of velocity change for the date of 21 October 2010 with a reference date of 12 October 2010 using parameters values of l^* = 0.1 km; v = 1.3km s^{-1}, λ = 1 km ; and varying σ_m of 0.05 (a), 0.1 (b), and 0.5 (c).

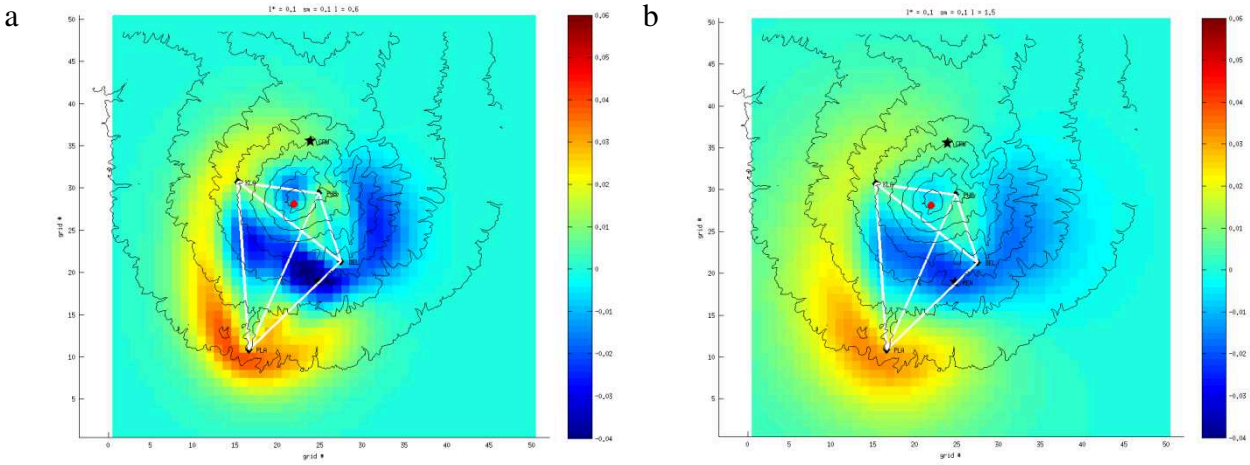

Fig. D.2 Same as Fig. D.1 using parameters values of l^* = 0.1 km; v = 1.3 km s^{-1}; σ_m = 0.1 km ; and varying λ of 0.6 (a) and 1.5 km (b).

We also performed tests for different values of l* and v. Some of the corresponding maps of VV are represented in Fig. D.3 and Fig. D.4 respectively. Smaller l* of 0.05 leads to VV that is too squeezed around the seismic network, whereas, higher l* of 1 km causes the VV to spread out.

a b

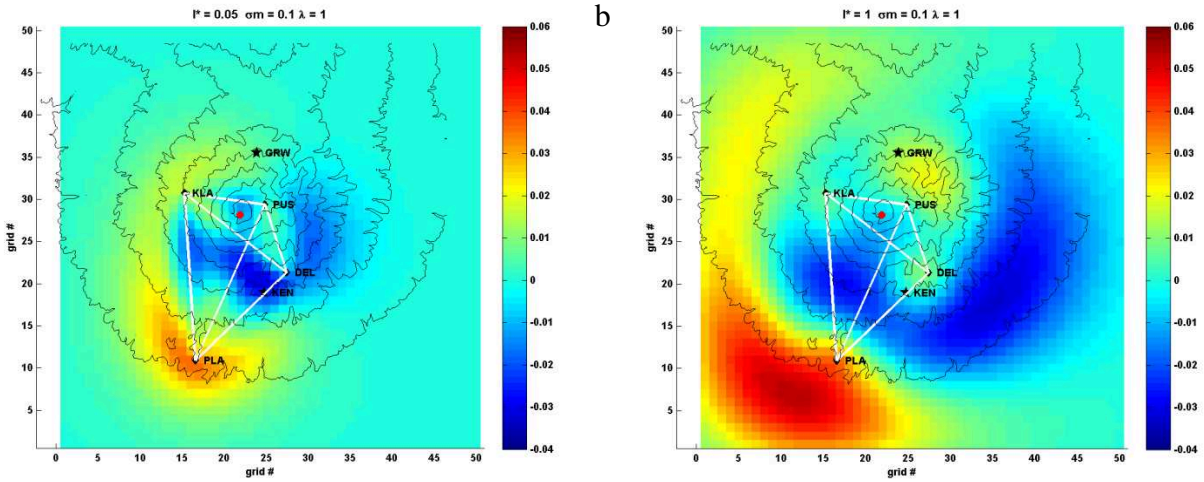

Fig. D.3 Same as Fig. D.1 using parameters values of λ = 1 km; v = 1.3 km s^{-1}; σ_m = 0.1 km ; and varying l* of 0.05 (a) and 1 km (b).

a b

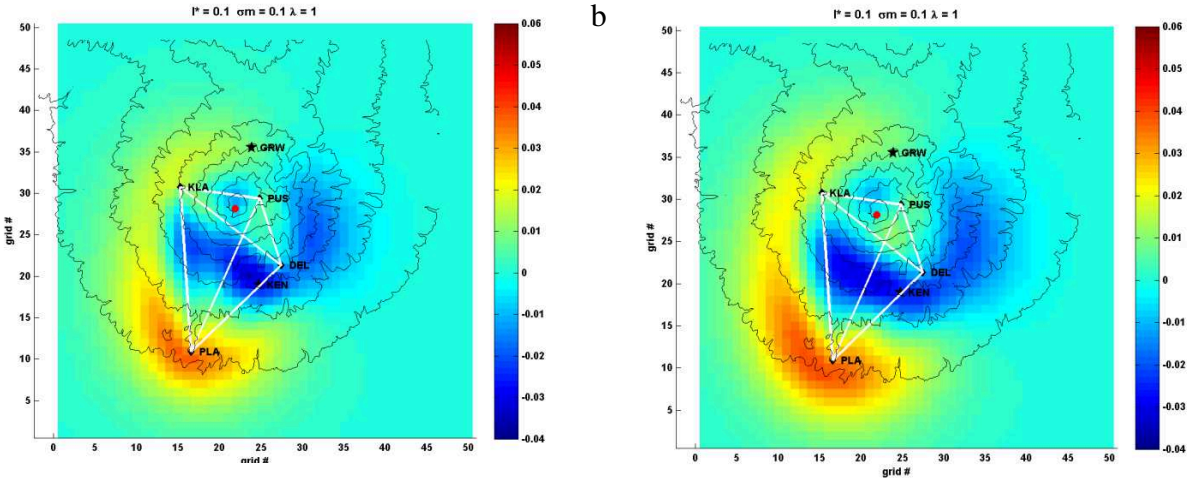

Fig. D.4 The same as Fig. D.1 using parameters values of l* = 0.1 km; λ = 1 km; σ_m = 0.1 km ; and varying v of 1 (a) and 2 km s^{-1} (b).

D.2 Comparison of the calculated and observed AVV

The figures below represent the calculated VV overlaid with their corresponding observed AVV for the 3 last stages of 23 October (Fig. D.5), 25 October (Fig. D.6), and 3 November (Fig. D.7). The first stage is already presented in chapter 6. In general these figures show good fitting.

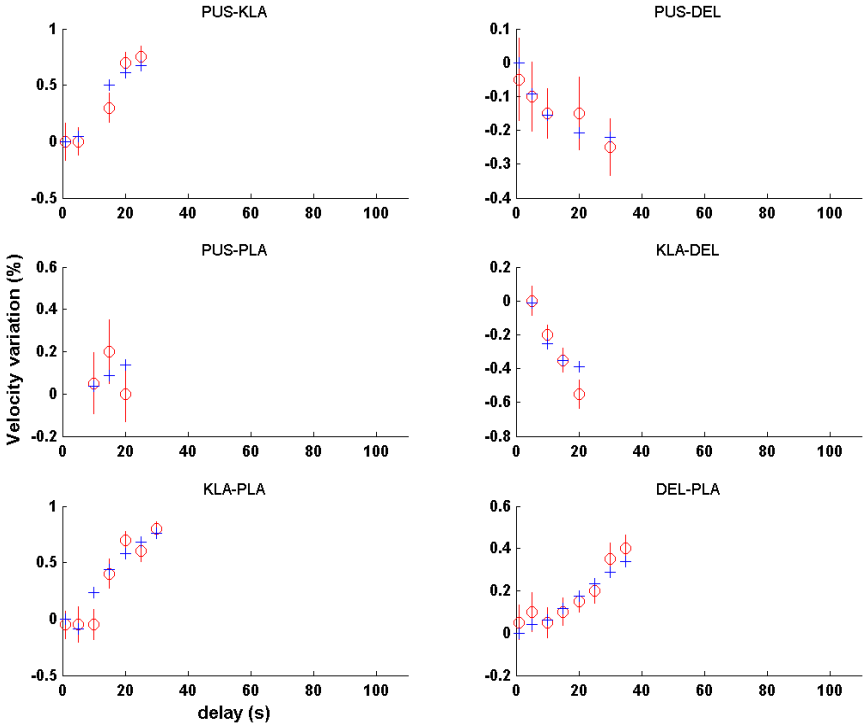

Fig. D.5 Modelled AVV (blue crosses) and measured AVV (red circles with error bars) of each station pairs at different time lags for the stage of 23 October.

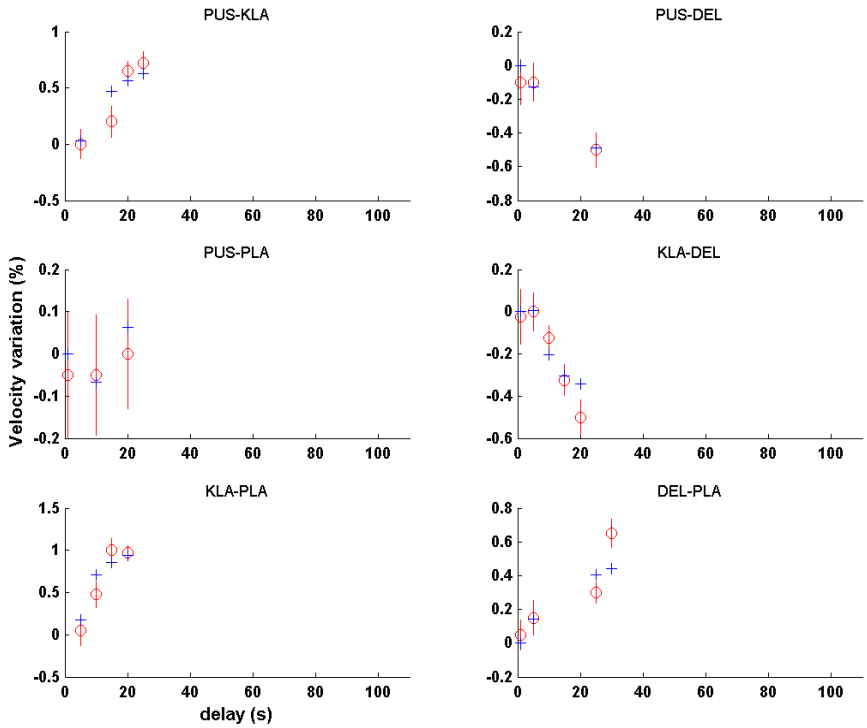

Fig. D.6 The same as Fig. D.5 for the stage of 25 October

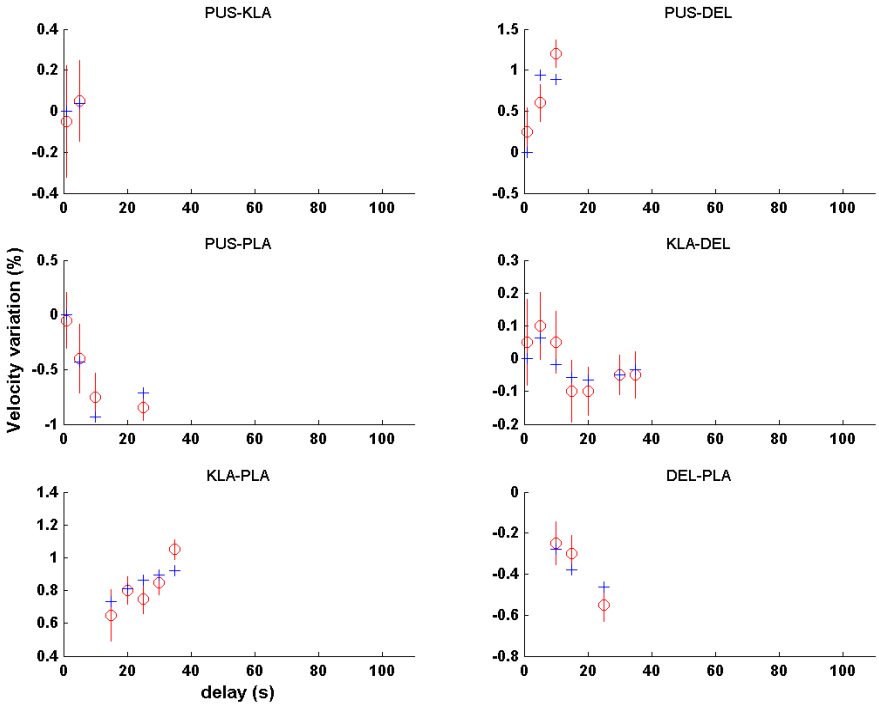

Fig. D.7 The same as Fig. D.5 for the stage of 3 November

References

Aisyah, N., Sumarti, S., Sayudi, D.S., Budi-Santoso, A., Muzani, M., Dwiyono, S., Sunarto, Kurniadi, 2010. Aktivitas G. Merapi Periode September – Desember 2010 (Erupsi G. Merapi 26 Oktober – 7 November 2010). Balai Penyelidikan dan Pengembangan Teknologi Kegunungapian, Bulletin Berkala Merapi, 07/03.

Akaike, H., 1998. Markovian Representation of Stochastic Processes and Its Application to the Analysis of Autoregressive Moving Average Processes, in: Parzen, E., Tanabe, K., Kitagawa, G. (Eds.), Selected Papers of Hirotugu Akaike, Springer Series in Statistics. Springer New York, pp. 223–247.

Akram, J., & Eaton, D. 2012. Adaptive microseismic event detection and automatic time picking. 2012 CSEG Annual Convention. (pp. 1–5). Calgary.

Allen, R., 1978. Automatic earthquake recognition and timing from single traces. Bulletin of the Seismological Society of America, 68, 1521-1532.

Anderson, O.L., Oda, H., Isaak, D., 1992. A model for the computation of thermal expansivity at high compression and high temperatures: MGO as an example. Geophysical Research Letters 19, 1987–1990.

Anggono, T., Nishimura, T., Sato, H., Ueda, H., Ukawa, M., 2012. Spatio-temporal changes in velocity associated with 2000 activity of Miyakejima volcano as inferred from cross-correlation analyses of ambient noise, Journal of Volcanology and Geothermal Research 247–248 (2012) 93–107.

Arámbula-Mendoza, R., Lesage, Ph., Valdés-González, C., Varley, N.R., Reyes-Dávila, G., Navarro, C., 2011. Seismic activity that accompanied the effusive and explosive eruptions during the 2004-2005 period at Volcán de Colima, Mexico, Journal Volcanology and Geothermal Research, 205, 30-46, doi:10.1016/j.jvolgeores.2011.02.009.

Arsadi, E., Suparta, S., Nishimura, S., 1995. Subsurface structure of Merapi inferred from magnetotelluric, gravimetric and geomagneticsurveys. Merapi Volcano Decade International Workshop, Yogyakarta, October.

Beauducel, F., Cornet F.H., Suhanto E., Duquesnoy, T., Kasser, M., 2000. Constraints on magma flux from displacements data at Merapi volcano, Java. Journal of Geophysical Research, 105, 8193-8204.

Beauducel, F., Cornet, F.-H., 1999. Collection and three-dimensional modeling of GPS and tilt data at Merapi volcano, Java. Journal of Geophysical Research, 104(B1), 725-736.

Beisser, M., Erzinger, J., Westerhaus, M., Zimmer, M., Zschau, J. (1996): MERAPI: Ein Hochrisikovulkan als Labor der Geowissenschaften - In: Zweijahresbericht / Geoforschungszentrum Potsdam; 1994/1995, Geoforschungszentrum, 69-77.

Bell A. F., Greenhough J., Heap M. J., Main I. G., 2011a. Challenges for forecasting based on accelerating rates of earthquakes at volcanoes and laboratory analogues, Geophysical Journal International, 185, 718-723.

Bell A. F., Naylor M., Heap M. J., Main I. G., 2011b. Forecasting volcanic eruptions and other material failure phenomena: An evaluation of the failure forecast method, Geophysical Research Letter, 38, L15304, doi:10.1029/2011GL048155.

Benoit, J.P., McNutt, S.R., Barboza, V., 2003. Duration-amplitude distribution of volcanic tremor. Journal of Geophysical Research: Solid Earth 108, n/a–n/a.

Berthommier, P., Camus, G., Condomines, M., Vincent, P.-M.,1990. Le Merapi (Centre Java): Eléments de chronologie d'un strato-volcan andésitique. Comptes rendus de l'Académie des Sciences Paris 311 (II), 213–218.

Bignami, C., Ruch, J., Chini, M., Neri, M., Buongiorno, M.F., Hidayati, S., Sayudi, D.S., Surono, 2013. Pyroclastic density current volume estimation after the 2010 Merapi volcano eruption using X-band SAR. Journal of Volcanology and Geothermal Research 261, 236–243.

Boué, A., Lesage, P., Cortés, G., Benítez, C., Ibáñez, J., Alvarez, I., De La Torre, A., Gutierrez, L., Arámbula, R., González-Amézcua, M., Reyes-Dávila, G., 2012. Improving the Material Failure Forecast Method (FFM) for eruption prediction by automatic classification of volcano-seismic signals. Cities on Volcanoes 7, Colima, Mexique.

Boué A., Lesage P., Cortés G., Benítez M.C., Ibáñez J., Alvarez I., de la Torre A., Gutierrez L., Arámbula R., González-Amézcua M., Reyes-Dávila G., 2013. Automatic classification of seismo-volcanic signals as a tool to improve eruption forecasting. IAVCEI Scientific Assembly, Kagoshima.

Borisova, A.Y., Martel, C., Gouy, S., Pratomo, I., Sumarti, S., Toutain, J.-P., Bindeman, I.N., de Parseval, P., Metaxian, J.-P., Surono, 2013. Highly explosive 2010 Merapi eruption: Evidence for shallow-level crustal assimilation and hybrid fluid. Journal of Volcanology and Geothermal Research 261, 193–208.

Brenguier, F., Shapiro, N.M., Campillo, M., Ferrazzini, V., Duputel, Z., Coutant, O., Nercessian, A., 2008. Towards forecasting volcanic eruptions using seismic noise. Nature Geosci 1, 126–130.

Budi-Santoso, A., Lesage, P., Dwiyono, S., Sumarti, S., Subandriyo, Surono, Jousset, P., Metaxian, J.-P., 2013. Analysis of the seismic activity associated with the 2010 eruption of Merapi Volcano, Java. Journal of Volcanology and Geothermal Research 261, 153–170.

Burton, M., Allard, P., Muré, F., Spina, A.L., 2007. Magmatic Gas Composition Reveals the Source Depth of Slug-Driven Strombolian Explosive Activity. Science 317, 227–230.

Byrdina, S., Friedel, S., Wassermann, J., Zlotnicki, J., 2003. Self-potential variations associated with ultra-long-period seismic signals at Merapi volcano. Geophysical Research Letters 30, n/a–n/a.

Byrdina, S., Rücker, C., Zimmer, M., Friedel, S., Serfling, U., 2012. Self potential signals preceding variations of fumarole activity at Merapi volcano, Central Java. Journal of Volcanology and Geothermal Research 215-216, 40–47.

Campillo, M., 2006. Phase and correlation in 'random' seismic fields and the reconstruction of the Green's function. Pure and Applied Geophysics, 163, 475-502.

Camus, G., Gourgaud, A., Mossand-Berthommier, P.C., Vincent, P.M., 2000. Merapi (Central Java, Indonesia): an outline of the structural and magmatological evolution, with a special emphasis ti the major pyroclastic events, Journal of Volcanology and Geothermal Research, 100:139-163. Doi:10.1016/S0377-0273(00)00135-9

Cannata, A., 2012. Crustal changes at Mt. Etna volcano accompanying the 2002-2003 eruption as inferred from a repeating earthquake analysis. Geophysical Research Letters.

Cannata, A., Alparone, S., Ursino, A., 2013. Repeating volcano-tectonic earthquakes at Mt. Etna volcano (Sicily, Italy) during 1999–2009. Gondwana Research 24, 1223–1236.

Cattaneo, M., Augliera, P., Spallarossa, D., Lanza, V., 1999. A Waveform Similarity Approach to Investigate Seismicity Patterns. Natural Hazards 19, 123–138.

Charbonnier, S.J., Germa, A., Connor, C.B., Gertisser, R., Preece, K., Komorowski, J.-C., Lavigne, F., Dixon, T., Connor, L., 2013. Evaluation of the impact of the 2010 pyroclastic density currents at Merapi volcano from high-resolution satellite imagery, field investigations and numerical simulations. Journal of Volcanology and Geothermal Research 261, 295–315.

Chen, K.H., Rau, R.-J., Hu, J.-C., 2009. Variability of repeating earthquake behavior along the Longitudinal Valley fault zone of eastern Taiwan. Journal of Geophysical Research: Solid Earth 114, n/a–n/a.

Chouet, B. ,1988. Resonance of a ?uid driven crack: Radiation properties and implications for the source of long-period events and harmonic tremor, Journal of Geophysical Research, 93, 4375–4400.

Chouet, B., 1996. Long-period volcano seismicity: its source and use in eruption forecasting. Nature, 380, 309-316.

Chouet, B., Dawson P., Arciniega-Ceballos, A., 2005. Source mechanism of Vulcanian degassing at Popocatépetl Volcano, Mexico, determined from waveform inversions of very long period signals, Journal of Geophysical Research, 110, B07301, doi:10.1029/2004JB003524.

Clarke, D., Zaccarelli, L., Shapiro, N.M., Brenguier, F., 2011. Assessment of resolution and accuracy of the Moving Window Cross Spectral technique for monitoring crustal temporal variations using ambient seismic noise. Geophysical Journal International 186, 867–882.

Commer, M., Helwig, S.L., Hördt, A., Scholl, C., Tezkan, B., 2006. New results on the resistivity structure of Merapi Volcano (Indonesia), derived from three-dimensional restricted inversion of long-offset transient electromagnetic data. Geophysical Journal International, 167, 1172-1187.

Cornelius RR, Voight B, 1995. Graphical and PC-software analysis of volcano eruption precursors according to the Materials Failure Forecast Method (FFM). Journal of Volcanology and Geothermal Research, 64, 295–320

Cornelius, R.R., Voight, B., 1994. Seismological aspects of the 1989-1990 eruption at Redoubt volcano, Alaska: the materials failure forecast method (FFM) with RSAM and SSAM seismic data. Journal of Volcanology and Geothermal Research, 62, 469-498.

Costa, F., Andreastuti, S., Bouvet de Maisonneuve, C., Pallister, J.S., 2013. Petrological insights into the storage conditions, and magmatic processes that yielded the centennial 2010 Merapi explosive eruption. Journal of Volcanology and Geothermal Research 261, 209–235.

Cronin, S.J., Lube, G., Dayudi, D.S., Sumarti, S., Subrandiyo, S., Surono, 2013. Insights into the October–November 2010 Gunung Merapi eruption (Central Java, Indonesia) from the stratigraphy, volume and characteristics of its pyroclastic deposits. Journal of Volcanology and Geothermal Research 261, 244–259.

Damby, D.E., Horwell, C.J., Baxter, P.J., Delmelle, P., Donaldson, K., Dunster, C., Fubini, B., Murphy, F.A., Nattrass, C., Sweeney, S., Tetley, T.D., Tomatis, M., 2013. The respiratory health hazard of tephra from the 2010 Centennial eruption of Merapi with implications for occupational mining of deposits. Journal of Volcanology and Geothermal Research 261, 376–387.

De Bélizal, E., Lavigne, F., Hadmoko, D.S., Degeai, J.-P., Dipayana, G.A., Mutaqin, B.W., Marfai, M.A., Coquet, M., Mauff, B.L., Robin, A.-K., Vidal, C., Cholik, N., Aisyah, N., 2013. Rain-triggered lahars following the 2010 eruption of Merapi volcano, Indonesia: A major risk. Journal of Volcanology and Geothermal Research 261, 330–347.

De la Cruz-Reyna S., Reyes-Dávila, G. A., 2001. A model to describe precursory material-failure phenomena: applications to short-term forecasting at Colima volcano, Mexico Bulletin of Volcanology, 63,297–308

Deichmann, N., Garcia-Fernandez, M., 1992. Rupture geometry from high-precision relative hypocentre locations of microearthquake clusters. Geophysical Journal International 110, 501–517.

Dunn, M.M., 2004. Relocation of Eastern Tennessee Earthquakes Using hypoDD [WWW Document]. URL http://scholar.lib.vt.edu/theses/available/etd-08162004-152254/ (accessed 1.14.14).

Endo, E. T., Murray, T.L., 1991. Real-time Seismic Amplitude Measurement (RSAM): A volcano monitoring and prediction tool, Bulletin of Volcanology, 53, 533– 545.

Endo, E.T., Murray, T.L., Power, J.A. 1996, A comparison of preeruption real-time seismic amplitude measurements for eruptions at Mount St. Helens, Redoubt volcano, Mount Spurr, and Mount Pinatubo. In Newhall, C.G., Punongbayan, R.S., Fire and Mud: Eruptions and lahars of Mount Pinatubo, Philippines. Philippine Institute of Volcanology and Seismology and University of Washington Press, Seattle, 233-247.

Ferretti, D.F., Miller, J.B., White, J.W.C., Etheridge, D.M., Lassey, K.R., Lowe, D.C., Meure, C.M.M., Dreier, M.F., Trudinger, C.M., Ommen, T.D. van, Langenfelds, R.L., 2005. Unexpected Changes to the Global Methane Budget over the Past 2000 Years. Science 309, 1714–1717.

Friedel, S., Brunner, I., Jacobs, F. & Rücker, C., 2000. New Results from DC Resistivity Imaging along the Flanks of Merapi Volcano. In: Decade volcanos under investigation (Hrsg. Buttkus, B., Greinwald, S. & Ostwald, J.), Mitteilungen der Deutschen Geophysikalischen Gesellschaft, Sonderband IV/2000, 23-29. Deutsche Geophysikalische Gesellschaft. ISSN 0947-1944.

Friedel, S., Byrdina, S., Jacobs, F., Zimmer, M., 2004. Self-potential and ground temperature at Merapi volcano prior to its crisis in the rainy season of 2000–2001. Journal of Volcanology and Geothermal Research 134, 149–168.

Froment, B., 2011. Utilisation du bruit sismique ambiant dans le suivi temporel de structures géologiques. Université de Grenoble.

Fukuzono T, Terashima H , 1985. Experimental study of slope failure in cohesive soils caused by rainfall. In: Int Symp on Erosion, Debris Flow and Disaster Prevention. Tsukuba, Japan

Gambino, S., Cammarata, L., Rapisarda, S., 2009. High precision locations of long-period events at La Fossa Crater (Vulcano Island, Italy). Ann. Geophys. 52, 137–147.

Gentili, S., Michelini, A., 2006. Automatic picking of P and S phases using a neural tree. J Seismol 10, 39–63.

Giggenbach, W.F., Goguel, R.L., Division, N.Z.D. of S. and I.R.C., 1989. Collection and Analysis of Geothermal and Volcanic Water and Gas Discharges. Chemistry Division, Department of Scientific and Industrial Research.

Got J.L., Monteiller V., Guilbert J., Marsan D., Cansi Y., Maillard C., Santoire J.P, 2011. Strain localization and fluid migration from earthquake relocation and seismicity analysis in the western Vosges (France), Geophysical Journal International, 185, 365-384.

Gutenberg, B., Richter, C.F., 1956. Earthquake Magnitude, Intensity, Energy and Acceleration (second paper), Bulletin of Seismological Society of America, 46, 2, 105-146.

Hadziioannou, C., 2011. Ondes sismiques en milieu complexe?: mesure des variations temporelles des vitesses. Université de Grenoble, UNIVERSITE DE GRENOBLE.

Hadziioannou, C., Larose, E., Coutant, O., Roux, P., Campillo, M., 2009. Stability of Monitoring Weak Changes in Multiply Scattering Media with Ambient Noise Correlation: Laboratory Experiments. arXiv:0904.3384 [physics].

Hamilton, W.B., 1979. Tectonics of the Indonesian region (No. PP - 1078). United States Geological Survey.

Han, L., Wong, J., C. Bancroft, J., and R. Stewart, R., 2008. Automatic time picking and velocity determination on full waveform sonic well logs. In: CREWES Research Report Volume 20.

Hansen, B.E., 1992. Testing for parameter instability in linear models. Journal of Policy Modeling 14, 517–533.

Hidayat, D., Chouet, B., Voight, B., Dawson, P. Ratdomopurbo, A., 2002. Source mechanism of very-long-period signals accompanying dome growth activity at Merapi volcano, Indonesia. Geophysical Research Letter, 29, 23, 2118, doi:10.1029/2002GL015013.

Hidayat, D., Voight, B., Langston, C., Ratdomopurbo, A., Ebeling, C., 2000. Broadband seismic experiment at Merapi Volcano, Java, Indonesia: very-long-period pulses embedded in multiphase earthquakes. Journal of Volcanology and Geothermal Research, 100, 215-231.

Hidayati, S., Ishihara, K., Iguchi, M., Ratdomopurbo, A., 2008. Focal mechanism of volcano-tectonic earthquakes at Merapi volcano, Indonesia. Indonesian Journal of Physics, 19(3): 75-82.

Innocenti, S., Andreastuti, S., Furman, T., del Marmol, M.-A., Voight, B., 2013. The pre-eruption conditions for explosive eruptions at Merapi volcano as revealed by crystal texture and mineralogy. Journal of Volcanology and Geothermal Research 261, 69–86.

Jackson, J.E., 1988. A users guide to principal components, Wiley.

Jenkins, S., Komorowski, J.-C., Baxter, P.J., Spence, R., Picquout, A., Lavigne, F., Surono, 2013. The Merapi 2010 eruption: An interdisciplinary impact assessment methodology for studying pyroclastic density current dynamics. Journal of Volcanology and Geothermal Research 261, 316–329.

Johnson, J.B., Lees, J.M., Gerst, A., Sahagian, D., Varley, N., 2008. Long-period earthquakes and co-eruptive dome inflation seen with particle image velocimetry. Nature 456, 377–381.

Jolly, A., Neuberg J., Jousset P., Sherburn S., 2012. New source process for evolving repetitious earthquakes at Ngauraohoe volcano, New Zealand. Journal of Volcanology and Geothermal Research, 215-216, 26-36, doi:10.1016/j.jvolgeores.2011.11.010.

Jousset, P., Budi-Santoso, A., Jolly, A.D., Boichu, M., Surono, Dwiyono, S., Sumarti, S., Hidayati, S., Thierry, P., 2013. Signs of magma ascent in LP and VLP seismic events and link to degassing: An example from the 2010 explosive eruption at Merapi volcano, Indonesia. Journal of Volcanology and Geothermal Research 261, 171–192.

Juan I. Sabbione, D.V., 2010. Automatic first-breaks picking: New strategies and algorithms. Geophysics 75.

Küperkoch, L., Meier, T., Lee, J., Friederich, W., Working Group, E., 2010. Automated determination of P-phase arrival times at regional and local distances using higher order statistics. Geophysical Journal International 181, 1159–1170.

Kieffer, S.W., 1984. Seismicity at Old Faithful Geyser: an isolated source of geothermal noise and possible analogue of volcanic seismicity. Journal of Volcanology and Geothermal Research 22, 59–95.

Kitamura, K., Masuda, K., Takahashi, M., Nishizawa, O., 2006. The influence of pore fluids on seismic wave velocities under high temperature and high pressure conditions: Development of a new technique with gas apparatus at AIST, Japan. Earth, Planets, and Space 58, 1515–1518.

Kilburn, C.R.J., 2003. Multiscale fracturing as a key to forecasting volcanic eruption. Journal of Volcanology and Geothermal Research, 125, 271-289.

Kilburn, C.R.J., Voight, B., 1998. Slow rock fracture as eruption precursor at Soufriere Hills volcano, Montserrat. Geophysical Research Letter, 25, 3665-3668.

Klein, F. W., 1978. Hypocenter location program HYPOINVERSE; Part I: Users guide to Versions I, 2, 3, and 4, U.S. Geol. Surv., Open-File Rep. 78-649,113 pp.

Komorowski, J.-C., Jenkins, S., Baxter, P.J., Picquout, A., Lavigne, F., Charbonnier, S., Gertisser, R., Preece, K., Cholik, N., Budi-Santoso, A., Surono, 2013. Paroxysmal dome explosion during the Merapi 2010 eruption: Processes and facies relationships of associated high-energy pyroclastic density currents. Journal of Volcanology and Geothermal Research 261, 260–294.

Konstantinou, K.I., Schlindwein, V., 2002. Nature, wavefield properties and source mechanism of volcanic tremor: a review. Journal of Volcanology and Geothermal Research, 119, 161-187.

Koulakov I. Jakovlev A.,, Lühr B.G., 2009. Anisotropic structure beneath central Java from local earthquake tomography, Geochemistry Geophysics Geosystems., 10, Q02011, doi:10.1029/2008GC002109.

Koulakov, I., Bohm, M., Asch, G., Lühr, B.-G., Manzanares, A., Brotopuspito, K.S., Fauzi, P., Purbawinata, M.A., Puspito, N.T., Ratdomopurbo, A., Kopp, H., Rabbel, W., Shevkunova, E., 2007. P and S velocity structure of the crust and the upper mantle beneath central Java from local tomography inversion. Journal of Geophysical Research, 112(B8), B08310, doi: 10.1029/2006JB004712.

Koyanagi R.Y. and Kojima, G., 1984. Evaluation of the radio telemetered network at Merapi Volcano Observatory. USGS-HVO, Hawai.

Kurz, J.H., Grosse, C.U., Reinhardt, H.-W., 2005. Strategies for reliable automatic onset time picking of acoustic emissions and of ultrasound signals in concrete. Ultrasonics 43, 538–546.

Kusumadinata, K., Hadian, R., Hamidi, S. and Reksowirogo, L.D., 1979. Data dasar Gunung api Indonesia. Catalogue of references on Indonesian Volcanoes with Eruptions in Historical Time, VSI, Bandung 820 pp.

Lühr, B.-G., Maercklin, N., Rabbel, W., Wegler, U., 1998. Active seismic measurements at the Merapi Volcano, Java, Indonesia. Mitteilungen der Deutschen Geophysikalischen Gesellschaft, III, 53-56.

Lahr, J.C., 1999. HYPOELLIPSE: A computer program for determining local earthquake hypocentral parameters, magnitude and first-motion patterns. U.S. Geological Survey Denver Federal Center, Denver, USA, Open-file report 99-23, paper (112 pp.) and online (http:// greenwood.cr.usgs.gov/pub/open-file-reports/ofr-99-0023).

Lahr, J.C., Chouet, B.A., Stephens, C.D., Power, J.A., Page, R.A., 1994. Earthquake classification, location, and error analysis in a volcanic environment: implications for the magmatic system of the 1989-1990 eruptions at redoubt volcano, Alaska. United States Geological Survey.

Lance, G.N., Williams, W.T., 1966. Computer Programs for Hierarchical Polythetic Classification ("Similarity Analyses"). The Computer Journal 9, 60–64.

Larose, E., Hall, S., 2009. Monitoring stress related velocity variation in concrete with a 2 x 10(-5) relative resolution using diffuse ultrasound. J. Acoust. Soc. Am. 125, 1853–1856.

Lee, W.H.K. and Lahr, J.C., 1975. HYPO71 (Revised): A computer program for determining hypocenter, magnitude, and first motion pattern of local earthquakes. U .S. Geol. Surv., Open-File Rep., 75-311,113 pp.

Legrand, D., S., Kaneshima, H., Kawakatsu, 2000. Moment tensor analysis of near-field broadband waveforms observed at Aso Volcano, Japan. Journal of Volcanology and Geothermal Research, 101(1-2), 155-169, doi: 10.1016/S0377-0273(00)00167-0.

Lesage, Ph., Mora, M., Alvarado, G., Pacheco, J., Metaxian, J.-Ph., 2006. Complex behavior and source model of the volcanic tremor at Arenal volcano, Costa Rica. Journal of Volcanology and Geothermal Research, 157, 49-59.

Lesage, Ph., Surono, 1995. Seismic precursors of the February 10, 1990 eruption of Kelut volcano, Java. Journal of Volcanology and Geothermal Research, 65, 135-146.

Lesage, Ph., Reyes-Dávila, G., Arámbula-Mendoza, R., 2013 (submitted). Large tectonic earthquakes induce sharp temporary decreases of seismic velocity in a volcano, Journal Volcanology and Geothermal Research.

Lube, G., Cronin, S.J., Thouret, J.-C., Surono, 2011. Kinematic characteristics of pyroclastic density currents at Merapi and controls on their avulsion from natural and engineered channels. Geological Society of America Bulletin 123, 1127–1140.

Luehr, B.-G., Koulakov, I., Rabbel, W., Zschau, J., Ratdomopurbo, A., Brotopuspito, K.S., Fauzi, P., Sahara, D.P., 2013. Fluid ascent and magma storage beneath Gunung Merapi revealed by multi-scale seismic imaging. Journal of Volcanology and Geothermal Research 261, 7–19.

Müller, A., Haak, V., 2004. 3-D modeling of the deep electrical conductivity of Merapi volcano (Central Java): integrating magnetotellurics, induction vectors and the effects of steep topography. Journal of Volcanology and Geothermal Research 138, 205–222.

Müller, M., Hördt, A., Neubauer, F.M., 2002. Internal structure of Mount Merapi, Indonesia, derived from long-offset transient electromagnetic data. Journal of Geophysical Research, 107, ECV2-1-ECV2-14.

Maercklin, N., 1999. Polarisationsanalyse refraktionsseismischer Daten vom Vulkan Merapi, Indonesien.

McGarr, A.,1976. Seismic moments and volume changes. Journal of Geophysical Research. 81 (B8): doi: 10.1029/OJGREA0000810000B8001487000001. Issn: 0148-0227.

McKee, C. O., D. A. Wallace, R. A. Almond, and B. Talai, Fatal hydroeruption of Karkar volcano in 1979: Development of a maar-like crater, in Cooke-Ravian Volume of Volcanological Papers, edited by R. W. Johnson, Geol. Surv. P. N. G. Mem., 10, 63–84, 1981a.

McNutt, S. R., Volcanic tremor, in Encyclopedia of Earth System Science, vol. 4, 417–425, Academic, San Diego, Calif., 1992.

McNutt, S.R., 1996. Seismic monitoring of volcanoes: A review of the state of the art and recent trens. In: Scarpa, R., and R. Tilling (eds) Monitoring and Mitigation of Volcanic Hazards, Chapter3, Springer-Verlag, Berlin,p. 99-146.

McNutt, S.R., 2000. Volcanic Seismicity, Chapter 63 of Encyclopedia of Volcanoes, Sigurdsson, H., B. Houghton, S.R. McNutt, H. Rymer, and J. Stix (eds.), Academic Press, San Diego, CA, 1015-1033.

Mei, E.T.W., Lavigne, F., Picquout, A., de Bélizal, E., Brunstein, D., Grancher, D., Sartohadi, J., Cholik, N., Vidal, C., 2013. Lessons learned from the 2010 evacuations at Merapi volcano. Journal of Volcanology and Geothermal Research 261, 348–365.

Metaxian, J.-P., Lesage, P., Valette, B., 2002. Locating sources of volcanic tremor and emergent events by seismic triangulation: Application to Arenal volcano, Costa Rica. Journal of geophysical research 107, ECV10.1–ECV10.18.

Michael Commer, S.L.H., 2006. New results on the resistivity structure of Merapi Volcano (Indonesia), derived from three-dimensional restricted inversion of long-offset transient electromagnetic data. Geophysical Journal International 167, 1172 – 1187.

Molina, I., Kumagai, H., Yepes, H., 2004. Resonances of a volcanic conduit triggered by repetitive injections of an ash-laden gas. Geophysical Research Letters 31, n/a–n/a.

Mulugeta Dugda, A.K., 2010. Ratios in Higher Order Statistics (RHOS) values of Seismograms for Improved Automatic P-Phase Arrival Detection.

Nadeau, O., Williams-Jones, A.E., Stix, J., 2013. Magmatic–hydrothermal evolution and devolatilization beneath Merapi volcano, Indonesia. Journal of Volcanology and Geothermal Research 261, 50–68.

Neuberg, J.W., Tuffen, H., Collier, L., Green, D., Powell, T., Dingwell, D., 2006. The trigger mechanism of low-frequency earthquakes on Montserrat. Journal of Volcanology and Geothermal Research 153, 37–50.

Neumann van Padang, M., 1931. Der Ausbruch des Merapi (Mittel Java) im Jahre 1930. Z. Vulkanol. 14, 135–148.

Neumann van Padang, M., 1951. Indonesia, Part I, Catalogue of the active volcanoes of the world including solfatara fields. Int. Volcanol. Assoc., Napoli (Part 6.3-25, Merapi).

Newhall, C., Bronto, S., Alloway, B., Banks, N.G., Bahar, I., del Marmol, M.A., Hadisantono, R.D., Holcomb, R.T., MCGeehin, J., Miksic, J.N., Rubin, M., Sayudi, S.D., Sukhyar, R., Andreastuti, S., Tilling, R.I., Torley, R., Trimble, D., Wirakusumah, A.D., 2000. 10000 years of explosive eruptions of Merapi Volcano, Central Java: archaeological and modern implications. Journal of Volcanology and Geothermal Research, 100, 9-50.

Niederleithinger E., Stahler S., Nowak T.-R., 2010. Detection of Subtle Changes in Materials by Coda Wave Interferometry (Germany). 10th European Conference on Non-Destructive Testing. Report : 4.2.18.

Norman, G.R., Streiner, D.L., 2008. Biostatistics. B.C. Decker, Hamilton; Lewiston, NY.

Obermann, A., Planès, T., Larose, E., Campillo, M., 2013a. Imaging preeruptive and coeruptive structural and mechanical changes of a volcano with ambient seismic noise. Journal of Geophysical Research: Solid Earth 118, 6285–6294.

Obermann, A., Planès, T., Larose, E., Sens-Schönfelder, C., Campillo, M., 2013b. Depth sensitivity of seismic coda waves to velocity perturbations in an elastic heterogeneous medium. Geophys. J. Int. ggt043.

Ohminato, T., Chouet, B., Dawson, P., Kedar, S., 1998. Waveform inversion of very long period impulsive signals associated with magmatic injection beneath Kilauea Volcano, Hawaii. Journal of Geophysical Research, 103, B10, 23,839-23862.

Okada, H., Watanabe, H., Yamashita, H., Yokoyama, I., 1981. Seismological significance of the 1977–1978 eruptions and the magma intrusion process of usu volcano, Hokkaido. Journal of Volcanology and Geothermal Research 9, 311–334.

Paasschens, J.C.J., 1997. Solution of the time-dependent Boltzmann equation. Phys. Rev. E 56, 1135–1141.

Pacheco, C., Snieder, R., 2005. Time-lapse travel time change of multiply scattered acoustic waves. The Journal of the Acoustical Society of America 118, 1300–1310.

Paige, C.C., Saunders, M.A., 1982. LSQR: An Algorithm for Sparse Linear Equations and Sparse Least Squares. ACM Trans. Math. Softw. 8, 43–71.

Panagiotakis, C., Kokinou, E., Vallianatos, F., 2008. Automatic -Phase Picking Based on Local-Maxima Distribution. IEEE Transactions on Geoscience and Remote Sensing 46, 2280–2287.

Pandolfi, D., Bean, C.J., Saccorotti, G., 2006. Coda wave interferometric detection of seismic velocity changes associated with the 1999 M = 3.6 event at Mt. Vesuvius. Geophysical Research Letters 33, n/a–n/a.

Picquout, A., Lavigne, F., Mei, E.T.W., Grancher, D., Noer, C., Vidal, C.M., Hadmoko, D.S., 2013. Air traffic disturbance due to the 2010 Merapi volcano eruption. Journal of Volcanology and Geothermal Research 261, 366–375.

Planès, T. (2013), Imagerie de changements locaux en régime de diffusion multiple. Ph D Thesis, Université de Grenoble, Grenoble, France.

Poupinet, G., Ratdomopurbo, A., Coutant, O., 1996. On the use of earthquake multiplets to study fractures and the temporal evolution of an active volcano. Ann. Geophys. 39.

Power, J., Lahr, J.C., Page, R.A., Chouet, B., Stephens, C., Harlow, D.H., Murray, T.L., Davies, J.N., 1994. Seismic evolution of the 1989-1990 eruption sequence of Redoubt volcano, Alaska. Journal of Volcanology and Geothermal Research, 62, 69-94.

Pyle, D. 2000. Sizes of volcanic eruptions. In Sigurdsson et al., Encyclopedia of Volcanoes, 888 Academic Press, San Diego, 263-270.

Qamar, A., St. Lawrence, W., Moore, J.N., Kendrick, G., 1983. Seismic signals preceding the explosive eruption of Mount St. Helens, Washington, on 18 May 1980. Bulletin of Seismological Society of America, 73(6): 1797-1813.

Ratdomopurbo, A., 1995. Etude Sismologique du Volcan Merapi et Formation du dôme de 1994. PhD Thesis, Université Joseph Fourier-Grenoble I, France.

Ratdomopurbo, A., G. Poupinet, 1995. Monitoring a temporal change of seismic velocity in a volcano: application to the 1992 eruption of Mt. Merapi (Indonesia), Geophysical Research Letter, 22 (7), 775-778,

Ratdomopurbo, A. Poupinet, G., 2000. An overview of the seismicity of Merapi volcano, (Java, Indonesia), 1983-1995. Journal of Volcanology and Geothermal Research, 100, 193-214.

Ratdomopurbo, A., Beauducel, F., Subandriyo, J., Agung Nandaka, I.G.M., Newhall, C.G., Suharna, Sayudi, D.S., Suparwaka, H., Sunarta, 2013. Overview of the 2006 eruption of Mt. Merapi. Journal of Volcanology and Geothermal Research 261, 87–97.

Rebscher, D., Westerhaus, M., Welle, W., Nandaka, I.G.M.A., 2000. Monitoring ground deformation at the decade volcano Gunung Merapi, Indonesia. Physics and Chemistry of the Earth, Part A: Solid Earth and Geodesy 25, 755–757.

Richter, C.F., 1935. An instrumental earthquake magnitude scale, Bulletin of the Seismological Society of America, 25: 1-32.

Richter, C.F., 1958. Elementary Seismology. Freeman, San Fransisco., 768 pp.

Richter, G., Wassermann, J., Zimmer, M., Ohrnberger, M., 2004. Correlation of seismic activity and fumarole temperature at the Mt. Merapi volcano (Indonesia) in 2000. Journal of Volcanology and Geothermal Research 135, 331–342.

Riedel, C., Maercklin, N., Rabbel, W., Wegler, U., Lühr, B.G., 1999. Die seismische Untergrundstruktur des Vulkans Merapi (Java, Indonesien), in: 59. Jahrestagung, Deutsche Geophysikalische Gesellschaft. Braunschweig, Germany.

Ritter, O., Hoffmann-Rothe, A., Müller, A., Dwipa, S., Arsadi, E.M., Mahfi, A., Nurnusanto, I., Byrdina, S., Echternacht, F., Haak, V., 1998. A magnetotelluric profile across Central Java, Indonesia. Geophysical Research Letters 25, 4265–4268.

Rowe, C. 2000. Correlation-Based Phase Pick Correction and Similar Earthquake Family Identification in Large Seismic Waveform Catalogs, Ph.D. Thesis, New Mexico Institute of Mining and Technology, Socorro.

Rust, A.C., Balmforth, N.J., Mandre, S., 2008. The feasibility of generating low-frequency volcano seismicity by flow through a deformable channel. In: S.J. Lane and J.S. Gilbert (Editors), Fluid motions in volcanic conduits: a source of seismic and acoustic signals. Geological Society, Special Publications, London, pp. 45-56.

Saccorotti, G., Bianco, F., Castellano, M., Del Pezzo, E., 2001. The July-August 2000 seismic swarms at Campi Flegrei volcanic complex, Italy. Geophysical Research Letter, 28(13), 2525-2528.

Saepuloh, A., Urai, M., Aisyah, N., Sunarta, Widiwijayanti, C., Subandriyo, Jousset, P., 2013. Interpretation of ground surface changes prior to the 2010 large eruption of Merapi volcano using ALOS/PALSAR, ASTER TIR and gas emission data. Journal of Volcanology and Geothermal Research 261, 130–143.

Saragiotis, C.D., Hadjileontiadis, L.J., Panas, S.M., 2002. PAI-S/K: A robust automatic seismic P phase arrival identification scheme. IEEE Transactions on Geoscience and Remote Sensing 40, 1395–1404.

Sato, H., 1993. Energy Transportation In One- and Two-Dimensional Scattering Media: Analytic Solutions of the Multiple Isotropic Scattering Model. Geophysical Journal International 112, 141–146.

Sens-Schönfelder, C., 2008. Synchronizing seismic networks with ambient noise. Geophysical Journal International 174, 966–970.

Sens-Schönfelder, C., Wegler, U., 2006. Passive image interferometry and seasonal variations of seismic velocities at Merapi Volcano, Indonesia. Geophysical Research Letters 33,

Shang, T. & Gao, L., 1988. Transportation theory of multiple scattering and its application to seismic coda waves of impulsive source, Sci. Sinica, 31, 1503-1514.

Shimozuru, D., Miyazaki, T., Gyoda, N., Matahelumual, J., 1969.Volcanological survey of Indonesian volcanoes: Part 2. Seismic observation at Merapi Volcano. Bull. Earth. Res. Inst. 47, 969–990.

Shokouhi, P., Niederleithinger, E., Zoëga, A., Barner, A., Schöne, D., 2010. Using Ultrasonic Coda Wave Interferometry For Monitoring Stress-Induced Changes In Concrete. Presented at the 23rd EEGS Symposium on the Application of Geophysics to Engineering and Environmental Problems.

Sidik, M., 1989. Penyelidikan kakas gravitasi di Gunung Merapi, Gunung Merbabu dan sekitarnya. Report of Gadjah Mada University, Yogyakarta, Indonesia, 165 pp.

Smith, R. Kilburn, C. R. J., Sammonds, P. R., 2007. Rock fracture as a precursor to lava dome eruptions at Mount St Helens from June 1980 to October 1986. Bulletin of Volcanolology 69, 681–693, DOI 10.1007/s00445-006-0102-5

Snieder, R., Grêt, A., Douma, H., Scales, J., 2002. Coda Wave Interferometry for Estimating Nonlinear Behavior in Seismic Velocity. Science 295, 2253–2255.

Sparks, R.S.J., 2003. Forecasting volcanic eruptions. Earth and Planetary Science Letters 210, 1–15.

Sri-Sayudi D., Muzani M., Nurnusanto I., 2007. Sebaran awanpanas dan daya tampung sungai-sungai yang terisi material erupti 2006. Edisi Khusus Merapi 2006: Laporan dan Kajian Vulkanisme Erupsi. Pusat Vulkanologi dan Mitigasi Bencana Geologi.

Stähler, S.C., Sens-Schönfelder, C., Niederleithinger, E., 2011. Monitoring stress changes in a concrete bridge with coda wave interferometry. The Journal of the Acoustical Society of America 129, 1945–1952.

Stehly, L., Campillo, M., Shapiro, N.M., 2007. Traveltime measurements from noise correlation: stability and detection of instrumental time-shifts. Geophysical Journal International, 171: 223-230, doi: 10.1111/j.1365-246X.2007.03492.x.

Stephens, C., Chouet, B.A., Page, R.A., Lahr, J.C., Power, J.A., 1994. Seismological aspects of the 1989-1990 eruptions at Redoubt volcano, Alaska: the SSAM perspective. Journal of Volcanology and Geothermal Research, 62: 153-182.

Suharna, Budi-Santoso A., Dwiyono S., Jilal M., 2007. Statistik dan analisis seismisitas Merapi 2006. Edisi Khusus Merapi 2006: Laporan dan Kajian Vulkanisme Erupsi. Pusat Vulkanologi dan Mitigasi Bencana Geologi.

Surono , Jousset P., Pallister J., Boichu M., Buongiorno M. F. , Budi-Santoso A., Costa F., Andreastuti S., Prata F., Schneider D. , Clarisse L., Humaida H., Sumarti S., Bignami C., Griswold J., Carn S. and Oppenheimer C., 2012. The 2010 explosive eruption of Java's Merapi volcano - a '100-year' event. Journal of Volcanology and Geothermal Research, 241-242, 121-135

Tarantola, A., Valette, B., 1982. Generalized nonlinear inverse problems solved using the least squares criterion. Reviews of Geophysics 20, 219–232.

Thelen, W.A., Allstadt, K., De Angelis, S., Malone, S.D., Moran, S.C., Vidale, J., 2013. Shallow repeating seismic events under an alpine glacier at Mount Rainier, Washington, USA. Journal of Glaciology 59, 345–356.

Thomson, R., 1985. A note on restricted Maximum Likelihood Estimation with an alternative outliers model. Journal of the Royal Statistical Society: Series B, 47, 53-55.

Tibuleac, I.M., Nolet, G., Caryl, M., Koulakov, I., 2003. P wave amplitudes in a 3-D earth. Geophysical Journal International 155, 1–10.

Tokarev PI (1963) On a possibility of forecasting of Bezymianny volcano eruptions according to seismic data. Bull Volcanol 26:379–386

Tokarev PI (1966) Eruptions and seismic regime of the Klyuchevskaya group volcanoes. Nauka, Moscow, pp 1–118 (in Russian)

Tokarev, P.I., 1971. Forecasting volcanic eruptions from seismic data. Bulletin of Volcanology, 35, 243-250.

Tokarev, P.I., 1985. The prediction of large explosions of andesitic volcanoes. Journal of Geodynamics, 3, 219-244.

Tong, C., 1995. Characterization of seismic phases—an automatic analyser for seismograms. Geophys. J. Int. 123, 937–947.

Traversa, P., Lengliné, O., Macedo, O., Metaxian, J. P., Grasso, J. R., Inza, A., Taipe, E., 2011. Short term forecasting of explosions at Ubinas volcano, Perú, Journal of Geophysical Research, 116, B11301, doi:10.1029/2010JB008180.

Troll, V.R., Deegan, F.M., Jolis, E.M., Harris, C., Chadwick, J.P., Gertisser, R., Schwarzkopf, L.M., Borisova, A.Y., Bindeman, I.N., Sumarti, S., Preece, K., 2013. Magmatic differentiation processes at Merapi Volcano: inclusion petrology and oxygen isotopes. Journal of Volcanology and Geothermal Research 261, 38–49.

Tutuncu, A.N., Podio, A.L., Sharma, M.M., 1994. Strain Amplitude and Stress Dependence of Static Moduli in Sandstones and Limestones. 1st North American Rock Mechanics Symposium.

Untung, M., Sato, Y., 1978. Gravity and geological studies in Java, Indonesia. Special publication, GSI and GSJ, Joint research program on regional tectonics.

van der Neut, J. R.,M. K. Sen, and K.Wapenaar, 2007, Monitoring effective stress changes in fault zones from time-lapse seismic reflection data—A model study: 69th Annual Conference and Exhibition, EAGE, Extended Abstracts, PO61.

Vetterling, W.T., 1992. Numerical recipes example book (C). Cambridge University Press, Cambridge; New York.

Voight B, 1988. A method for prediction of volcanic eruptions. Nature 332, 125–130

Voight, B., 1989. A relation to describe rate-dependent material failure. Science 2

Voight, B., Constantine, E. K., Sismowidjoyo, S., Torley, R., 2000. Historical eruptions of Merapi Volcano, Central Java, Indonesia, 1768-1998. Journal of Volcanology and Geothermal Research, 100, 69-138.

Voight, B., Cornelius, R.R., 1991. Prospects for eruption prediction in near real-time. Nature 350, 695–698.

Wagner D., Koulakov, I., Rabbel, W., Lühr, B-G., Wittwer, A., Kopp, H., Bohm, M., Asch, G., the MERAMEX scientists, 2007. Joint inversion of active and passive seismic data in Central Java, Geophysical Journal International, 170, 923-932.

Wahyudi, 1986. Penyelidikan gaya berat di Gunung Merapi. Report of Gadjah Mada Univ., Yogyakarta, Indonesia, 136 pp.

Waite, G. P., Chouet, B. A., Dawson, P. B., 2008. Eruption dynamics at Mount St. Helens imaged from broadband seismic waveforms: Interaction of the shallow magmatic and hydrothermal systems, Journal of Geophysical Research, 113, B02305, doi:10.1029/2007JB005259

Waldhauser, F., 2001. HYPODD--A program to compute double-difference hypocenter locations, U.S. Geologic Survey Open-File Report.

Waldhauser, F., 2012. HYPODD--A program to compute double-difference hypocenter locations (Updated), U.S. Geologic Survey Open-File Report.

Waldhauser, F., Ellsworth, W.L., 2000. A Double-Difference Earthquake Location Algorithm: Method and Application to the Northern Hayward Fault, California. Bulletin of the Seismological Society of America 90, 1353–1368.

Wassermann, J., Ohrnberger, M., 2001. Automatic hypocenter determination of volcano induced seismic transients based on field coherence –an application to the 1998 eruption of Mt. Merapi, Indonesia, Journal of Volcanology and Geothermal Research, 110, 57-77.

Weaver, R., Froment, B., Campillo, M., 2009. On the correlation of non-isotropically distributed ballistic scalar diffuse waves. The Journal of the Acoustical Society of America 126, 1817–1826.

Wegler, U., Lühr, B.-G., Ratdomopurbo, A., 1999. A repeatable seismic source for tomography at volcanoes. Annali di Geofisica, 42(3), 565-571.

Wegler, U., Lühr, B.-G., 2001. Scattering behavior at Merapi volcano (Java) revealed from an active seismic experiment. Geophysical Journal International, 145, 3, 579-592, 10.1046/j.1365-246x.2001.01390.x.

Wegler, U., Lühr, B.-G., Snieder, R., Ratdomopurbo, A., 2006. Increase of shear wave velocity before the 1998 eruption of Merapi volcano (Indonesia), Geophysical Research Letter, 33, L09303, doi:10.1029/2006GL025928.

West, M., 2008. Tools and topics in seismic waveform cross-correlation.

West, M., 2010. Correlation Toolbox.

Westerhaus, M., Altmann, J., Heidbach, O., 2008. Using topographic signatures to classify internally and externally driven tilt anomalies at Merapi Volcano, Java, Indonesia. Geophysical Research Letters 35, n/a–n/a.

Withers, M., Aster, R., Young, C., Beiriger, J., Harris, M., Moore, S., Trujillo, J., 1998. A comparison of select trigger algorithms for automated global seismic phase and event detection. Bulletin of the Seismological Society of America 88, 95–106.

Wong, J., Han, L., Bancroft, J.C., Stewart, R.R., 2009. Automatic time-picking of first arrivals on noisy microseismic data, in: 2009 CSPG CSEG CWLS Convention. Calgary, Canada.

Wu, C., 2007. Temporal change of seismic velocity and site response for different scales and implications for nonlinearity (Thesis). Georgia Institute of Technology.

Yokoyama, I., 1988. Seismic energy release from volcanoes. Bulletin of Volcanology, 50, 1-13.

Yokoyama, I., Suryo, I., Nazhar, B., 1970. Volcanological Survey of Indonesian Volcanoes, Pt. 4, Gravity Survey in Central Java. Earthq. Res. Inst. Bull. 48, 317–329.

Young, K.D., Voight, B., Subandriyo, Sajiman, Miswanto, Casadevall, T.J., 2000. Ground deformation at Merapi Volcano, Java, Indonesia: distance changes, June 1988–October 1995. Journal of Volcanology and Geothermal Research 100, 233–259.

Zaccarelli, L., Shapiro, N.M., Faenza, L., Soldati, G., Michelini, A., 2011. Variations of crustal elastic properties during the 2009 L'Aquila earthquake inferred from cross-correlations of ambient seismic noise. Geophysical Research Letters 38, n/a–n/a.

Zhan, Z., Tsai, V.C., Clayton, R.W., 2013. Spurious velocity changes caused by temporal variations in ambient noise frequency content. Geophys. J. Int. ggt170.

Zhang, H., 2003. Automatic P-Wave Arrival Detection and Picking with Multiscale Wavelet Analysis for Single-Component Recordings. The Bulletin of the Seismological Society of America 93, 1904–1912.